Institute of Physical and Theoretical Chemistry

Characterization of organic molecules at metal/electrolyte interfaces

Tomasz Kosmala

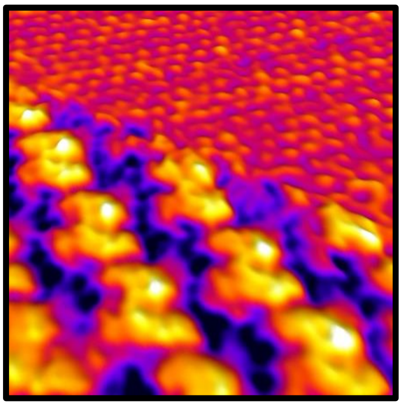

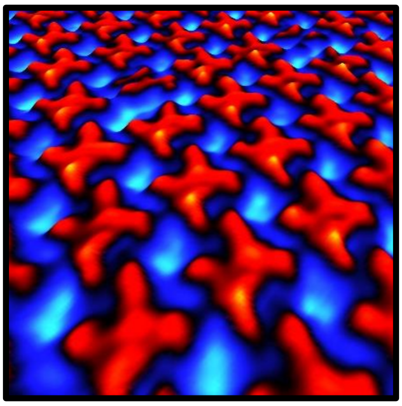

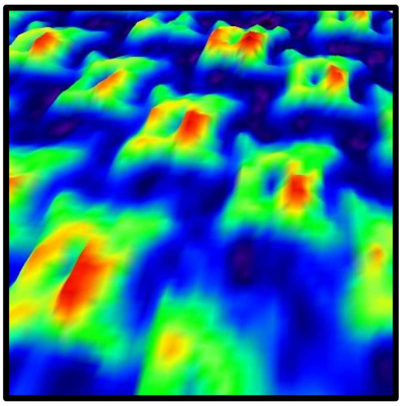

Characterization of organic molecules at metal/electrolyte interfaces

Dissertation
zur Erlangung des Doktorgrades (Dr. rer. nat.)
der
Mathematisch-Naturwissenschaftlichen Fakultät
der
Rheinischen Friedrich-Wilhelms-Universität Bonn

vorgelegt von

Tomasz Kosmala

aus

Lubin, Poland

Bonn 2015

Angefertigt mit Genehmigung der Mathematisch-Naturwissenschaftlichen

Fakultät der Rheinischen Friedrich-Wilhelms-Universitat Bonn

1. Gutachter: Prof. Dr. Klaus Wandelt
2. Gutachter: Prof. Dr. Thomas Bredow

Tag der Promotion: 03/03/2016

Erscheinungsjahr: 2017

*Dedicated to my beloved parents, **Ewa** and **Zbigniew Kosmala**,*

my brother and my homeland

Contents

I Introduction and outline

II Theoretical background

III Experimental

IV Self-assembly of porphyrin molecules on iodine-modified gold surfaces – results

V Discussion and Conclusions

List of abbreviations

CE	Counter Electrode
CV	Cyclic Voltammogram
E	Working potential vs Pt/PtI
EC-STM	Electrochemical Scanning Tunneling Microscopy
fcc	face-centered cubic
GDR	Oxidative Gold Dissolution Reaction
H_2TMPyP	5,10,15,20-Tetrakis-(N-methylpyridinium-4-yl) porphyrin Tetrakis-(p-toluolsulfat)
H_2TTMAPP	5,10,15,20-Tetrakis (4-trimethylammoniophenyl) porphyrin tetra (p-toluenesulfonate)
I_t	Tunneling Current
IHP	Inner Helmholtz Plane
LEED	Low Energy Electron Diffraction
ML	Monolayer
NND	Nearest Neighbor Distance
OER	Oxygen Evolution Reaction
OHP	Outer Helmholtz Plane
RE	Reference Electrode
RHE	Reversible Hydrogen Electrode

STM	Scanning Tunneling Microscopy
U_b	Bias Voltage
UHV	Ultra High Vacuum
WE	Working Electrode

List of Figures

List of Tables

List of Movies

Chapter I

Introduction and outline

Nowadays, the self-assembly of atoms and molecules plays a considerable role in a range of fields: chemistry, physics, biology, materials science. This subject is a key concept in supramolecular chemistry, biological systems and nanotechnology. As a "bottom-up" technique, it is a promising route to create surface patterns, electronic devices with nanometer dimension, and complex organic structures [1,2].

Most supramolecular architectures are assembled from simpler well-studied structural and functional molecular building-blocks via non-covalent weak forces which often reveal a directional character [3-7]. This creates molecular architectures which exhibit a significantly higher complexity than the individual molecular building-blocks following Lehn's definition of supramolecular chemistry as the "chemistry beyond the molecule" [4,8]. In order to control the ordering process of supramolecular architectures one can take advantage of well-defined single crystal surfaces which can operate as electronic and/or geometric templates due to the operation of specific adsorbate-substrate interactions. These supramolecular structures are composed according to the symmetry and periodicity of the substrate surface. In contrast to the assembly of supramolecular architectures in solution and in the 3D solid-state where assembly is govern only by the specific and directional intermolecular interactions between the building blocks, on surfaces a complex interplay between adsorbate-adsorbate and adsorbate-substrate interactions controls the 2D phase formation behaviour. Therefore, it is not surprising that the resultant structure pattern and intermolecular spacings of these 2D supramolecular aggregates on surfaces are different from those found in the solution phase or in the 3D solid-state [9]. Since larger organic molecules tend to be thermally labile, these molecules are better deposited from solution. Furthermore, if these molecules are deposited electrochemically in the form of ions (from their solvable salts) the electrochemical potential is a further very useful control parameter which allows to influence the self-assembly process. Thus, the electrochemical solid-liquid interfaces is a good choice in order to study the 2D self-organization process of organic molecules.

It is well-know that the solid/liquid interface plays a fundamental role in a diverse range of phenomena encountered in biological, chemical and physical processes, for example in many electrochemical, electrocatalytic and biological reactions. In the case of a metal in contact with an electrolyte, a lot of interesting processes can be carried out on the metal surface, such as adsorption/desorption of species from the electrolyte like anions and cations, e.g. organic ions, surface reactions like corrosion/passivation, deposition/growth of new compounds, etching/plating etc.. Unraveling the atomic structure at a solid/liquid interface and of processes occurring at this interface with atomic/molecular resolution is, therefore, one of the major challenges of today's surface science to investigate and to understand the elementary steps of these processes with model systems in order to apply them effectively in our daily life.

In order to exploit this route much fundamental research combining organic chemistry and modern surface physics is indispensable. On the one hand organic chemistry is able to synthesize almost any type of molecule that is desired. These molecules may then be used to create self-assembled arrays on a substrate surface. On the other hand characterization of these molecular layers requires modern surface physical methods, in particular high resolution scanning probe microscopy. Thus, by combining in-situ Scanning Tunneling Microscopy (STM) with submolecular resolution with more traditional electrochemical techniques such as Cyclic Voltametry (CV) enables to investigate such self-assembly phenomena at solid-liquid interfaces in the presence of anions and organic molecules as a function of electrode potential.

In this work porphyrins are chosen to study the self-assembly on iodide-modified Au(100) surfaces. Porphyrins are well-known to play a very important role in natural vital processes such as in heme for the transfer and storage of oxygen in blood or chlorophyll for the photosynthesis of green plants [10]. Furthermore they open a range of potential applications in cancer therapy [11-14], or as catalysts [15] and sensors [16,17]. In this framework two kinds of porphyrins, namely 5,10,15,20-Tetrakis-(N-methylpyridinium-4-yl) porphyrin Tetrakis-(p-toluolsulfat), in short H_2TMPyP, and 5,10,15,20-Tetrakis (4-trimethylammoniophenyl) porphyrin tetra (p-toluenesulfonate), abbreviated as H_2TTMAPP, are used for the investigations. Due to their attractiveness some applications of H_2TMPyP and H_2TTMAPP can be found in the literature. In the form of water soluble cationic porphyrins (H_2TMPyP, Metal-TMPyP, Metal-TTMAPP) these molecules are applied in cancer photodynamic therapy [18-20] due to their binding affinity to synthetic and natural DNA [21-24]. The photo-induced redox reactions in a hybrid film of a cationic porphyrin (H_2TMPyP) led to their applications in the construction of efficient solar energy storage devices and novel light-stimulated sensors [25]. Furthermore, H_2TMPyP molecules were proven to be good sensors for the detection of benzene [26] and heavy metal ions (Hg^{2+}, Pb^{2+}, Cd^{2+}) [28], likewise H_2TTMAPP molecules were proven to be cation sensing molecules (Zn^{2+}, Cu^{2+}) [27]. That is why, the study of the properties of these adsorbed porphyrin is of special interest.

In fact, highly ordered adlayers of H_2TMPyP were already found on various iodide modified electrode surfaces such as I/Au(111) [29-32], I/Pt(100), I/Ag(111) [33-34], I/Cu(111) and I/Cu(100) [35]. However studies on the self-assembly of porphyrins on the iodide precovered Au(100) surface have not yet been reported. Furthermore, there are no records of self-assembly of H_2TTMAPP on iodide-modified single crystal surface yet.

In this dissertation the self-assembly of these porphyrin molecules was investigated at gold/electrolyte interface by using in situ STM, and the work is organized in 5 chapters. This "Introduction and outline" chapter presents the motivation for doing this work and the outline of the thesis. In Chapter 2 is presented a short overview about electrochemistry at metal/electrolyte interfaces, the fundamental interactions in molecular self-assembly, the principle theory of cyclic voltammetry measurements and the theory and principle of operation of Scanning Tunneling Microscopy. Chapter 3 describes the experimental setup and the preparation of electrolytes, tips and the sample, the Au(100) substrate and its modification by iodine, and the molecular adsorbates used in this work. In Chapter 4 are presented the results of the self-assembly of the porphyrin molecules on the I/Au(100) surface. The Chapter 5 comes with the discussion and conclusion of all results for this work.

Chapter II

Theoretical Background

2.1 Introduction

Solid/liquid interfaces are omnipresent in nature and belong to the most intensively studied subjects in physical chemistry. Many scientifically and technologically relevant processes occur at solid/liquid interfaces, i.e. wetting, adsorption, corrosion, electron transfer and heterogeneous catalysis. Studying the structure and reaction processes at solid/liquid interfaces is of particular importance in electrochemistry and surface science, and will further our understanding of catalysis, surface modification, biological processes, sensors, electronic devices, etc.. Therefore, an atomic-scale understanding of the interfacial structure is necessary to control the manufacture of new low-dimensional materials and surface structures. In this chapter, the conventional structure models of electrified solid-liquid interfaces are presented, as well as the occurrence of reactions and molecular self-assembly at those interfaces. Furthermore, cyclic voltammetry and scanning tunneling microscopy are described as methods which enable to investigate such reactions and self-assembly phenomena at solid-liquid interfaces in the presence of anions and organic molecules as a function of electrode potential [32,35].

2.2 Structure of the solid-liquid interface

At the border of two phases, due to potential difference between the liquid electrolyte and an electrically conducting solid a charge is accumulated and an electric double layer is formed. Overall the interface between the two phases must be electrically neutral. For instance, a positively charged electrode attracts negative ions and repels positive ones. As a result of this near the surface a charge (q_e) is accumulated which results from the excess of negative ions. The value of this charge will be compensated by the same value but opposite sign of surface charge (q_s), i.e. $q_s + q_e = 0$. This surface charging can be carefully controlled by the applied ”Galvani” potential of the electrode.

A number of models for the double layer have been proposed differing in the spatial distribution of the accumulated counter-charges in the surface near electrolyte region [36-39].

2.2.1 The Helmholtz model

One of the first models of the electric double layer was introduced by Helmholtz in 1879. Helmholtz assumed that the ions contained in an electrolyte solution either in the positive or negative state are arranged in a single layer parallel to the metal surface negatively/positively charged, because they are attracted by pure electrostatic forces. The resultant "double-layer" at the metal/electrolyte interface is thus a kind of a flat capacitor, the conductive plates of which are charged in the metal and the oppositely charged adsorbed ion layer. The distance between the capacitor plates is approximately equal to the sum of the radii of the surface atoms and the *solvated* anions.

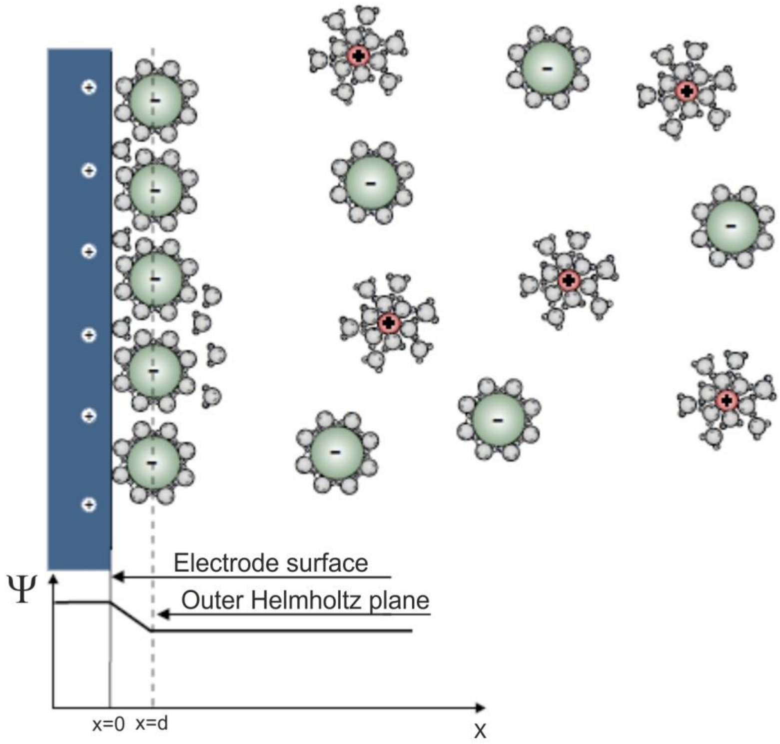

Figure 2.1: The Helmholtz model.

The potential drop $\Psi(x)$ across the double-layer can be described by the solution of the Poisson equation:

$$\frac{d^2\Psi(x)}{dx^2} = \frac{\rho(x)}{\varepsilon\varepsilon_0} \tag{2.1}$$

where ρ represents the charge density, ε the dielectric constant of water and ε_0 the dielectric constant of the vacuum.

For the Helmholtz – model the solution of this equation is given by:

$$\frac{d\Psi(x)}{dx} = const, \tag{2.2}$$

i.e. the potential drop occurs in a linear manner between the metallic surface and the so called outer Helmholtz plane through the centres of the adsorbed hydrated ions (see Fig. 2.1). The Helmholtz model, however, does not include factors such as, diffusion/mixing in solution, the possibility of direct ("specific") absorption of non-hydrated ions on the surface, and the interaction between solvent dipole moments and the electrode.

2.2.2 The Gouy-Chapman model

Louis Georges Gouy (1910) and David Leonard Chapman (1913) made significant improvements by introducing a diffuse model of the electrical double layer (Fig. 2.2). The competition between the forces of electrostatic attraction and thermal diffusive forces causes a diffuse distribution of charge carriers within the electric double layer. Gouy and Chapman assumed that one charged layer is evenly distributed on the conductive surface immersed in the electrolyte. A second compensative charge layer is found in the solution and has a diffuse nature. They assumed also that the ions are regarded as point charges. This, however, is also a major weakness of the model because the point charge ions can come arbitrarily close to the surface, what will be shown below.

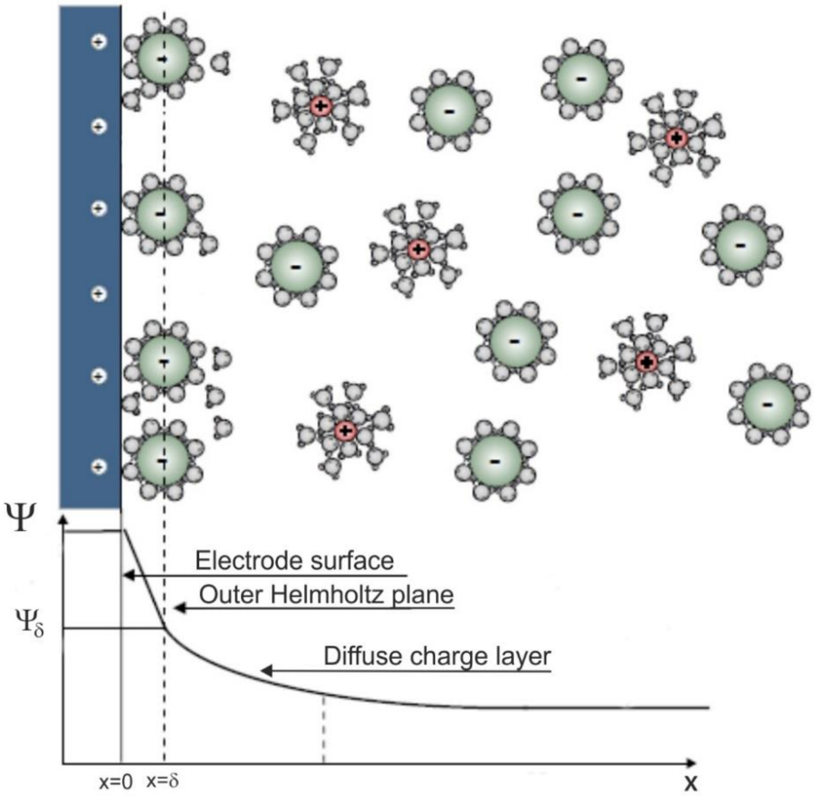

Figure 2.2: The Gouy-Chapman model.

Using the Boltzmann equation for describing the distribution of charges in the diffuse electric double layer as well as the spatial charge density, and using the Poisson equation, one gets:

$$\frac{d^2\Psi(x)}{dx^2} = \frac{2n_0 z^2 e^2 \Psi(x)}{\varepsilon\varepsilon_0 kT} \tag{2.3}$$

where n_0 is the total ion concentration, k is the Boltzmann constant, z is the ion valency and *e* is the electron charge.

Combining the many constants equation (2.3) can be rewritten as:

$$\frac{d^2\Psi(x)}{dx^2} = \kappa^2 \Psi(x) \tag{2.4}$$

Under the condition that the potential drop is small, i.e. $z\Psi_0 < 25mV$ and using common boundary conditions ($\Psi(0) = \Psi_0$ and $\Psi(\infty) = 0$) the following simple solution for the partial differential equation of second order is obtained:

$$\Psi(x) = \Psi_0 e^{-\kappa x} \tag{2.5}$$

Thus, it follows an exponential decay of the potential and the space charge density as a function of the distance to the electrode.

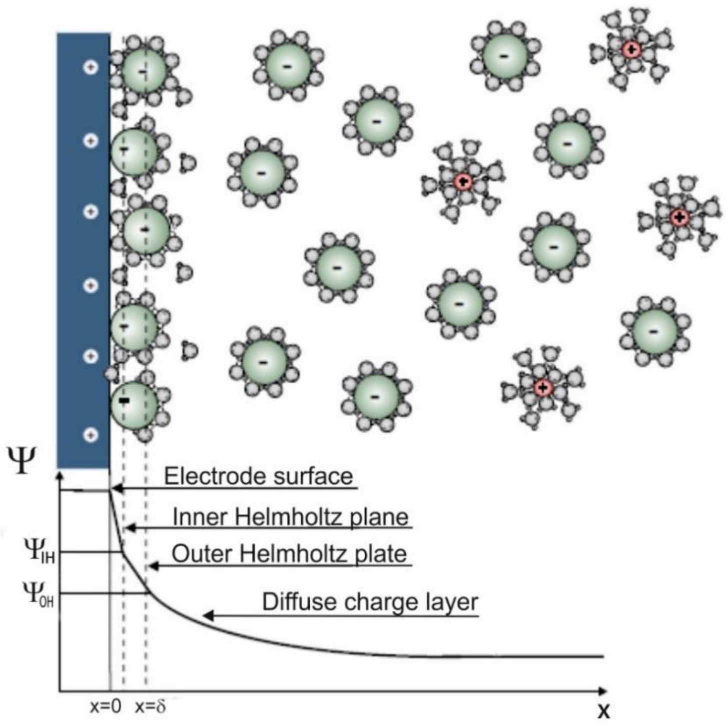

Figure 2.3: The Gouy-Chapman-Stern-Grahame model.

κ is given by:

$$\kappa = \sqrt{\frac{2n_0 z^2 e^2}{\varepsilon\varepsilon_0 kT}} \tag{2.6}$$

and is the inverse Debye-Hückel length, also called the thickness of the double layer ($\delta = 1/\kappa$). The Debye-Hückel length can be thought of as the approximate radius of the ionic atmosphere of an ion. For z=1, the approximate δ values calculated for electrolyte concentrations of 1mM and 10μM are 10nm and 1μm, respectively. Consequently the screening of the surface charge increases with the concentration of the acting ion, and the double layer thickness decreases. Therefore the Gouy-Chapman Model theory is valid only in the limit of low concentrations. The theory breaks down when the concentration of the electrolyte is greater than about 100 mM.

2.2.3 The Gouy-Chapman-Stern-Grahame model

The Gouy-Chapman model provides a better approximation of reality than does the simple Helmholtz model, but it still has limited quantitative application. Stern adapted the Gouy-Chapman model to take into account the fact that ions have finite size, and consequently have a closest approach to the electrode of the order of their radius. This model for the electrode/electrolyte interface proposes the existence of two regions: The Inner and the Outer Helmholtz Plane (IHP or OHP) as depicted in Fig. 2.3. The electric double layer consists of a rigid part with linear potential change up to the outer Helmholtz plane and a diffuse part with exponential potential change. The total capacity is then given by:

$$\frac{1}{C} = \frac{1}{C_H} + \frac{1}{C_{diff}} \tag{2.7}$$

C_H is due to the Helmholtz layer and C_{diff} arises from the diffuse layer.

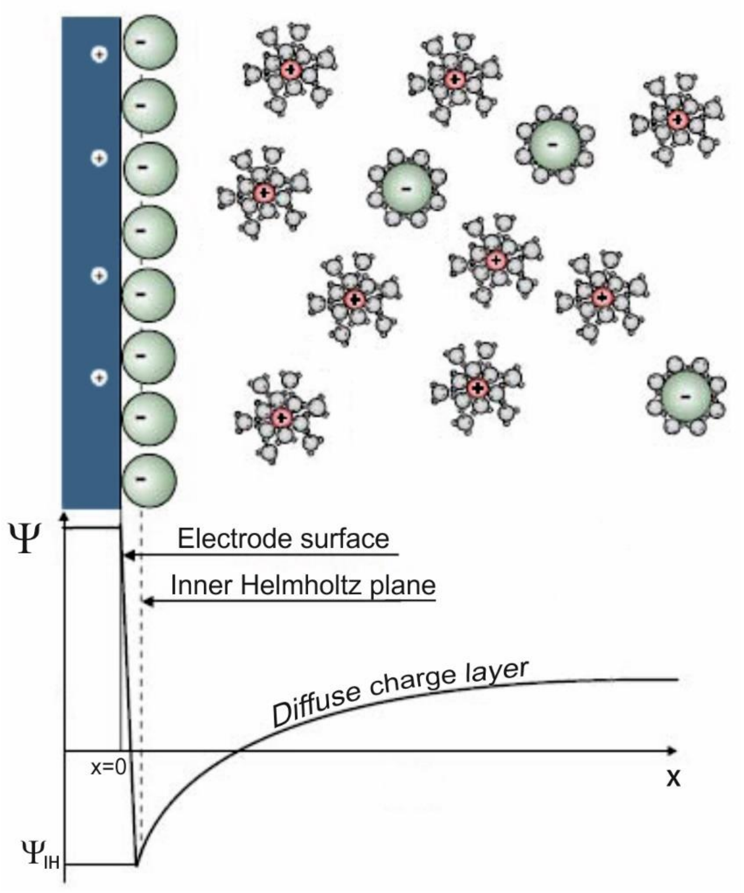

Figure 2.4: Strong specific anion adsorption.

Stern also considered the effect of “specific” interactions between the ions and the electrode surface suggesting the distinction between ions, which were adsorbed on the electrode *without* hydration sphere and ions which approach the surface only to closest distance *with* hydration sphere. A more appropriate explanation gave Grahame in 1947. He suggests that, although the closest approach to the electrode is determined by solvent molecules, it may also be possible for some ionic or uncharged species to penetrate into this region (Fig. 2.3). This could come about if the ions loose partially or completely their solvation shell. Ions in direct contact are called: *specifically adsorbed*. Anions like SO_4^{2-}, Cl^-, Br^- or I^- with relatively weakly bound solvation water have a tendency to specific adsorption. In many cases, specific anion adsorption leads to the formation of a condensed anion layer. As show in Fig. 2.4. the potential decreases linearly between the electrode surface and the inner Helmholtz plane, and afterward, re-increases exponentially towards the value in the bulk solution. This strong specific anion adsorption forms a condensed, ordered and laterally immobile layer, which can be well observed by microscopic methods such as the electrochemical scanning tunneling microscopy (EC-STM). Furthermore, such a layer can be used as a template for the self-assembly of organic molecules, particularly if they are positively charged in their cationic state.

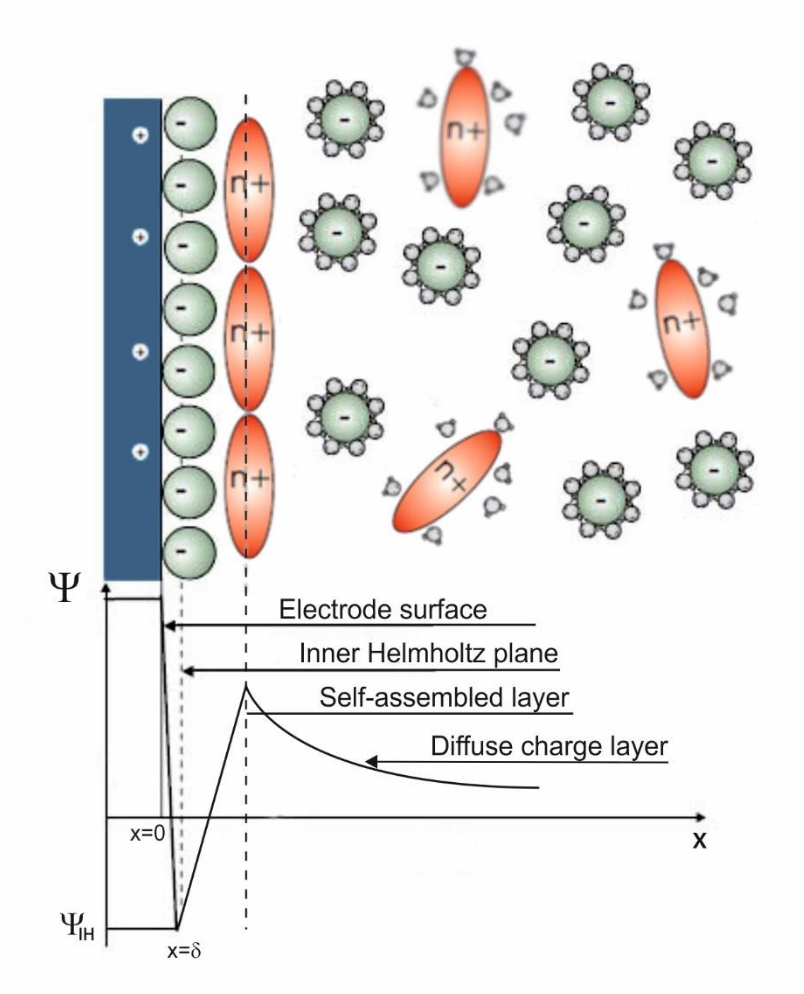

Figure 2.5: The self-assembly of organic cations on a specifically adsorbed anion layer.

2.3 Reactions at solid-liquid interfaces

A reaction at a solid-liquid interface is a heterogeneous chemical process involving the transfer of electrons to or from the surface which is generally a metal or a semiconductor. The charge transfer may be an anodic reaction whereby a species is oxidised by the loss of electrons to the electrode, e.g.

$$2H_2O - 4e^- \rightarrow O_2 + 4H^+ \tag{2.8}$$

$$2Cl^- - 2e^- \rightarrow Cl_2 \tag{2.9}$$

$$Ce^{3+} - e^- \rightarrow Ce^{4+} \tag{2.10}$$

Inversely, the reaction may be a cathodic process in which a species is reduced by the gain of electrons from the electrode, e.g.

$$2H_2O + 2e^- \rightarrow H_2 + 2OH^- \tag{2.11}$$

$$Cu^{2+} + 2e^- \rightarrow Cu \tag{2.12}$$

$$Fe^{3+} + e^- \rightarrow Fe^{2+} \tag{2.13}$$

By convention, the current density for an anodic process is a positive quantity while for a cathodic process it is a negative quantity. The amount of reduction at the cathode and oxidation at the anode must be equal due to the need to maintain an overall charge balance [36].

The electrode reactions can be vary with different electroactive species like organic or inorganic, neutral or charged, a species dissolved in solution, the solvent itself, a film on the electrode surface or the electrode material itself. The many types of reactions at solid-liquid interface are also illustrates pictorially in Fig. 2.6.

In general at the electrochemical environment, two possible charge transfer reactions can be distinguished: an electron transfer reaction, where the charge carriers are electrons, and there is no other mass transport through the interface, e.g. (2.13), and an ion transfer reaction, where the charge carriers are ions, i.e. there is mass transport through the interface, e.g. (2.12).

However, even the simplest reactions taking place at the solid-liquid interface where two species O (oxidized species) and R (reduced species) interconvert into each other (which are completely stable and soluble in the electrolyte medium containing an excess of an electrolyte which is electro-inactive):

$$O \quad + \; ne^{-} \; \leftrightarrow \; R \tag{2.14}$$

are usually more complex because they may be multistep processes. Therefore, to maintain a current it is vital to supply the reactant to the electrode surface and also to remove the product, as well as for the electron transfer reaction at the surface to occur. Accordingly, for example, under experimental conditions where O is reduced to R, the reaction at the solid-liquid interface must have three steps:

$$O_{bulk} \xrightarrow{mass\ transport} O_{electrode} \tag{2.15}$$

$$O_{electrode} \xrightarrow{electron\ transfer} R_{electrode} \tag{2.16}$$

$$R_{electrode} \xrightarrow{mass\ transport} R_{bulk} \tag{2.17}$$

and since the reduction rate, and thus the cathodic current, is govern by the rate of the overall sequence, it depends on the rate of the slowest step. Thus to understand the characteristics of such a reaction at the solid-liquid interface, one needs detailed knowledge about both mass transports and about the electron transfer processes.

An examination of reactions (2.8) – (2.13) and the sketches in Figure 2.6 quickly shows that electrode reactions are commonly not that simple. They can involve multiple electron transfer, and at least three additional types of basic steps also occur like: adsorption-desorption (which is in our case an important phenomenon and will be more described below), phase formation and coupled chemical reactions [36].

The adsorption/desorption of species from/into the electrolyte onto/from the electrode surface are common processes as a results of interactions between adsorbats and surfaces, depending on the nature of the respective surface and the adsorbat. As mentioned in the previous section 2.2 adsorption can be specific or non-specific.

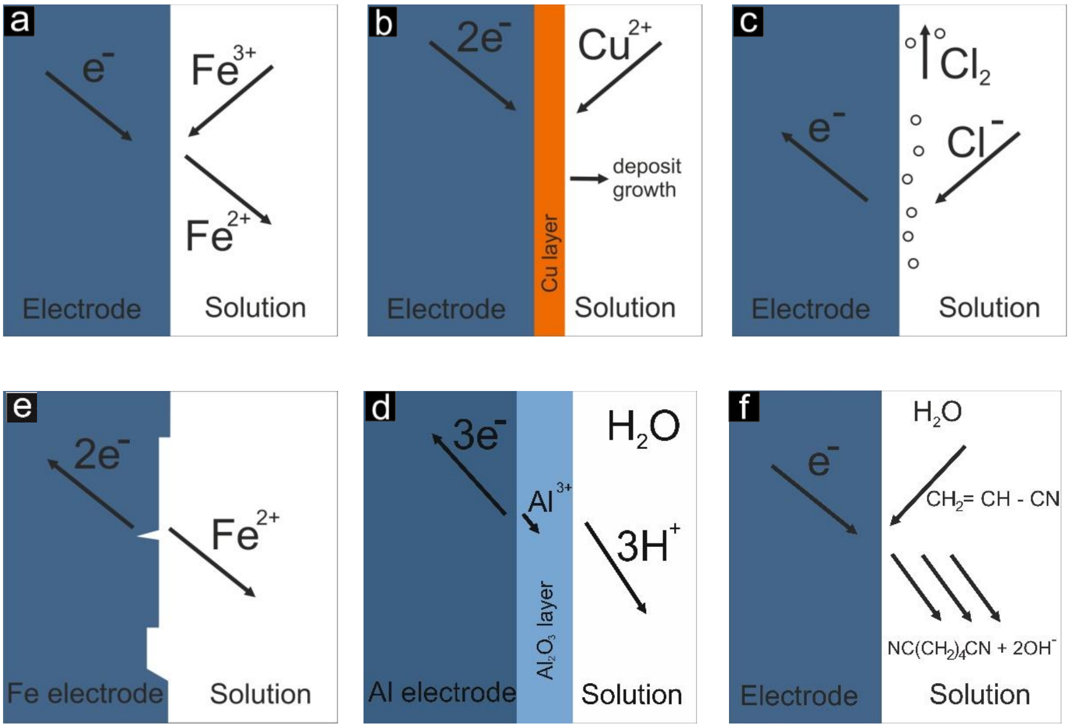

Figure 2.6: Schematic view of some types of reactions at solid-liquid interface. a) simple electron transfer, e.g. $Fe^{3+} + e^- \to Fe^{2+}$; b) metal deposition, e.g. $Cu^{2+} + 2e^- \to Cu$; c) electrolysis with gas evolution, e.g. $2Cl^- - 2e^- \to Cl_2$; d) corrosion, e.g. $Fe - 2e^- \to Fe^{2+}$; e) oxide film formation, e.g. $2Al + 3H_2O - 6e^- \to Al_2O_3 + 6H^+$; f) electron transfer with coupled chemistry, e.g. $2(CH_2 = CH - CN) + 2H_2O + 2e^- \to NC(CH_2)_4CN + 2OH^-$.

The surface-adsorbate interaction may be merely electrostatic (e.g. the adsorption of cations or anions on a surface of opposite charge), of van der Waals type, dipolar, or due to the formation of hydrogen bridge bonds or of a covalent bond, etc. or a mixture of them.

Adsorption and phase transitions of ions on a charged electrode surfaces strongly depend on the electrode potential, since for each value of the potential the electrode will have a characteristic surface charge. If the electrode is more positively charged it will adsorb anions more strongly, while a more negatively charged surface can lead to desorption of anions. In some cases, the surface coverage Θ, i.e. the fraction of the surface covered by the adsorbate, clearly varies with electrode potential, such as, for example, reflected in the so-called electro-compression/decompression of iodide on Au (100) and Au (111) [32,50,57].

An un-charged species can also adsorb on an electrode surface. The adsorption in fact must be considered as a competition between all species in the system which interact with the electrode surface. While the charged electrode promotes the adsorption of ions of opposite charge or dipoles, the adsorption of neutral molecules occurs most strongly when competition from charged species is at a minimum, and this is the case when the electrode is uncharged, i.e. at the so-called "potential of zero charge". Hence the surface coverage of species depends on the solvent, electrolyte, molecular structure and concentration and the concentration of any other species in the system as well as the nature of the electrode surface.

The relation between coverage of an adsorbate and its concentration in solution in many case can be expressed by an adsorption isotherm. There are several isotherms which differ in the extent and method of taking into account lateral interactions between adjacent adsorbate species such as: 1) The Langmuir isotherm - a fundamental monolayer isotherm which neglects lateral interaction, 2) the Frumkin isotherm – an interaction isotherm considering lateral interaction, 3) the Temkin isotherm – a heterogeneous surface isotherme, etc...

The adsorption and desorption of adsorbates on electrode surfaces in many cases can be qualitatively characterized by cyclic voltammetry. Since adsorption and desorption processes are surface limited processes, changes in the double layer capacity and partial charge transfer from adsorbates to the electrode lead to the appearance of current peaks or waves in a cyclic voltammogram [35] (see section 2.5).

2.4 Molecular self-assembly at solid/liquid interface

Molecular self-assembly is a spontaneous process by which molecules associate under equilibrium conditions into stable, structurally defined arrangements joined by intermolecular interactions, without guidance or management from an outside source. It is a key concept in supramolecular chemistry, biological systems and nanotechnology. As a “bottom-up” technique, it is a promising route to create surface patterns, electronic devices with nanometer dimension, and complex organic structures [1,2]. For these reasons the molecular self-assembly on solid surface has been intensively studied in recent years. We can distinguish two different strategies of self-assembly of molecules on solid surfaces, namely in ultrahigh vacuum (UHV) and at solid/liquid interfaces.

The molecular self-assembly process at solid/liquid interfaces proved that large organic molecules, which are not intact volatile, are better deposited from solution. Furthermore, if these molecules are deposited electrochemically in the form of ions (from their solvable salts) the electrochemical potential is a further very useful control parameters which allows to influence the self-assembly process. The self assembly process itself is governed by interactions between the adsorbing molecules (intermolecular interactions), the adsorbed molecules and the substrate, and the molecules and the solvent. Non-covalent intermolecular interaction which can govern the self-assembly of molecules may be [35]:

- *Electrostatic interactions* are attractive or repulsive interactions and occur between charged species. They are relatively strong compared to other non-covalent interactions, and are not directional.

- *Hydrogen bonding* is the attractive interaction of a hydrogen atom with an electronegative atom of an adjacent molecule. These interactions occur only when the interacting functional groups are properly oriented, and they are weak (but stronger than van der Waals interactions) and directional.

- *Van der Waals interactions* are due to always attractive dispersion forces between atoms and molecules, also on surfaces. These interactions are weak but play a fundamental role in many fields of science. They are non-directional and less specific than other non-covalent interactions, in fact they act between all kinds of molecules.

- *Hydrophobic "interactions"* occur between non-polar molecules and are the major driving force for hydrophobic molecules to aggregate, e.g. on a surface in aqueous solution.

- *π –π interactions* occur between aromatic moieties when aromatic rings are present facing each other, and are caused by intermolecular overlapping of p-orbitals in π-conjugated systems; they become stronger with increasing number of π-electrons.

2.5 The cyclic voltammetry

Cyclic voltammetry [36-38] is an electro-analytical technique in which information about the analyte is derived from the measurement of a current (Faradaic or capacitive current) as a function of a potential applied to an electrode. It is perhaps the most effective and common electro-analytical technique available for the mechanistic study of redox systems.

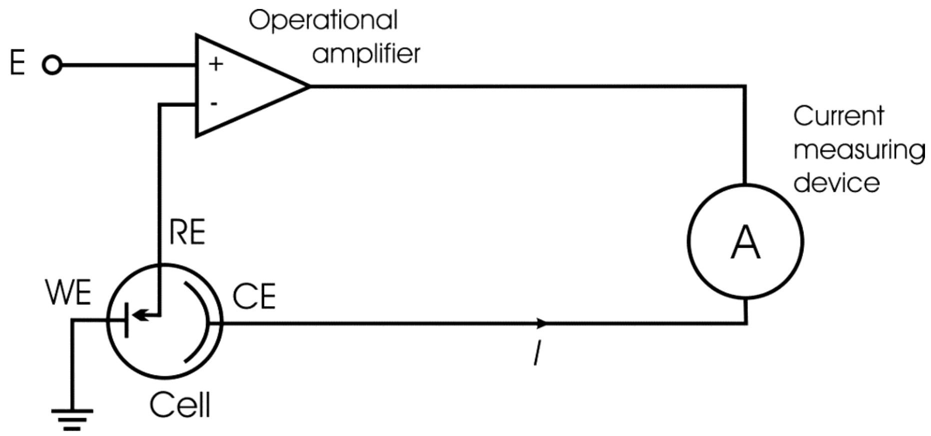

Figure 2.7: The principle of a potentiostat.

Cyclic voltammetry measurements are carried out using an electrochemical cell consisting of three electrodes immersed in a solution containing the analyte and an excess of non-reactive electrolytes called supporting electrolyte. One of the three electrodes is the working electrode (WE), where the redox process takes place. The second electrode is the counter electrode (CE) which has the purpose to supply the current required by the working electrode without in any way limiting the measured response of the cell. The third electrode is a reference electrode (RE). Its role is to provide a fixed potential which does not vary during the experiment, e.g. it should be independent of current density.

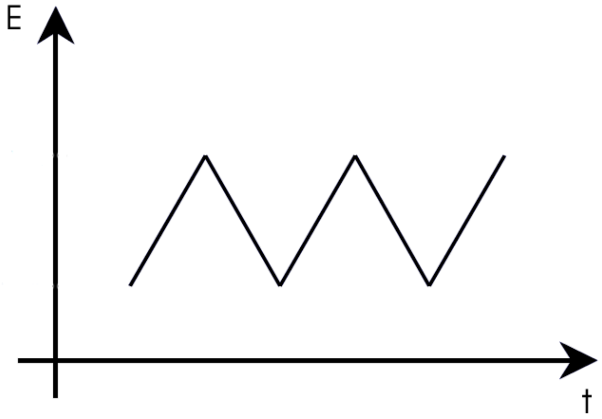

Figure 2.8: A triangular waveform is applied to the working electrode.

The idea of this experiment is to applied a repetitive triangular potential waveform (Fig. 2.8) to the working electrode and to measure the resultant current. The potential is measured between the reference electrode and the working electrode and the potential of the WE is controlled versus the RE, using a potentiostat (Fig. 2.7). The current is measured between the working electrode and the counter electrode.

Experimental results are plotted as a graph of current versus potential; a typical voltammogram for a reversible reaction is shown in Fig. 2.9. The voltammogram exhibits two asymmetric peaks, one cathodic (c) and one anodic (a) peak due to a redox reaction. For a redox reaction induced at a working electrode, the rate determining step may be any one of the following individual steps depending on the system: rate of mass transport of the electro-active species to the electrode, rate of adsorption or desorption at the electrode surface, rate of the electron transfer between the electro-active species and the electrode, rate of the transformation of one solid phase into another, or rates of the individual chemical reactions which are part of the overall reaction scheme.

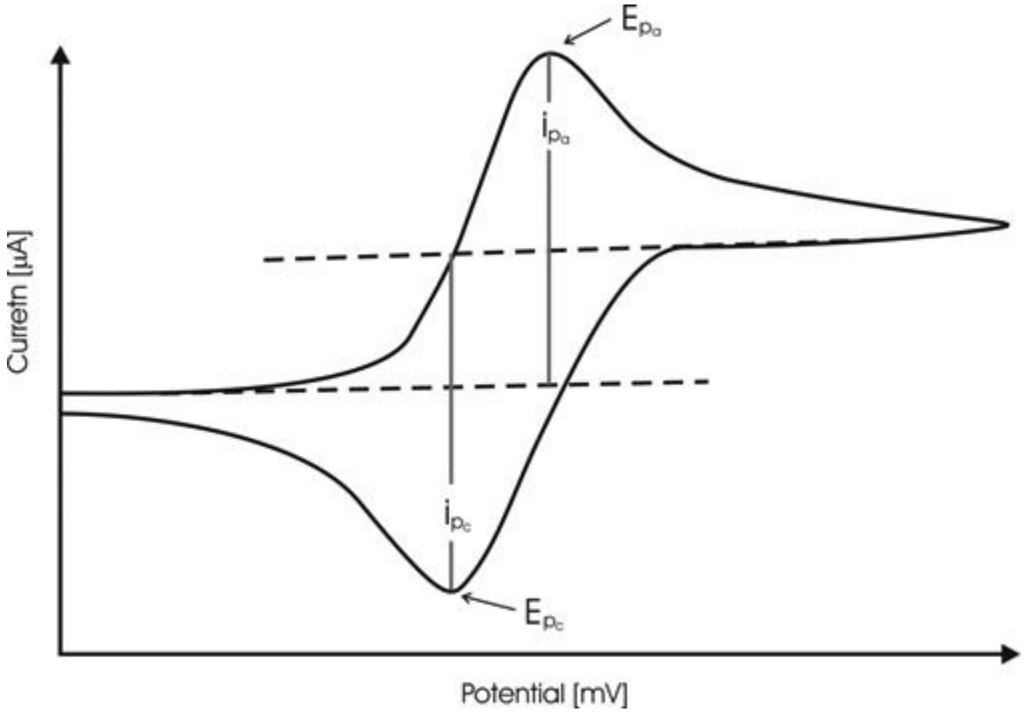

Figure 2.9: A typical cyclic voltammogram where i_{pc} / E_{pc} and i_{pa} / E_{pa} denote the cathodic and anodic peak current/potential, respectively, for a reversible reaction.

The cyclic voltammogram is characterized by several parameters. Four of these observables are the cathodic and anodic peak currents, and the respective cathodic and anodic peak potentials.

The expression of the peak current (Amp.) for a reversible couple (at 298 K) is given by the Randles–Sevcik equation:

$$I_p = 0{,}446 nFAC\sqrt{\frac{nFvD}{RT}} \tag{2.18}$$

where: n is the number of electrons appearing in the half-reaction for the redox couple, υ is the rate at which the potential is swept (V / sec), F is Faraday's constant (96485 C / mol), A is the electrode area (cm^2), R is the universal gas constant (8.314 J/ mol K), T is the absolute temperature (K), and D is the analyte's diffusion coefficient (cm^2/sec).

The peak height, I_p, is directly proportional to the concentration of electroactive species in solution and to the square roots of the sweep rate and the diffusion coefficient. The current peaks are commonly measured with respect to the extrapolated baseline current preceding the peak (see dashed line in Fig. 2.9). Provided that the charge–transfer reaction is reversible, i.e. that the electron transfer process is fast, and that the redox products are stable, the ratio of the reverse-to-forward peak currents $i_{p,r} / i_{p,f}$ is unity. In addition, for such a system the separation between peaks is given by (for an *n* electron transfer reaction) at all scan rates:

$$\Delta E_p = E_{p_a} - E_{p_c} = \frac{59}{n} mV \tag{2.19}$$

Thus, the peak separation can be used to determine the number of electrons transferred. However, the measured value is generally higher due to uncompensated solution resistance and non-linear diffusion. In cases for slow electron transfer kinetics the value of $\Delta Ep = 59/n$ mV increases with increasing scan rate.

2.6 Scanning Tunneling Microscopy

The inventors of the first Scanning Tunneling Microscope (STM) were Gerd Binning and Henrich Rohrer from IBM's research laboratory in Rüschlikon near Zürich [40]. In 1978 they began to study growth processes, surface structures and electrical properties of very thin layers of oxides. The invention of the tunneling microscope in 1982 allowed them to observe the surface reconstruction of the Si(111)7x7 and of the gold Au (110) surface with atomic resolution [40]. STM has revolutionized the field of surface science since it allows the direct imaging of surface structure and dynamics on the atomic scale. For this great achievement four years later they won the Nobel Prize for Physics.

The STM has first been used in ultra high vacuum (UHV) environment but it can also be used to obtain images of surfaces in contact with air or liquids. In 1986 Sonnenfeld and Hansma introduce the first STM working at solid-liquid interfaces [81].

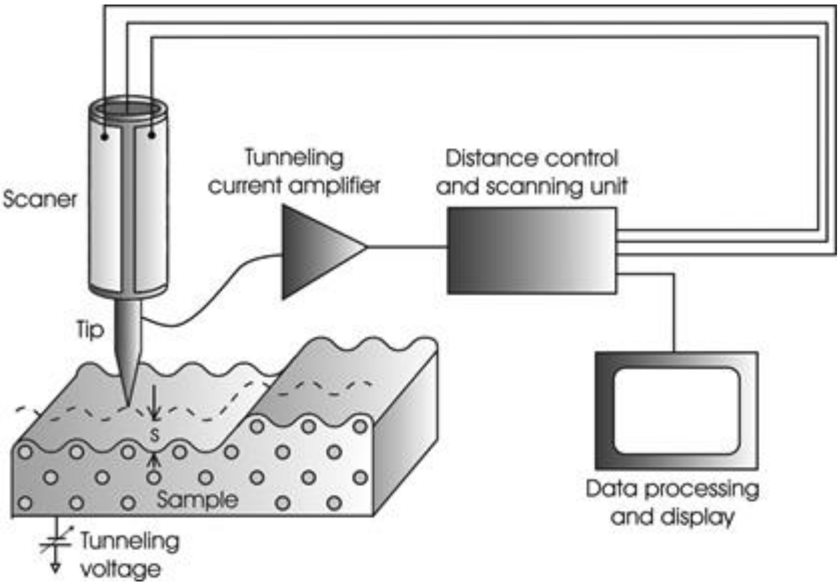

Figure 2.10: Working principle of the Scanning Tunneling Microscope (STM).

2.6.1 Tunneling effect

The STM is based on the concept of the quantum tunneling effect through a potential barrier [32, 41-42]. A potential barrier exists between two conducting electrodes, a scanning tip and sample, which are not in immediate contact. The basic idea is to bring the scanning tip in close proximity (a few Å) to a conductive sample. By applying a tunneling voltage, the so-called "bias voltage, of $U \leqslant 4V$ between the tip and the sample a small electric current (0.01nA-50nA) can flow from the sample to the tip or reverse (depending on the polarity), although the tip is not in physical contact with the sample. This phenomenon is called tunneling effect. By scanning the tip across the surface and detecting the tunneling current a map of the surface can be generated with a spatial resolution in the order of atomic distances. The resulting tunneling current is a function of the tip position with respect to the sample surface, the applied voltage, and the local density of states of the sample. The scheme of the working principle is shown on Fig. 2.10.

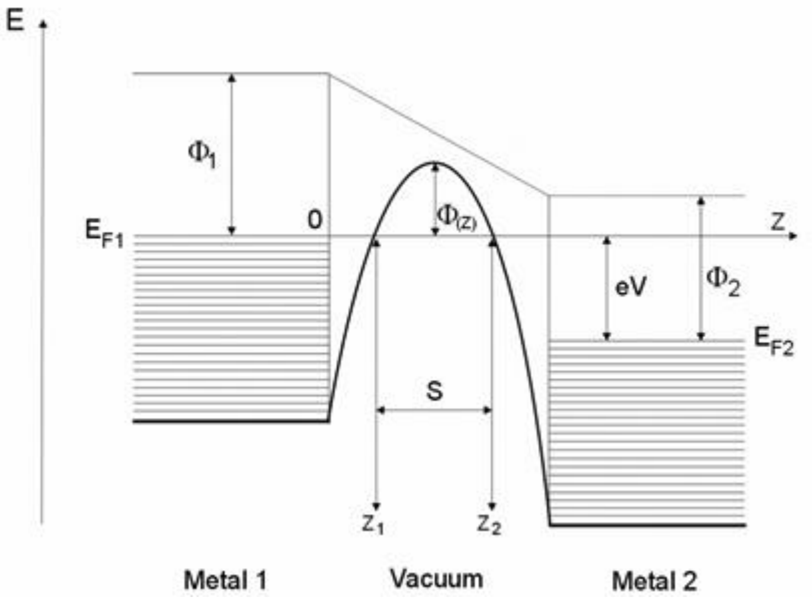

Figure 2.11: Potential barrier between two polarized metals by voltage V; s - barrier width, Φ_1,Φ_2 - work function for metal 1 and 2, E_{F1},E_{F2} - Fermi levels for metal 1 and 2.

Consider a system of two metals polarized by a voltage V (bias voltage) and a distance s apart. The potential barrier occurring between the two metals may have the height $\Phi(z)$. This situation is shown Fig. 2.11.

As a result of the applied potential V the Fermi levels of the two electrodes are shifted against each other. Opposite of the occupied states on the left side there are unoccupied states on the right side. As a consequence there is some probability that electrons will tunnel from the left side to the other side of the potential barrier.

In order to calculate the transition probability T between the occupied and unoccupied states let us consider the simplified case of a one-dimensional rectangular potential barrier (see Fig. 2.12).

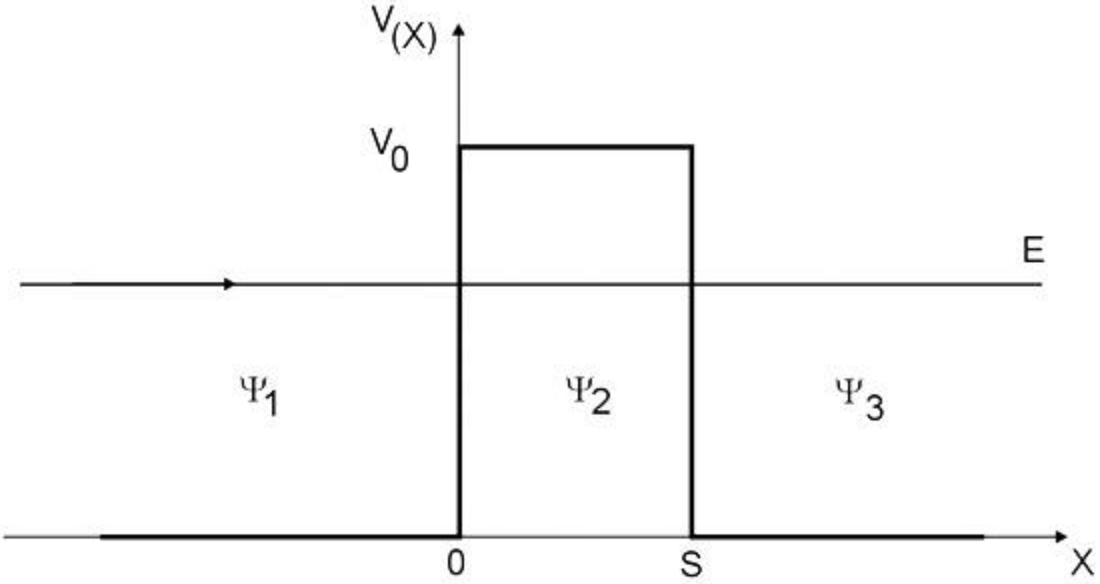

Figure 2.12: Domains relevant to the one-dimensional rectangular potential barrier, for the case $E < V_0$.

Imagine an electron moving with energy E from the left in the right direction. The electron encounters on its way the potential barrier with height V_o and width s. According to classical physics an electron having a higher energy than the barrier, i.e.

E>V_o passes easily *over* the barrier. However, if its energy E is smaller than the potential barrier V_o the electron cannot penetrate into or cross the potential barrier.

However, according to quantum mechanics, the situation is completely different. Even if E>V_o, there is some probability for the electron to be reflected at the barrier into the opposite direction. In turn, in the situation when the energy of the electron is smaller than the potential barrier, E<$V_{o,}$ there is also a probability that the electron crosses the potential barrier into the forward direction. Exact calculation of the transition probability in the rectangular barrier problem requires the Schrödinger's equation to be solved in the three regions: before, in and behind the barrier. In quantum mechanics the motion of the electron is describes by a wave function Ψ. This function is a solution of the Schrödinger equation, which looks as follows (for the one-dimensional problem):

$$\frac{\hbar^2}{2m}\frac{\partial^2\Psi}{\partial x^2}+(E-V)\Psi=0 \qquad (2.20)$$

where Ψ is a wave function, E is the energy of the moving electron, V is a potential field.

The potential function is zero for x < 0, constant V_o for 0 < x < s and again zero for x > s, as depicted in Fig. 2.12. The Schrödinger equation for the three domains appears as:

$$\frac{\hbar^2}{2m}\frac{\partial^2\Psi}{\partial x^2}+E\Psi=0 \qquad \text{for domains 1 and 3, where V=0} \qquad (2.21)$$

$$\frac{\hbar^2}{2m}\frac{\partial^2\Psi}{\partial x^2}+(E-V_0)\Psi=0 \qquad \text{for domain 2, where } V=V_o \qquad (2.22)$$

Writing Ψ_1 and Ψ_3 for the solution of (2.21) and Ψ_2 for the solution of (2.22), one obtains:

$$\Psi_1 = A_1 e^{ikx} + B_1 e^{-ikx}; \quad \frac{\hbar^2 k^2}{2m} = E \tag{2.23}$$

$$\Psi_2 = A_2 e^{\kappa x} + B_2 e^{-\kappa x}; \quad \frac{\hbar^2 \kappa^2}{2m} = E - V_0 \tag{2.24}$$

$$\Psi_3 = A_3 e^{ikx} \qquad ; \quad \frac{\hbar^2 k^2}{2m} = E \tag{2.25}$$

where $A_1 e^{ikx}$ represents the incident wave, $B_1 e^{ikx}$ the reflected wave, and $A_3 e^{ikx}$ the transmitted wave.

The coefficients A_1, B_1, A_2, B_2, A_3, have to be found from the boundary conditions of the wave function at $x = 0$ and $x = s$. The wave function and its derivative have to be continuous everywhere, so:

$$\Psi_1(0) = \Psi_2(0) \qquad \Psi_2(s) = \Psi_3(s) \tag{2.26}$$

$$\Psi_1'(0) = \Psi_2'(0) \qquad \Psi_2'(s) = \Psi_3'(s) \tag{2.27}$$

These conditions lead to the equations:

$$\begin{aligned} &A_1 + B_1 = A_2 + B_2 \\ &A_2 e^{\kappa s} + B_2 e^{\kappa s} = A_3 e^{iks} \\ &ikA_1 - ikB_1 = \kappa A_2 + \kappa B_2 \\ &\kappa A_2 e^{\kappa s} + \kappa B_2 e^{\kappa s} = ikA_3 e^{iks} \end{aligned} \tag{2.28}$$

The transition probability is defined as:

$$T = \frac{|J_{trans}|}{|J_{inc}|} \tag{2.29}$$

where J_{trans} is the current density of the transmitted wave, and J_{inc} is the current density of the incident wave.

And the current density itself is defined as (for the one-dimensional problem):

$$J(x) = \frac{\hbar}{2mi}\left(\Psi^*(x)\frac{d\Psi}{dx} - \Psi(x)\frac{d\Psi}{dx}^*\right) \tag{2.30}$$

Writing J_{inc} for the solution of 2.23 (only part of incident wave) and J_{trans} for the solution of (2.25), the transition probability follows as:

$$T = \frac{|A_3|^2}{|A_1|^2} \tag{2.31}$$

Solving equations (2.28) using algebra, the transition probability becomes:

$$T = \frac{4k^2\kappa^2}{(\kappa^2 - k^2)^2 \sinh^2(\kappa s) + 4k^2\kappa^2 \cosh^2(k\kappa)} \tag{2.32}$$

Considering the equations: $\cosh^2(x) - \sinh^2(x) = 1$ and $k = {}^1/_\hbar \sqrt{2mE}$, $\kappa = {}^1/_\hbar \sqrt{2m(V_0 - E)}$ one gets:

$$T = \frac{1}{1 + \dfrac{V_0^2}{4E(V_0 - E)} \sinh^2\left(\sqrt{\dfrac{2m(V_0 - E)}{\hbar^2}} s \right)} \tag{2.33}$$

This equation can be simplified by assuming that the potential barrier is high ($E << V_0 \rightarrow V_0 - E \approx V_0$, $V_0/E >> 1$)) and wide ($\kappa s \gg 1, \sinh(\kappa s) \approx {}^1\!/_2\, e^{\kappa s} >> 1$) and neglecting the one in the denominator (it is a small value compare to the rest). Then we obtain:

$$T \approx 16 \frac{E}{V_0} \exp\left(-\sqrt{\frac{8mV_0}{\hbar^2}} s \right) \tag{2.34}$$

Changing the symbol for the barrier height V_0 to Φ like in Fig. 2.11, and including the density of electronic states of both metals (sample and tip) the equation for the transition probability becomes:

$$T \propto \exp\left(-\left(\frac{8m}{\hbar^2} \right)^{1/2} \Phi^{1/2} s \right) \frac{1}{N_s(E)} \frac{1}{N_t(E - eV)} \tag{2.35}$$

According to Fermi's golden rule one can write the current flowing from the tip to the sample and correspondingly from the sample to the tip as:

$$I_{t \rightarrow s} = \int T N_s(E) N_t(E - eV) f_t(E - eV)[1 - f_s(E)]\ dE \tag{2.36}$$

$$I_{s \rightarrow t} = \int T N_s(E) N_t(E - eV)[1 - f_t(E - eV] f_s(E)\ dE \tag{2.37}$$

where: $f(E) = [\exp\left(\frac{E-E_f}{k_B T}\right) + 1]^{-1}$ is the Fermi-Dirac distribution, $N(E)$ is the density of states.

The occupied tip states (N_t, f_t) can tunnel into unoccupied sample states $(N_s, [1 - f_s])$. The origin of the common energy scale is chosen to be that of the sample, and thus the tip energy scale is shifted by ΔE = eV.

The total current flowing from the tip to the sample is then:

$$I = I_{t\to s} - I_{s\to t} = \int TN_t(E-eV)N_s(E)\left[f_t(E-eV) - f_s(E)\right]\, dE \tag{2.38}$$

At temperature T=0 the Fermi-Dirac distribution is a step function and one can write the total current flowing from the tip to the sample as:

$$I(T=0K) = \int_{E_F}^{E_F+eV} TN_t(E-eV)N_s(E)dE \tag{2.39}$$

The remaining integrand expression, dependent on the energy, may be approximated by constants for low voltage V, e.g. $N_t(E) = N_{t_0}, N_s(E) = N_{s_0}$. Finally the expression for the tunneling current results as:

$$I = TN_{t_0}N_{s_0}eV \propto \exp\left(-2\left[\frac{8\pi^2 m\Phi}{h^2}\right]^{1/2} s\right)eV \tag{2.40}$$

This equation shows that a current between the tip and sample depends linearly on the voltage and exponentially on the tunneling distance s.

2.6.2 Tunneling through an electrolyte

The principle of tunneling through an electrolyte solution are still not completely well understood and theoretical description is still being developed further [71-72]. Several aspects differing from tunneling processes in vacuum have to be taken into account to understand the process involved. The experimental data show that in solution the tunneling barrier height is significantly lower than in vacuum [73-74]. One of the explanations of this behaviour is that the work function is lowered by an adsorbed layer of the water molecules. Moreover, this water layer generates an oscillating two-dimensional network of maxima and minima of the potential energy surface due to the distribution and movement of the oxygen (maxima) and hydrogen (minima) atoms in the water molecules. Since the time spent by an electron in the barrier through an assumed gap of 10 Å, is at least two orders of magnitude shorter than the time needed for the molecules of the liquid to move about [75] an individual tunneling event through the barrier can be assumed to be static. Furthermore, it was shown that the potential energy surface with the minima at the position of the hydrogen atoms increases the tunneling probability. Therefore, a model was proposed in which electrons tunnel via a series of virtual intermediate states localized on the hydrogen atoms [72]. The overall tunneling current for an STM experiment, however, represents a time average due to the computing capabilities of the controller limiting the speed of information processing and the movement of the tip along the surface is several orders of magnitude slower that the movement of water molecules. Therefore, the influence of the water layer between tip and surface should average and have no significant influence on the recorded tunneling current [71]. On the other hand several groups have observed by conducting distance tunneling spectroscopy a nonexponential decay in the presence of ordered adlayers, which means that the local charge density distribution, even as a time average, is not uniform, and this can lead to a nonuniform potential barrier distribution [76-77].

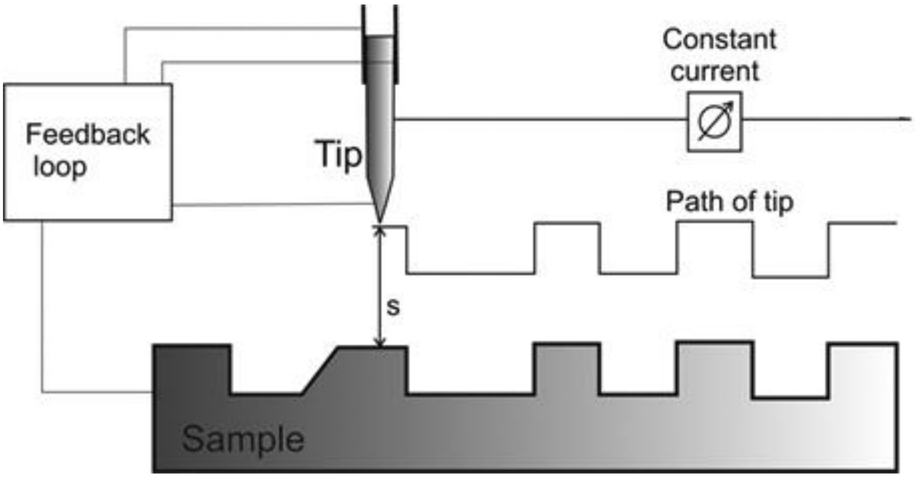

Figure 2.13: Constant-current mode.

2.6.3 Modes of operation

The Scanning Tunneling Microscope can be designed to scan the sample in one of two modes: constant-current (Fig. 2.13) or constant-height mode (Fig. 2.14) [42].

2.6.3.1 Constant-current mode

In the constant-current mode, by using a feedback loop the tip is vertically adjusted in such a way that the current always stays constant. For example, when the feedback loop detects an increase of the tunnel current, the feedback loop generates a voltage which is applied to the piezoelectric scanner to increase the distance between sample and tip in order to restore the fixed value of the current.

Vertical movement of the scanner and the registration of the distance changes between the tip and the sample generate a kind of topographic image of the surface. This constant-current mode should be used for samples with unknown topography, in particular rough surfaces, in order to minimize the risk that the tip hits a protrusion of the sample. The measurements are with high precision, but take, due to the movement of the tip, more time than in the following constant-height mode.

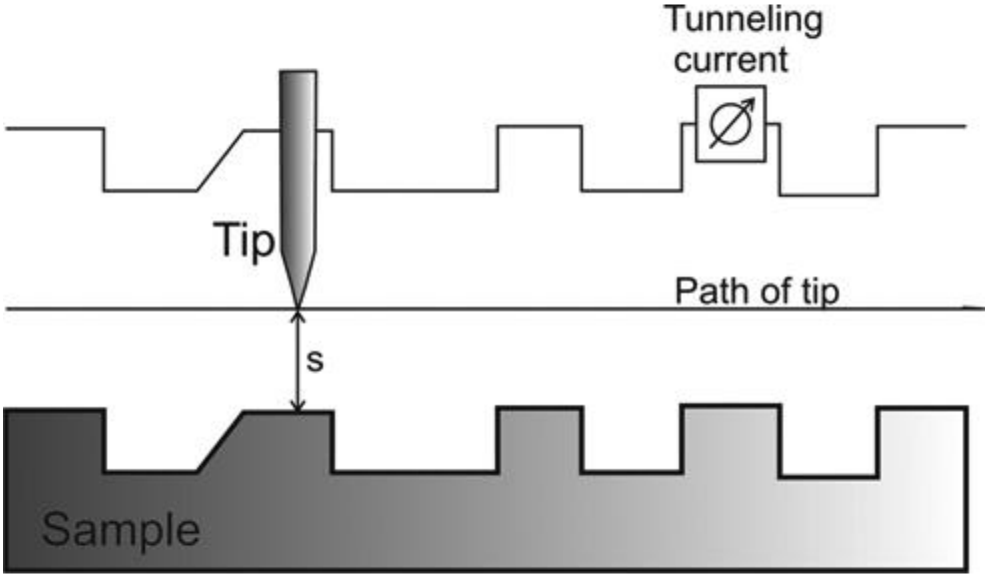

Figure 2.14: Constant-height mode.

2.6.3.2 Constant-height mode

In the constant-height mode the vertical position of the tip is not changed. The tunneling current varies depending on the continuous changes of the distance s between the tip and sample due to local changes in topographic and electronic properties. The current as a function of the lateral position represents an (apparent) topographic image of the surface. The constant-height mode is faster than the constant-current mode because the system does not have to move the scanner up and down, but this mode is only appropriate for atomically flat surfaces as otherwise there is a high risk of a tip crash.

2.6.4 Technical aspects

In this section are described basic technical aspects of a Scanning Tunneling Microscope, which are necessary to obtaining high resolution images [43]:

- The coarse and fine positioning system in order to bring the tip into the tunneling regime (distance from a few mm down to 0.01Å) and to control the exact movement in lateral directions.
- The electronic circuit to control the tip-sample distance in the constant current mode.
- The vibration isolation system to stabilized the distance between tip and sample.
- The tip itself, i.e. the shape of its very end which mainly determines the resolution and, thus, the accurate representation of the surface morphology on the atomic scale.

2.6.4.1 Positioning

The scanning of the sample by the tip is controlled by two positioners: a coarse and a fine positioner (scanner). Using two positioners is necessary because of the large distance range the tip has to be controlled. For the construction of the positioner/scanner piezo crystals (quartz, $BaTiO_3$) or piezoceramic material ($Pb(Ti,Zr)O_3$ (PZT)) are used, which enable positioning of the scanning tip with an accuracy of less than one tenth of an Angstrom in all three dimensions. This is based on the phenomenon of the so-called piezoelectric effect.

The Piezoelectric Effect we can define as: applying stress on a piezo material causes electric polarisation. Opposite situation: an electric field applied to a piezo material causes mechanical strain and is called Inverse Piezoelectric Effect. The definitions of the parameters for describing the piezoelectric effect are shown in Fig. 2.15.

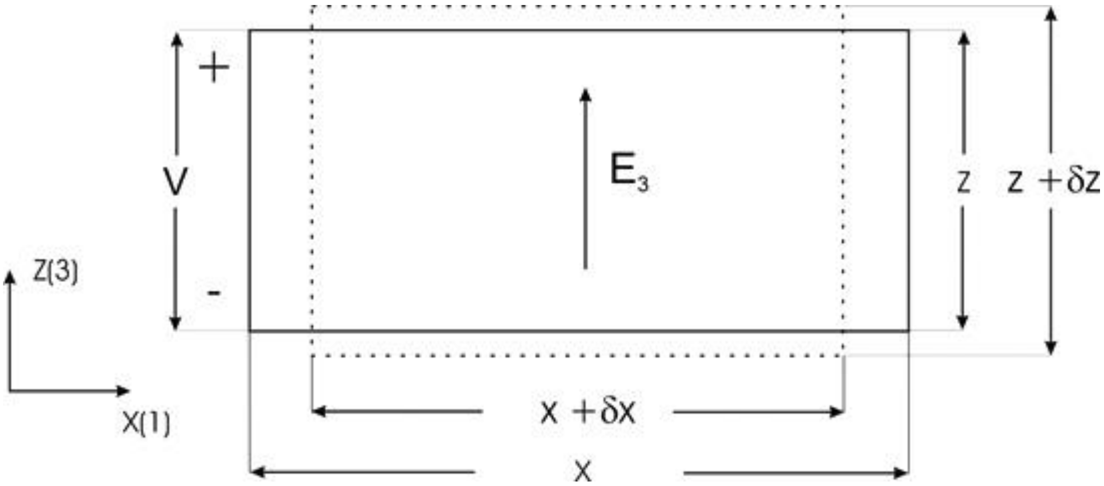

Figure 2.15: A rectangular piece of piezoelectric material, with a voltage V applied across its thickness, causes a strain in the x as well as the z directions.

In the following the directions x, y and z are labeled as 1, 2 and 3, respectively. Applying a voltage V to a rectangular piece of piezoelectric material, inside it the electrical field intensity is:

$$E_3 = \frac{V}{z} \tag{2.41}$$

As a result strain is generated, which can be described by a tensor with xx and zz components:

$$S_1 = \frac{\delta x}{x} \tag{2.42}$$

$$S_3 = \frac{\delta z}{z} \tag{2.43}$$

The piezoelectric coefficients are defined as the ratios of the strain components over a component of the applied electrical field strength. Thus one gets:

$$d_{31} = \frac{S_1}{E_3} \tag{2.44}$$

$$d_{33} = \frac{S_3}{E_3} \tag{2.45}$$

The piezoelectric constants have dimensions of meters/volt in SI units. Changes of the length of piezo material by applying one volt are in the range from several to tens of nanometers. Due to this sensitivity the materials are used in STM for precise movements of the scanning tip.

One can distinguish three types of piezo scanners (tripod scanner, bimorph and tube scanner), and three types of coarse positioner (mechanical positioner, louse and beetle).

After the invention by Binnig and Smith in 1986 very soon a tube scanner (Fig. 2.16.) became the predominant STM scanner [43]. This is due to its simple design, its high piezo constants and high resonance frequencies. It consists of a tube, made out of piezo material, and is covered inside and outside with metal, which acts as electrodes. The outside electrode is sectioned into four quadrants. Due to its design the control of motions in all three dimensions is very simple by just one actuator element. A deviation in xy-direction is generated by a different bias voltage applied to the two opposite electrodes. For example by applying voltage $-U_x$ and $+U_x$ to electrodes at opposite sides of the tube the lateral displacement Δx of the tube is given by:

$$\Delta x = \frac{2\sqrt{2}d_{31}l^2U_x}{\pi Dh} \tag{2.46}$$

where *l* is the length of the tube, *h* is the wall thickness of the tube and *D* is the diameter of the tube.

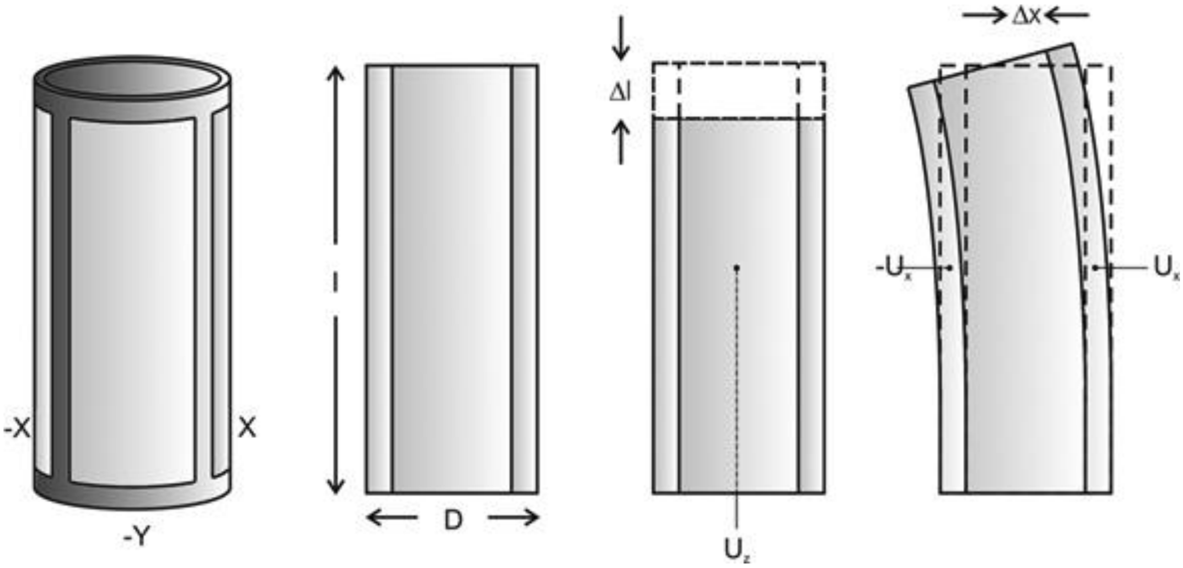

Figure 2.16: 3-dimensional and schematic side view of tube scanner.

A motion in z-direction (along the longitudinal axis) can be achieved by applying a voltage between the inner and the four outer electrodes. The vertical displacement Δl of the top of the tube scanner is calculated by:

$$\Delta l = \frac{d_{31} l U_z}{h} \tag{2.47}$$

For example typical dimensions of a piezo tube (PZT-5H) are as follows. Length: 12.7 mm, diameter 6.35 mm, wall thickness: 0.51 mm, which results in a piezo constant for x and y directions of 123 Å /V and 68 Å /V in z-direction. The equations (2.46) and (2.47) show that the length of the tube is the most effective design parameter to tune the piezo constant since the x,y-piezo constant is squarely dependent on the tube length.

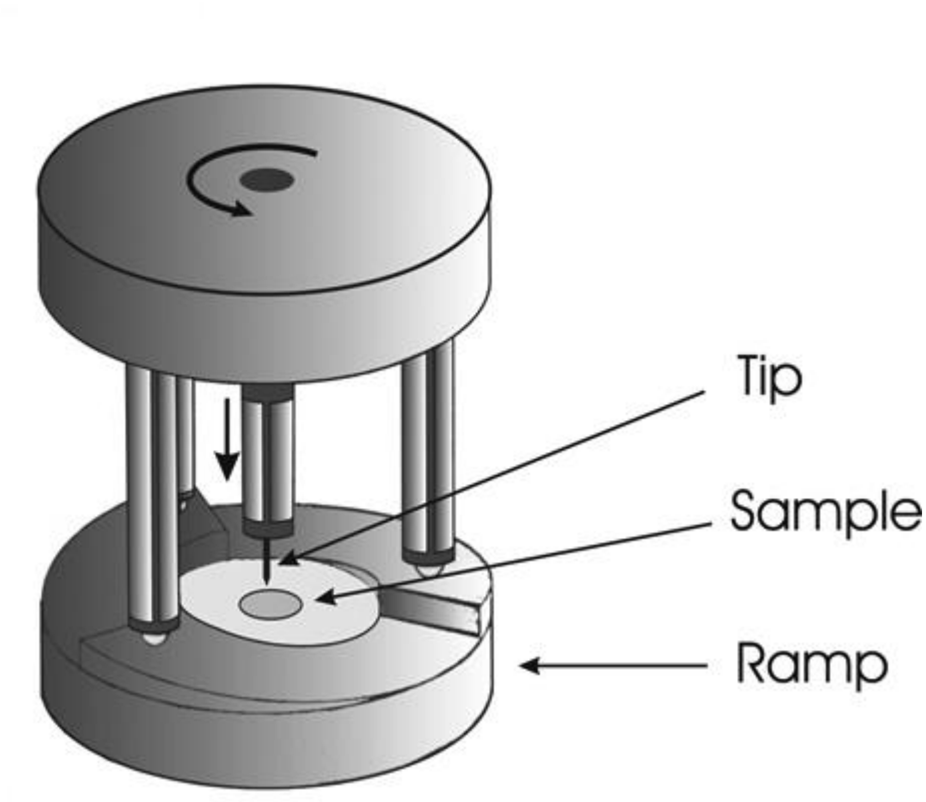

Figure 2.17: Sketch of the beetle STM design, principle of the slip stick motion.

The Beetle type coarse positioner was first introduced by Besocke in 1987. It is a popular design mostly because of its simple and small design and vibrational and thermal stability. Generally the beetle consists of a plate with three piezoelectric tubes, standing on a cylindrical ramp. At the end of the tubes balls are fixed. The sample is mounted in the middle of the ramp ring. By applying a voltage to the piezoelectric feets, the plate is rotated. Reducing the voltage quickly causes the balls to slip on the ramp due to the inertia of the ring. By repeating this "stick-and-slip" procedure the tip-surface distance can be reduced or increases by a rotational “walk” on the ramp ring (see Fig. 2.17.) [43].

2.6.4.2. Electronic circuit

For measurements in constant-current mode in order to prevent tip crash on the sample, a feedback circuit is necessary to control the z-piezo (Fig. 2.18).

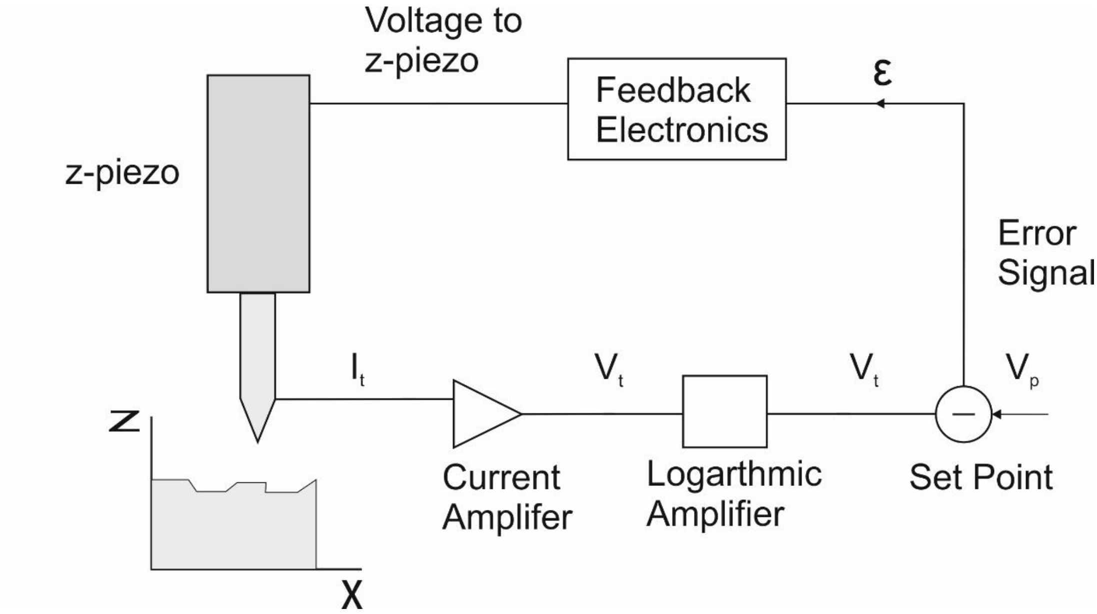

Figure 2.18: Block schematic of a typical STM feedback loop.

By a current amplifier the tunneling current is converter to voltage. Since the current is exponentially dependent on the tip-sample distance, the signal is linearized with a logarithmic amplifier. The output signal of the logarithmic amplifier is compared with a predefined voltage which represents the current set point. The error signal is passed to the feedback electronics, which applies a voltage to the z-piezo to keep the difference between tunneling current and current set point small [43].

2.6.4.3 Vibration isolation

Effective vibration isolation is one of the key elements in achieving atomic resolution by STM. As a consequence of the fact that the tunneling current depends exponentially on the gap between tip and sample, even the smallest vibrations can affect the stability of the instruments. The typical corrugation amplitude in the constant-current mode for STM images is about 0.1 Å. Therefore it is absolutely necessary to reduce inner vibrations (lowest internal resonance frequency of typical STMs 1-10 kHz) and to isolate the system from external vibrations to less than 0.01 Å amplitude. The environmental vibrations are caused by machines running at or near laboratories at frequencies typically between 10 to 100 Hz, by ventilation ducts, transformers and motors at frequencies between 6 and 65 Hz, as well as by walking and working in laboratories with frequencies range of 1 to 3 Hz. All of these environmental vibrations excite vibrations of the building which are transmitted to the STM. Therefore primary attention has to be given to the frequency range between 1 and 100 Hz.

We can distinguish several vibration isolation systems like suspension springs, eddy-current damper, stacks of plates and elastomers and pneumatic systems. Most popular vibration isolation systems used for STMs are suspension springs and plate-elastomer stacks. Furthermore they are typically used in combination to exclude vibrations of low and high resonance frequencies. With suspension spring systems it is easy to suppress very low resonance frequencies by combining a large mass with a soft suspension. For showing this we can use simple formulas for the resonance frequency for vertical and lateral motion:

$$f_{vertical} = \frac{1}{2\pi}\sqrt{\frac{k}{m}}$$

$$f_{lateral} = \frac{1}{2\pi}\sqrt{\frac{g}{L}} \qquad (2.48)$$

where *k* is the spring constant, *m* is a block of mass suspended by the spring, *L* is the spring length and *g* is the gravitational acceleration.

Thus, in order to produce a suspension-spring system with a resonance frequency of 1 Hz, the weight of the mass should stretch the spring by 25 cm. Furthermore a suspension spring system is cheap and simple to build. A plate-elastomer stack is a system using a stack of metal plates separated by rubber pieces. As the elastic material is quite stiff, the resonance frequencies of the various stages are quite high. So this system is effective only for vibrations with relatively high frequencies (>50 Hz) [43].

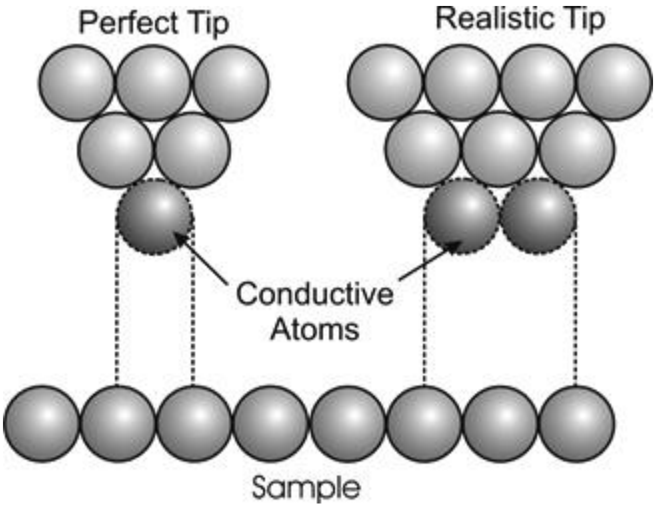

Figure 2.19: Scheme of an ideal and real tip.

2.6.4.4. Tip

The scanning tip is the trickiest part in the scanning tunneling microscope. The resolution of the microscope and the quality of images mainly depends on the apex and the shape of the tip. Due to the fact that the tunneling current decays exponentially with tip-sample separation, only the front most atom on a good STM tip interacts with the closest atom on the sample and thus the effective diameter of the tip becomes very small (of the order of atomic dimension). Then ideally the tip should be ending in exactly one atom (Fig. 2.19). On larger scales, the geometry of the tip may be convoluted with the surface structure, as illustrated rather simplistically in Fig. 2.20. Scans with an atomically sharp tip of a surface region, which contains atomic protrusion, trenches and pits would provide an accurate representation of the surface morphology (Fig. 2.20a). However, if the tip is pyramidal-shaped or blunt, then vice versa the surface feature may effectively image the tip (Fig. 2.20b). Double-tip effects may also occur, if two asperities are formed in close proximity at the end of the tip.

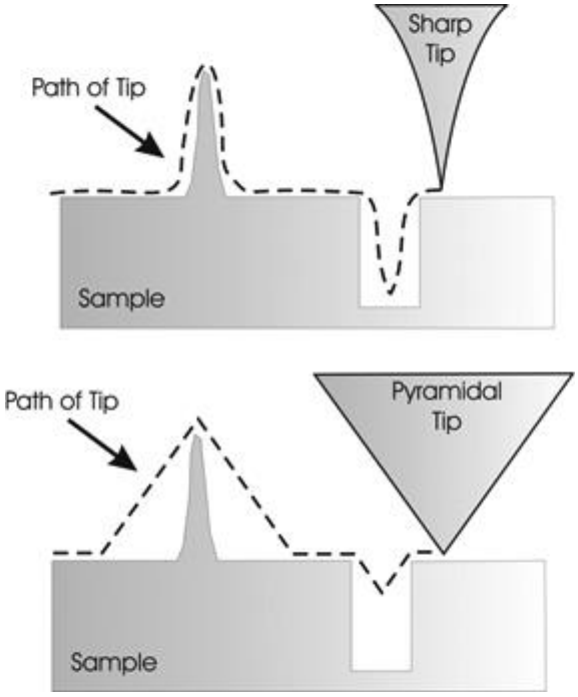

Figure 2.20: (a) Imaging with a sharp tip a small surface feature yields an STM image which accurately represents the surface topography. (b) Imaging with a pyramidal tip a sharp surface feature has the consequence that an image of the tip is formed.

The most commonly used materials to produce the tips are tungsten, platinum or Pt-Ir wire of diameter 0.2-0.5mm due to their stability in high electric fields and, when operated in air or corrosive liquids, their chemically stability. STM tips can be fabricated by simple mechanical procedures such as grinding or cutting metal wires. The tips made in this way have at the end a lot of so-called mini-tips, and their shape has a large opening angle and a large radius of curvature (in the range of 0.1 to 1 μm), so that they are only useful for imaging samples with atomically flat surfaces. Therefore the most common method to fabricate sharp tips is electrochemical etching. This method can provide tips with reproducible and desirable shapes and sizes. The general idea of etching is to immerse a fine metal wire (0.1-1mm diameter) in an appropriate electrochemical etching solution. By applying a voltage (1-15V) between the tip and a counter-electrode the etching process is started. Due to the enhanced etch rate at the electrolyte-air interface, a neck is formed in the wire. When the neck is thin enough the wire fractures due to the weight of that part of the wire immersed in the solution. As a result a sharp tip is formed [32,35,42-43].

Chapter III

Experimental

3.1 Instrumentation

3.1.1 Introduction

The electrochemical scanning tunneling microscope (EC-STM) used in this work permits to study a surface with atomic resolution at the solid-liquid interface in combination with Cyclic Voltammetry. The potentiodynamic EC-STM presented here is a Beetle-type and has been developed in the Wandelt workgroup [44]. In this chapter, not only the working principle of the EC-STM is described but also every aspect of the experiment like preparing of electrolytes, tips, samples and also in more detail the reference electrode.

3.1.2 The Electrochemical Scanning Tunneling Microscope

The EC-STM presented here is a four-electrode system, i.e. the electrochemical cell with three electrodes (the working electrode (WE), the reference electrode (RE), and the counter electrode (CE)) and the STM tip as the fourth electrode [44].

The working principle of the potentiodynamic EC-STM system is shown in Fig. 3.1. In the case of a normal three-electrode arrangement (without tip in the electrochemical cell) the system is able to measure cyclic voltammograms. When the three-electrode configuration (WE, RE, CE) is controlled by a potentiostat and the tip is in the electrochemical cell it is possible to take *potentiostatic* images (switch S in position 1), i.e. during imaging the potential of the sample is held constant at a specified value versus the reference electrode. The bias voltage then defines the potential of the tip versus the reference electrode which has to be chosen such that the Faradaic current through the tip is minimal, because due to its superposition on the tunneling current could disturb the proper tip height control. When the switch S is in position 2 the sample potential is independent from the tip potential. In such a case the four electrodes are controlled by a bipotentiostat which allows to take *potentiodynamic* images, i.e., the potential of the sample versus the reference electrode can be varied during imaging without changing the tip potential versus the reference electrode thereby preventing Faradaic currents through the tip

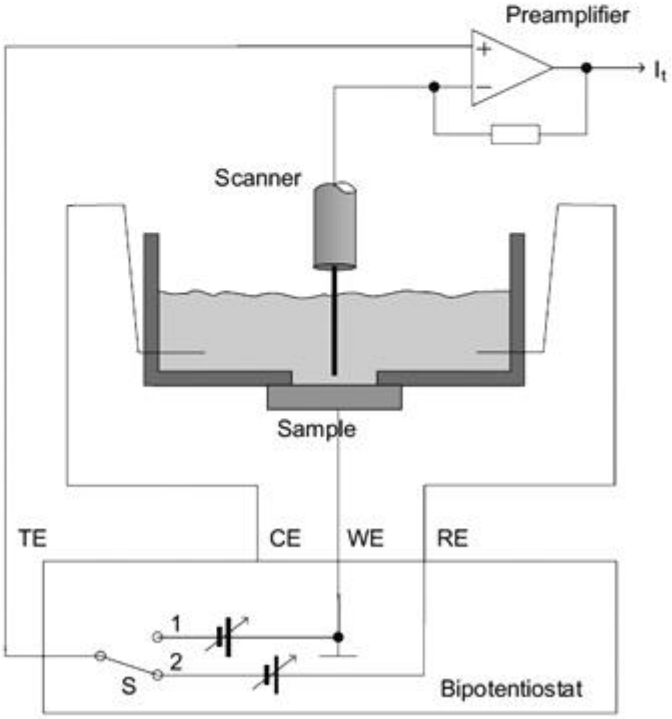

Figure 3.1: Principle of the potential control for potentiostatic and potentiodynamic imaging with the Electrochemical Scanning Tunneling Microscope (EC-STM). TE is the tip electrode, CE is the counter electrode, WE is the working electrode, S is a switch, I_t is the tunneling current. [35]

Figure 3.2 shows a photography of the complete EC-STM system. The main part of the EC-STM is the tunneling unit and an electrochemical cell which are placed in the aluminium chamber (1). The chamber serves as a closed volume for the protective gas (Argon) and as a shielding against electromagnetic and acoustic noise. For vibration damping the STM stands on a brass stack separated by rubber pieces (for damping higher frequencies larger than 100Hz) within the aluminium chamber and the whole chamber stands on a heavy granite plate (2) which is suspended with steel springs (3) from the ceiling. This damping stage effectively protects the STM from outer vibrations (low frequency regime less than 1 Hz). The electrolyte from the electrolyte supply system (4) is deaerated by purified protective argon gas (because oxygen often reacts with adsorbates of interest, especially biological molecules which disturbed the CV measurements) and is then fed into the electrochemical cell. The house pump (5) prevents overflow of liquid from the electrochemical cell, the overflow could pollute the electrolyte or even cause damage to the tunneling unit. The operation of the electrochemical cell is controlled by the bipotentiostat (6) and the cyclic voltammograms are recorded by a computer (7). The STM control unit (8) is used to control the tunneling unit and a computer (9) for controlling the movement of the scanner and recording the STM images.

Figure 3.2: Picture of the EC-STM system: 1) aluminium chamber for the STM; 2) heavy granite plate; 3) steel springs connected with the ceiling; 4) electrolyte supply and gas purification system; 5) hose pump; 6) bipotentiostat; 7) computer for displaying the cyclic voltammograms; 8) STM control unit; 9) computer for controlling the STM unit and displaying STM images.

Figure 3.3 shows the disassembled mechanical setup of the STM and Fig. 3.4 a photography of the assembled setup of the STM. The electrochemical cell consists of an inner cell made from Ketron ® having contact with the electrolyte, and is placed in a stainless steel cell case, see Figure 3.5. The sample is fixed from the bottom by adjusting three screws against a Kalrez ® sealing ring pressed to the electrochemical cell. Thus only the well prepared front side of the sample is exposed to the electrolyte. After fixing the prepared sample in the electrochemical cell this cell is mounted into the STM-base and connected to the bipotentiostat. Then the front of the chamber is closed by a Plexiglas plate.

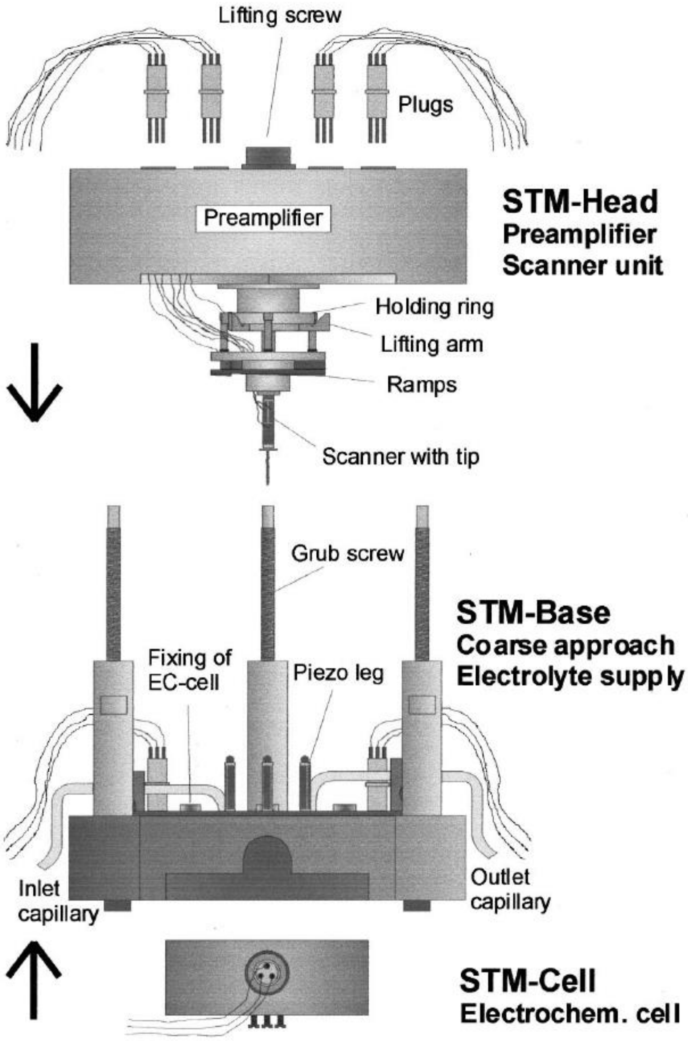

Figure 3.3: Disassembled setup of STM [30].

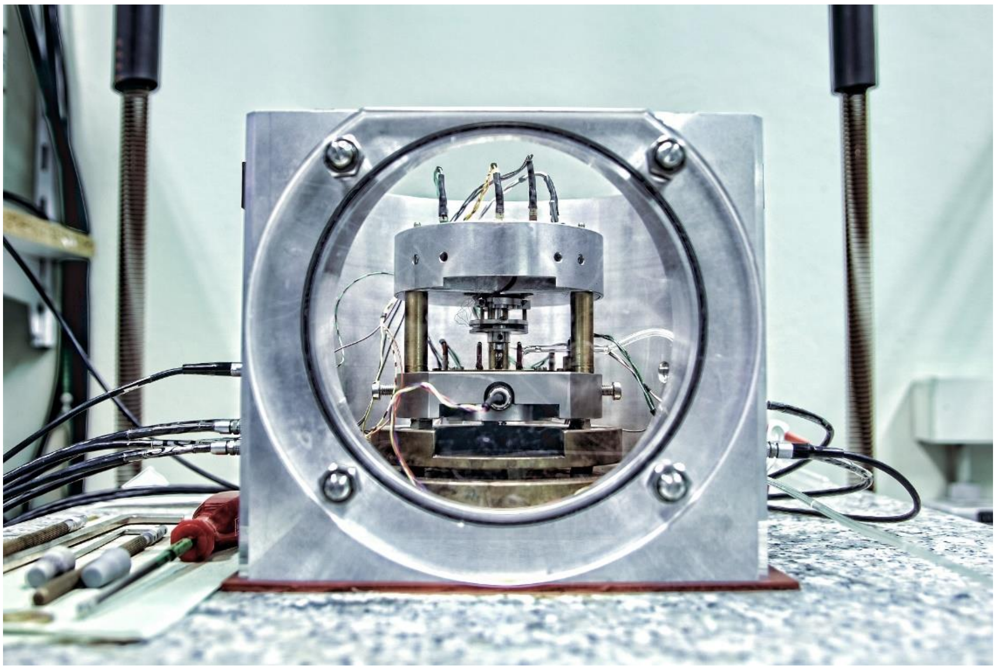

Figure 3.4: Assembled setup of STM in aluminium chamber.

The valve with protective gas is opened and Argon is flowing into the chamber displacing the air. The STM-base plate is machined out of stainless steel and supports the three piezo-legs, the electrolyte capillaries and the grub screw for fixing the STM-head. After filling the electrochemical cell with the electrolyte under potential control the STM-head with the already installed tip in the scanner, is put down onto the grub screws. The STM-head carries the scanner unit and the preamplifier. Then the electrical connections are made and the scanner unit is lowered down by turning the lifting screw thereby setting down the ramped ring with the scanner freely, onto the piezo-legs. The scanner unit is now mechanically decoupled from the STM head except for the tunneling and electrode wires. Then the chamber and valve with protective gas is closed keeping the protective argon atmosphere inside. Afterwards, the previously locked granite plate carrying the aluminium chamber are made to hang freely from the ceiling. From now on the scanner unit is controlled by the STM control unit (to control tunneling current and bias) and the computer (to control tip-to-sample approach and, after the tunneling tip has reached the tunneling regime, all the fine movements as well as images recording). The potential applied to the electrodes is controlled by the bipotentiostat unit. More technical details about this EC-STM can be found in ref. [44].

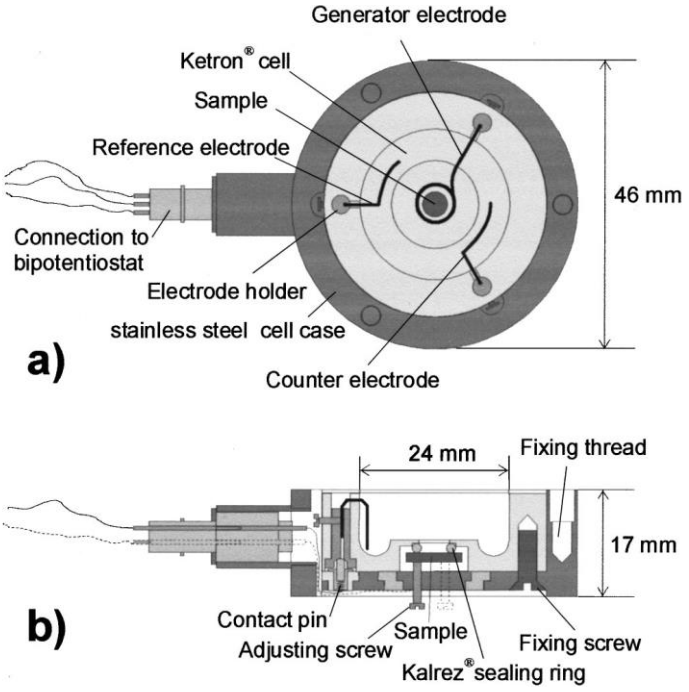

Figure 3.5: Electrochemical cell: a) top view; b) cross section. [30]

3.1.3 The integrated quasi-reference electrode

In all measurements in this thesis no classical (external) reference electrode (e.g., RHE, calomel electrode, Ag/AgCl electrode) was used but an internal (inside the electrochemical cell) platinum wire was used as a quasi-reference electrode [45]. The advantage of this electrode is the higher purity. Contamination from hoses or a separating membrane glass frit can be ruled out. There is no affect of concentration and fluctuations generated by the moving of ions through the hose connection to or from an external electrode. A disadvantage of this reference electrode is that the potential is depending on the supporting electrolyte in the cell, so that after exchanging electrolyte the potential is changed. Also, by competing reactions occurring with different ion species of the electrolyte, in particular the adsorption of oxygen from the decomposition of water, the potential may change up to 100 mV. Furthermore a platinum quasi reference electrode shows a small drift of potential with time. The off-set of the electrode potential between platinum quasi-reference electrode and a RHE is approximately 580mV in negative direction.

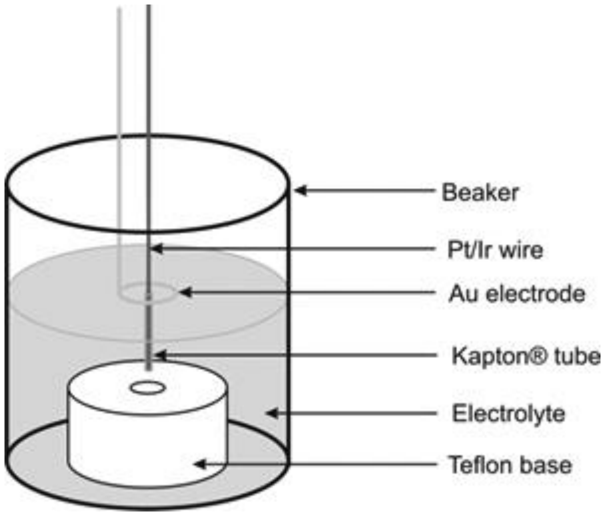

Figure 3.6: Scheme to electrochemical etching of Pt/Ir wire.

3.1.4 Preparation of electrolytes

All electrolytes were prepared by using deionized water from a Millipore® - Pure water system with a specific resistance of 18MΩcm and a residual amount of organic impurities in the low ppb regime. The basic chemicals used have the highest commercially available quality level. All electrolyte containers and flasks are made of glass with Teflon valves. Before use they are first kept for several days in peroxosulfuric acid $(H_2SO_5)_2$ and then one to two days in potassium hydroxide (2M KOH) and finally thoroughly rinsed with Millipore water. Before each measurement the electrolyte is degassed with Argon 5.0 for about 1 hour.

All of these precautions guarantee that the prepared electrolytes are of highest quality and that the measurements are conducted at the highest purity level.

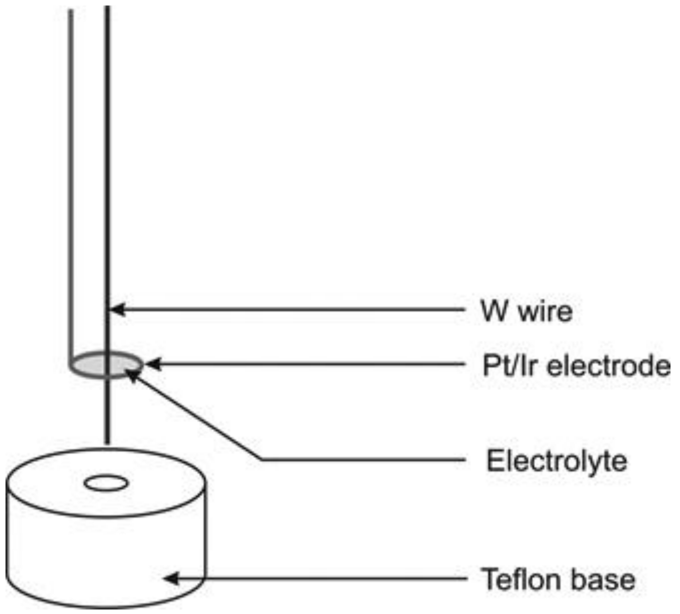

Figure 3.7: Scheme for electrochemical etching of W wire.

3.1.5 Preparation of tips

For all measurements presented in this thesis Platinum/Iridium (alloy of Pt 90% and Ir 10%) and Tungsten tips where used. Platinum/Iridium tips are stable at all potentials in the used electrolytes, in contrast to Tungsten tips which can dissolve at high potential. The disadvantage of Pt/Ir tips is their lower hardness, so that they are easier to deform mechanically. This makes their preparation more difficult. The Pt/Ir- and W-tips have been made by using an electrochemical etching method but in two different ways.

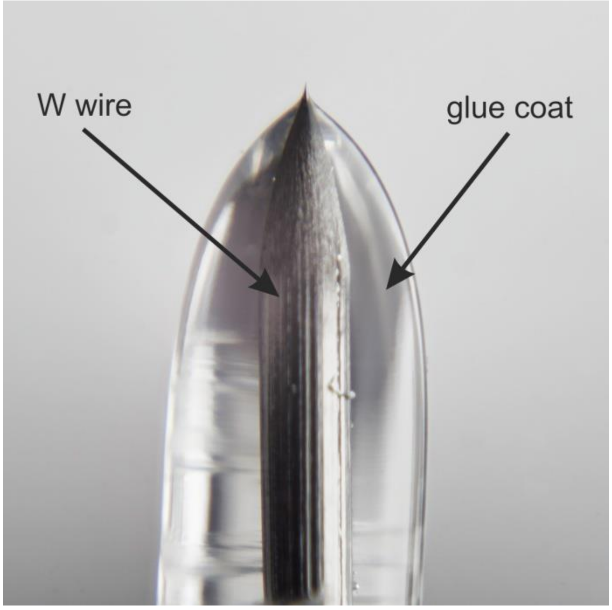

Figure 3.8: Picture of a prepared Tungsten tip.

The Platinum/Iridium tips are electrochemically etched from a 0.25 mm diameter wire in a 2M KOH /4M KSCN solution (Fig. 3.6). A gold wire loop as a working electrode is placed in the surface plane of a solution. Inside the golden loop is placed a Pt/Ir wire as counter electrode covered with about 7mm Kapton® tube and is immersed into the electrolyte. The Platinum/Iridium wire is dipped far into the electrolyte that only a very small unprotected area (upper part of wire) is exposed to the electrolyte and only that part of the wire is etched. Between the Platinum/Iridium wire and the gold wire loop a DC voltage of 2 V is applied, superimposed with a rectangular AC voltage of 10 V_{SS}, and a frequency of 1 kHz, which starts the etching process. The etching process is continued until the Pt/Ir wire falls off into the teflon base. After carefully removing the Kapton® tube the tip is rinsed with high purity water. After the tip became dry it is coated by passing it through a drop of hot glue in order to minimize any Faraday current through it which is superimposed on the tunneling current and would influence the measurements. Only the most anterior tip remains uncovered due to its high curvature.

Figure 3.9: Picture of the Au(100) sample.

The Tungsten tips were electrochemically etched from a 0.25 mm diameter wire in a 2M KOH solution (Fig. 3.7). A Pt/Ir wire loop as a working electrode is shortly immersed in the electrolyte to suspend a thin lamella of electrolyte. The tungsten wire is then pierced through this lamella. Between the Tungsten wire and the Pt/Ir wire loop a rectangular AC voltage of 12 V and a frequency of 100 Hz is applied. After 2 minutes the amplitude of the alternating voltage is reduced to 6 V for 1.5 minutes, then the voltage is reduced to 4 V and the etching process is continued until the free end of the tungsten wire falls off. The tip is rinsed with high purity water. After the tip became dry it is also coated by passing it through a drop of hot glue. Figure 3.8 presents a coated Tungsten tip.

3.1.6 Preparation of sample

In this study, a Au(100) sample was used and prepared by mechanical polishing (diameter 8 mm, thickness 3 mm, surface misorientation <0.5^0, roughness

<0.03 μm) from the company MaTeck GmbH Jülich (Fig. 3.9), of which only a central area of 4mm diameter is exposed on the electrolyte (see Fig. 3.5b).

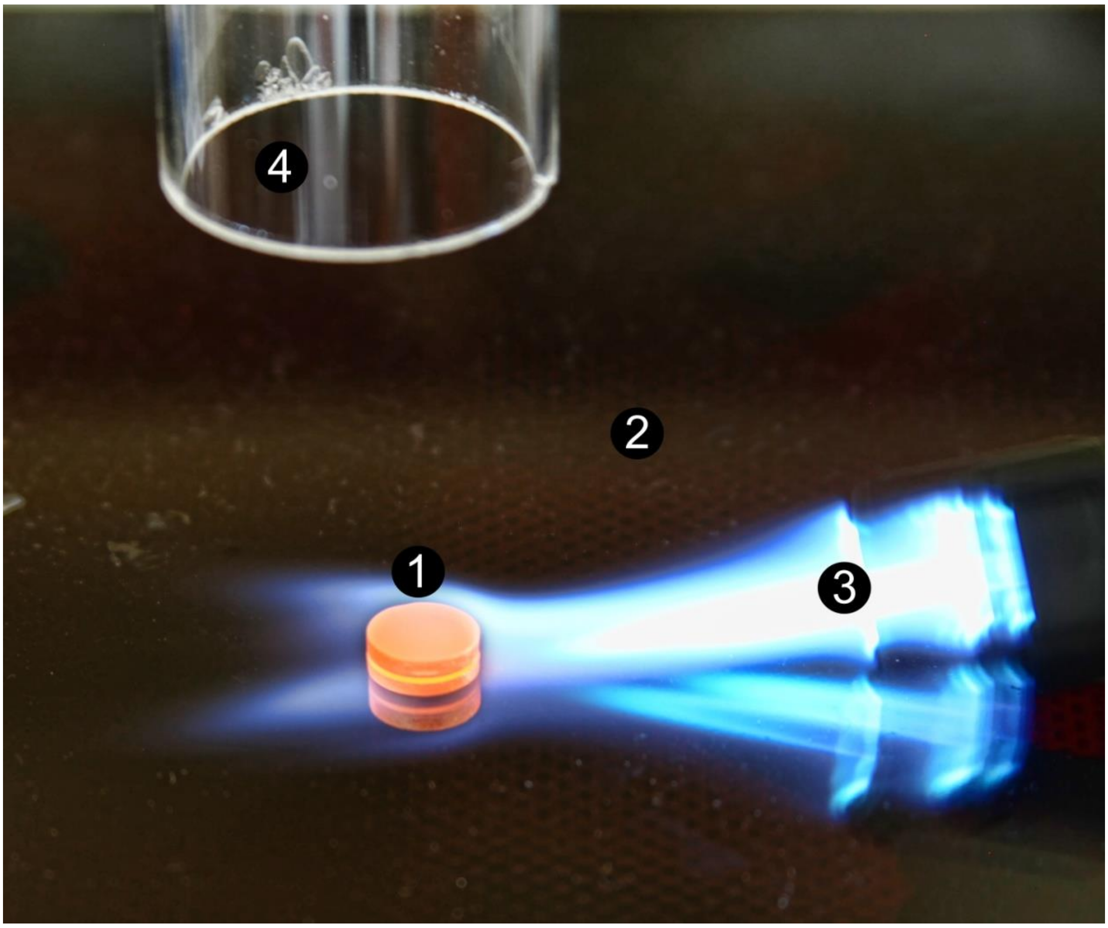

Figure 3.10: Picture of the annealing process: 1) sample of Au (100) with mirror image from 2) Ceran® plate; 3) butane gas flame; 4) glass tube to supply Argon.

Before mounting into the electrochemical cell the crystal is annealed (Fig. 3.10). For this purpose, the sample (1) is placed on a Ceran® plate (2) and is annealed by a butane gas flame (3) for 3 minutes up to faint red glow (600 – 700°C). Subsequently, the crystal is cooled down to room temperature (about 15 minutes) in an atmosphere of argon (4). Then it is heated again to a red glow and cooled for 6 minutes. This process cleans and smoothes the surface.

To prevent re-contamination of the surface the installation in the electrochemical cell is done as quickly as possible and then a protective drop of Millipore ®-water is placed on the crystal.

3.2 Substrates

3.2.1 Gold surface

3.2.1.1 Introduction

Gold [46] is a chemical element with the symbol Au (from Latin: aurum, "shining dawn") and an atomic number of 79 with the electron configuration [Xe] $4f^{14}$ $5d^{10}$ $6s^1$. It is the heaviest of the so-called coinage metals of the 11th Group in the periodic table. It is of yellow colour and of very low hardness (2.5 in Mohs scale). Gold melts at 1337.33 K and boils at 3129 K. It is a noble metal and with only one stable isotope, ^{197}Au. Chemically, gold is a transition metal and can form trivalent and univalent cations in solutions. Compared with other metals, pure gold is chemically least reactive, but it is attacked by aqua regia, i.e. a mixture of acids, forming chloroauric acid, but not by the individual acids, and by alkaline solutions of cyanide. Gold dissolves in mercury, forming amalgam alloys, but does not react with it. Gold is insoluble in nitric acid, which dissolves silver and base metals. That's why it has long been used to confirm the presence of gold in items.

Besides the use for decorative purposes in jewellery and coins gold has many modern industrial applications including dentistry and electronics. Gold has traditionally found use because of its good resistance to oxidative corrosion and excellent quality as a conductor of electricity.

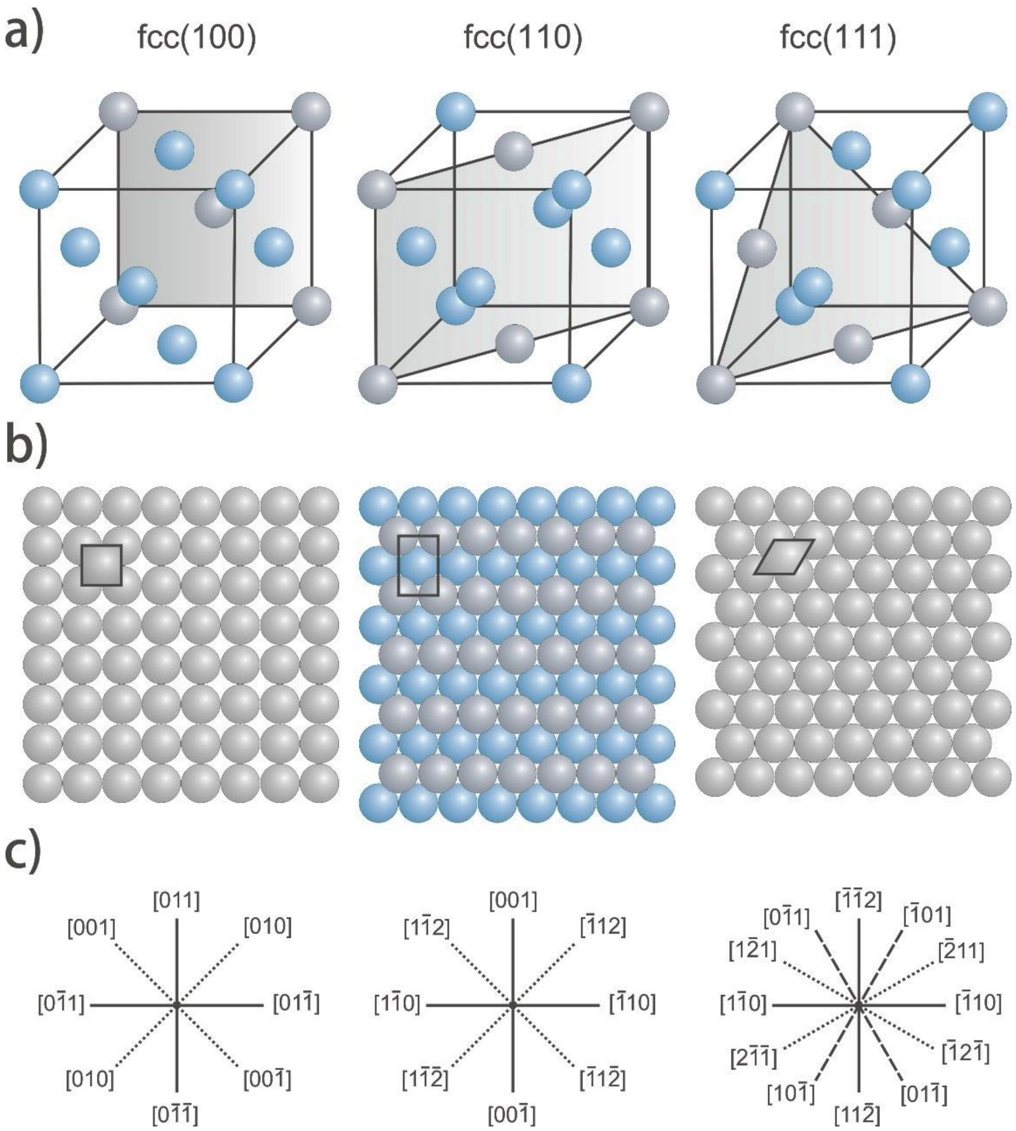

Figure 3.11: Upper surfaces of face centered cubic structures:

a) the location of the surfaces in the unit cell,

b) hard sphere model of the upper surface,

c) surface crystallographic directions in the upper layers.

3.2.1.2 Au(100) surface

Elemental gold crystallizes [47] in an face centered cubic (fcc) structure (Fig.3.11). The lattice constant of the unit is 4.08 Å and the atomic radius 1.44 Å.

The nearest neighbour distance Au-Au is 2.88 Å. The Au(100) surface was chosen in this thesis.

The (100) surface is obtained by cutting the fcc metal parallel to a surface of the fcc cubic unit cell; this results in a surface with an atomic arrangement of 4-fold symmetry. The Au(100) surface is known to reconstruct into a distorted hexagonal phase [53]. The structure is incommensurate and is often referred to as a (28x5) or c(26x68) structure, distorted and rotated by 0.81^0 about the crystallographic [001] direction. The incommensurability and the rotation of the lattice are affected by the geometry of the surface steps [48,53].

The first experiments with a Au(100) surface were done in UHV environment but the reconstruction of the gold surface may also be observed in electrochemical environment, where it shows a potential dependent behavior [49,50,55]. In fact, the reconstruction of the Au(100) surface can be controlled by the electrode potential. Interestingly, the reconstruction is lifted when the surface is positively charged, i.e. when electrons are removed from the surface. Furthermore through the interaction with an adsorbate, the reconstruction is lifted, i.e. a relatively low iodine coverage ($\theta \sim 0.1$) is sufficient to convert the hexagonally reconstructed Au(100) surface into an ordered (1x1) structure (see Fig. 3.12a) [51,52].

3.2.2 Iodine-modified gold surfaces

3.2.2.1 Introduction

Ion adsorption at single crystal electrode surfaces has been investigated intensively in recent years thanks to the development of both in situ and ex situ techniques. The results obtained by those methods have helped understanding the structure of the adsorbed ion layers as well as the processes that occurred at the electrode surface. An adlayer of iodine is known to protect highly sensitive surfaces of metal single crystals from the surrounding atmosphere, furthermore iodine adlayers turned out to be a good templates for the self-assembly of organic molecules [29-35,56]

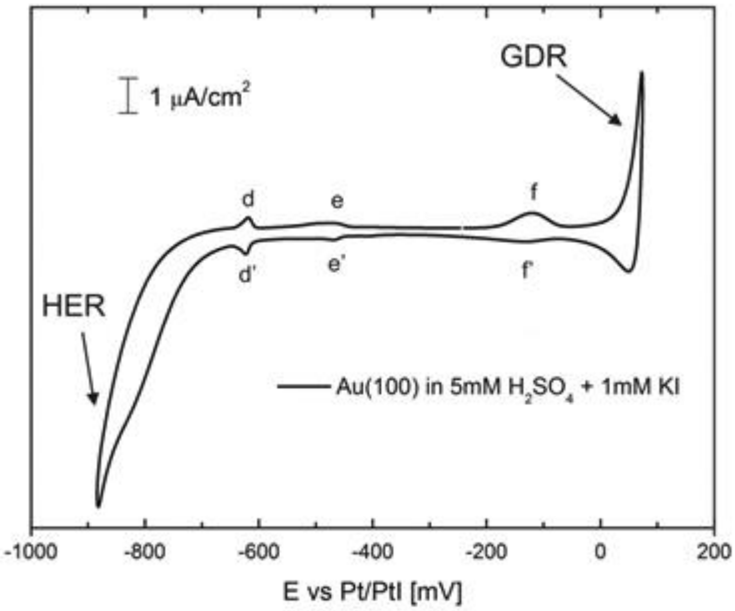

Figure 3.12: Cyclic voltammogram of a Au(100) surface in a 5mM H_2SO_4 + 1mM KI electrolyte, dE/dt = $10mVs^{-1}$.

3.2.2.2 Iodine-modified Au(100) surface

Exposing the Au(100) electrode to an aqueous acid solution containing iodide[1] leads to a spontaneous specific adsorption of iodide on the gold surface in the potential range between the onset of the oxidative gold dissolution reaction (GDR) [58] and close to the onset of the hydrogen evolution reaction (HER). Iodine-modified Au(100) surfaces have been widely studied by in situ and ex situ techniques [50-52,57]. The structure of the iodine adlayer was found to be strongly dependent on the electrode potential due to a so-called electro-compression and –decompression process [50,57]. In this section the results of iodine adsorption on a Au(100) surface are presented, which are comparable to those found in others work [50-52,57].

---

[1] Since charge of adsorbed species is not known (in particular, iodine is the most covalently bound of all halogens), bound on the surface we speak about iodine, while in the solution we have iodide.

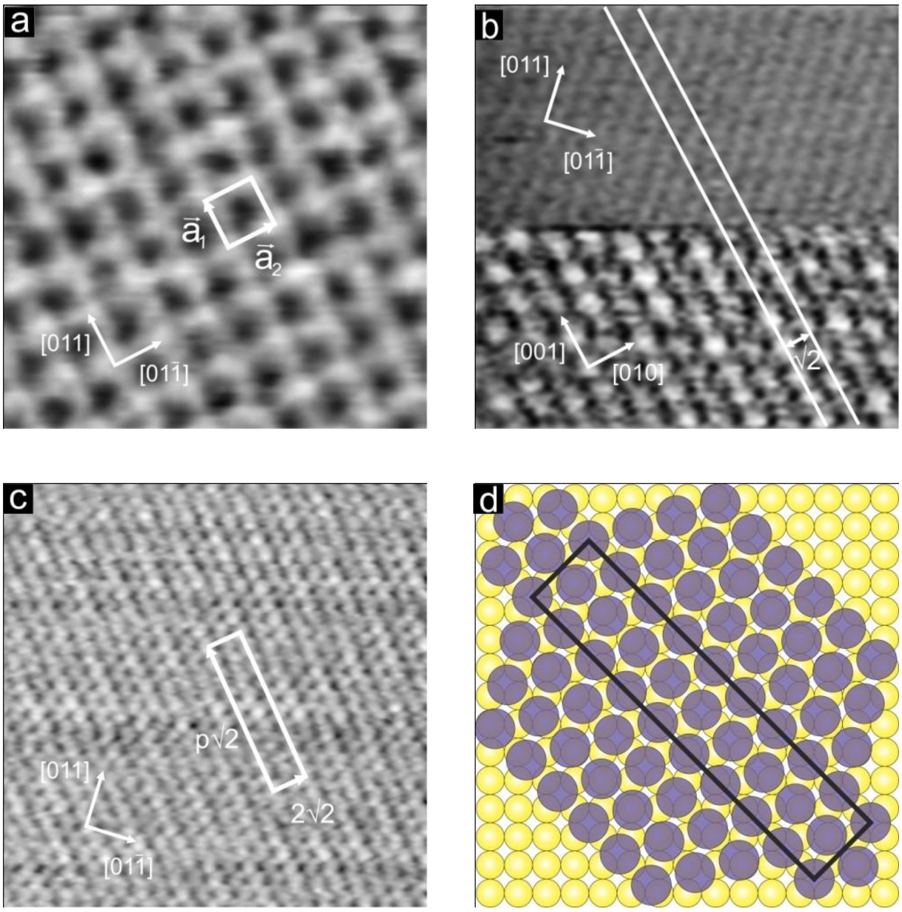

Figure 3.13: In situ STM images obtained of a Au(100) surface in 5mM H_2SO_4 + 1mM KI solution; **a)** image of the bare, unreconstructed (1x1) Au(100) surface structure, recorded below the d/d' peaks pair in Fig. 3.12; image parameters: 2.54nm x 2.54nm, I_t = 1nA, U_b = 20mV, E = -650mV vs Pt/PtI; **b)** a composite image of the bare gold surface and the iodine phase I obtained by the changing work potential from -650mV (upper half) to -570mV (lower half) vs Pt/PtI; image parameters: 5.80nm x 5.80nm, I_t = 5nA, Ub = -68mV; **c)** large-scale image of the compressed phase I structure, where p=10; image parameters: 9.34nm x 9.34nm, I_t = 5nA, U_b = -68mV, E = -570mV vs Pt/PtI; **d)** ball-model of the (2√2 x p√2) structure, where p=10.

Figure 3.12 shows a typical cyclic voltammetry curve for the Au(100) electrode in 5mM H_2SO_4 +1mM KI solution with a sweep rate of 10mV/s. As is well-know the occurrence of a potential-induced phase transition or adsorption/desorption is typically signalled by current features in a CV arising from the (non-faradic) redistribution of electronic charge. In the CV one observes three pairs of such current waves within the whole potential window. At negative electrode potentials on the left side of the peak pair d/d’ a square-planar array of dots is observed in the STM image (see Fig. 3.13a). A closest distance between two dots is approximately 2.9Å, which corresponds to the interatomic distance on an unreconstructed (1x1) Au(100) gold surface.

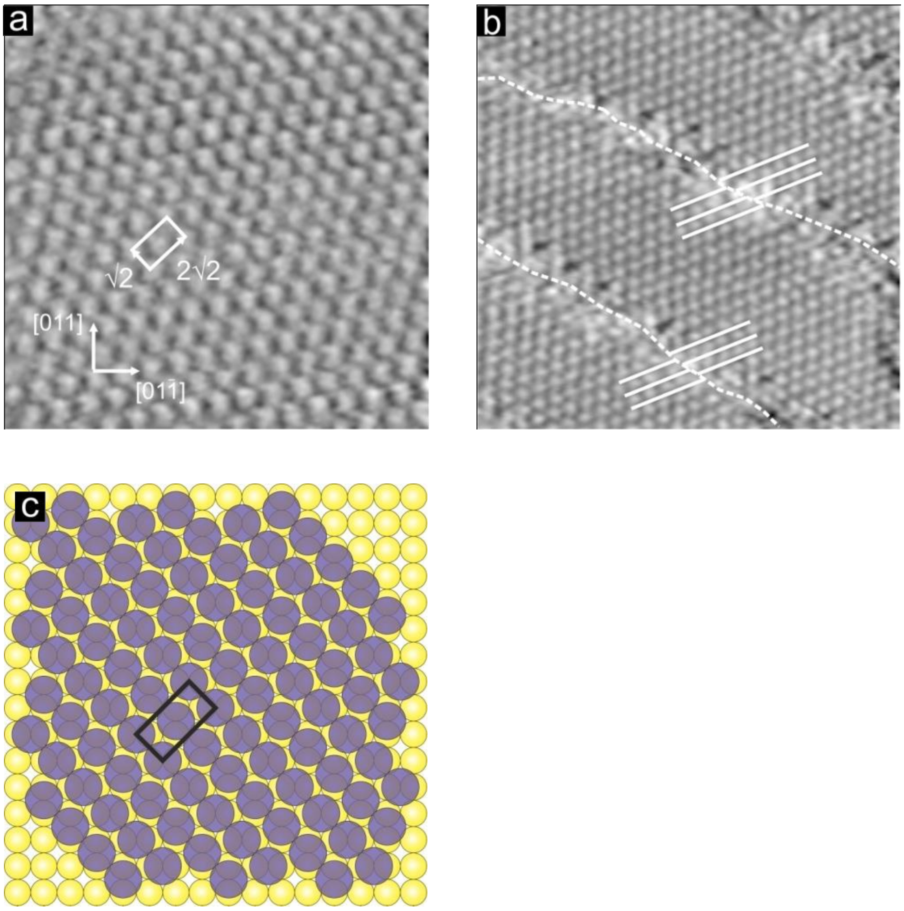

Figure 3.14: In situ STM images obtained from a Au(100) surface in 5mM H_2SO_4 + 1mM KI solution; a) high-resolution STM image of the (2√2x√2) iodine phase II structure; image parameters: 6.71nm x 6.71nm, I_t = 1nA, U_b = -93mV, E = -400mV vs Pt/PtI; b) large-scale image of the (2√2x√2) iodine structure showing translational domains; image parameters: 1.27nm x 11.27nm, I_t = 5nA, U_b = -68mV, E= -400mV vs Pt/PtI; c) ball-model of the (2√2x√2) iodine phase II structure.

The first type of ordered iodine structure, appears when the potential is swept or stepped in positive direction across the peak pair d/d' (-618/-623mV vs Pt/Pt/I). Figure 3.13b presents a composite image of the bare gold surface (upper half image) and iodine phase I (lower half image) acquired by stepping the potential from -650mV to -570mV vs Pt/PtI. A pseudo-hexagonal array of bigger spots is now seen, which indicate the presence of an ordered iodine adlayer. It can be clearly seen that iodine rows are lying along the [001] direction (i.e., 45^0 to the substrate rows). Two straight lines in Figure 3.13b drawn along iodine rows show that the rows are spaced evenly with the distance between them of √2-times the Au-Au distance (i.e., 4.08Å). On the large-scale image (see Fig. 3.13c) it is seen that every atomic row has a characteristic long range periodic modulation that runs along the [001] direction, alternating in the intensity from bright to dark with a periodicity of approximately nine iodine-iodine distances. The reason of this modulation is a periodic variation in binding site of the iodine anions, from 4-fold hollow to atop back to 4-fold hollow. It should be noted that this periodicity is changing with the applied work potential, i.e. by increasing the potential the iodine coverage increases which means that this phase shows electro-compressibility. Perpendicular to the [001] direction every second iodine anion exhibits the same brightness, i.e. occupies the same binding site. Therefore a rectangular (2√2 x p√2) unit cell can be proposed with essentially fixed 2√2 dimension in the [010] direction and continuously varying p√2 dimension along the [001] direction. The p parameter (as first defined by Gao et al. [50]) used here is referring to the amount of uniaxial compression, where higher values of p correspond to a more compressed structure, thus the p√2 term relates to the largest dimension (periodicity) of the unit cell. The nearest neighbor distance (NND) along the p√2 direction is changing from close to 4.5Å down to approximately 4.2Å, which corresponds to an increase in coverage from $\theta \approx 0.46 \; to \; \theta \approx 0.49,$ and 4.6Å along the other atomic row direction [50].

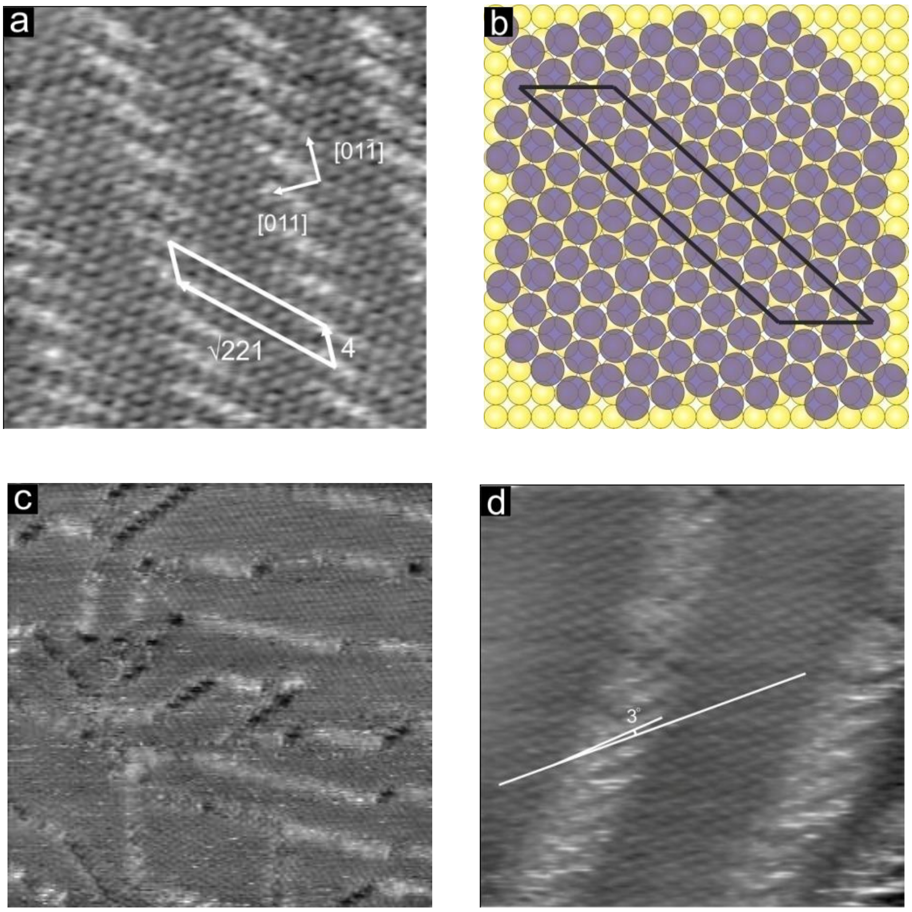

Figure 3.15: In situ STM images obtained from a Au(100) surface in 5mM H_2SO_4 + 1mM KI solution; a) high-resolution STM image of the pseudo-hex-rot iodine phase III structure; image parameters: 13.73nm x 13.73nm, I_t = 1nA, U_b = -93mV, E = -150mV vs Pt/PtI; b) ball-model of the (4x√221) iodine phase III structure; c) flexible iodine superstructure, image parameters: 27.46nm x 27.46nm, I_t = 1nA, U_b = -324mV, E = -300mV vs Pt/PtI; d) high-resolution STM image of the flexible iodine superstructure, image parameters: 13.93nm x 13.93nm, I_t = 5nA, U_b = -339mV, E = -300mV vs Pt/PtI.

The next iodine phase occurs when the potential is swept or stepped in positive direction above the peak pair e/e’ (-431/-421mV vs Pt/PtI). The increased potential results in a compression of phase I along the p√2 direction to a situation where each atom occupies essentially the same type of binding site (i.e., p → ∞), such a structure can be described by a (2√2x√2) unit cell. Figure 3.14a shows an STM image of this (2√2x√2) iodine phase II, where no modulation of height is observed anymore. All iodine anions are now situated in 2-fold bridging sites (see ball-model on Fig. 3.14d) yielding $\theta = 0.5$ [50]. Comparison with the (2√2x10√2) model in Figure 3.13d shows that the p√2 rows are shifted diagonally across into 2-fold sites in Figure 3.14d. The NND for the (2√2x√2) structure along the √2 direction is 4.08Å and 4.56Å along the two diagonals of the unit cell.

Figure 3.14b displays an interesting additional feature namely translational domains of the (2√2x√2) structure. The white dashed lines mark the domain boundaries, while the white full lines show the shift between two neighboring domains. The displacement between two domains corresponds to half the distance between adjacent √2 rows (2.05Å) and it is shifted along one of the directions diagonal to the √2 rows. This translational domains demonstrate the ease by which sets of iodine atoms can move jointly between adjoining √2 sites.

The (2√2x√2) structure is stable only within a narrow potential region, approximately from -420 to -320mV vs Pt/PtI. At even higher potentials, corrugated structures again become apparent. The next structure appears at potential higher than -170mV vs Pt/PtI where the peak pair f/f' starts to appears in the CV. Figure 4.15a corresponds to a pseudo-hex-rot iodine phase III that is rotated by about 2.6° with respect to the substrate √2 direction, and consequently exhibits a periodic alteration of the binding sites yielding the observed modulation (brighter atoms). A ball model that approximates this phase III is shown in Figure 4.15b. This phase shows electro-compressibility. Results from LEED studies show that the rotation increases with the coverage to reach a saturation value of around 3.5°, which is accompanied by a change in the iodine coverage from above $\Theta \approx 0.5$ to $\Theta \approx 0.56$ [51]. NND for this structure is around 4.3Å, i.e. the interatomic spacing along the "near-√2" direction is increased slightly, and in the other two directions between 4.3 and 4.4Å, shorter than the previous value of 4.56Å.

In the potential regime between -320mV to -170mV, bordered by phase II and III, a flexible superstructures is observed containing local arrangements periodically characteristic of both phase II and III. Figures 4.15c and d show such heterogeneous adlayer.

3.3 Adsorbates

3.3.1 Porphyrin molecule

Porphyrins are a group of organic compounds, which consist of four pyrrole rings (pentagonal rings of four carbon atoms with a nitrogen atom at one corner C_4H_5N) cyclically connected to each other by methine groups (–CH=). The simplest molecule of this group is porphine whose chemical structure is shown in Fig. 3.16. Porphin is an aromatic system containing 22 π-electrons, but only 18 of them are delocalized according to Hückel's rule of aromaticity (4n+2 delocalized π-electrons, where n=4) [10]. The size of the pophyrin macrocycle is perfect to bind most metals (e.g. Fe, Zn, Cu, Ni, and Co) ions into its central cavity thereby producing metalloporphyrins [32].

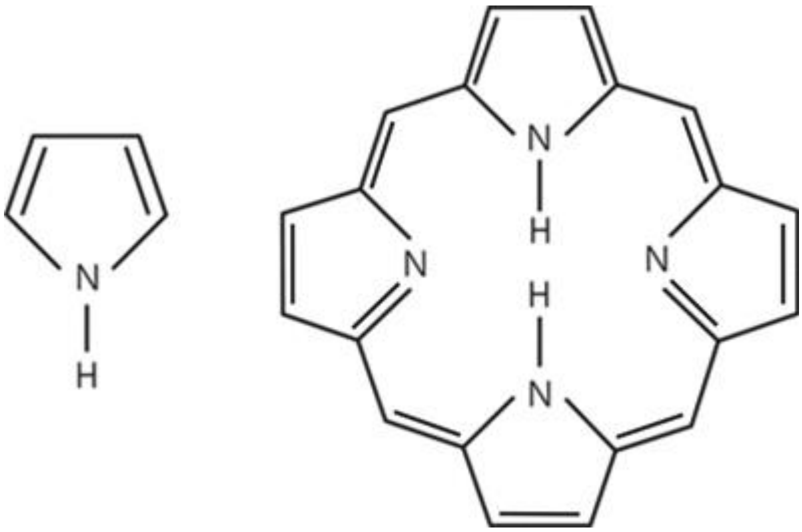

Figure 3.16: Structure of the pyrrole ring and of the simplest porphyrin: porphine.

Porphyrins (both free base porphyrin and metalloporphyrins) are widespread in nature, they are involved in a wide variety of important biological processes ranging from transport of oxygen in blood to the photosynthesis of plants, from catalysis to pigmentation changes. For example, heme proteins which contain iron porphyrins play many roles, like oxygen storage and transport (myoglobin and hemoglobin), electron transport (cytochromes b and c), and oxygen activation and utilization (cytochrome P450 and cytochrome oxidase). Chlorophylls which have a central Mg^{2+} ion and pheophytins which are metal free are found in the photosynthetic apparatus of plants and bacteria [10]. Furthermore, they also find applications in technology and medicine as chemical sensors [13], as electro-catalysts for the reduction of inorganic and organic nitro-compounds [12], and to produce drugs for the photodynamic therapy [11]. Due to the involvement of porphyrins in many biological processes and their physical and chemical properties porphyrins are extremely interesting for research projects in many disciplines of chemistry and physics, like electronics, photophysics, opto-electronics, solar cells, catalysis and electrochemistry [32].

In order to take advantage of these important properties, the production of highly ordered porphyrin arrays with nanometer dimensions on well-defined surfaces is receiving more and more interest [1,59,60]. The technique of choice to achieve these ordered arrays is the self-assembly of these molecules on metal surfaces. There are two ways of producing ordered porphyrin layers: 1) from the vapor phase in ultrahigh vacuum [61-66] (due to their large delocalized electron system, the molecules are very stable, and intact volatile) , and 2) from a solution phases using an electrochemical environment [29,30,33-35,56].

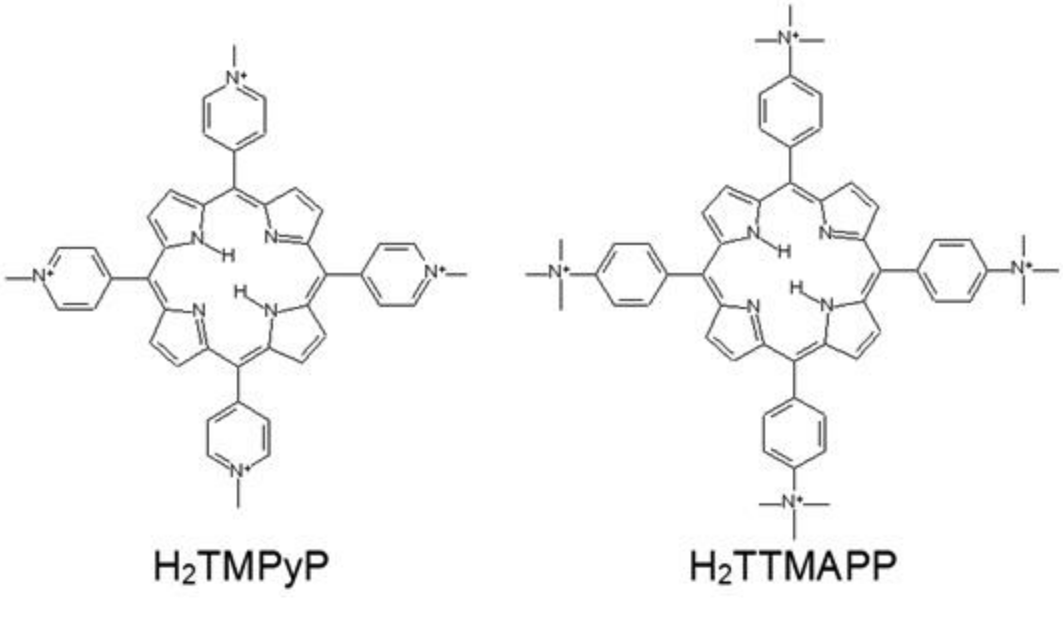

Figure 3.17: Structures of H_2TMPyP and $H_2TTMAPP$ molecules.

3.3.2 The H_2TMPyP and H_2TTMAPP molecules

Two kinds of porphyrin molecules (see Fig. 3.17) were chosen in this work to study their self-assembly on an iodine-modified Au(100) surface: 1) the H_2TMPyP-molecule: 5,10,15,20-Tetrakis-(N-methylpyridinium-4-yl)-21H,23H-porphyrin Tetrakis-(p-toluolsulfat), and 2) the H_2TTMAPP-molecule: 5,10,15,20-Tetrakis(4-trimethylammoniophenyl) porphyrin tetra(p-toluenesulfonate). Due to their attractiveness some applications of H_2TMPyP and H_2TTMAPP can be found in the literature. In the form of water soluble cationic porphyrins (H_2TMPyP, Metal-TMPyP, Metal-TTMAPP) these molecules are applied in cancer photodynamic therapy [18-20] due to their binding affinity to synthetic and natural DNA [21-24]. The photo-induced redox reactions in a hybrid film of a cationic porphyrin (H_2TMPyP) lead to their applications in the construction of efficient solar energy storage devices and novel light-stimulated sensors [25]. Furthermore, H_2TMPyP and H_2TTMAPP molecules were proven to be good sensors for the detection of benzene (H_2TMPyP) [26], heavy metal ions (Hg^{2+}, Pb^{2+}, Cd^{2+}) (H_2TMPyP) [28] and metal ions (Zn^{2+}, Cu^{2+}) (H_2TTMAPP) [54].

From UHV studies it is know that adsorbed porphyrins on the bare metal surface lie flat due to their large π systems which have the tendency to maximize the π bonding to the surface [67]. In the electrochemical environment it is expected that electrostatical interactions of the porphyrin cations with the charged metallic electrode surface dominate. The main difference to an adsorbed porphyrin layer in UHV, however, is the fact that the electrode surface in contact with an electrolyte is already modified by the presence of specifically adsorbed anions from the pure supporting electrolyte. These adsorbed anions (in this work: iodine) are expected to be almost uncharged, so that, the iodine-porphyrin interaction is mainly van der Waals bonding [29,30,35] In fact, highly ordered adlayers of H_2TMPyP were already found on various iodine modified electrode surfaces such as I/Au(111) [29-32], I/Pt(100), I/Ag(111) [33-34], I/Cu(111) and I/Cu(100) [35]. However, studies on the self-assembly of porphyrins on I/Au(100) surface have not yet been reported. Furthermore, there are no records of self-assembly of H_2TTMAPP on halides-modified gold single crystal surface.

Both porphyrin species were supplied by Frontier Scientific (in salt form) and are of high purity, water soluble and halide free. Therefore, both compounds, H_2TMPyP and H_2TTMAPP, were used without further purification to prepare the solutions, which contain the molecules in cationic form.

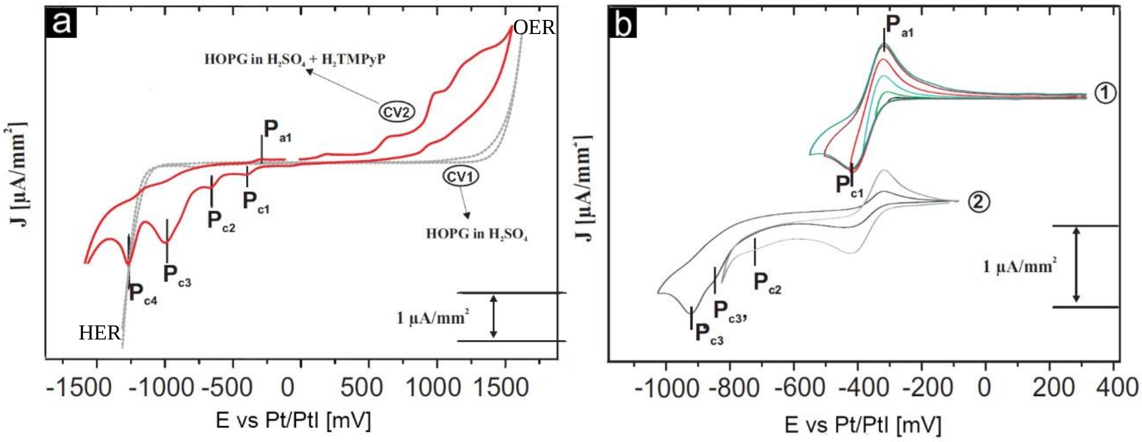

Figure 3.18: Cyclic voltammograms of HOPG in porphyrin containing 5 mM H_2SO_4 acidic electrolyte. Scan rate 20 mV/s. a) CV1: Survey CV of HOPG in the pure supporting electrolyte (5 mM H_2SO_4) and CV2: Survey CV of HOPG in the working electrolyte (5 mM H_2SO_4 + 1 mM H_2TMPyP); b) CVs of HOPG in the working electrolyte with decreasing cathodic limits [35].

3.3.2.1 Electrochemistry of the H_2TMPyP molecule in acidic solution

According to the results shown by Nguyen Thi Minh Hai (see review [35] and papers cited therein) using CV measurements of an HOPG crystal in 5 mM H_2SO_4 + 1 mM H_2TMPyP solution (see Fig. 3.18) the porphyrin molecules undergo several redox processes. The CV of HOPH in the supporting electrolyte shown in Figure 3.18a is limited by the two reactions: oxygen evolution reaction (OER) at the anodic limit and the reductive hydrogen evolution reaction (HER) at the cathodic limit, without appearance of any other cathodic and anodic peaks between these two reactions demonstrating that the HOPG surface is not affected by the presence of the halide anions. In contrast, the CV with the electrolyte containing porphyrin molecules presents a complex series of reduction and oxidation peaks. It was found that the complete reduction of this porphyrin involves 6 electrons in total occuring in several individual steps. The first step corresponds to the peak couple P_{c1}/P_{a1} (-420mV/-338mV vs Pt/PtI) – this process is reversible (see Fig. 3.18b). In this first reversible reduction step two electrons are involved and the reduction product is phlorin[2] according to:

$$[H_2TMPyP(0)]^{4+} + 2e^- + 2H^+ \leftrightarrow [H_4TMPyP(-II)]^{4+} \qquad (3.1)$$

This shows that the first two-electron reduction step influences the poprhyrin core but not the redox-active pyridyl group. Furthermore, the reduction product itself can undergo again an acid/base reaction with pK_{a2} of 0.96 creating phlorin, according to:

$$[H_5TMPyP(-II)]^{5+} \xleftrightarrow{pK_{a2}} H^+ + [H_4TMPyP(-II)]^{4+} \qquad (3.2)$$

Therefore, the final products of the first two-electron reduction steps are mainly $[H_5TMPyP(-II)]^{5+}$ and $[H_4TMPyP(-II)]^{4+}$ cations due to the acid-base equilibrium in Eq. 3.2. These porphyrin products are suggested to remain stable between the oxidation peak of P_{a1} and the next electron-reduction step which corresponds to peak $P_{c3'}$ (-853mV vs Pt/PtI). In this second reduction process are again two electrons involved according to:

$$[H_5TMPyP(-II)]^{5+} + 2e^- + 2H^+ \rightarrow [H_7TMPyP(-IV)]^{5+} \qquad (3.3)$$

$$[H_4TMPyP(-II)]^{4+} + 2e^- + 2H^+ \rightarrow [H_6TMPyP(-IV)]^{4+} \qquad (3.4)$$

The final reduction product – the porphyrinogen - is created when the potential is swept below the cathodic peak P_{c3} (-920mV vs Pt/PtI), which also involves a two-electron transfer in accordance with:

---

[2] phlorin: $H_2TMPyP(-II)$ – a reduced form of the free base porphyrin

$$\left[H_7TMPyP(-IV)\right]^{5+} + 2e^- + H^+ \rightarrow \left[H_8TMPyP(-VI)\right]^{4+} \tag{3.5}$$

$$\left[H_6TMPyP(-IV)\right]^{4+} + 2e^- + 2H^+ \rightarrow \left[H_8TMPyP(-VI)\right]^{4+} \tag{3.6}$$

The second and third reduction are irreversible processes due to the absence of the corresponding oxidation peaks $P_{c3'}$ and P_{c3} in the potential window of gold (from -1000mV to 50mV vs Pt/PtI).

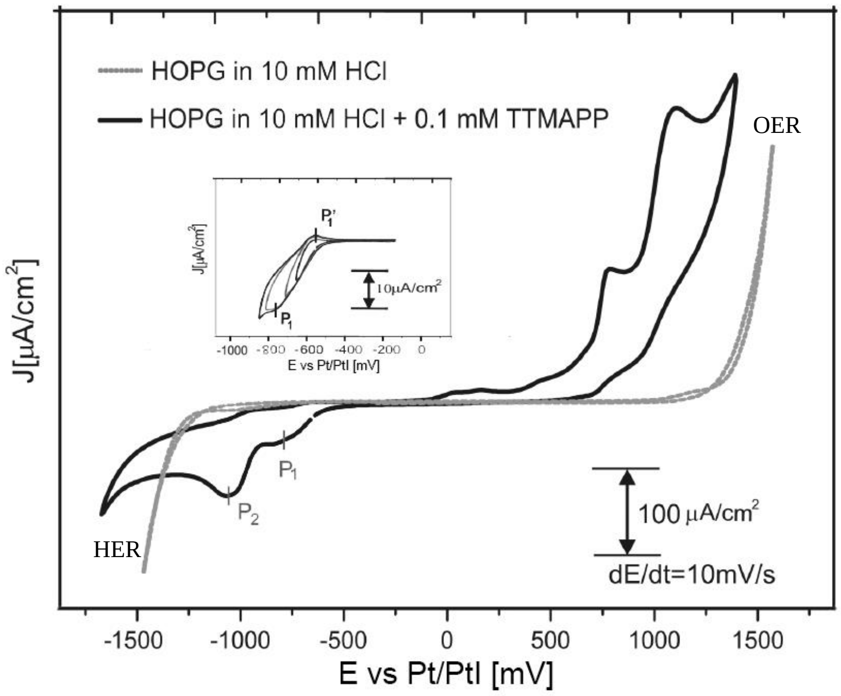

Figure 3.19: Cyclic voltammograms of HOPG in pure 10 mM HCl supporting electrolyte (dashed grey curve) and in 10 mM HCl + 0.1 mM H_2TTMAPP solution (solid black curve); inset figure indicates the quasi-reversible reduction-reoxidation pair of peaks relating to the first two-electron transfer step; scan rate 10 mV/s. [56]

3.3.1.2 Electrochemistry of the H_2TTMAPP molecule in acidic solution

Thanh Hai Phan in his work (see review [56] and papers cited therein) has shown using CV measurements with an HOPG crystal in 10 mM HCl + 0.1 mM H_2TTMAPP solution (see Fig. 3.19) that the porphyrin molecules undergo several redox processes. The dashed grey curve in Figure 3.19 represent a CV of HOPG in the pure electrolyte (10 mM HCl). The broad potential window is limited, as mentioned in the previous section, by the hydrogen evolution reaction (HER) and by the oxygen evolution reaction (OER), respectively, without the appearance of any other cathodic and anodic peaks. The solid black curve in Figure 3.19 shows a CV in the electrolyte containing the porphyrin molecules. In the potential window several anodic and cathodic current peaks are recorded belonging to the redox reactions of the H_2TTMAPP molecules. As in the case of the H_2TMPyP molecules it was found that the complete reduction of this porphyrin involves 6 electrons in total, but consists of several individual steps. The first porphyrin redox process corresponds to the peak couple $P_1/P_{1'}$ (-790mV/-630mV vs Pt/PtI) – this process is quasi-reversible. In the potential range above the first redox process til 420mV vs Pt/PtI the molecules undergo an acid/base reaction forming stable porphyrin diacid instead of the cationic $[H_3TTMAPP(0)]^{5+}$ species according to:

$$[H_2TTMAPP(0)]^{4+} + 2H^+ \xleftrightarrow{K_1} [H_4TTMAPP(0)]^{6+} \qquad (3.7)$$

Therefore, the first reversible reduction step which involves two electrons is described by the following sequence:

$$[H_2TTMAPP(0)]^{4+} + 2e^- + 2H^+ \leftrightarrow [H_4TTMAPP(-II)]^{4+} \qquad (3.8)$$

$$[H_2TTMAPP(0)]^{6+} + 2e^- \leftrightarrow [H_4TTMAPP(-II)]^{4+} \qquad (3.9)$$

This manifests that the first two-electron reduction step takes place on the porphyrin core rather than on the positively charged trimethylammonio-phenyl groups. Moreover, these reduction products can be protonated via an acid/base reaction with K_2 of 0.96 according to:

$$[H_4TTMAPP(-II)]^{4+} + H^+ \xleftrightarrow{K_2} [H_5TTMAPP(-II)]^{5+} \qquad (3.10)$$

Consequently, the final products of the first two-electron transfer step are $[H_5TTMAPP(-II)]^{5+}$ and $[H_4TTMAPP(-II)]^{4+}$ due to the acid-base equilibrium in Eq. 3.10. These reduced porphyrin spieces are suggested to remain stable within the intermediate potential between the oxidation peak $P_{1'}$ and the next reduction peak P_2. In this second/final reduction step are involved four electrons according to either:

$$[H_4TTMAPP(-II)]^{4+} + 4e^- + 4H^+ \leftrightarrow [H_8TTMAPP(-VI)]^{4+} \quad (3.11)$$

or

$$[H_5TTMAPP(-II)]^{5+} + 4e^- + 3H^+ \leftrightarrow [H_8TTMAPP(-VI)]^{4+} \quad (3.12)$$

The second reduction process which is assigned to the reduction peak P_2 is an irreversible process. Moreover, the peak P_2 appear in the potential range more negative than HER of the gold electrode.

It should be noted, that the corresponding re-oxidation peaks were only observed when HOPG was used as the working electrode but were completely absent in the case of chloride modified copper (100) and (111) surfaces [56,78,79]. These phenomena was assigned to the presence (on Cu(100)) or non-presence (on HOPG) of specifically adsorbed anions.

Comparing the electrochemical behaviour of the H_2TMPyP and $H_2TTMAPP$ molecules a significant difference between them is the reduction potential. The first reduction of the H_2TMPyP molecules take place at P_{c1} = -420mV vs Pt/PtI, while the corresponding process for $H_2TTMAPP$ occurs at P_1 = -790mV vs Pt/PtI. It was suggested that in both cases the two-electron reduction affects the inner ring system of the porphyin molecules, therefore, this shift in potential indicates the higher stability of the $H_2TTMAPP$ ring against reduction. An explanation proposed by Thanh Hai Phan [56] attributes this deviation to the impact of the functional groups on the porphyrin core. In the case of $H_2TTMAPP$ the trimethylammonio $(CH_3)_3N^+$ groups, which are well known as strong polar groups, interferes with the electron density of the π ring system, while the polar effects of the methyl (CH_3) substituents in the H_2TMPyP molecules are close to zero. Therefore, the $(CH_3)_3N^+$ groups tend to prevent electrons at the porphyring ring to be delocalized resulting in the alteration of the electrochemical behaviour.

Chapter IV

Self-assembly of porphyrin molecules on iodine-modified gold surfaces – results

4.1 Introduction

The goal of this chapter is to make a contribution to the characterization of the redox chemistry and the structural features of the self-assembly of two exemplary kinds of free base porphyrins – 5,10,15,20-Tetrakis-(N-methylpyridinium-4-yl)-21H, 23H-porphyrin (H_2TMPyP) and 5,10,15,20-Tetrakis (4-trimethylammoniophenyl) porphyrin ($H_2TTMAPP$) – on iodine-modified gold surfaces. It was found that both can form highly ordered layers on the anion modified gold surfaces even in the potential regime where the molecules are under reductive condition. Specifically iodine modified Au(100) surfaces served here as substrates for the adsorption experiments, whose structural properties have been presented in subsection 3.2.2.2.

The self-assembly process of supramolecular structures on a metal surface at the solid/liquid interface is well known to depend on a number of factors. Therefore, in order to control the self-assembly process and to create new ordered porphyrin structures on the iodine modified gold surfaces it is fundamental to understand in detail the influence of the individual parameters on their lateral ordering. In consequence, the following factors that may have impact on the self-assembly have been investigated and will be discussed in this chapter in detail, such as:

- The substrate symmetry: it is known that surface crystallographic orientation has a significant impact on the molecular self-assembly due to the difference in molecular contact to the surface. The gold substrate Au(100) was first chosen here due to its 4-fold (rotational) symmetry of the surface layer atoms.

- The nature of the preadsorbed anions: here the halogen iodide was used on the Au(100) surfaces. Adsorbed iodine layers are firstly almost uncharged [35] on metal surfaces and secondly form different adsorbate structures as a function of electrode potential. Due to the latter the anionic buffer layers are expected to govern the molecular ordering on the surface.

- The electrode potential: This parameter controls the anionic layer de/readsorption, and its structural phase transitions and likewise electron transfer reactions, de/readsorption and phase transitions of the organic layer.

4.2 H_2TMPyP adsorption on iodine-modified Au(100) surface

4.2.1 Cyclic voltammetry

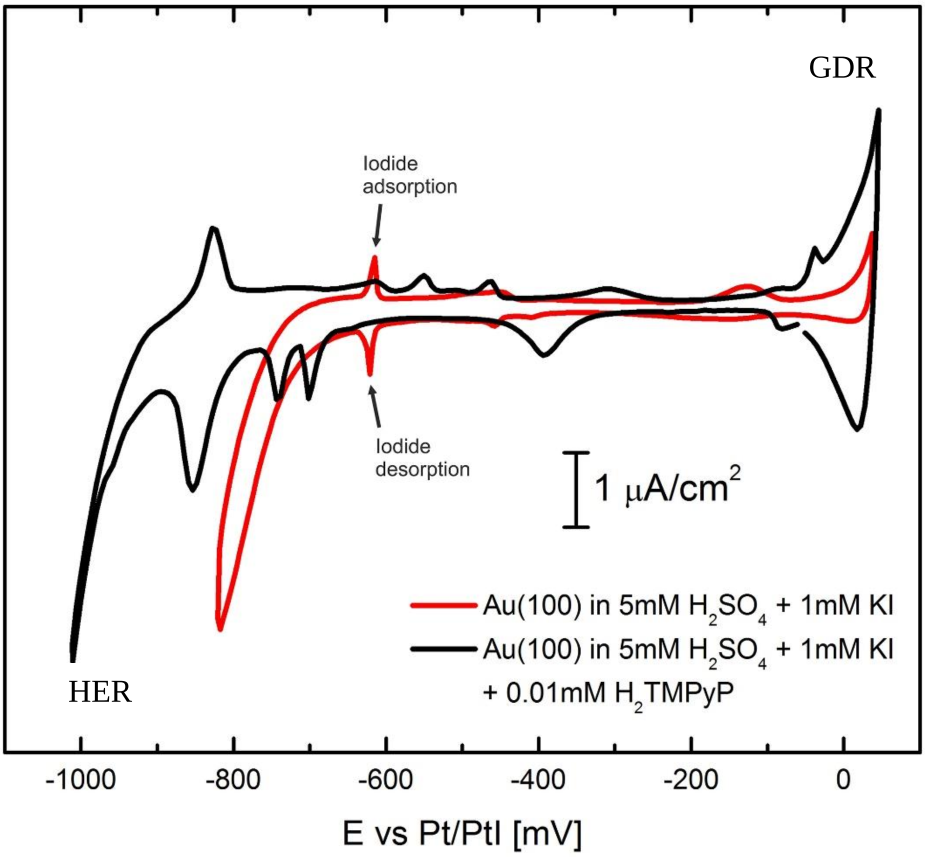

Figure 4.1: Cyclic voltammogram of a Au(100) surface in 5mM H_2SO_4 + 1mM KI electrolyte solution (red curve) and in the H_2TMPyP containing electrolyte (black curve, 5mM H_2SO_4 + 1mM KI + 0.01mM H_2TMPyP), dE/dt = $10 mVs^{-1}$.

Fig. 4.1 shows survey cyclic voltammograms (CVs) of a Au(100) electrode in the absence (red curve) and presence (black curve) of porphyrin species in an 5mM H_2SO_4 + 1mM KI electrolyte with a sweep rate of 10mVs^{-1}. The potential window of the Au(100) electrode in the 5mM H_2SO_4 + 1mM KI solution is limited by two chemical reactions, the oxidative gold dissolution reaction (GDR) [58] at the anodic limit and the reductive hydrogen evolution reaction (HER) at the cathodic limit.
After exchanging the 5mM H_2SO_4 + 1mM KI electrolyte for the one containing the H_2TMPyP molecules we observe drastic changes in the CV curve. The first observation is, that the presence of the porphyrin species has impact on the hydrogen evolution reaction, in that there is a considerable shift of the HER ($\Delta E \approx 185$mV) towards lower potentials, i.e. the HER is retarded by the presence of the molecules.

A further modification from the CV of the porphyrin-free solution concerns the appearance of several anodic and cathodic current waves within the whole potential window. These additional current features can be assigned to porphyrin redox processes as well as to structural changes or adsorption or desorption of molecules or iodine on the surface. First of all the shape of CV curves of organic species depends strongly on the chosen cathodic potential limit. By decreasing the limit of the cathodic potential systematically, a precise correlation of the cathodic to the respective anodic current wave in the reverse potential sweep can be achieved as shown in Fig. 4.2 and in the movie (move1.mp4) on the attached CD.

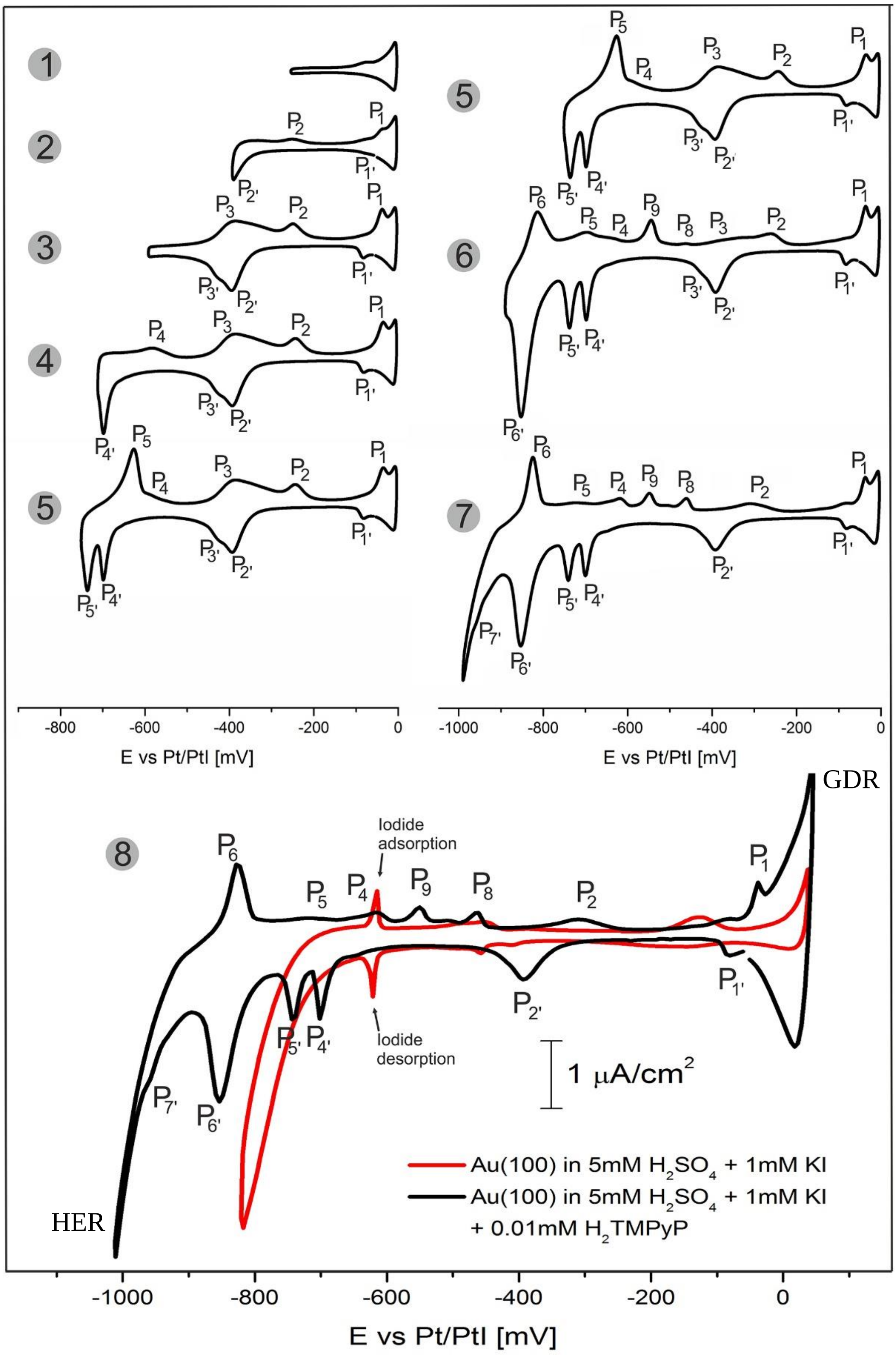

Figure 4.2: Appearance of anodic and cathodic current waves in the CV of Au(100) in the H_2TMPyP containing electrolyte upon changing the cathodic potential limit, dE/dt= 10mVs^{-1}.

When restricting the cathodic potential limit to E = -250mV, no peak pair appears in curve 1 in Fig.4.2. Extending the potential limit further to E = -390mV causes the appearance of two peak pairs $P_1/P_{1'}$ and $P_2/P_{2'}$ (curve 2 in Fig. 4.2). Continuing to decrease the cathodic potential limit to -590mV a third peak pair $P_3/P_{3'}$ emerges in curve 3 in Fig. 4.2. A fourth peak pair $P_4/P_{4'}$ becomes visible in curve 4 at a cathodic potential limit of -710mV, as shown in curve 4. The curve 5 with a cathodic potential limit at -750mV presents the next peak pair, namely P_5/ $P_{5'}$. Extending the potential limit further to E = -890mV one further peak pair $P_6/P_{6'}$ as well as two more peaks P_8 and P_9 in the reverse anodic sweep (curve 6 in Fig. 4.2) emerge. Furthermore, it is also seen that a third peak pair $P_3/P_{3'}$ start to disappear and it vanishes completely in curve 7 in Fig. 4.2 with cathodic potential limit of -990mV, where one also observes the emergence of the cathodic peak $P_{7'}$. It is clear that once the cathodic potential limit exceeds the critical value where the peak pair $P_6/P_{6'}$ appears the peak pair $P_3/P_{3'}$ disappears in the following sweep cycles, irrespective of the cathodic potential limit. Moreover the cathodic peak $P_{6'}$ decreases in the following sweep cycles, although the anodic peak P_6 stays constant. This correlation is more clearly observed in Fig. 4.3 when the Au(100) electrode is swept in the same electrolyte solution containing porphyrin molecules at a higher concentration.

At this state, combining the CV features of H_2TMPyP molecules on an HOPG electrode (see Sec. 3.3.1.1) and the Au(100) electrode, it is possible to propose an assignment for peak pair $P_3/P_{3'}$ and the cathodic peaks $P_{6'}$ and $P_{7'}$. It seems that peak pair $P_3/P_{3'}$ correspond to the first redox reaction (peak couple P_{c1}/P_{a1} in Fig. 3.18), which involves a two-electron transfer, where peak $P_{3'}$ represents the reduction step and $P_{3,}$ accordingly, the re-oxidation of the H_2TMPyP molecules [35]. This process is reversible. Moreover, the potential differences between peaks $P_{3'}$ and $P_{6'}$ is $\Delta E \approx 430\text{mV}$ and between $P_{6'}$ and $P_{7'}$ is $\Delta E \approx 74\text{mV}$ which correspond to the differences between peaks P_{c1}, $P_{c3'}$ and P_{c3} on graphite. Due to the fact that the corresponding oxidation peaks of $P_{c3'}$ and P_{c3} do not lie within the potential window of gold this process is irreversible. Therefore, after reaching the critical value of the work potential where the cathodic peak $P_{6'}$ appears the molecules on the electrode surface are reduced and in the reverse anodic potential sweep they stay in this second reduction form. Consequently the oxidation peak P_3 decreases by the amount of molecules the species underwent the second reduction step. Accordingly in the next cathodic sweep the cathodic peaks $P_{3'}$ and $P_{6'}$ are decreased. Subsequently repeating this potential sweep cycle leads to the disappearance of the peak pair $P_3/P_{3'}$. Peak $P_{6'}$ is decreased to a constant value since the observed counter peak P_6 is still observed, which indicates that not only the second reduction step takes place in the cathodic peak $P_{6'}$ but also another process.

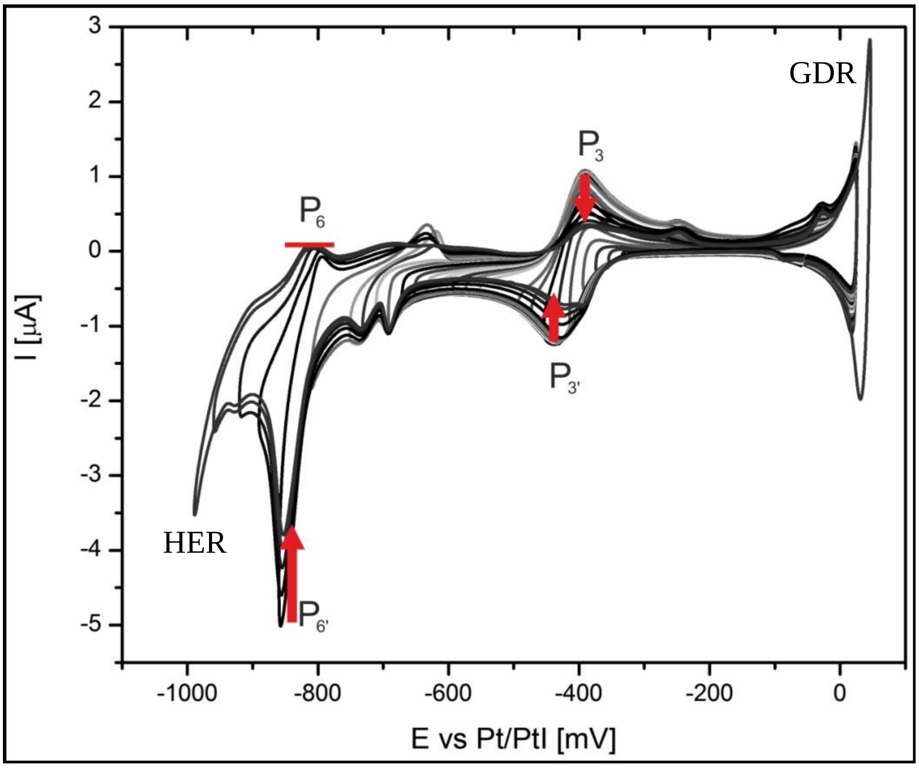

Figure 4.3: Series of CVs of a Au(100) electrode in 5mM H_2SO_4 + 1mM KI electrolyte solution containing 0.05mM H_2TMPyP with gradually decreasing cathodic potential limit, dE/dt = $10mVs^{-1}$.

The redox activity of the H_2TMPyP molecules as manifested by the peak systems $P_3/P_{3'}$, $P_{6'}$ and $P_{7'}$ can be clearly proven by concentration-dependent CV measurements. The peak current densities of $P_3/P_{3'}$, $P_{6'}$ and $P_{7'}$ scale up almost linearly with the porphyrin concentration in solution as predicted by the Randles-Sevcik equation [36] (see Sec. 2.5)

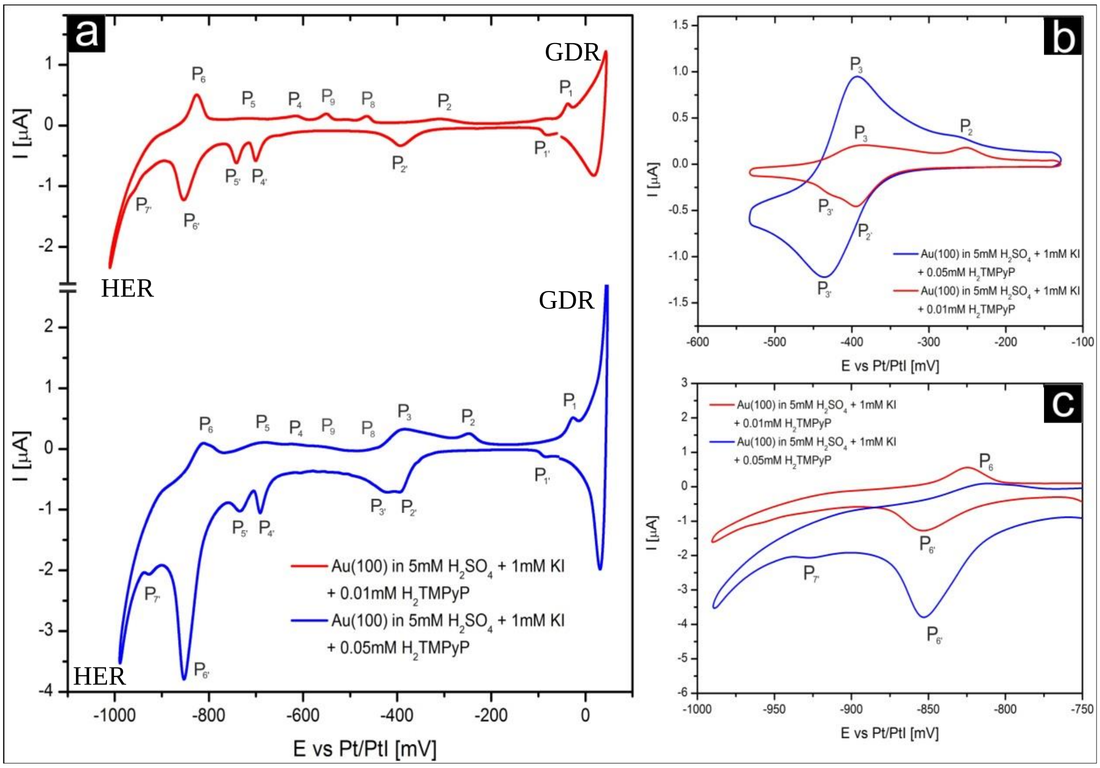

Figure 4.4: CVs of Au(100) in 5mM H_2SO_4 + 1mM KI + 0.01mM H_2TMPyP solution (red line) and Au(100) in 5mM H_2SO_4 + 1mM KI + 0.05mM H_2TMPyP solution (blue line), dE/dt= $10mVs^{-1}$; CVs taken with two different concentrations in a) the hole potential window, b) limited to the first redox reaction, and c) limited to the second redox reaction.

Although changing the concentration from 0.01mM to 0.05mM of H_2TMPyP molecules in solution increases the current density of the double layer in the entire spectrum of the CV (Fig.4.4a) with the most significant changes being observed especially on the peak pair $P_3/P_{3'}$ and the cathodic peaks $P_{6'}$ and $P_{7'}$. Fig. 4.4b presents the concentration dependence of the peak pair $P_3/P_{3'}$ with the cathodic potential limit in the CV experiment to E ≈-530mV, where essentially only the first redox reaction of the porphyrin redox system plays a role which is unaffected from changes that occur after reaching the cathodic peak $P_{6'}$ described above. At first we observe an increase in the peak maximum of P_3 from I_{P3} = 0.20µA (red line) to I_{P3} = 0.96µA (blue line) by increasing the porphyrin concentration by a factor of 5, while the peak heights of $P_2/P_{2'}$ seem to be almost independent of the porphyrin concentration in solution. Furthermore in the CV obtained for the 5mM H_2SO_4 + 1mM KI + 0.05mM H_2TMPyP solution P_2 is visible only at the anodic potential sweep. Fig. 4.4c shows the concentration dependence for the peaks $P_{6'}$ and $P_{7'}$. The increase in the peak maximum of $P_{6'}$ from $I_{P6'}$ = -1.26µA (red line) to $I_{P6'}$ = -3.78µA (blue line) is not linear which, however, can be explained by the concomitant occurrence of another process which was mentioned above. Peak $P_{7'}$ is located on the shoulder of the HER which affects its measurement.

Nevertheless this concentration dependence of $P_3/P_{3'}$ and $P_{6'}$ and $P_{7'}$ proves the redox activity of the H_2TMPyP molecules and, additionally, indicates the dominance of bulk solution redox processes in the voltammetric behaviour in the 5mM H_2SO_4 + 1mM KI + 0.05mM H_2TMPyP solution. Moreover it also indicates that the rest of the current features represent other surface processes such as phase transitions, desorption/adsorption of porphyrin molecules or iodine, etc.

Therefore, comparing the CVs in the presence and absence of porphyrin molecules in solution we can assign the peak pair $P_{4'}/P_4$ to a peak pair d'/d of desorption/adsorption of iodine on the surface. Interestingly, it can be observed that the desorption peak $P_{4'}$ of iodine in the presence of porphyrin molecules is shifted to more negative potential than peak d'. The explanation is simply that the organic over layer hinders the iodine desorption; the repulsive force between the negatively charged gold substrate and the iodine must be increased further in order to overcome the organic overlayer.

More information about the origin of each current feature in the CV can be obtained from in-situ STM measurements which will be described in the following.

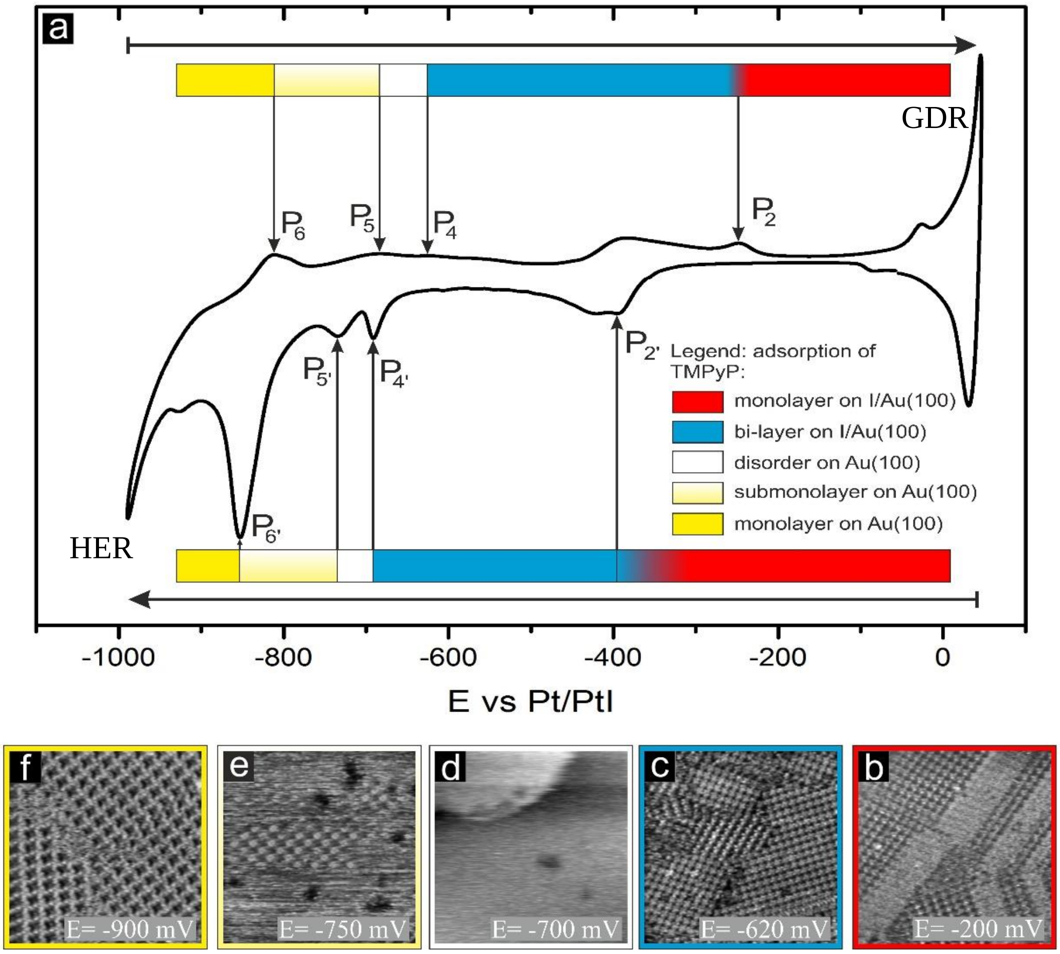

Figure 4.5: Potential window of an I modified Au(100) divided in five adsorption intervals of H_2TMPyP molecules.

4.2.2 In-situ STM investigation

Following the discussion in the previous section, the electrochemical characterisation of H_2TMPyP adsorption on an I modified Au(100) gives a clear impression of the complexity of this system. In order to present it in a simple way it can be divided into four regimes within the Au potential window, each one of which representing drastic changes in the surface morphology due to the applied electrode potential. These regimes were initially defined by the STM measurements, but the changes are strictly correlated with the observed current features in the CV curve (see Fig. 4.5) and are listed below from positive to negative potential regimes:

1. The first regime (red colour in Fig. 4.5) starts from the GDR and reaches to the peak pair $P_{2'}/P_2$ where we observe a self-assembly of a monolayer of H_2TMPyP molecules on the I/Au(100) surface. The Figure 4.5b shows an exemplary STM image taken within this potential regime. In this potential range one observes five different ordered porphyrin phases. This monolayer regime is describe in detailed in section 4.2.2.1.

2. The next regime (blue colour in Fig. 4.5) is located between the peak pairs $P_{2'}/P_2$ and $P_{4'}/P_4$ where a bi-layer of porphyrin molecules on the I/Au(100) surface occurs. Therefore, the peak pair $P_{2'}/P_2$ is characterize as a phase transition between a monolayer/bi-layer and bi-layer/monolayer regime, respectively. An exemplary STM image of this regime is presented in Figure 4.5c. In this potential window again five H_2TMPyP molecule structures were found, which are described in detail in section 4.2.2.2.

3. The third regime (white and white-yellow colour in Fig. 4.5) extends from peak pair $P_{4'}/P_4$ over $P_{5'}/P_5$ to $P_{6'}/P_6$. The peak pair $P_{4'}/P_4$ as described in the previous section corresponds not only to the desorption/adsorption of iodine but also to the disordering/ordering of the porphyrin layer. Accordingly, between the peak pairs $P_{4'}/P_4$ and $P_{5'}/P_5$ a disordering of the H_2TMPyP molecules on the I-free (1x1) Au(100) surface is observed (see Fig.4.5d). Below the peak pair $P_{5'}/P_5$ but above $P_{6'}/P_6$ sporadically a sub-monolayer of porphyrin molecules occurs on the I-free (1x1) Au surface (see Fig.4.5e). This regime is described in detail in section 4.2.2.3.

4. The fourth and last regime (yellow colour in Fig. 4.5) is located between $P_{6'}/P_6$ (peak $P_{6'}$ determines a second reduction of the H_2TMPyP molecules) and the HER reaction and represents the ordered monolayer of porphyrin molecules on the I-free (1x1) Au(100) surface. An exemplary STM image of this regime is shown in Figure 4.5f. This regime is described in detail in section 4.2.2.4.

In the following sections the color-code introduced in Fig. 4.5 is used throughout the rest of this thesis for the edging of the STM images.

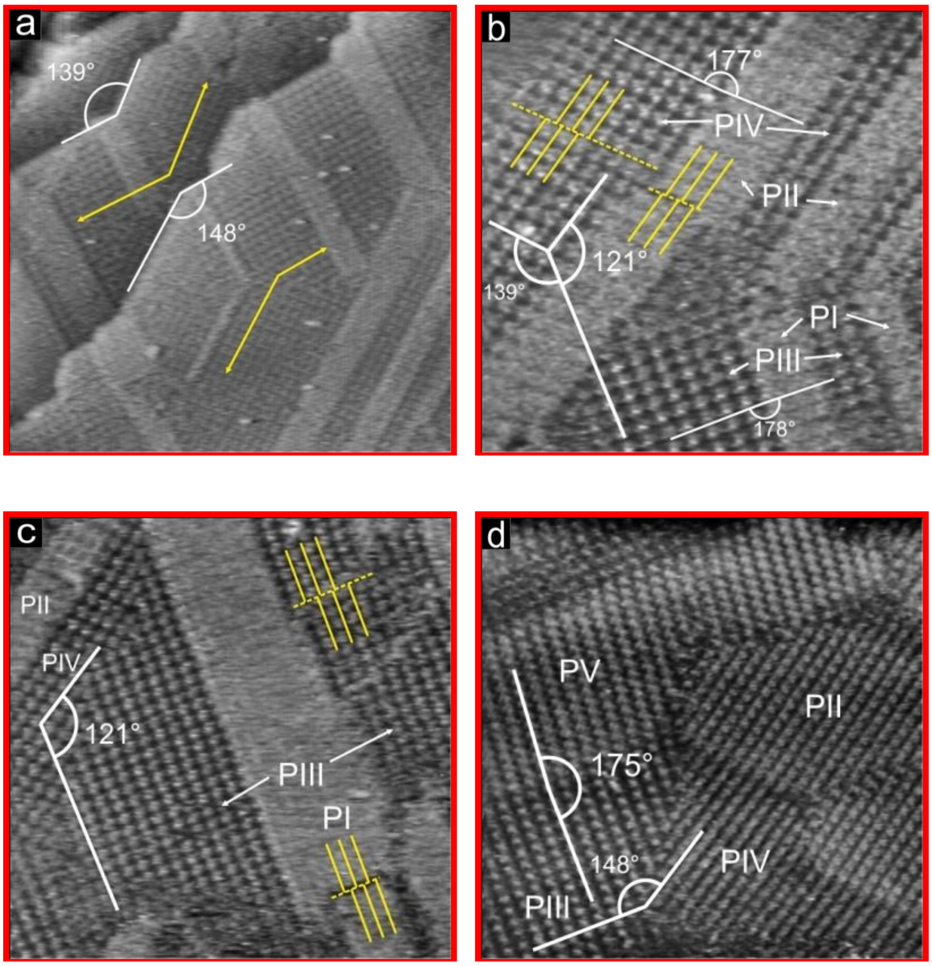

Figure 4.6: Self-assembly of H_2TMPyP on an iodine-modified Au(100) electrode in the monolayer regime. a) 83.55nm x 83.55nm, I_t = 1nA, U_b = -320mV, E= -200mV vs Pt/PtI, b) 42.35nm x 42.35nm, I_t = 1nA, U_b = -472mV, E= -200mV vs Pt/PtI, c) 56.47nm x 56.47nm, I_t = 1nA, U_b = -491mV, E= -200mV vs Pt/PtI, d) 56.47nm x 56.47nm, I_t = 1nA, U_b = -303mV, E= -200mV vs Pt/PtI.

4.2.2.1 Monolayer adsorption of H_2TMPyP on I/Au(100) surface

The measurements started with the preparation of a highly ordered iodine layer on the Au(100) surface which prior to porphyrin adsorption was checked by

STM (see Section. 3.2.2.2). Then this iodine-modified Au(100) surface was exposed to a 5mM H_2SO_4 + 1mM KI solution containing 0.01mM H_2TMPyP in order to adsorb the porphyrin molecules. STM measurements were carried out just after the electrolyte exchange immediately showing the porphyrin adsorption on top of the I/Au(100) substrate.

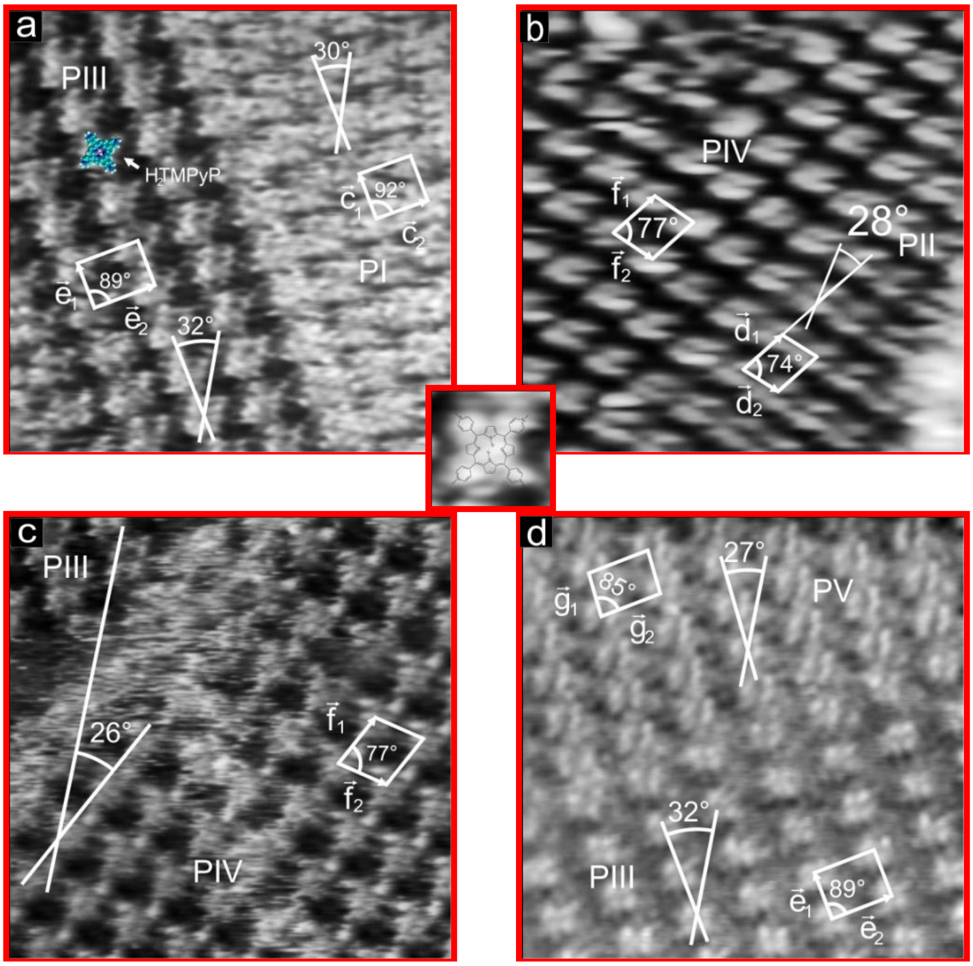

Figure 4.7: High-resolution images of the ordered H_2TMPyP adlayer on an iodine-modified Au(100) electrode in the monolayer regime. a) 14.12nm x 14.12nm, I_t = 1nA, U_b = -472mV, E= -200mV vs Pt/PtI. b) 14.15nm x 14.15nm, I_t = 1nA, U_b = -291mV, E= -200mV vs Pt/PtI. c) 14.12nm x 14.12nm, I_t = 1nA, U_b = -472mV, E= -200mV vs Pt/PtI. d) 14.12nm x 14.12nm, I_t = 1nA, U_b = -303mV, E= -200mV vs Pt/PtI.

The monolayer regime is situated between the GDR and the peak pair $P_2/P_{2'}$ (-250/-395mV vs Pt/PtI). Typical large scale STM images acquired at -200mV vs Pt/PtI and measured soon after the electrolyte exchange showing the surface structure of the H_2TMPyP adlayer on top of the I/Au(100) surface are displayed in Fig. 4.6. Each bright dot represents one porphyrin molecule. It is seen that the molecules are self-assembled into an ordered layer of molecular rows covering the atomically flat terraces. First of all, one can clearly see that the orientation of step edges is dominated by the arrangement of the molecules in such a way that step edges are parallel to the direction of the molecular rows (see yellow lines in Fig.4.6a). Furthermore, careful examination of Fig. 4.6a-d yields the coexistence of five porphyrin phases. Within each phase translation domains are observable which are denoted with yellow solid lines and the domain boundary between them marked by dashed yellow lines (see Fig. 4.6b-c).

	P_I	P_{II}	P_{III}	P_{IV}	P_V
lattice constants [± 0.05nm]	$c_1 = 1.61$ $c_2 = 1.80$	$d_1 = 1.94$ $d_2 = 1.56$	$e_1 = 1.61$ $e_2 = 2.06$	$f_1 = 1.94$ $f_2 = 1.76$	$g_1 = 1.46$ $g_2 = 2.06$
angle [± 1°]	92°	74°	89°	77°	85°
molecule rotation [$\alpha \pm 1°$]	+30° vs $\bar{c}_1$	-28° vs $\bar{d}_1$	+32° vs $\bar{e}_1$	+26° vs $\bar{f}_1$	+27° vs $\bar{g}_1$
surface concentration [molecules/cm^2]	$3.453 \cdot 10^{13}$	$3.437 \cdot 10^{13}$	$3.016 \cdot 10^{13}$	$3.014 \cdot 10^{13}$	$3.333 \cdot 10^{13}$

Table 1. Parameters of individual phases in Fig. 4.6.

The high resolution images in Figs. 4.7a-d of the molecular shape reveal that the molecules are lying flat on the substrate due to the large molecular π system which has the tendency to maximize the π bonding to the surface [29-32,35,56]. Each flat-lying porphyrin molecule can be recognized as a square shaped feature with characteristic four additional lobes placed at the corners of a square (see inset in Fig.4.7). The center to center distance measured diagonally between the spots is 1.2 ± 0.1nm. This corresponds to the distance between two diagonally located pyridinium units. The porphyrin molecules within each phase are arranged in rows. Fig. 4.7a shows the coexistence of two phases, P_I and P_{III}. The lattice unit-cell for the Phase I can be drawn as show in Figure 4.7a with the lattice parameters of c_1 = 1.61 ± 0.05nm and c_2 = 1.80 ± 0.05nm with an angle of ca. 92° between them. Individual molecules within one row are rotated by about +30° with respect to the row direction parallel to the $\overline{c_1}$ vector. Each unit cell includes one H_2TMPyP molecule, which corresponds to a surface concentration of ca. $3.453 \cdot 10^{13}$ molecules/cm^2. Fig. 4.7b displays the coexistence of phases P_{II} and P_{IV}. Phase II with its corresponding unit-cell is presented in the lower part of Figure 4.7b. The lattice constants are d_1 = 1.94 ± 0.05nm and d_2 = 1.56 ± 0.05nm enclosing an angle of 74°. All molecules within one row are rotated with respect to the row direction along the $\overline{d_1}$ vector by about -28°. As in the case of Phase I each unit cell includes one porphyrin molecules, consequently resulting in a surface concentration of ca. $3.437 \cdot 10^{13}$ molecules/cm^2. Phase III with denoted unit-cell is presented in the left part of Figure 4.7a. The lattice constants are e_1 = 1.61 ± 0.05nm and e_2 = 2.06 ± 0.05nm enclosing an angle of ca. 89°. Individual molecules within one row are rotated by about +32° with respect to the row direction parallel to the $\overline{e_1}$ vector. Furthermore, vectors $\overline{c_1}$ of Phase I and $\overline{e_1}$ of Phase III have the same value and direction. The unit-cell of Phase III as indicated in Fig. 4.7a and c contains one porphyrin molecules which corresponds to a surface concentration of ca. $3.016 \cdot 10^{13}$ molecules/cm^2. Phase IV with its corresponding unit-cell is shown in Figures 4.7b and c. The nearest neighbour distance between porphyrin molecules of Phase IV were found to be f_1 = 1.94 ± 0.05nm and f_2 = 1.76 ± 0.05nm with an angle of about 77°. In this case the symmetry axes of the porphyrin molecules in this case are rotated with respect to the molecular row direction parallel to $\overline{f_1}$ by an angle of about +26°. Furthermore the $\overline{f_1}$ vector is parallel to the $\overline{d_1}$ vector and both have the same value. Each unit-cell of Phase IV contains one molecule which corresponds to a surface concentration of ca. $3.014 \cdot 10^{13}$ molecules/cm^2. It should be noted that the surface concentrations of the two phases Phase III and IV are essentially equal. Finally the unit-cell of Phase V is illustrated in Figure 4.7d. The lattice constants are $g_1 = 1.46 \pm 0.05$nm and $g_2 = 2.06 \pm 0.05$nm enclosing an angle ca. 85°. All molecules within one row are rotated with respect to the row direction parallel to the $\overline{g_1}$ vector by about +27°. Moreover, vectors $\overline{g_1}$ and $\overline{e_1}$ are parallel to each other and have the same value. Each unit cell contains again one porphyrin molecule which corresponds to a surface concentration of ca. $3.333 \cdot 10^{13}$ molecules/cm^2.

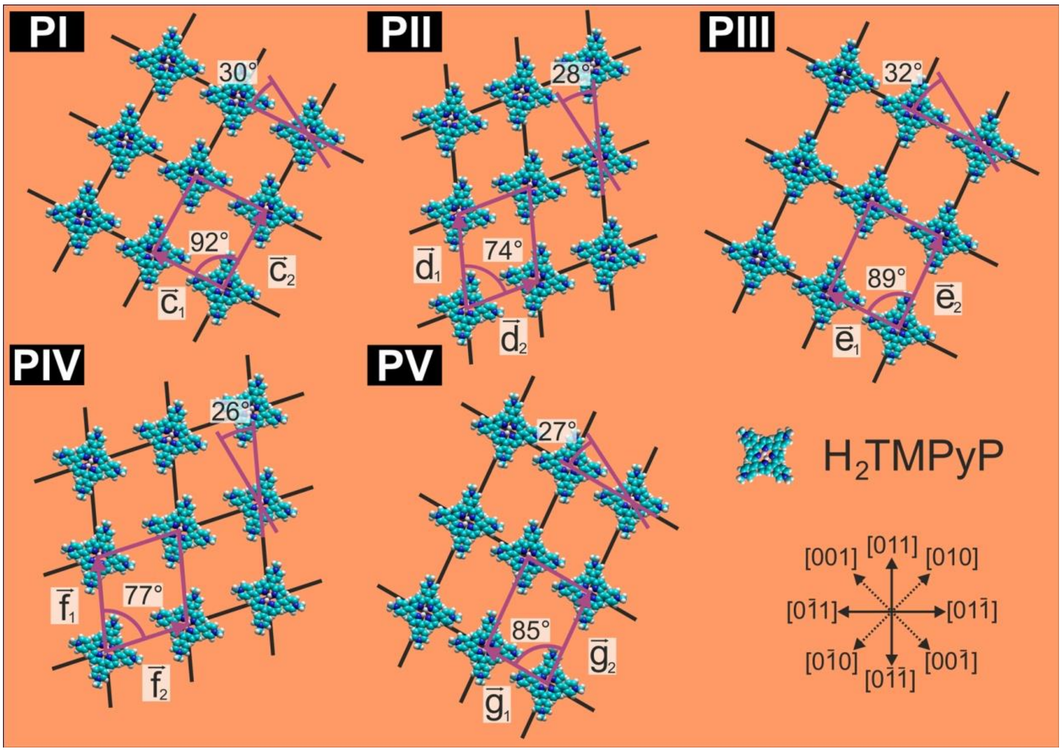

Figure 4.8: Schematic models of the five ordered H_2TMPyP molecular phases in the monolayer regime on I/Au(100), with the denoted vectors of the unit cells and the angles between them.

The summary of the parameters described above for each phase can be found in Table 1. Based on the experimental results of the symmetry and orientation of the H_2TMPyP molecules, a schematic model of the ordered H_2TMPyP molecules is proposed for each phase in Fig. 4.8. As can be seen the surface concentration for the last described Phase V lies in the middle of those phases mentioned before. Furthermore, Phase V was observed rather rarely in comparison to the Phases I-IV and only when the adsorption process of the porphyrin molecules started at an electrode potential of ca. -200mV vs Pt/PtI, and it vanished altogether after changing the potential to where the Phases I-IV were observed within more broad potential regimes. This suggests that Phase V is less stable than Phases I-IV and is observable only under specific conditions, e.g. after adsorption at -200mV vs Pt/PtI and within a narrow range of electrode potential. At this point several questions arise: In which exact potential regimes are Phases I-IV stable? Is there a competition between these phases due to their different surface concentrations, and if there is competition what is the reason of it? In order to answer these questions two experiments provide further information:

1. Potentiodynamic STM experiment: It is obvious that the electrode potential has a strong influence on the self-assembly process of the organic molecules on the electrode surface. Changing the electrode potential can induce a phase transition inside an ordered porphyrin layer even without any electron transfer process. As presented in subsection 4.2.1 within the monolayer potential range the porphyrin molecules do not undergo any redox process, i.e. no electron transfer process occurs. Hence, the phase transitions which occurs within the monolayer regime are not caused by a variation in the chemical state of the porphyrin but only by a variation of the interaction between the porphyrin molecules and the substrate.

2. Structural correlation between the porphyrin adlayer and the substrate lattice underneath: By changing the tunnelling conditions (namely the bias voltage) a so called resonant tunnelling occurs [68, 69]. At a high bias voltage almost all electrons flow through a resonate tunnelling process via the quantized energy level in the potential well. These discrete energy levels correspond to the levels of the molecular orbitals or a band generated by the periodic arrangement of the molecules, which enables imaging of the organic molecules. On the other hand, at a lower bias voltage the normal tunnelling process dominates the current density, in which electrons tunnel through the

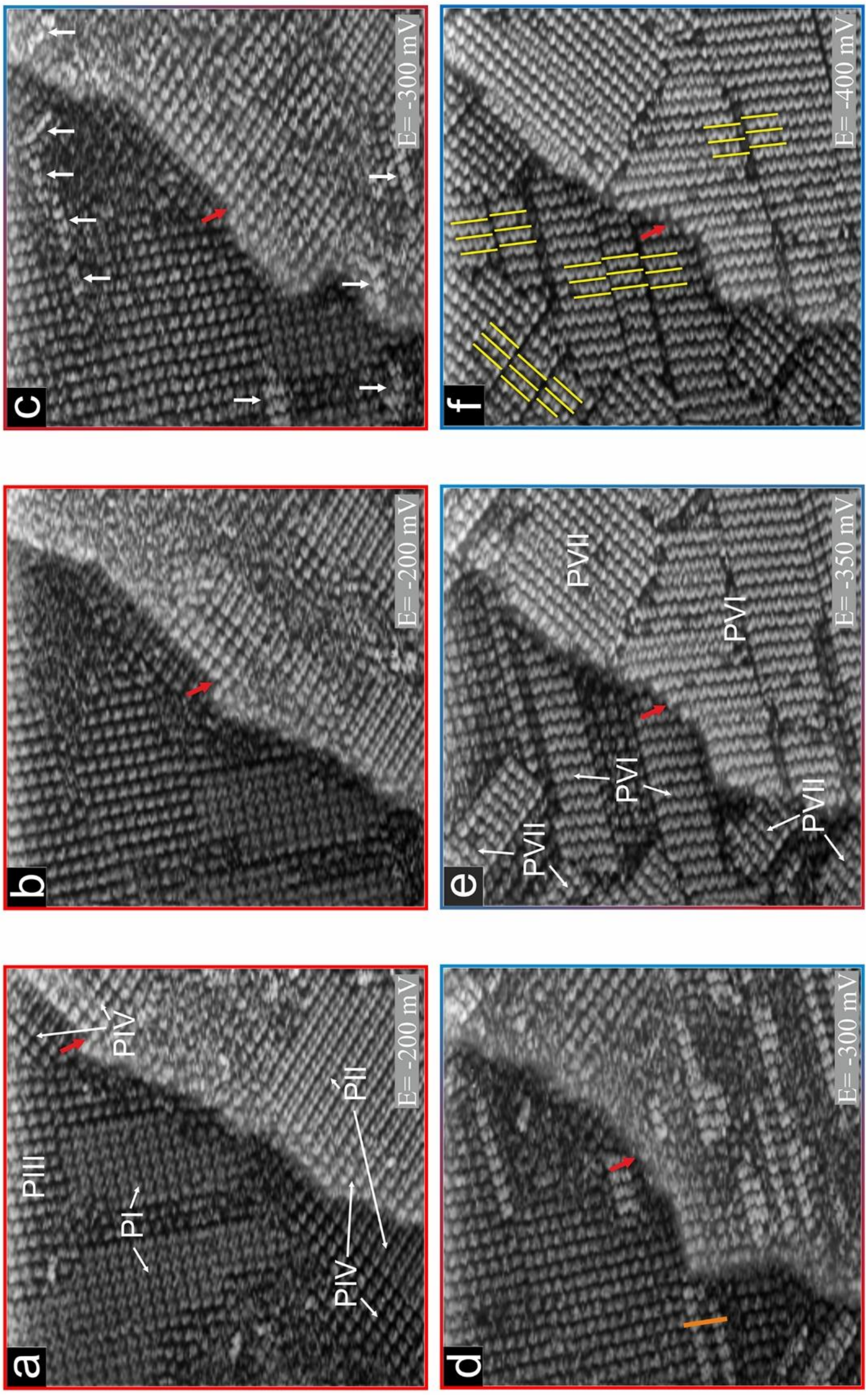
a
PIII
PI
PIV
PIV
PII
E= -200 mV
b
E= -200 mV
c
E= -300 mV
d
E= -300 mV
e
PVII
PVI
PVII
PVII
PVI
E= -350 mV
f
E= -400 mV

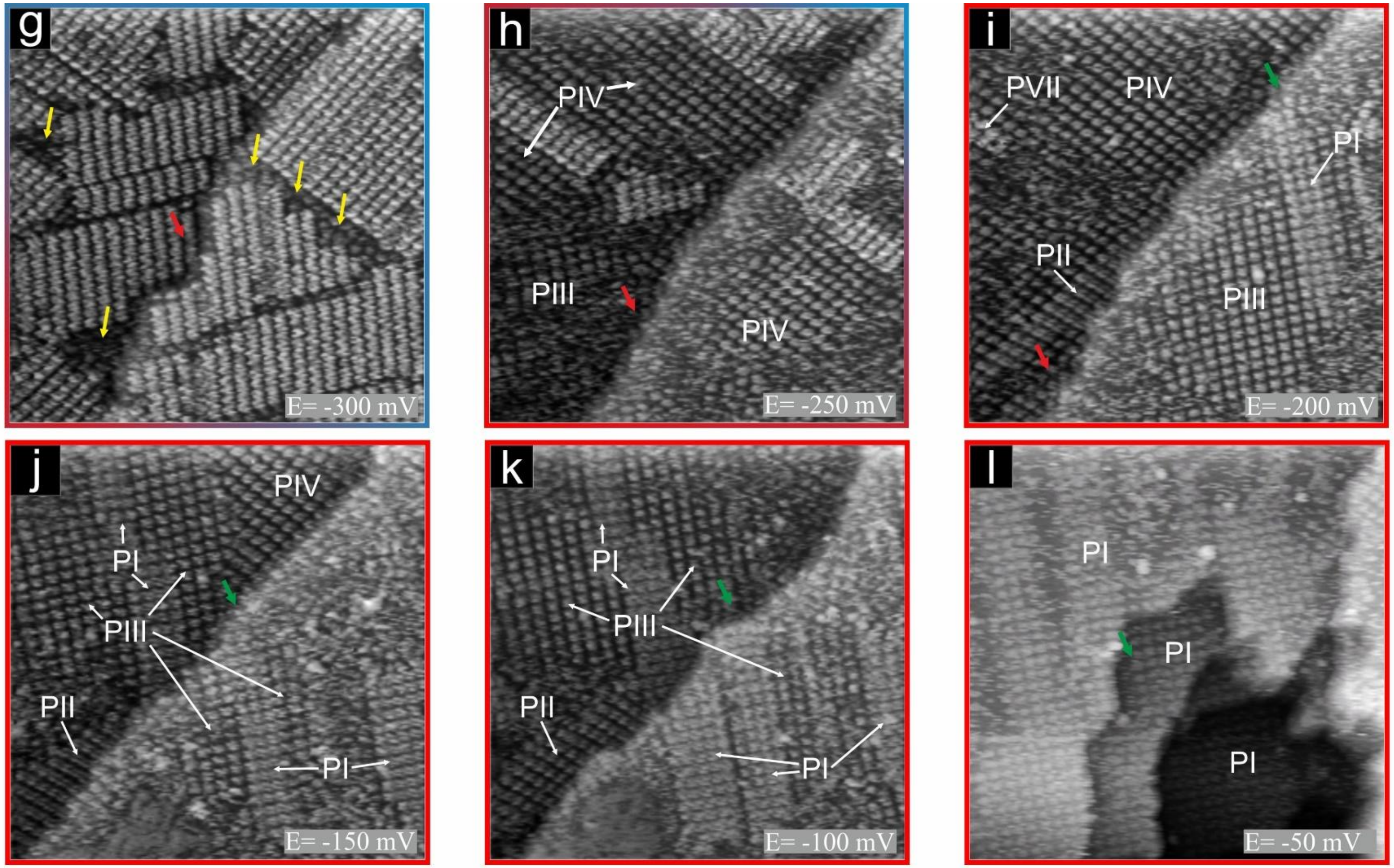

Figure 4.9: Potential induced phase transition of molecular H_2TMPyP adlayer on an I/Au(100) electrode surface, STM series: 50.32nm x 50.32nm; a) I_t = 1nA, U_b= -291mV; b) I_t = 1nA, U_b= -267mV; c) I_t = 1nA, U_b = -267mV; d) I_t = 1nA, U_b = -267mV; e) I_t = 1nA, U_b = -208mV; f) I_t = 1nA, U_b = -208mV; g) I_t = 1nA, U_b = -208mV; h) I_t = 1nA, U_b = -208mV; i) I_t = 1nA, U_b = -250mV; j) I_t = 1nA, U_b = -477mV; k) I_t = 1nA, U_b = -461mV; l) I_t = 1nA, U_b = -461mV.

potential well without interacting with the localized discrete levels, i.e., electrons tunnel as if there were nothing between the tip and substrate. Furthermore, in some case at an intermediate/low bias voltages a tunnel process may occur in which electrons tunnel mainly through the potential well with small interaction with the localized discrete levels of the molecules, so that the obtained image is a superposition of features of both the substrate and adsorbate. This experiment enables a direct correlation between the structure of the organic adlayer and that of the underlying iodine and gold lattice.

4.2.2.1.1 Potentiodynamic STM measurements.

The potentiodynamic STM measurement was started at -200mV vs Pt/PtI (see Fig.4.4) revealing a highly ordered porphyrin layer with the first four phases described above (see Fig. 4.9a-b). The red arrow on the Figure 4.9a-i indicates always the same position on the surface which in the following figures is, due to the thermal drift, drifted away and a new green arrow is added to point at a new area of the surface (see Fig. 4.9j-k). From the starting point, the electrode potential was carefully scanned in the cathodic direction. Phase I and II start to shrink while Phase III and IV grow. When the potential reached -300mV vs Pt/PtI Phase I and II in short time are finally replaced by Phase III and IV (see Fig. 4.9c-d). Furthermore, new bright spots appear in the images (see white arrows in Fig. 4.9c) which represent the growth of a completely new ordered phase of porphyrin molecules. Moreover in Fig. 4.9d is denoted a short orange line along which the height profile of Fig. 4.10a was taken. Between the bright and dark spots the height difference is around 0.3nm. This value approximately matches the thickness of one flat lying porphyrin molecule on the surface [70]. Furthermore, the small STM image (see low part of a Fig. 4.10b-c) demonstrates that all molecules lie flat on the surface, which follows from their square shape with four lobes placed at the corners representing the four pyridyl groups. The same value is observed for the line profile in Fig. 4.10d along the orange line in Fig. 4.10b, where are clearly visible single molecules. Moreover it is distinctly seen that the higher (brighter) molecules stay on-top of the first lower ones (dark) which is a common observation for H_2TMPyP molecules [35]. These observations suggest that the new bright spot represent a bi-layer adsorption on the surface, i.e. adsorption of molecules in the second layer.

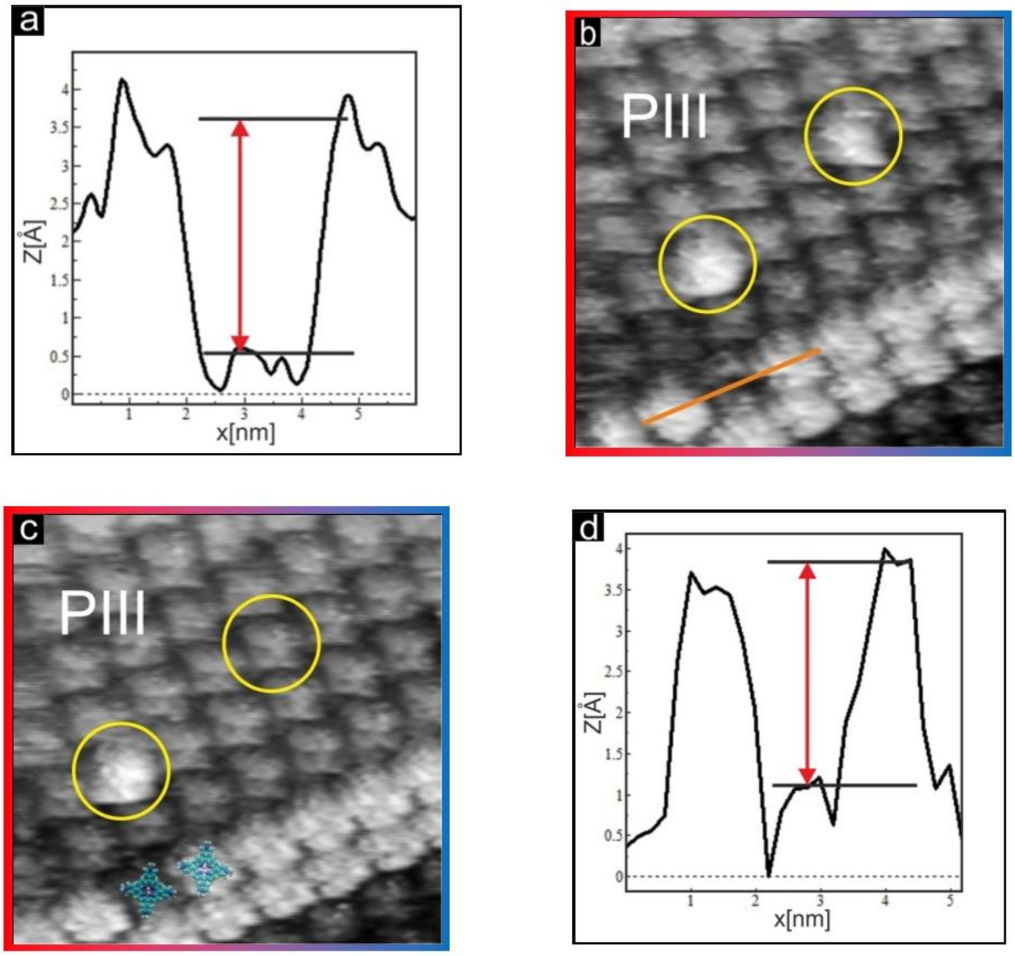

Figure 4.10: a) Cross section along the orange line in Fig. 4.9d; b) 13.64nm x 13.64nm, I_t = 1nA, U_b = -440mV, E= -275mV vs Pt/PtI; c) 13.64nm x 13.64nm, I_t = 1nA, U_b = -440mV, E= -275mV vs Pt/PtI; d) cross section along the orange line in Fig. 4.10b.

Interestingly, in Figure 4.10b, marked by yellow circles, one can occasionally see adsorption of single molecules on the monolayer phase P_{III} (a similar observation was made for phase P_{IV}). These single molecules were found to be quite mobile. The shapes of the mentioned single molecules are fuzzy compared to those adsorbed in the new bi-layer phases, which indicates their mobility. Besides, from the successively recorded STM images in Fig. 4.10b-c one observes the desorption of one molecule from the upper yellow circles (Fig. 4.10d). From these observations it is obvious that P_{III} and P_{IV} are not energetically favourable for the adsorption of H_2TMPyP molecules in the second layer. An overall impression of the adsorption of single molecules on top of the monolayer phase is presented in the movie on the attached CD (move2.mp4).

Further reduction of the electrode potential leads to an increase of the bi-layer phase instead of Phase III and IV which are finally completely replaced when the potential reaches the maximum of peak $P_{2'}$ at -395mV vs Pt/PtI (see Fig. 4.9d-f). The potential was systematically decreased down to -500mV vs Pt/PtI without any significant changes on the surface; then the potential was swept back into positive direction. No changes where noticed until the electrode potential reached again -300mV vs Pt/PtI. At this potential a disordering of the lateral structure at the domain boundaries as well as desorption of second layer porphyrin molecules start to take place (see yellow arrows in Fig. 4.9g). When the electrode potential has reached the anodic peak P_2 at -250mV vs Pt/PtI again the bi-layer phases have almost completely vanish. At a potential of ca. -200mV vs Pt/PtI, represented by Fig. 4.9i, the Phases I and II reappeared on the surface. Changing the electrode potential even further in the anodic direction leads to an increasing coverage of Phase I and II in place of Phase III and IV (see Fig. 4.9j-k) and finally a complete replacement of the latter two phases. Moreover, at a potential of -100mV vs Pt/PtI which is represented by Fig. 4.9k an oxidative gold dissolution reaction starts at the step-edges. After reaching the electrode potential of -50mV vs Pt/PtI where the oxidative gold dissolution reaction proceeds very strongly (see Fig. 4.9l) Phase II vanished from the surface altogether while Phase I was still clearly observable.

Figure 4.11 exhibits a CV in which the stable potential regimes of the four Phases I-V are denoted. So, first of all, from the potentiodynamic STM measurements we observe a competition between these phases as manifested by their different surface concentrations. Furthermore, comparing the structural changes on the surface with the surface concentration of porphyrin molecules for each phase we observe a strict relationship between the potential regime of each phase and its surface concentration, i.e. Phase I has the highest surface concentration ($3.453\cdot10^{13}$ molecules/cm^2) and its existence regime is at the most positive potentials in comparison to the other phases. Next, Phase II with a lower concentration than Phase I, namely $3.437\cdot10^{13}$ molecules/cm^2, occurs at somewhat lower potentials. Finally, the two Phases III and IV with the lowest surface concentrations (of $3.016\cdot10^{13}$ molecules/cm^2 and $3.006\cdot10^{13}$ molecules/cm^2, respectively) among the monolayer phases have their potential regimes at the most negative potentials.

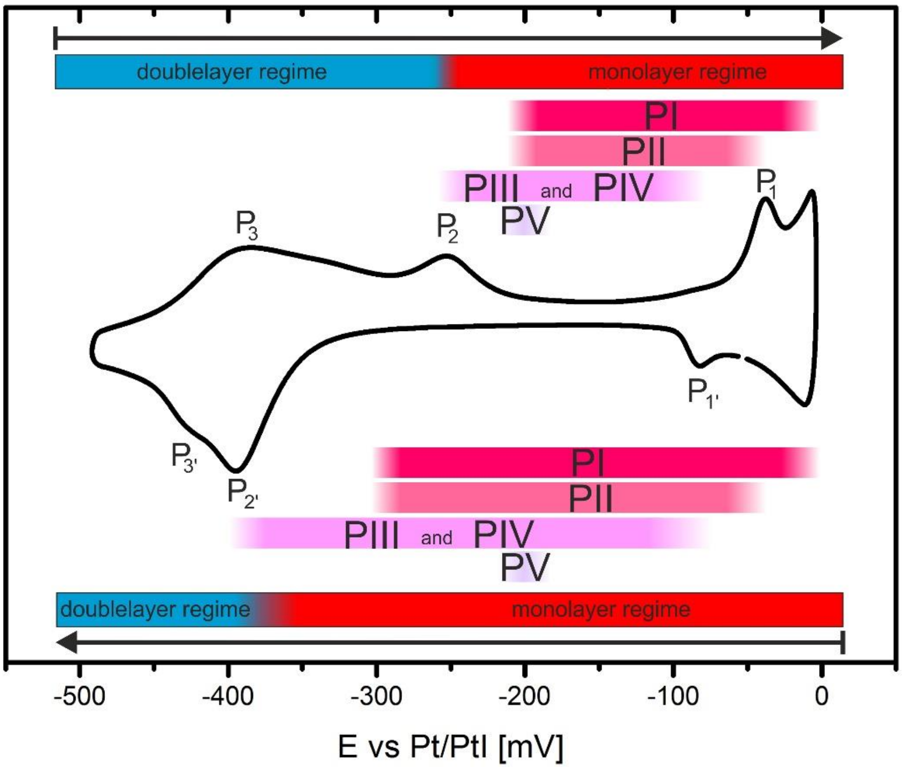

Figure 4.11: Diagram of H_2TMPyP adsorption regimes of Phases I-V.

4.2.2.1.2 Structural correlation between porphyrin adlayer and the substrate lattice.

The previous section gave us answers about the competition between various phases of adsorbed H_2TMPyP based on their different surface concentrations and in which potential regimes those phases are stable. It was found a strict correlation between the surface concentration and the potential regimes of highest stability of each phase. In this section we investigate what the reasons are for this correlation and if there is a connection to the iodine lattice underneath. In order to acquire information about the structural correlation between the porphyrin adlayer (here for Phase I and III) and the substrate lattice underneath a set of STM images (Fig.4.12a-b and Fig.4.12d-e) of 14.12nm x 14.12nm were recorded successively at the same surface area. It is well known that by changing the tunnelling conditions (namely tunneling bias) a resonant tunneling may occurs [68,69]. At high bias voltage (e.g. U_b=-416mV in Fig. 4.12a and U_b=-472mV in the lower half part of Fig. 4.12d), almost all electrons flow through the resonant tunnelling process via the quantized energy levels in the potential well. These discrete energy levels correspond to the levels of the molecular orbitals or the band generated by the periodic arrangement of the molecules. Thus, tunneling through these states accentuates the contribution of the organic molecules to the respective STM images molecules. On the other hand, at lower bias voltage (e.g. U_b=-9mV in the upper-left part of Fig. 4.12d and left part of Fig.4.12e), the normal tunnelling process dominates the current density, in which electrons tunnel through the potential well without interacting with the localized discrete levels, i.e., electrons tunnel as if there were nothing between the tip and the substrate. Furthermore, in some cases at an intermediate/low bias voltage it is possible to observe a tunnel process in which dominant tunneling through the potential well is superimposed by small interactions with the localized discrete levels so that the obtained image comprises features that can be associated with a combination of contributions from both the substrate and the adsorbate (see e.g. Fig. 4.12b. at U_b=-13mV and upper-right part of Fig. 4.12d and right part of Fig. 4.12e at U_b=-9mV). Such images enable a direct correlation between the structure of the organic overlayer and that of the underlying iodine and gold lattice. Moreover, the simultaneous observation of features from both the molecules on the one hand and iodine or gold underneath on the other hand (Fig. 4.12b and e) strongly suggest that the observed bias dependence of images is not primarily due to physical displacement of molecules from the substrate by the tip at low bias voltages. After close analysis of the images presented in Figure 4.12 it is possible to present accurate models of adsorption of two phases (P_I and P_{III})

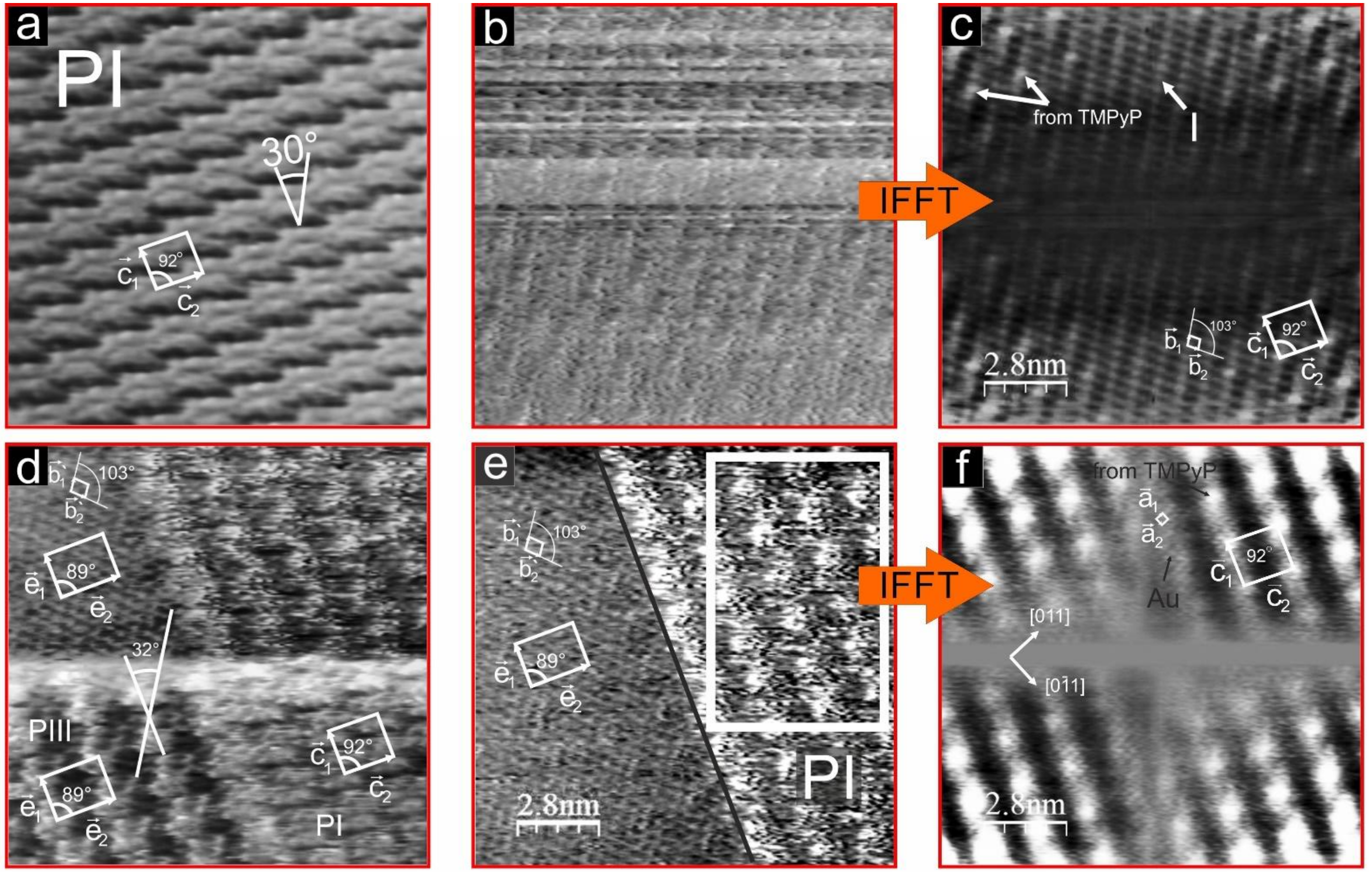

Figure 4.12: Structure correlation between the H_2TMPyP layers of phases I and III and the underlying respective iodine and gold layer, a) Porphyrin layer of phase I at high tunneling bias, 14.12nm x 14.12nm, I_t = 1nA, U_b = -416mV, E= -200mV vs Pt/PtI, b) Iodine layer underneath phase I at low tunneling bias, 14.12nm x 14.12nm, I_t= 1nA, U_b = -13mV, E= -200mV vs Pt/PtI, c) a Reverse Fast Fourier Transform (IFFT) of the STM image (b), d) upper part: Iodine layer underneath phase III at low tunneling bias: U_b = -9mV, lower part: Porphyrin layer of phase III at high tunneling bias: U_b = -472mV, 14.12nm x 14.12nm, I_t = 1nA, E= -200mV vs Pt/PtI, e) left part: Iodine layer underneath phase I at low tunneling bias: U_b = -9mV, right part: combination of the Porphyrin layer and the substrate layer at low tunneling bias: U_b = -9mV, 14.12nm x 14.12nm, I_t = 1nA, E= -200mV vs Pt/PtI, f) a Reverse Fast Fourier Transform (IFFT) of the left part of STM image (e).

including structural relationship between them and the iodine and gold lattices underneath (see Fig. 4.13).The iodine layer under both molecular phases was found to be a *pseudo-hex-rot* phase, but since this phase is electro-compressive (iodine lattice becomes more compressed with increasing electrode potential), under each H_2TMPyP phase an iodine *pseudo-hex-rot* phase with different compression was found.

Phase I

The iodine lattice under Phase I is described by vectors $\overline{b_1}$ and $\overline{b_2}$ with directions of $[0\ 7\ 35]$ and $[0\ 11\ \bar{5}]$, respectively. The lattice constants are b_1 = 0.404 nm and b_2 = 0.410 nm enclosing an angle of 103° (see Fig.4.12c and Fig.4.13). Furthermore, each iodine row in the direction of the vectors $\overline{b_1}$ and $\overline{b_2}$ yields periodic atop binding of an iodine atom on a gold atom, every nineteenth and seventh iodine, respectively. The surface coverage for the iodine lattice under Phase I was calculated to be 0.52ML with respect to the gold lattice underneath, or $62.58 \cdot 10^{13}$ iodine/cm^2.

The H_2TMPyP layer of Phase I is described by vectors $\overline{c}_1$ and $\overline{c}_2$ with directions of $[0\ 1\ \bar{3}]$ and $[0\ 17\ 5]$, respectively. Therefore, the molecular rows of phase P_I do not follow any high symmetry direction of the substrate, neither of the iodine lattice nor of the Au(100) surface. Considering the molecular symmetry axis of individual molecules which are centered atop of iodine atom we observe that it coincides with the $[0\ 7\ 35]$ direction of close packed iodine rows. The unit cell $(\overline{c_1}, \overline{c_2})$ as depicted in Fig. 4.12a,c,d,f and Fig. 4.13 with the lattice parameters of c_1 = 1.61nm and c_2 = 1.80nm, enclosing an angle of 92°, contains one molecule and can be related to the iodine lattice by the matrix:

$$\begin{pmatrix} c_1 \\ c_2 \end{pmatrix} = \begin{pmatrix} 3 & -2 \\ 3 & 4 \end{pmatrix} \begin{pmatrix} \overline{b}_1 \\ \overline{b}_2 \end{pmatrix}$$

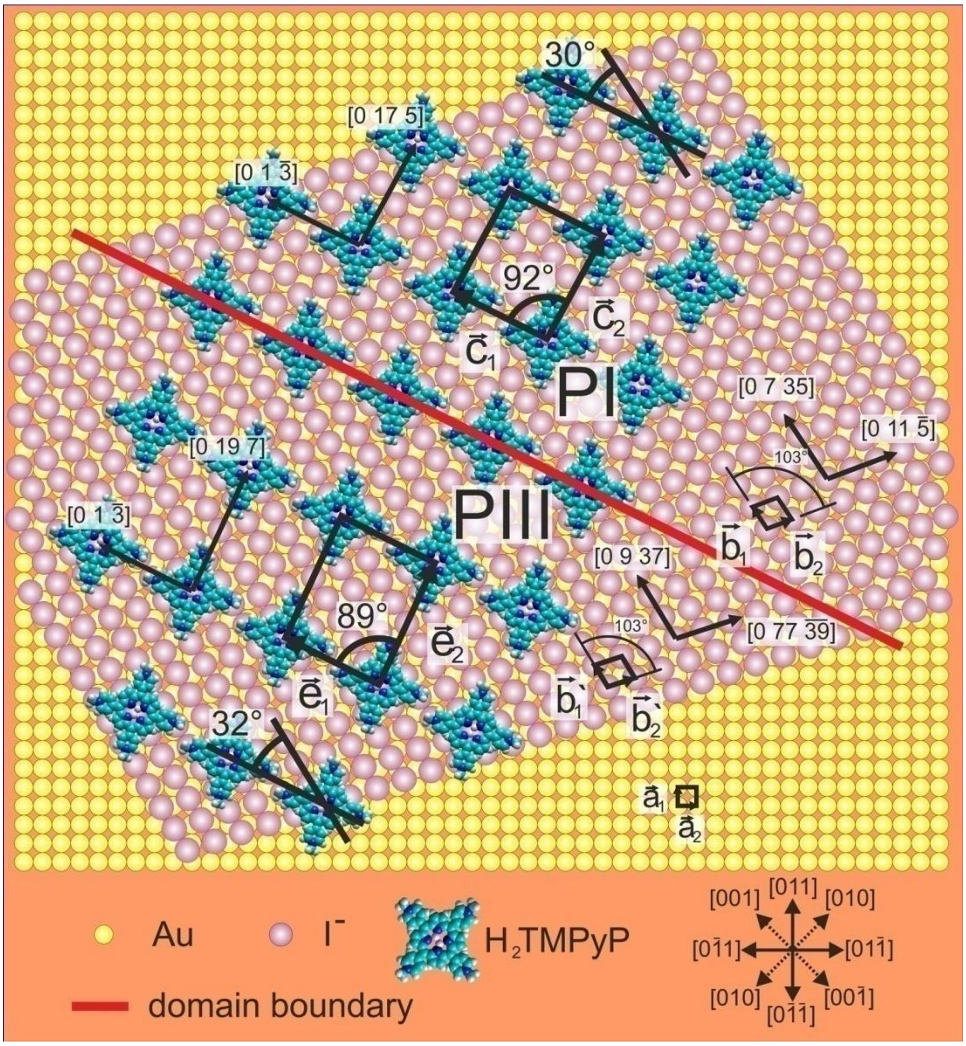

Figure 4.13: Structure models of the phases P_I and P_{III} on a iodine modified Au(100) surface.

and likewise to the gold lattice by the matrix:

$$\begin{pmatrix} \vec{c}_1 \\ \vec{c}_2 \end{pmatrix} = \begin{pmatrix} 2.5 & -5 \\ 5.5 & 3 \end{pmatrix} \begin{pmatrix} \vec{a}_1 \\ \vec{a}_2 \end{pmatrix}$$

On the basis of this model the surface coverage of the porphyrin adlayer is calculated to be 0.0286 ML relative to the density of the gold layer, or $3.453 \cdot 10^{13}$ molecules/cm^2.

Phase III

The iodine lattice under Phase III is described by vectors $\overline{b_1'}$ and $\overline{b_2'}$ with directions of $[0\ 9\ 37]$ and $[0\ 77\ \overline{39}]$, respectively. The lattice constants are b`₁ = 0.388nm and b`₂ = 0.439nm enclosing an angle of 103°. Furthermore, each iodine row in the direction of the vectors $\overline{b_1'}$ and $\overline{b_2'}$ leads to periodic atop binding of an iodine atom on a gold atom, every twenty-first and forty-first iodine, respectively. The surface coverage for the iodine lattice under Phase III was calculated to be 0.50ML with respect to the gold lattice underneath, or $59.81 \cdot 10^{13}$ iodine/cm^2.

Comparing the iodine lattice under Phase III to the iodine lattice under Phase I one finds a change in surface coverage from 0.50 ML to 0.52ML, due to electrocompression of the *pseudo-hex-rot* phase with increasing electrode potential. This observation agrees with observations from the previous section on the stable potential regime of Phases I and III (see Fig. 4.11), i.e. the potential regime of Phase I is situated at more positive potentials section than that of Phase III.

The unit-cell of Phase III is described by vectors $\overline{e_1}$ and $\overline{e_2}$ with directions of $[0\ 1\ \overline{3}]$ and $[0\ 19\ 7]$, respectively. Furthermore, the vector $\overline{e_1}$ has the same value and direction as vector $\overline{c_1}$ of Phase I. Moreover, the molecular rows of Phase III do not follow any high symmetry direction of the substrate, neither of the iodine lattice nor of the Au(100) surface. Considering the molecular symmetry axis of individual molecules which are centered atop of iodine atoms we observe that it coincides with the $[0\ 9\ 37]$ direction of close packed iodine rows. The unit cell $(\overline{e_1}, \overline{e_2})$ as depicted in Fig. 4.12d,e and Fig. 4.13 with the lattice parameters of e_1 = 1.61nm and e_2 = 2.06nm, enclosing an angle of 89°, contains one molecule and can be related to the iodine lattice by the matrix:

$$\begin{pmatrix} e_1 \\ e_2 \end{pmatrix} = \begin{pmatrix} 3 & -2 \\ 4 & 4 \end{pmatrix} \begin{pmatrix} \bar{b}'_1 \\ \bar{b}'_2 \end{pmatrix}$$

and likewise to the gold lattice by the matrix:

$$\begin{pmatrix} \overline{e}_1 \\ \overline{e}_2 \end{pmatrix} = \begin{pmatrix} 2.5 & -5 \\ 6.5 & 3 \end{pmatrix} \begin{pmatrix} \overline{a}_1 \\ \overline{a}_2 \end{pmatrix}$$

On the basis of this model the surface coverage of the porphyrin adlayer is calculated to be 0.025 ML relative to the density of the gold layer, or $3.02 \cdot 10^{13}$ molecules/cm^2. As presented in the previous subsection phase transitions inside the ordered porphyrin layer takes place between five phases (P_I-P_V) in the monolayer regime. In that potential range, the porphyrin molecules do not undergo any additional red-ox process, i.e. no electron transfer occurs. Hence, the phase transitions as seen in Fig. 4.9 are not caused by a variation in the chemical state of the porphyrin molecules but solely by a variation of the interaction between the porphyrin molecules and the substrate. Analysis of the two ordered phases I and III of porphyrin on I/Au(100) has shown a structural rearrangement with a concomitant change of the surface coverage by about 4.4% from Phase I to Phase III due to rearrangement of the iodine lattice underneath with a change of the surface coverage by about 17.7% from the iodine lattice under Phase I to the iodine lattice under Phase III. Moreover, the symmetry axes of individual molecules in both cases coincide with the direction of close packed iodine row.

This indicates that the self-assembly of the H_2TMPyP molecules is dominated by two contributions: i) the density of the iodine anion layer which determines the number of organic molecules which are attracted due to their cationic nature, and ii) the symmetry axes of individual molecules which coincide with the direction of close packed iodine rows and which results in the strongest electrostatic interaction with the iodine structure. Therefore, all these results show that the porphyrin-substrate interactions have the dominant influence on the ordering process of the H_2TMPyP molecules on iodine modified Au(100) surface.

Thus the so far presented explanation for the phase transition between Phase I and Phase III is the change of the iodine lattice underneath, but what is the reason for the difference of phases III and IV which have essentially equal surface concentrations and are stable in the same potential range?

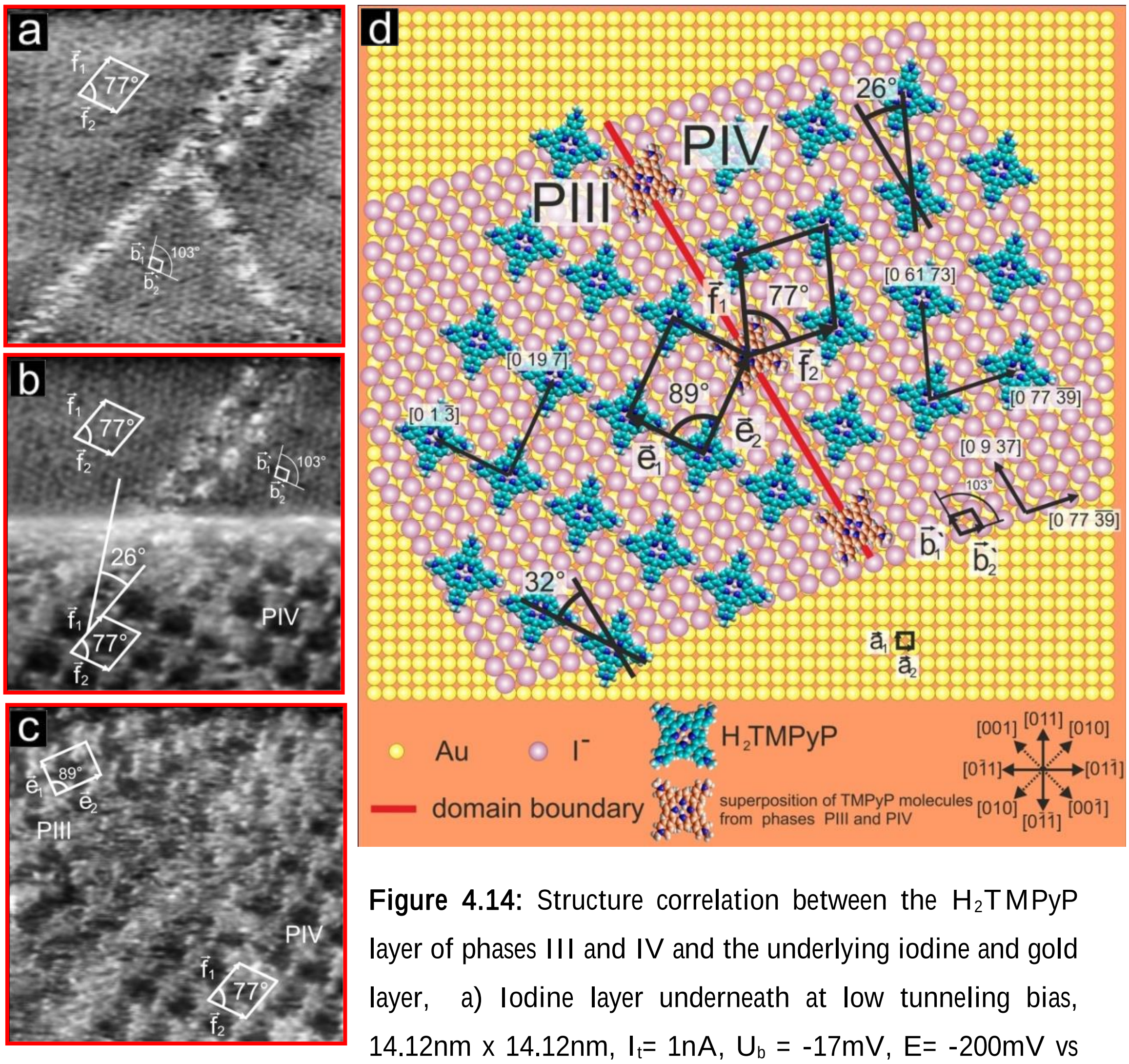

Figure 4.14: Structure correlation between the H_2TMPyP layer of phases III and IV and the underlying iodine and gold layer, a) Iodine layer underneath at low tunneling bias, 14.12nm x 14.12nm, I_t= 1nA, U_b = -17mV, E= -200mV vs Pt/PtI, b) upper part: Iodine layer underneath at low tunnelling bias: U_b = -17mV, lower part: Porphyrin layer at high tunnelling bias: U_b = -472mV, 14.12nm x 14.12nm, I_t = 1nA, E= -200mV vs Pt/PtI, c) Porphyrin layer at high tunnelling bias,14.12nm x 14.12nm, I_t = 1nA, U_b = -472mV, E= -200mV vs Pt/PtI, d) Structure model of the P_{III} and P_{IV} on iodine modified Au(100) surface.

Phase IV

In order to answer this question a structural correlation between the porphyrin adlayer (here for Phase III and IV) and the substrate lattice underneath has been made. Figs.4.14a-c represent a series of STM images of 14.12 nm × 14.12 nm which were recorded successively at the same surface area. The tunneling *bias* gradually changed from low (-14mV) to high (-472mV) values by going from Fig. 4.13a to c which emphasize contributions either from the substrate or from the molecular layer and thereby enable a direct correlation between the structure of the organic adlayer and that of the underlying iodine lattice. As a result, the iodine lattice underneath both phases III and IV is found to be the same, namely *pseudo-hex-rot* which was already described by the vectors $\overline{b_1'}$ and $\overline{b_2'}$ with directions of $[0\ 9\ 37]$ and $[0\ 77\ \overline{39}]$, respectively, and the lattice constants b`$_1$ = 0.388nm and b`$_2$ = 0.439nm enclosing an angle of 103°. Each iodine row in the direction of vectors $\overline{b_1'}$ and $\overline{b_2'}$ yields periodic atop binding of an iodine atom on a gold atom, every twenty-first and forty-first iodine, respectively. The surface coverage for the iodine lattice under Phase III was calculated to be 0.50ML with respect to the gold lattice underneath, or $59.81 \cdot 10^{13}$ iodine/cm^2.

The H_2TMPyP layer of Phase IV is described by vectors $\overline{f_1}$ and $\overline{f_2}$ with directions of $[0\ 61\ 73]$ and $[0\ 77\ \overline{39}]$, respectively. Consequently the molecular rows along the direction of vector $\overline{f_2}$ run parallel to the iodine high symmetry direction which is also $[0\ 77\ \overline{39}]$. The molecular symmetry axis of individual molecules which are centred atop of iodine atoms coincide with the $[0\ 9\ 37]$ direction of close packed iodine which is the same as in the case of Phase III. The unit cell as depicted in Fig.4.14a-d with the lattice parameters of f_1 = 1.94nm and f_2 = 1.76nm, enclosing an angle of 77°, contains one molecule and can be related to the iodine lattice by the matrix:

$$\begin{pmatrix} \bar{f}_1 \\ \bar{f}_2 \end{pmatrix} = \begin{pmatrix} 5 & 2 \\ 0 & 4 \end{pmatrix} \begin{pmatrix} \bar{b}'_1 \\ \bar{b}'_2 \end{pmatrix}$$

and likewise to the gold lattice by the matrix:

$$\begin{pmatrix} 5f_1 \\ 5f_2 \end{pmatrix} = \begin{pmatrix} 33.5 & -3 \\ 9.5 & 29 \end{pmatrix} \begin{pmatrix} a_1 \\ a_2 \end{pmatrix}$$

which in this case contains 25 molecules in the matrix. On the basis of this model the surface coverage of the porphyrin adlayer is calculated to be 0.025 ML relative to the density of the gold layer, or $3.014 \cdot 10^{13}$ molecules/cm^2. Consequently the surface coverage is the same for both phases P_{III} and P_{IV}.

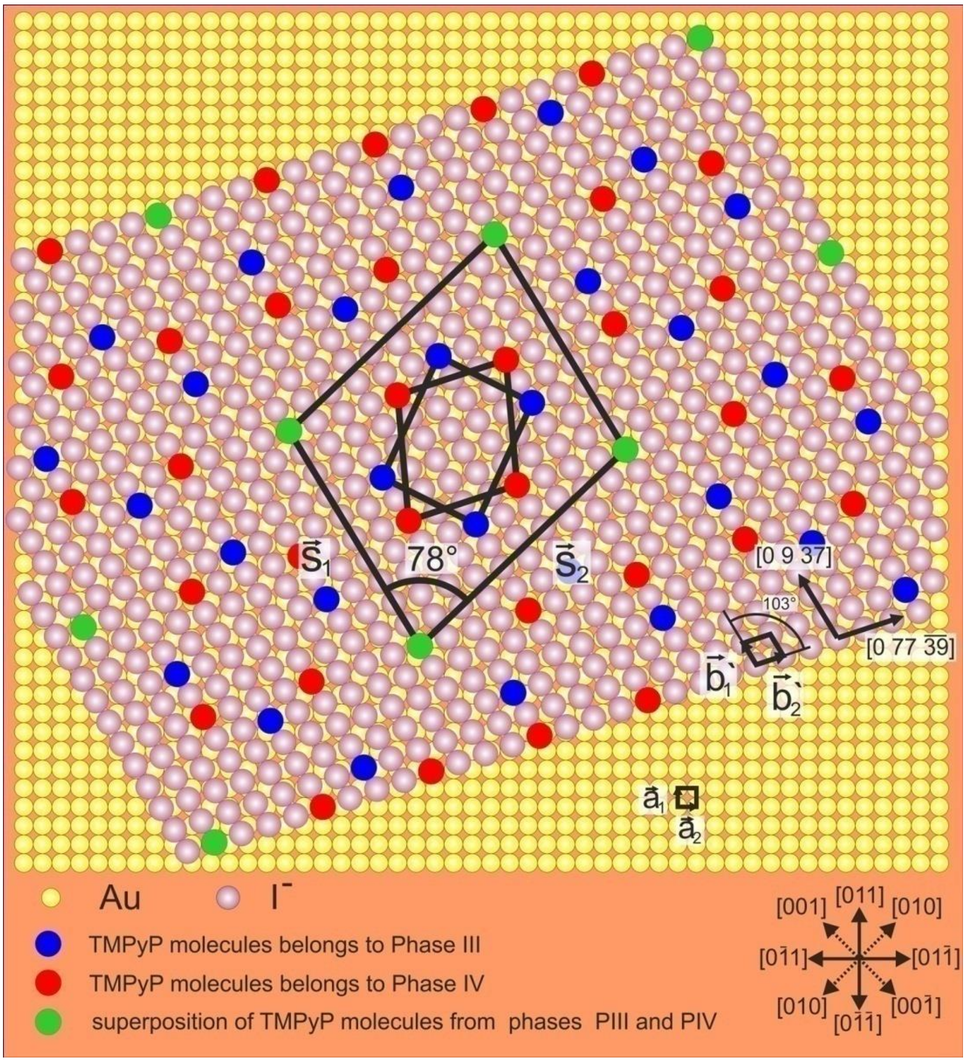

Figure 4.15: Structure model of superstructure created by superimposing of Phase III and IV.

The model in Fig. 4.14 is created with an ideal domain boundary between both phases by overlapping one point of the two unit-cells corresponding to a superposition of porphyrin molecules from both phases. As a consequence one can observe that the superposition of these molecules occurs regularly on close packed iodine rows in the direction $[0 \quad 9 \quad 37]$ every eleventh iodine atom. Furthermore, the common molecules from both phases III and IV (see the green atoms in Fig. 4.15) form a regular superstructure which is described by vectors $\bar{s_1}$ and $\bar{s_2}$ with directions of $[0\ 9\ 37]$ and $[0\ 43\ \bar{1}]$, respectively. The unit cell $(\bar{s_1}, \bar{s_2})$ as depicted in Fig. 4.15 with the lattice parameters of s_1 = 3.88nm and s_2 = 4.38nm, enclosing an angle of 78°, contains four molecules from Phase III and the same amount in the case of Phase IV, plus one additional molecule which is in common (green atom can be either blue or red) and can be related to the iodine lattice by the matrix:

$$\begin{pmatrix} \bar{s}_1 \\ \bar{s}_2 \end{pmatrix} = \begin{pmatrix} 11 & 0 \\ 5 & 10 \end{pmatrix} \begin{pmatrix} \bar{b}'_1 \\ \bar{b}'_2 \end{pmatrix}$$

and likewise to the gold lattice by the matrix:

$$\begin{pmatrix} \bar{s}_1 \\ \bar{s}_2 \end{pmatrix} = \begin{pmatrix} 11.5 & -7 \\ 10.5 & 11 \end{pmatrix} \begin{pmatrix} a_1 \\ a_2 \end{pmatrix}$$

On the basis of this model the surface coverage of the porphyrin adlayer for Phase III and IV is equal and was calculated to be 0.025 ML relative to the density of the gold layer, or $3.015 \cdot 10^{13}$ molecules/cm^2. This suggests that both phases adsorb with equal probability on the surface.

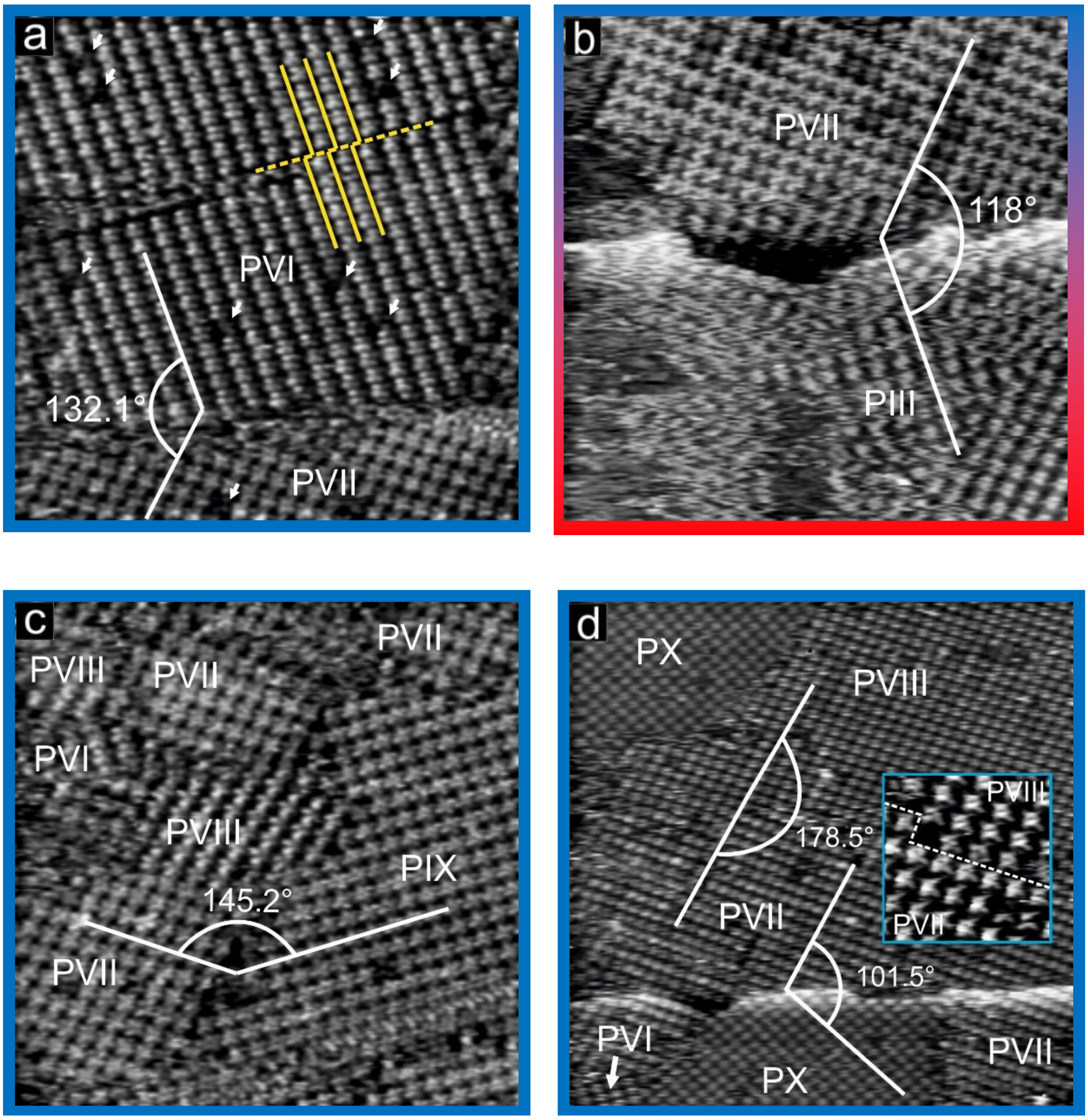

Figure 4.16: Ordered H_2TMPyP adlayer on an iodine-modified Au(100) electrode in the bi-layer regime. a) 41.48nm x 41.48nm, I_t = 1nA, U_b = -196mV, E = from -300mV to -200mV vs Pt/PtI, b) 41.48nm x 41.48nm, I_t = 1nA, U_b = -178mV, E= -640mV vs Pt/PtI, c) 41.48nm x 41.48nm, I_t = 1nA, U_b = -178mV, E= -620mV vs Pt/PtI, d) 69.14nm x 69.14nm, I_t = 2nA, U_b = -236mV, E= -600mV vs Pt/PtI.

4.2.2.2 Bi-layer adsorption of TMPyP on I/Au(100) surface

The experimental adsorption procedure is described in section 4.2.2.1. The iodine covered surface was examined first by STM. Then this iodine-modified Au(100) surface was exposed to a 5mM H_2SO_4 + 1mM KI solution containing

0.01mM H_2TMPyP in order to adsorb the porphyrin molecules. STM measurements were carried out just after the electrolyte exchange immediately showing the porphyrin adsorption on top of the I/Au(100) substrate.

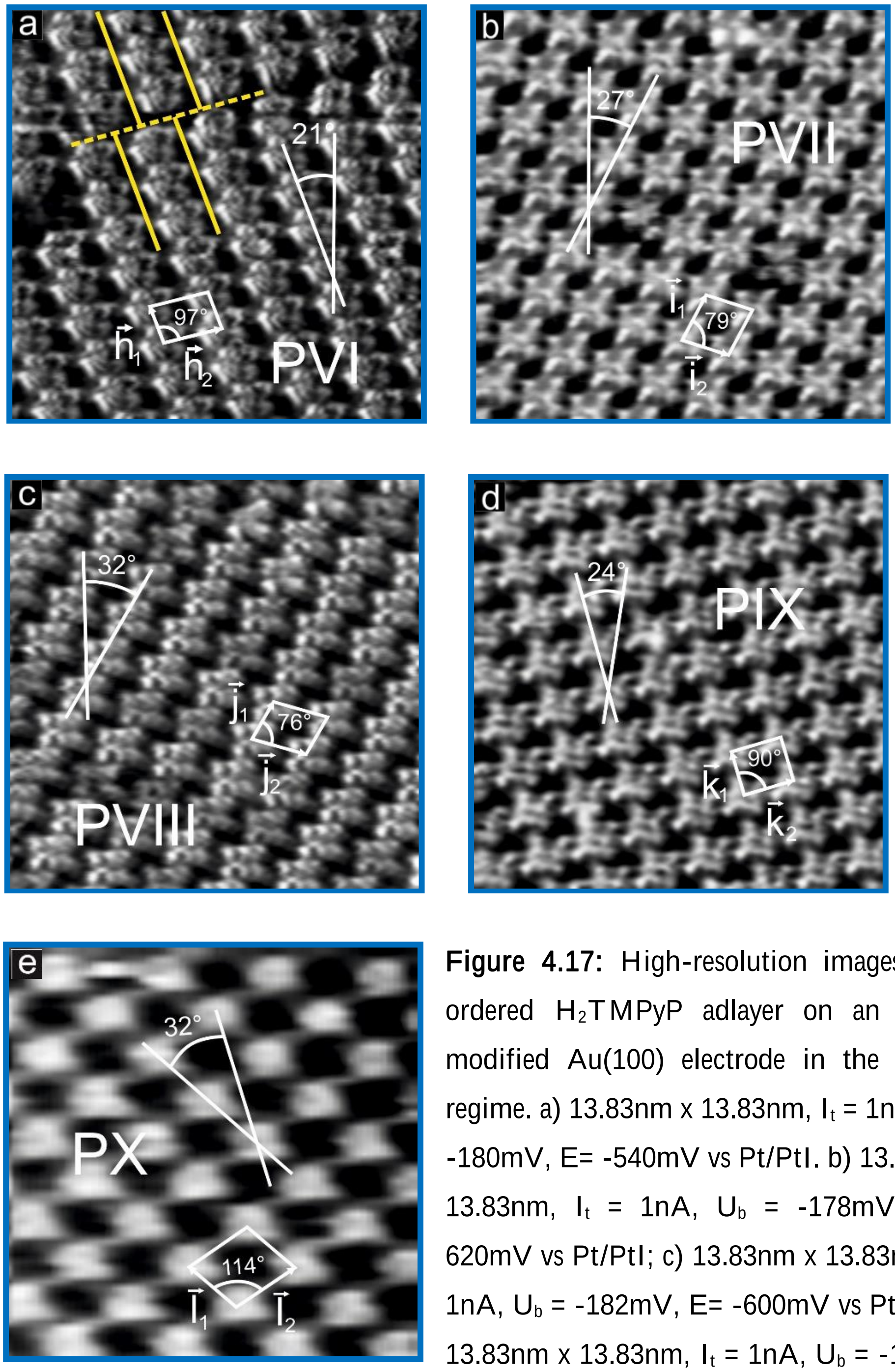

Figure 4.17: High-resolution images of an ordered H_2TMPyP adlayer on an iodine-modified Au(100) electrode in the bi-layer regime. a) 13.83nm x 13.83nm, I_t = 1nA, U_b = -180mV, E= -540mV vs Pt/PtI. b) 13.83nm x 13.83nm, I_t = 1nA, U_b = -178mV, E= -620mV vs Pt/PtI; c) 13.83nm x 13.83nm, I_t = 1nA, U_b = -182mV, E= -600mV vs Pt/PtI; d) 13.83nm x 13.83nm, I_t = 1nA, U_b = -178mV, E= -620mV vs Pt/PtI; e) 13.83nm x 13.83nm, I_t = 1nA, U_b = -182mV, E= -600mV vs Pt/PtI.

The bi-layer regime is situated between the peak pairs $P_2/P_{2'}$ (-250/-395mV vs Pt/PtI) and $P_4/P_{4'}$ (-615/-710mV vs Pt/PtI). Typical large scale STM images acquired within this bi-layer regime showing the surface structure of the H_2TMPyP adlayer on top of the I/Au(100) surface are displayed in Fig. 4.16. It is clearly seen that the terraces are covered almost entirely by porphyrin molecules which are self-assembled into an ordered layer of molecular rows. Furthermore, by thorough examination five new coexisting porphyrin phases, namely PVI - PX, are distinguishable in Figs. 4.16a-d. Like in the case of monolayer phases also translational domains are observable which are denoted with yellow solid lines and a domain boundary between them marked by a dashed yellow line (see Fig. 4.9f, 4.16b, 4.17a, 4.18c). Moreover, on all images in the bi-layer regime missing molecules in the second molecular layer can be detected, which are represented by dark spots on the STM images (marked by small white arrows in Fig. 4.16b and 4.18c).

The molecular arrangement within each phase of the porphyrin layer can be seen more clearly in the high resolution images in Fig. 4.17a-e. The molecules are ordered in rows. The shape of the individual molecules agrees with their square structure which, in turn, indicates that the molecules are lying flat on the surface. The unit-cell lattice for Phase VI can be outlined as shown in Figure 4.17a with the lattice parameters h_1 = 1.36 ± 0.05nm and h_2 = 2.05± 0.05nm and an angle of ca. 97° between them. Individual molecules within one row are rotated by about +21° with respect to the row direction parallel to the $\overline{h_1}$ vector. Each unit cell includes one H_2TMPyP molecule, which corresponds to a surface concentration of ca. $3.61 \cdot 10^{13}$ molecules/cm^2. The unit cell of Phase VII is presented in the Figure 4.17b. The lattice constants are i_1 =1.74 ± 0.05nm and i_2 = 1.63± 0.05nm enclosing an angle of about 79°. All molecules within one row are rotated by about -27° with respect to the row direction parallel to the $\overline{\imath_1}$ vector. As in the case of Phase VI each unit cell includes one porphyrin molecule, resulting in a surface concentration of ca. $3.59 \cdot 10^{13}$ molecules/cm^2. Furthermore, the angle between the vectors $\overline{h_1}$ and $\overline{\imath_1}$ is 180° - 132.1° = 47.9° (see Fig.4.16b). Moreover, Fig. 4.16a shows Phase III and VII with the angle of ca. 180° - 118°= 62° between the vectors $\overline{e_1}$ and $\overline{\imath_1}$.

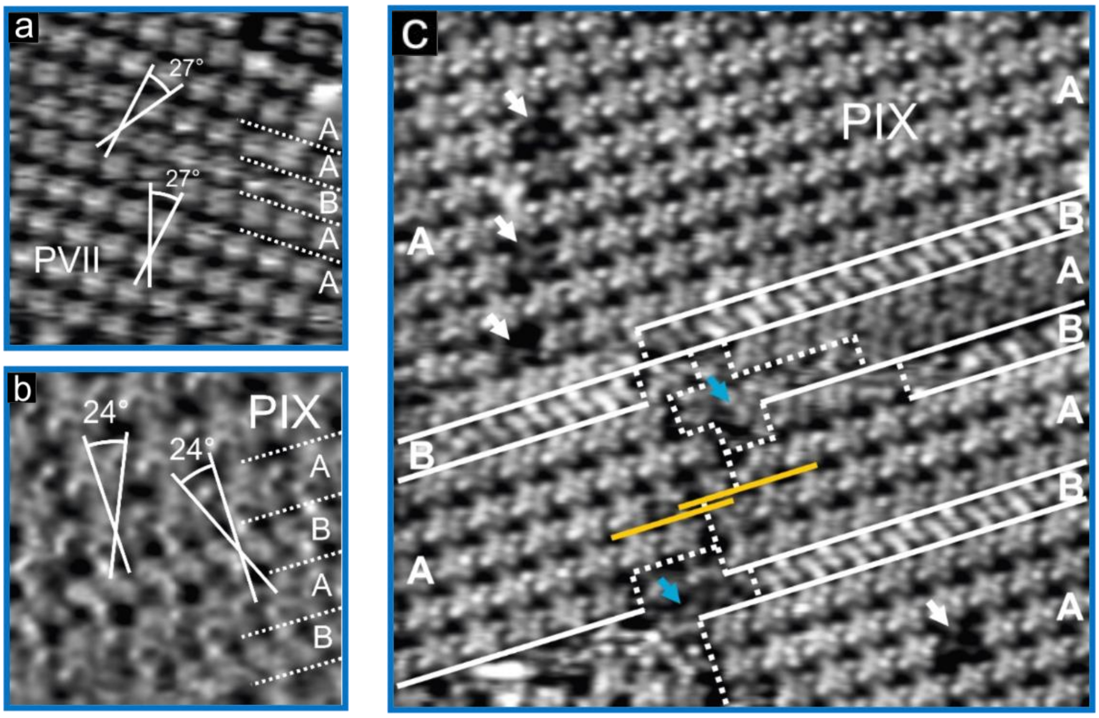

Figure 4.18: Ordered H_2TMPyP adlayer on an iodine-modified Au(100) electrode. Appearance of “mirror rows" (A and B) for the Phases P_{VII} and P_{IX}. a) 14.6nm x 14.6nm, I_t = 1nA, U_b = -236mV, E= -600mV vs Pt/PtI. b) 27.66nm x 27.66nm, I_t = 1nA, U_b = -175mV, E= -620mV vs Pt/PtI. c) 8nm x 8nm, I_t = 1nA, U_b = -175mV, E= -620mV vs Pt/PtI.

The unit cell of Phase VIII is presented in the Fig. 4.17c. The nearest neighbour distances between porphyrin molecules for P_{VIII} are found to be j_1 = 1.49 ± 0.05nm and j_2 = 1.96± 0.05nm, respectively, and the angle between the two unit vectors is ca. 76°. The symmetry axis of the H_2TMPyP molecules in this case is rotated by an angle of about -32° with respect to the molecular row direction parallel to $\overline{j_1}$. One porphyrin molecule is contained in each unit-cell which corresponds to a surface concentration of ca. $3.53 \cdot 10^{13}$ molecules/cm^2. The angle between the vectors $\overline{i_1}$ of Phase VII and $\overline{j_1}$ of Phase VIII is ca. 180° - 178.5° = 1.5° which is shown in the Figure 4.16d.

	P_{VI}	P_{VII}	P_{VIII}	P_{IX}	P_X
lattice constants [± 0.05nm]	h_1 = 1.36 h_2 = 2.05	i_1= 1.74 i_2 = 1.63	j_1 = 1.49 j_2 = 1.96	k_1 = 1.58 k_2 = 1.77	l_1= 1.62 l_2 = 1.78
angle [± 1°]	97°	79°	76°	90°	76°
molecule rotation [α ± 1°]	+21° vs $\bar{h}_1$	-27° vs $\bar{\iota}_1$	-32° vs $\bar{j}_1$	+24° vs $\bar{k}_1$	+32° vs $\bar{l}_1$
surface concentration [molecules/cm^2]	$3.614 \cdot 10^{13}$	$3.592 \cdot 10^{13}$	$3.529 \cdot 10^{13}$	$3.556 \cdot 10^{13}$	$3.574 \cdot 10^{13}$

Table 2. Parameters of individual bi-layer phases.

Figure 4.17d presents the unit cell of Phase IX. The lattice constants are k_1 = 1.74 ± 0.05nm and k_2 = 1.63± 0.05nm enclosing an angle of 90°. All molecules within one row are rotated by about +24° with respect to the row direction which is parallel to the $\overline{k_1}$ vector. The unit-cell of P_{IX} as indicated in Fig. 4.17d contains one porphyrin molecule which corresponds to a surface concentration of ca. $3.56 \cdot 10^{13}$ molecules/cm^2. As demonstrated in Fig. 4.16c the angle between the vectors $\overline{\iota_2}$ and $\overline{k_2}$ is found to be 180° - 145.2° = 34.8°.

The unit-cell of the lattice of Phase X is shown in Fig. 4.17e, with the lattice constants l_1 = 1.62 ± 0.05nm and l_2 = 1.78± 0.05nm with an angle of ca. 114° between them. Individual molecules within one row are rotated by about +32° with respect to the row direction which is parallel to the $\overline{l_1}$ vector. One unit-cell of P_X contains one H_2TMPyP molecule, which consequently corresponds to a surface concentration of ca. $3.57 \cdot 10^{13}$ molecules/cm^2. Furthermore, the angle between the vectors $\overline{\iota_1}$ and $\overline{l_1}$is 180° - 101.5° = 78.5° (see Fig. 4.16d).

An additional observation can be made for phases P_{VII} and P_{IX} where we can distinguish “mirror” rows (denoted as A and B in Fig. 4.18a-c), i.e. molecules in adjacent rows are rotated in the opposite direction. Moreover, within adjacent rows A and B the molecules are shifted against each other along the direction of the rows by half a lattice vector $\overline{\iota_1}$ in Phase VII and half a lattice vector $\overline{k_2}$ in Phase IX, respectively (see Fig. 4.18).

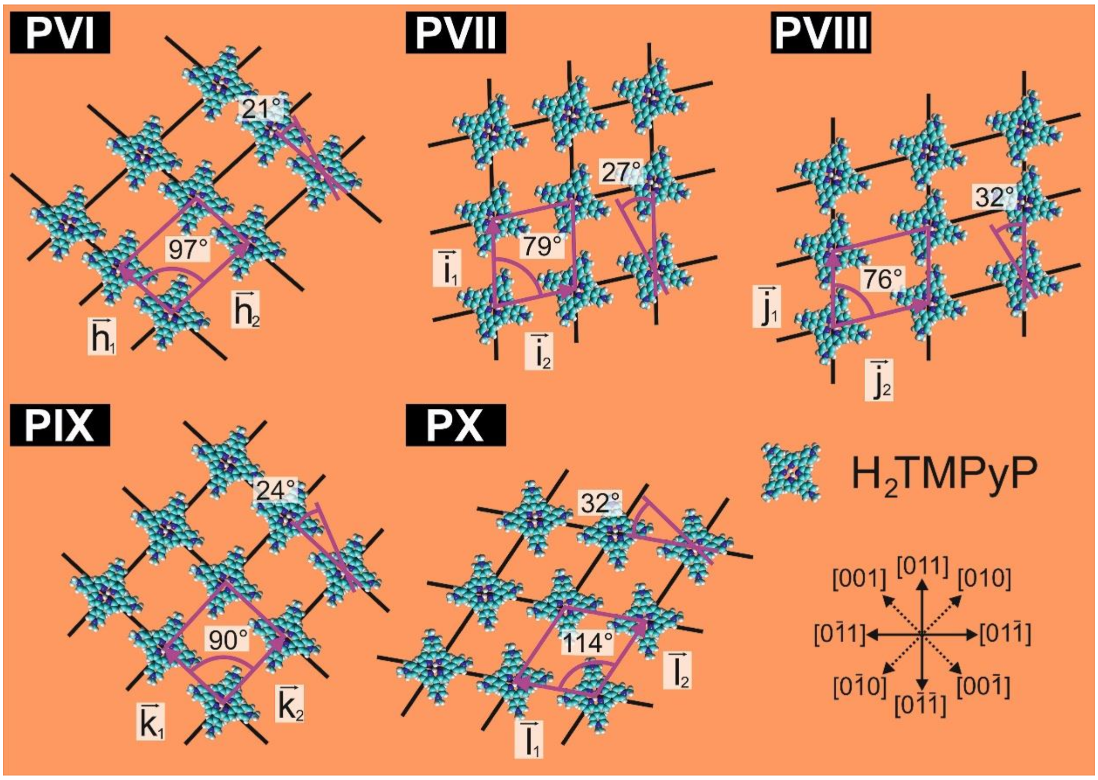

Figure 4.19: Schematic models of five ordered H_2TMPyP molecular phases in the bi-layer regime, with the corresponding vectors of the unit cells and the angles between them.

Table 2 summarizes the relevant parameters of all bi-layer phases VI - X. From the resultant symmetry and orientation of the H_2TMPyP molecule of each phase, representative models are proposed in Fig. 4.19. The surface concentration of porphyrin molecules within the bi-layer phases decreases in the sequence: $P_{VI}>P_{VII}>P_X>P_{IX}>P_{VIII}$. This result of different surface concentrations suggests again a competition between these phases. In order to check in which potential regime the

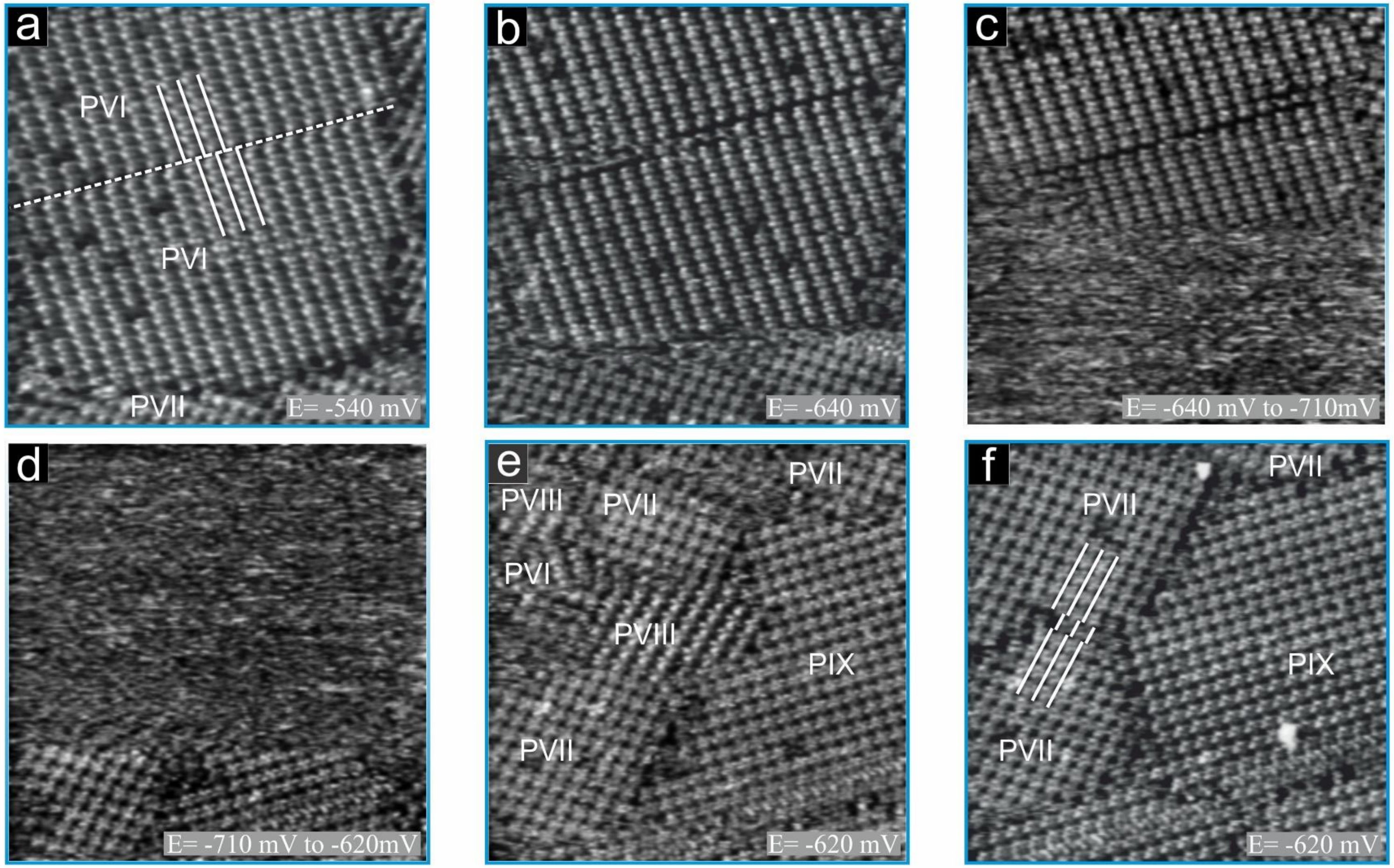

Figure 4.20: Potential induced phase transition of the molecular adlayer on an iodine modified Au(100) electrode surface, STM series: 41.48nm x 41.48nm; a) I_t = 1nA, U_b= -178mV; b) I_t = 1nA, U_b= -178mV; c) I_t = 1nA, U_b= -178mV; d) I_t = 1nA, U_b= -178mV; e) I_t = 1nA, U_b = -178mV; f) I_t = 1nA, U_b = -178mV.

Phases VI-X are stable and if there is any influence from the surface concentration potentiodynamic STM measurements were carried out. Hence, the porphyrin molecules in the bi-layer regime are beyond the first reduction step and do not undergo any further redox process, therefore, the phase transitions which occur in the bi-layer regime are not caused by a variation in the chemical state of the porphyrin but by a variation of the interaction between the porphyrin molecules and the substrate. Moreover, in order to confirm the influence of the substrate on the self-assembly of the porphyrin molecules a structural correlation between the porphyrin adlayer and the substrate lattice underneath was made.

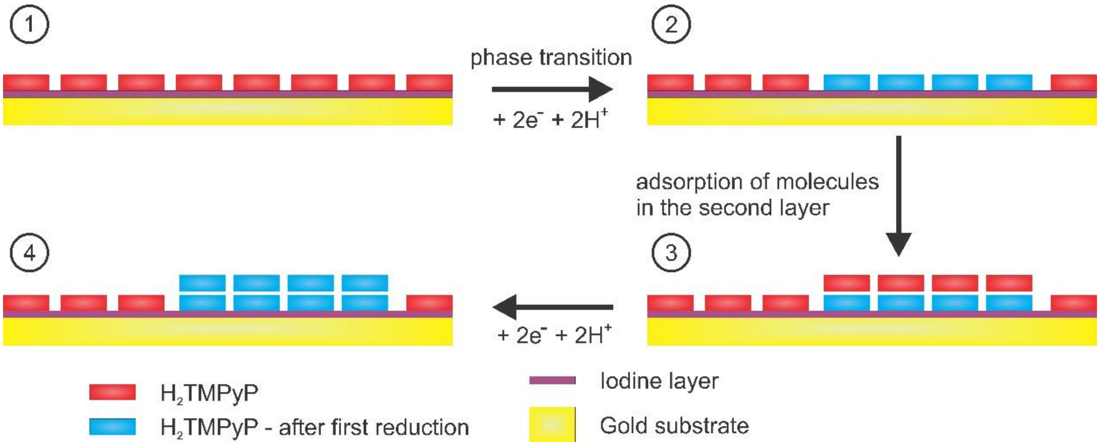

Figure 4.21: Proposed mechanism for the surface reduction of H_2TMPyP molecules.

4.2.2.2.1 Potentiodynamic STM measurements.

The potentiodynamic STM measurements are presented in the three sets of images in Fig. 4.9; 4.19 and 4.20. Figure 4.9 presented in section 4.2.2.1.1 shows a potential dependent series of STM images starting from the monolayer regime at -200mV vs Pt/PtI. From the starting point, the electrode potential was carefully scanned in the cathodic direction. When the electrode potential reaches -300mV vs Pt/PtI a phase transition starts to be observed from the monolayer structures (P_{III} and P_{IV}) to bi-layer phases (P_{VI} and P_{VII}), respectively (see Fig. 4.9c). Further reduction of the electrode potential leads to an increase of the bi-layer phase instead of Phase III and IV which are finally completely replaced when the potential reaches the maximum of peak $P_{2'}$ at -395mV vs Pt/PtI (see Fig. 4.9d-f). Though the potential was systematically decreased further down to -500mV vs Pt/PtI no more significant changes are detected on the surface. At this point it should be noted that the first reduction peak $P_{3'}$ is observed at the -430mV vs Pt/PtI but no significant changes were observed by STM by overcoming it. Therefore, from the STM observation it seems that peak $P_{2'}$ is related not only to a phase transition but also to the first reduction of adsorbed molecules, whereas the peak $P_{3'}$ corresponds to the reduction of molecules from the bulk solution. A schematic model of the changes is proposed in Fig. 4.21 and is described as follow: decrease of the working potential induces a structural phase transition and concomitant reduction of adsorbed molecules of the first layer (step 1→2 in Fig.4.21), which is accompanied by adsorption (step 2→3 in Fig. 4.21) and reduction of molecules in the second layer (step 3→4 in Fig. 4.21) with the same structure (⇒ bi- layer of uniform structure).

An even further decrease of the electrode potential is presented in Fig. 4.20a-c. The first STM image recorded at -540mV vs Pt/PtI shows again the two phases P_{VI} and P_{VII}. For both these phases no changes are recorded until the electrode potential reaches the cathodic peak $P_{4'}$ at -700mV vs Pt/PtI (see Fig. 4.20c). Peak $P_{4'}$ was assigned from the CV measurements (see Sec. 4.2.1) to the desorption of iodine from the surface and the concomitant disordering of the porphyrin overlayer. Sweeping the potential back into the positive direction leads to re-adsorption of the iodine and the porphyrin molecules on the surface (see Fig. 4.20d), once the peak P_4 at -620mV vs Pt/PtI is reached. Moreover, in the Figures 4.20e and f not only the phases P_{VI} and P_{VII} are visible but also the phases P_{VIII}, P_{IX} and P_X (in Fig. 4.20a) can be distinguished. It should be noted that Phases VIII, IX and X were not observed when the measurements started within the monolayer regime with a potential change in cathodic direction. Moreover, Phase VIII was only observed in the potential range between the anodic peaks P_4 and P_9 (-548mV vs Pt/PtI). Therefore, the peak P_9 is suggested to correspond to a phase transition current feature. Further changes due to an increase of the electrode potential in anodic direction are presented in the set of images in Figure 4.22. In the STM image of Figure 4.22a recorded at -600mV vs Pt/PtI, two phases are observable, namely P_{VII} and P_X.

Subsequent increase of the work potential leads to a continuous decrease of Phase X which completely vanishes when the potential is swept over the anodic peak P_8 at -461mV vs Pt/Pt/I (see Fig. 4.22d). Instead, Phase VII now covers the whole surface. A similar observation was made for the Phase IX, thus the anodic peak P_8 is proposed to be a phase transition current feature. An interestingly observation is that increasing the electrode potential induces an instability of the second layer of porphyrin molecules. This manifests itself in Figs. 4.22d-e, where vacancies in the second layer appear. Green and white circles indicate molecules which have disappeared and were added, respectively, between the STM images in Fig. 4.22d and Fig. 4.22e. Furthermore, it is seen that the same amount of molecules disappeared or reappeared on the surface showing the equilibrium with the solution under the given conditions. This instability starts to be observed when the electrode potential reaches the first oxidation peak P_3 which was related to the oxidation of porphyrin molecules in the bulk solution. It seems that the bi-layer in the first place works as mediator in the transfer of electrons to the porphyrin molecules close to the surface or to the second layer, which leads to desorption of porphyrin molecules in the second layer but in the same time readsorption of still reduced molecules from the bulk solution occurs. No other drastic changes are noticeable until the electrode potential reaches -300mV vs Pt/PtI. At the domain boundaries a disordering of the lateral structure as well as desorption of the second layer of porphyrin molecules starts to take place (see yellow arrows in Figure 4.9g). When the electrode potential reaches the anodic peak P_2 at -250mV vs Pt/PtI the bi-layer phases completely vanished and are replaced by monolayer phases (see. Fig. 4.9h,i and Fig. 4.22h,i). Therefore, it can be suggested that the peak P_2 is related not only to the phase transition but also the first oxidation of the porphyrin molecules on the surface.

Figure 4.23 displays a CV with the denoted stable potential regimes of the Phases VI-X. First of all from the potentiodynamic STM measurements we conclude a competition between these phases due to their different surface concentrations and the strong dependence from the starting point of electrode potential change. Namely measurements starting in the monolayer regime with the potential sweep in cathodic direction show the creation of Phases VI and VII which remain stable until the common desorption of iodine and porphyrin molecules from

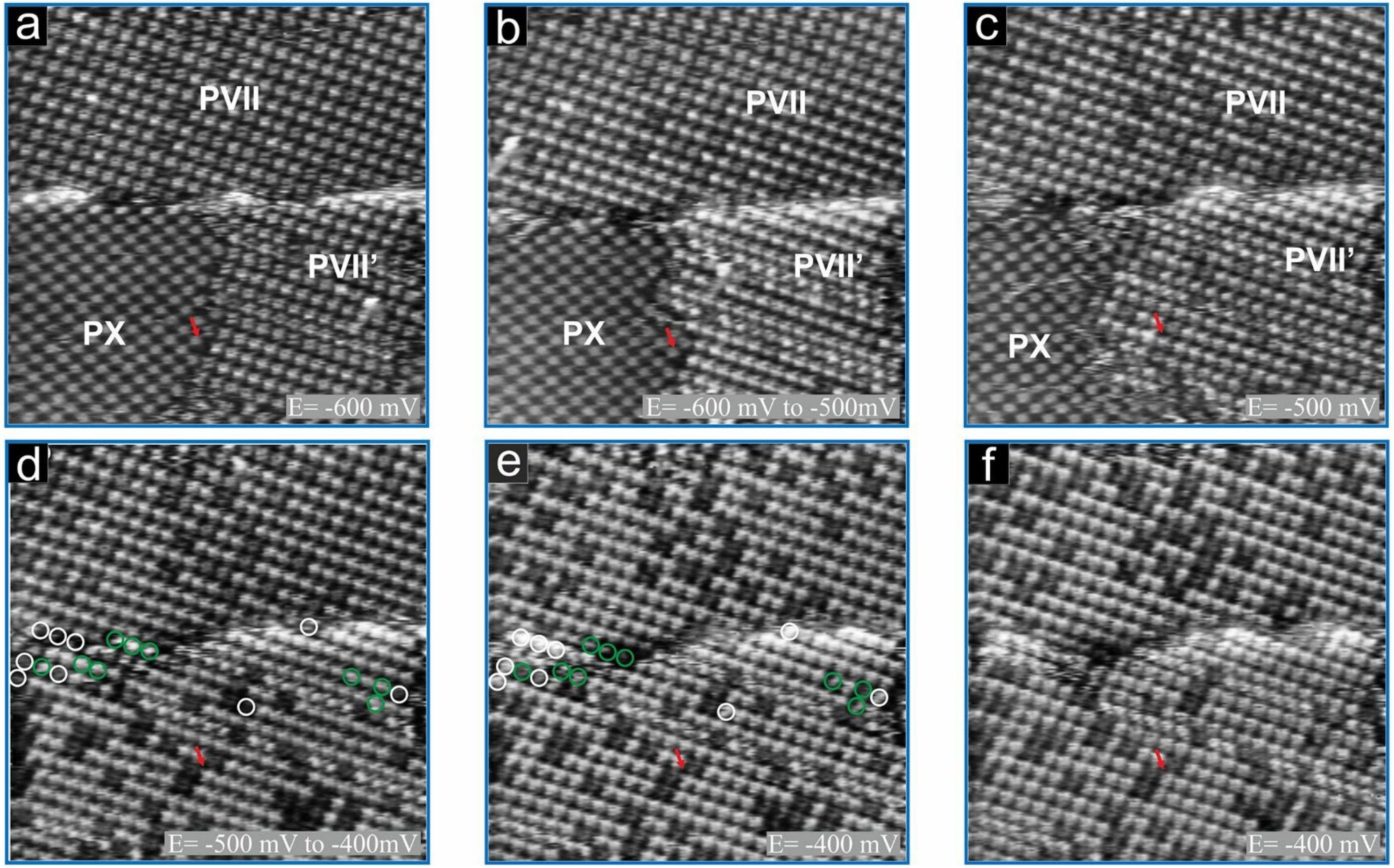
a
PVII
PVII'
PX
E= -600 mV
b
PVII
PVII'
PX
E= -600 mV to -500mV
c
PVII
PVII'
PX
E= -500 mV
d
E= -500 mV to -400mV
e
E= -400 mV
f
E= -400 mV

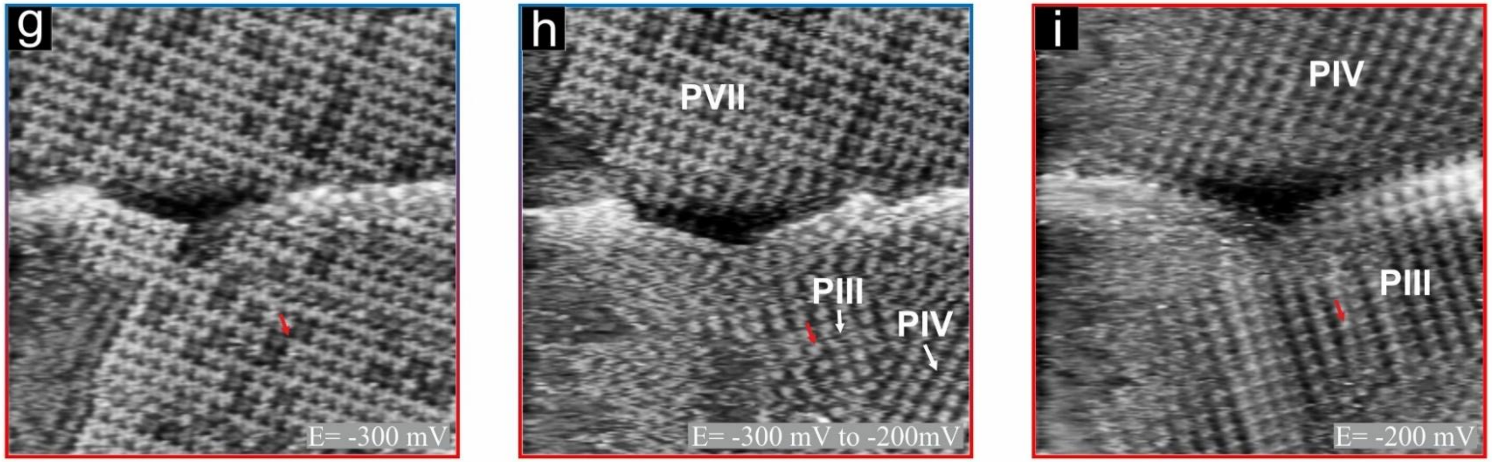

Figure 4.22: Potential induced phase transition of the molecular adlayer on the iodine modified Au(100) electrode surface, STM series: 41.48nm x 41.48nm; a) I_t = 1nA, U_b= -234mV; b) I_t= 1nA, U_b= -234mV; c) I_t = 1nA, U_b= -234mV; d) I_t = 1nA, U_b= -165mV; e) I_t = 1nA, U_b = -165mV; f) I_t = 1nA, U_b = -165mV; g) I_t = 1nA, U_b = -234mV; h) I_t = 1nA, U_b = -196mV; i) I_t = 1nA, U_b = -196mV.

the surface at very negative potentials takes place. Starting instead from the disordered regime at the very negative potentials and changing the potential in anodic direction leads to the observation not only of phases P_{VI} and P_{VII} but also of the phases P_{VIII} - P_X. This suggests a strong porphyrin-substrate interaction, in the cathodic sweep the adlayer of molecules prevents a change in the iodine structure till the combined desorption of iodine and molecules from the surface, which results in only two porphyrin structures, while in the anodic sweep the *simultaneous* adsorption of iodine and porphyrins molecules leads to the formation of all five bi-layer phases. Furthermore, comparing the changes of the surface concentration of the porphyrin molecules for each phase when sweeping in anodic direction we observe a strict relationship between the potential regime of each phase and its surface concentration, i.e. Phase VIII has the lowest surface concentration ($3.53 \cdot 10^{13}$ molecules/cm^2) and it first vanishes from the surface when the electrode potential is swept over the anodic peak P_9. The next two phases P_{IX} and P_X with the higher surface concentration (of $3.556 \cdot 10^{13}$ molecules/cm^2 and $3.574 \cdot 10^{13}$ molecules/cm^2, respectively) fade away when the potential is swept over the anodic peak P_8. Lastly, the two Phases VI and VIII with the highest surface concentrations ($3.614 \cdot 10^{13}$ molecules/cm^2 and $3.592 \cdot 10^{13}$ molecules/cm^2, respectively) stay longer on the surface until the electrode potential is swept over anodic peak P_2.

4.2.2.2.2 Structural correlation between the porphyrin adlayer and the substrate lattice underneath.

The previous subchapter gave answers about the competition between the various bi-layer phases due to their different surface concentration and about the potential regimes in which these phases are stable. The goal of this subchapter is to explain the co-existence and stability of phases P_{VI} and P_{VII} in the bi-layer potential regime by a possible relationship between the structures of overlayer and substrate. The method to relate the porphyrin lattice to the structure underneath is the same as that applied for the monolayer structures.

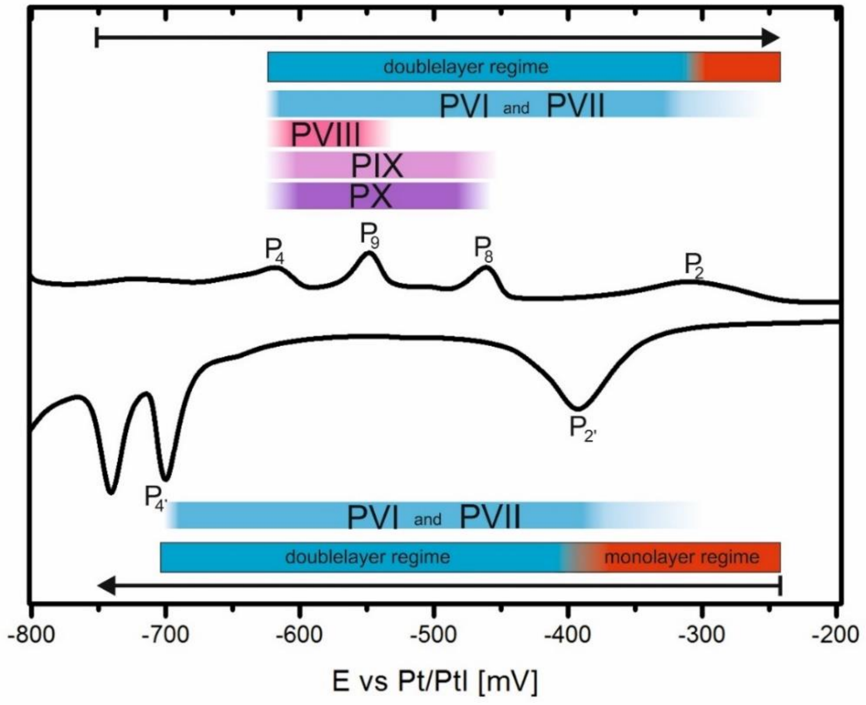

Figure 4.23: Diagram of H_2TMPyP adsoption regimes of Phases VI-X.

In order to acquire information about the structural correlation between the porphyrin adlayer (here for Phase VI and VII) and the substrate lattice underneath a set of STM images (Fig. 4.24a-c) of 9.90nm x 9.90nm were recorded successively, although due to the high thermal drift (which results in a displacement between the lattices of both the porphyrin phases and the iodine layer) only a general consideration can be presented.

Figure 4.24a shows the coexistence of the two molecular phases, P_{VI} and P_{VII} recorded at high tunnelling *bias* (-218mV) together with their unit cells. The gradual change of the tunnelling *bias* from high (-218mV) to low (-16mV) in Figure 4.24b and from low (-16mV) to high (-218mV) in Figure 4.24c enables us to tunnel through the molecular layer and to obtain a direct correlation between the structure of the organic adlayer and that of the underlying iodine lattice. As a result, the iodine lattice underneath both phases VI and VII is found to be the same. Moreover, the molecular rows of Phase VI along vector $\bar{k}_2$ and of Phase VII along vector $\bar{i}_1$ follow along the direction of close-packed iodine anions (see dashed lines on Fig. 4.24b-c).

Calculating the surface concentration of porphyrin molecules for both phases in relation to the iodine adlayer gives approximately the same coverage. This suggests that both phases VI and VII adsorb with equal probability and, hence, have the same stability in the bi-layer regime.

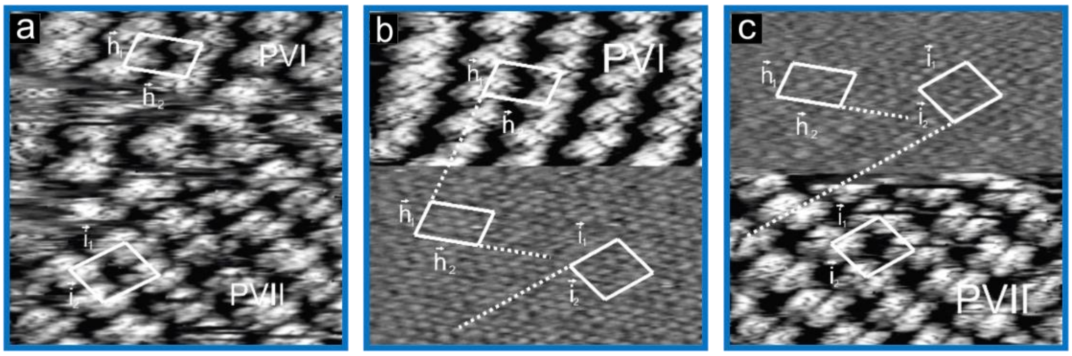

Figure 4.24: Structural correlation between the H_2TMPyP bi-layers of phases VI and VII and the underlying iodine, a) Porphyrin layer at high tunnelling bias, 9.90nm x 9.90nm, I_t= 5nA, U_b = -218mV, E= -450mV vs Pt/PtI, b) upper part: Porphyrin layer at high tunnelling bias: U_b = -218mV, lower part: Iodine layer underneath at low tunnelling bias: U_b = -16mV, 9.90nm x 9.90nm, I_t = 5nA, E= -450mV vs Pt/PtI, c) upper part: Iodine layer underneath at low tunnelling bias: U_b = -16mV, lower part: Porphyrin layer at high tunnelling bias: U_b = -218mV,I_t = 5nA, E= -450mV vs Pt/PtI.

4.2.2.3 Disordered and sub-monolayer adsorption of H_2TMPyP on Au(100) surface after I-desorption

The measurements started again with the preparation of a highly ordered iodine layer that was first checked by STM (see Section. 3.2.2.2). Then this iodine-modified Au(100) surface was exposed to a 5mM H_2SO_4 + 1mM KI solution containing 0.01mM H_2TMPyP in order to adsorb the porphyrin molecules. STM measurements were carried out just after the electrolyte exchange (in the bi-layer regime) immediately showing the porphyrin adsorption on top of the I/Au(100) substrate. Next the electrode potential was changed to values in the disordered regime which is situated between the peak pairs $P_{4'}/P_4$ (-710/-615mV vs Pt/PtI) and

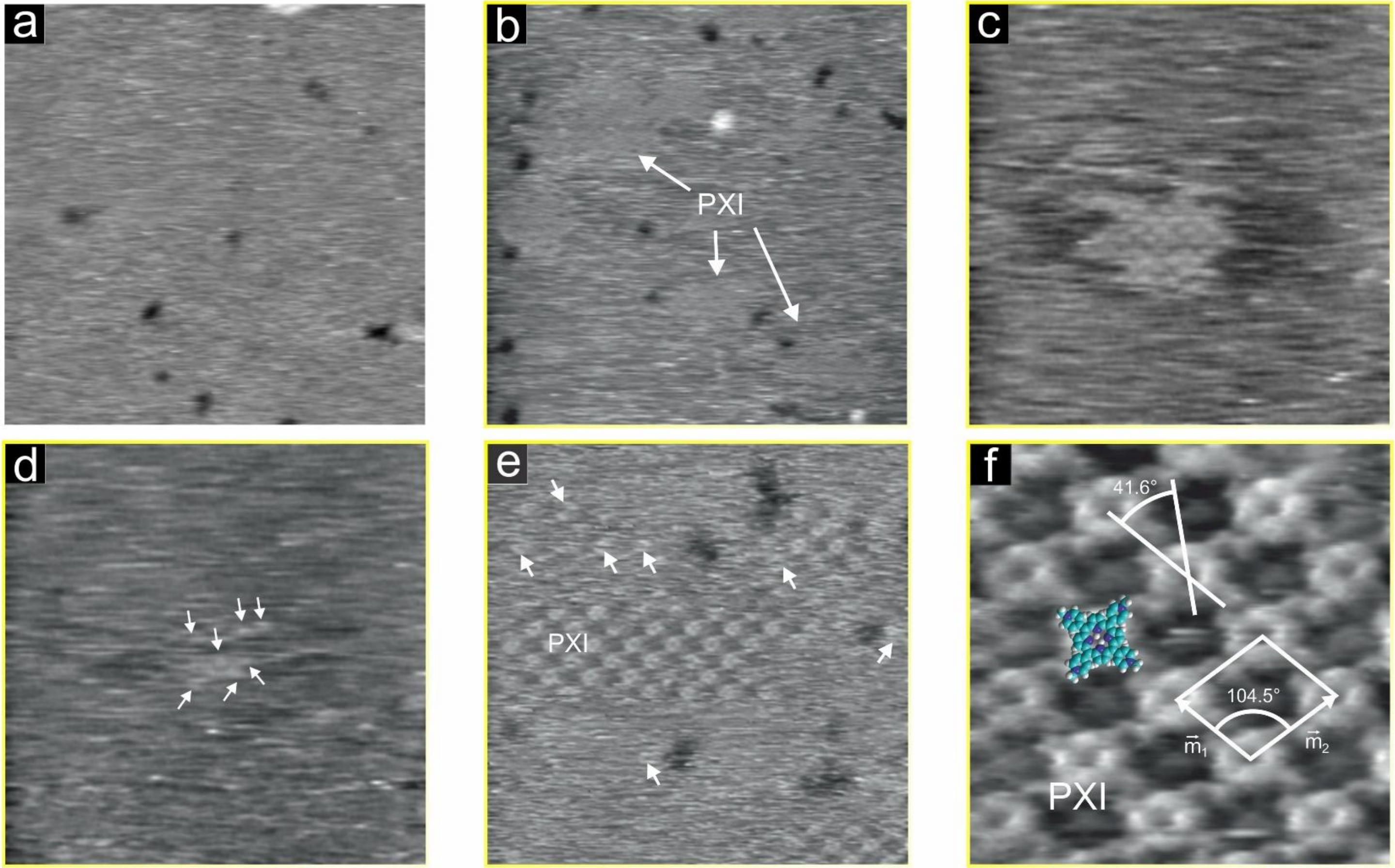

Figure 4.25: H_2TMPyP adsorption on an iodine-free Au(100) electrode at a) disorder regime; 69.14nm x 69.14nm, I_t = 1nA, U_b = -220mV, E = -720mV vs Pt/PtI; b-f) sub-monolayer regime: b) 69.14.nm x 69.14nm, I_t = 1nA, U_b = -220mV, E= -750mV vs Pt/PtI, c) 41.48nm x 41.48nm, I_t = 1nA, U_b = -182mV, E= -750mV vs Pt/PtI,d) 41.48nm x 41.48nm, I_t = 1nA, U_b = -182mV, E= -750mV vs Pt/PtI, e) 27.66nm x 27.66nm, I_t = 1nA, U_b = -220mV, E= -750mV vs Pt/PtI, f) 6.8nm x 6.8nm, I_t = 1nA, U_b = -220mV, E= -750mV vs Pt/PtI.

$P_{5'}/P_5$ (-740/-720mV vs Pt/PtI). The peak pair $P_{4'}/P_4$ was assigned previously (see sections 4.2.2.2.1 and section 4.2.1) to correspond not only to a desorption/adsorption of iodine but also to a disorder/order transition of the porphyrin layer. An exemplary image of this regime is presented in Fig. 4.25a. No ordered structure of H_2TMPyP molecules is observed. Changing the potential below peak pair $P_{5'}/P_5$ (see CV in Fig. 4.2) leads to the observation of a sub-monolayer of porphyrin molecules on the gold surface down to peak pair $P_{6'}/P_6$ (-853/-814mV vs Pt/Pt/I). A typical large scale STM image acquired within this sub-monolayer regime is presented in Figure 4.25b where islands of ordered porphyrin molecules on the surface are observed. From the successively recorded STM images (see Fig. 4.25c-d) it was found that these ordered islands are not stable. Figure 4.25c shows an ordered island of porphyrin molecules, while in the next STM scan of the same area this island has vanished although single molecules in the disordered layer are observable (see white arrows in Fig. 4.25d). Moreover, in a high-resolution image one observes disordered single molecules around ordered island. This indicates mobility in the sub-monolayer regime (see white arrows in Fig. 4.25e) and fluctuations which lead to the formation of unstable islands of porphyrin molecules on the iodine-free Au(100) surface, i.e. a 2D phase transition between a molecular gas and a condensed ordered phase (island).

A high resolution STM image as seen in Fig. 4.25f reveals more details about the molecular arrangement inside the self-assembled sub-monolayer island. The shape of the individual molecules agrees with their quadratic structure which, in turn, indicates again that the molecules are lying flat on the surface. The molecules are ordered in rows. The lattice unit-cell of this Phase XI is indicated in Figure 4.25f with the lattice parameters of $m_1 = 1.62 \pm 0.05$nm and $m_2 = 1.70 \pm 0.05$nm with an angle of ca. 104.5° between them. Individual molecules within one row are rotated by about +41.6° with respect to the row direction parallel to the $\overline{m_1}$ vector. Each unit cell includes one H_2TMPyP molecule, which corresponds to a surface concentration of ca. $3.751 \cdot 10^{13}$ molecules/cm^2.

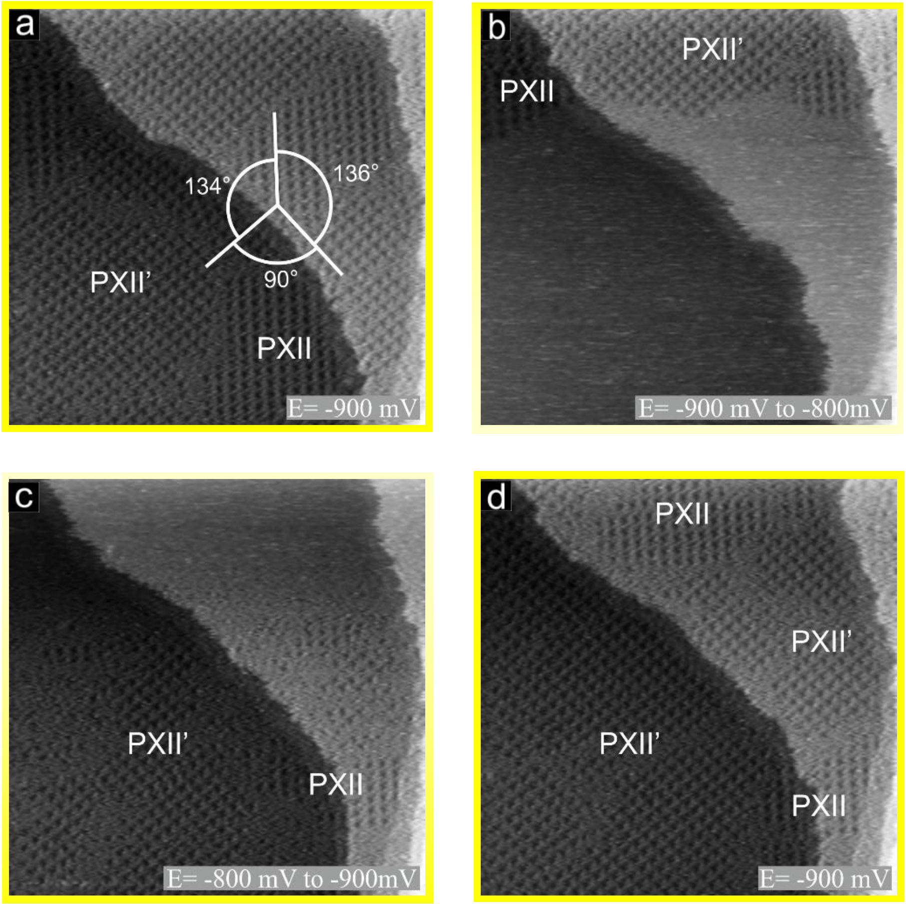

Figure 4.26: Potential induced phase transition of molecular adlayer on a iodine modified Au(100) electrode surface, STM series: 69.14nm x 69.14nm; a) I_t = 1nA, U_b = 254mV; b) I_t = 1nA, U_b = 254mV; c) I_t = 1nA, U_b = 254mV; d) I_t = 1nA, U_b = 254mV; e) I_t = 1nA, U_b = 254mV; f) I_t = 1nA, U_b = 254mV.

4.2.2.4 Monolayer adsorption of H_2TMPyP on Au(100) surface after I-desorption

The preparation and measurement procedures started with the preparation of highly ordered iodine layer that was previously checked by STM (see Section. 3.2.2.2). Then this iodine-modified Au(100) surface was exposed to a 5mM H_2SO_4 + 1mM KI solution containing 0.01mM H_2TMPyP in order to adsorb the porphyrin molecules. STM measurements were carried out just after the electrolyte exchange (at the bi-layer regime) immediately showing the porphyrin adsorption on top of the I/Au(100) substrate. Next the electrode potential was change to the working potential where an adsorption of monolayer porphyrin molecules on (1x1) Au(100) surface occurs. This regime is located between the peak pair $P_{6'}/P_6$ (-853/-814mV vs Pt/PtI) and HER. Peak $P_{6'}$, as was assignment in the section 4.2.1, corresponds to the second reduction of porphyrins molecules. Furthermore it was shown that the peak pair $P_{6'}/P_6$ corresponds to another surface process. In order to assign this peak pair a potentiodynamic STM measurements was done (see set of images on Fig. 4.26). The recorded series of STM images started at -900mV vs Pt/PtI (see Fig. 4.26a) revealing a highly ordered porphyrin layer with two rotational domains (P_{XII} and $P_{XII'}$). From the starting point, the electrode potential was change in anodic direction to -800mV vs Pt/PtI (see Fig. 4.26b), after crossing the peak P_6 a disordering of the H_2TMPyP molecules on the surface take place. Next the potential was swept back into cathodic direction (see Fig. 4.26c), and when the potential reached peak $P_{6'}$ a re-ordering of porphyrin molecules on the surface occurs. Comparing the images of Figure 4.26a and 4.26d we observe in both cases two rotational domains, although in different places in the same part of the surface. Therefore, we can conclude that the current futures $P_{6'}/P_6$ belong to ordering/disordering of H_2TMPyP molecules on the surface.

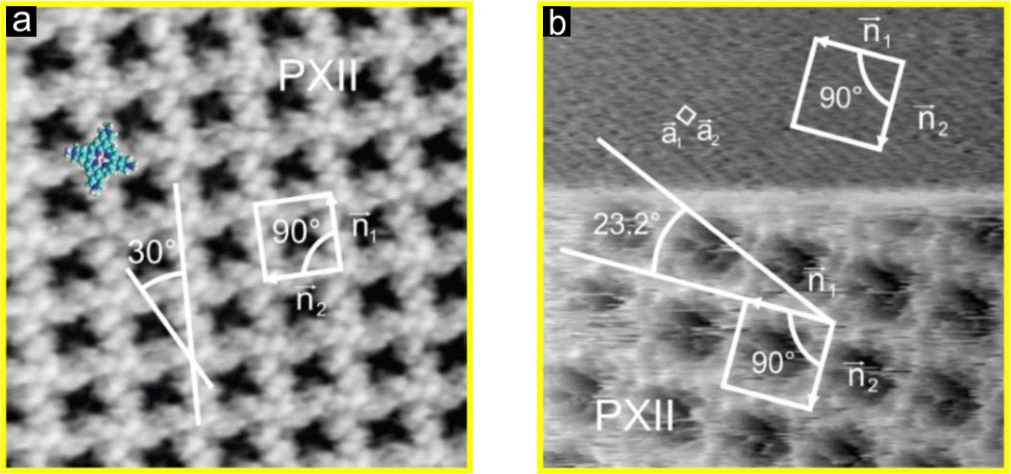

Figure 4.27: Self-assembly of H_2TMPyP on an iodine-free Au(100) electrode at monolayer regime. a) 13.83nm x 13.83nm, I_t = 5nA, U_b = 123mV, E = -850mV vs Pt/PtI, b) 11.11nm x 11.11nm, upper part: gold layer underneath at low tunnelling bias: U_b = -16mV, lower part: Porphyrin layer at high tunnelling bias: U_b = 157mV, I_t = 1nA, E = -900mV vs Pt/PtI.

Structural details of the porphyrin phase XII and its correlation with the gold lattice underneath can again be gained from high resolution images as shown in Fig. 4.27. The shape agrees with the square structure of the molecules which reveals that the molecules are lying flat on the substrate as observed in the previous sections. Within each domain of phase XII, all molecules have the same relative molecular orientation and form a square lattice (Fig. 4.27a-b). The lattice unit-cell of this Phase XII is indicated in Figure 4.27a-b with the lattice parameters of $n_1 = 2.19 \pm 0.05$nm and $n_2 = 2.19 \pm 0.05$nm with an angle of ca. 90° between them. The axis of each molecules is rotated with respect to the row direction (parallel to the $\overline{n_1}$ vector) by an angle of -30°. Each unit cell includes one H_2TMPyP molecule, which corresponds to a surface concentration of ca. $2.085 \cdot 10^{13}$ molecules/cm^2. The unit cell of phase XII as indicated in Fig. 4.27b can be related to the iodine-free gold (1x1) lattice by the matrix:

$$\begin{pmatrix} \overline{n}_1 \\ \overline{n}_2 \end{pmatrix} = \begin{pmatrix} 7 & -3 \\ -3 & -7 \end{pmatrix} \begin{pmatrix} \overline{a}_1 \\ \overline{a}_2 \end{pmatrix}$$

The molecular surface coverage is also calculated to be about 0.017 ML related to the gold lattice underneath.

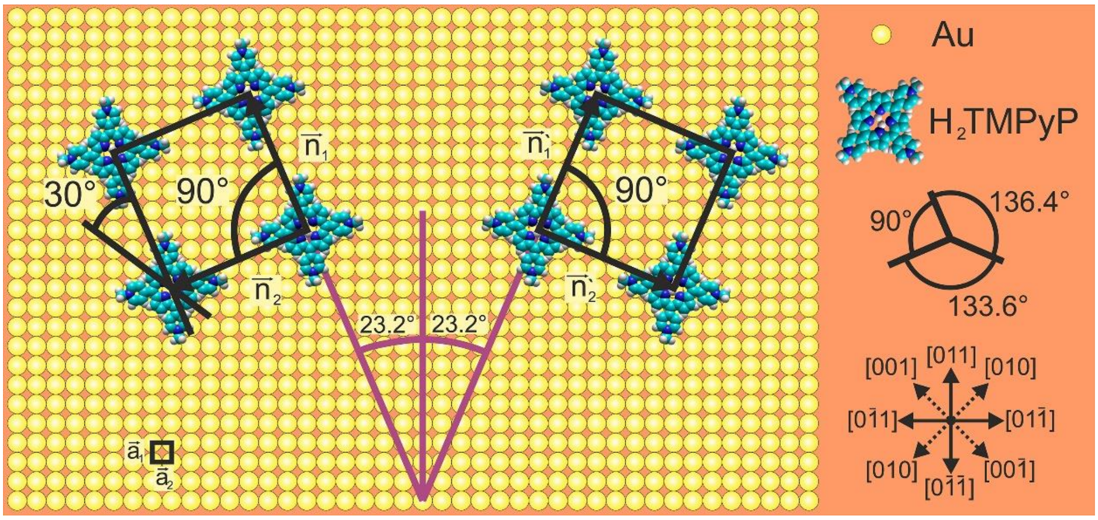

Figure 4.28: Structure model of the P_{XII} on iodine modified Au(100) surface with two mirror domains within one of four rotational domains.

A structure model of P_{XII} $(\overline{n_1},\overline{n_2})$ is presented in Fig. 4.28. By the symmetry of the lattice, a mirror structure $(\overline{n_1'},\overline{n_2'})$ with respect to a [0 1 1] direction must exist, indicating that these two rotational domains (P_{XII} and $P_{XII'}$) are two mirror domains. Taking the four-fold symmetry of the square substrate lattice into account, two more rotational H_2TMPyP domains rotated by 90° are expected. Consequently, the porphyrin molecules self-organize into four possible rotational domains on the iodine-free (1x1) Au(100) surface.

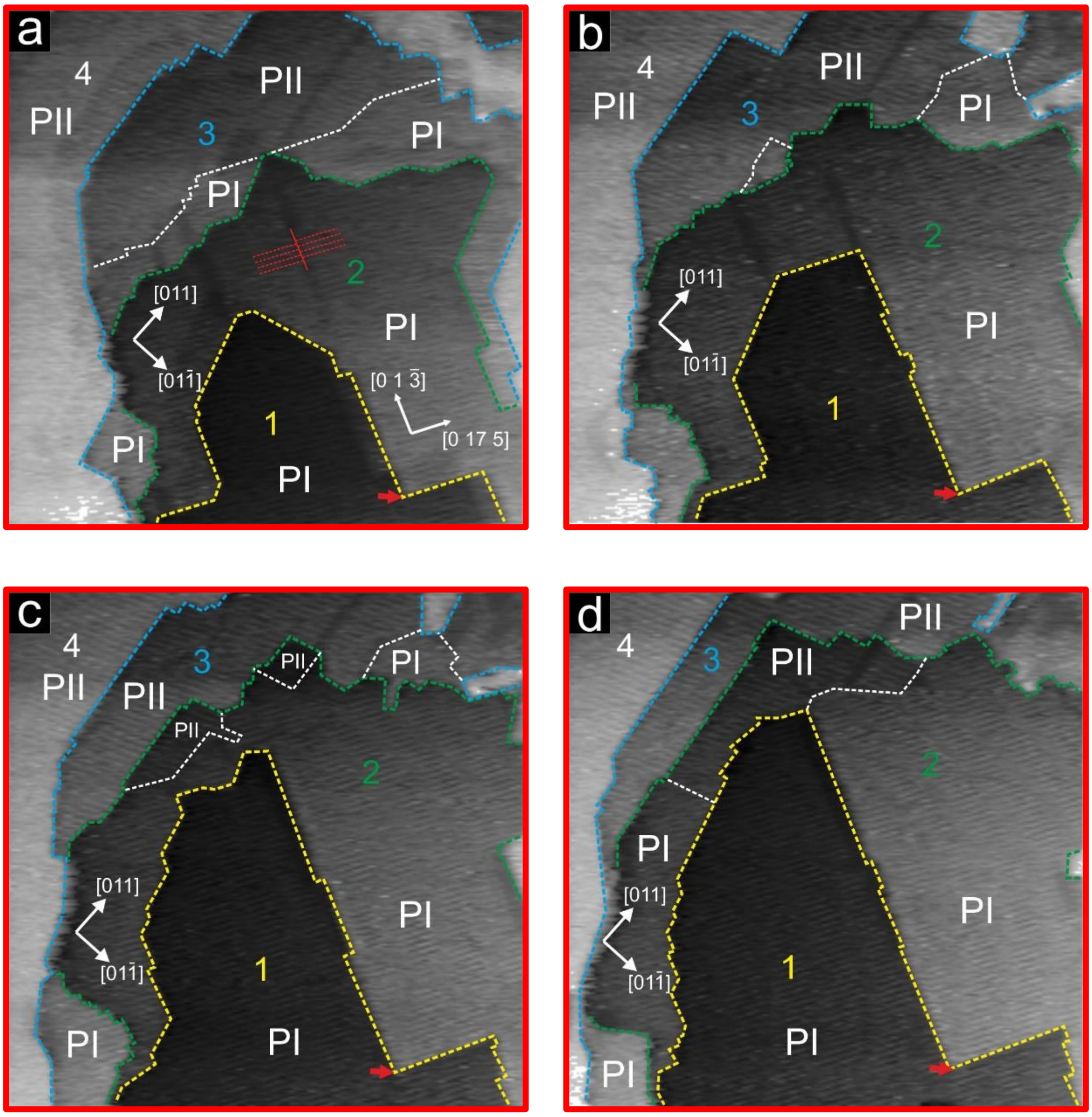

Figure 4.29: The oxidative gold dissolution reaction in the presence of H_2TMPyP on the I/Au(100), STM series: a-d) 127nm x 127nm, I_t = 1nA, U_b = -383mV, E = -100mV vs Pt/PtI.

4.2.2.5 The oxidative gold dissolution reaction in presence of H_2TMPyP molecules

The oxidative gold dissolution reaction in the presence of H_2TMPyP molecules is observed as the working potential is moved positively through ca. E = -150mV vs Pt/PtI (see section 4.2.2.1.1). In order to study this process, series of STM images as shown in Fig. 4.29 and 4.30 were recorded successively at the same surface areas and working potentials -100mV and -150mV vs Pt/PtI, respectively, representing the surface dynamics as a function of time (the red and blue arrow on the Figure 4.29a-d and Figure 4.30a-e, respectively, indicates always the same position on the surface). Fig. 4.29a shows a typical morphology of the H_2TMPyP layer adsorbed on the iodine-modified Au(100) electrode surface with two phases (P_I and P_{II}) and the step directions mainly along the molecular rows and along the diagonal of the unit cell of Phase I and II. In addition, four terraces labeled from 1 to 4, respectively, are inspected in order to investigate the dynamics of the GDR process. Dashed white lines represent a domain boundary between the Phases I and II on the same terrace. Moreover, translation domains are observable for both phases, e.g. for Phase I denoted with red dashed lines and the domain boundary between them marked by a red line. Comparing this image to the rest of the series, some conclusion can be drawn: the GDR process in the presence of porphyrins molecules takes place at the step-edges and it is governed by the H_2TMPyP layer, i.e. the dissolution of gold atoms proceeds along the molecular rows (in the case of P_I along $[0 \quad 1 \quad \bar{3}]$ and $[0 \quad 17 \quad 5]$ directions) and along the diagonal of the unit cell (in the case of P_I along $[0 \quad 5 \quad 3]$ and $[0 \quad 11 \quad \bar{5}]$ directions). Furthermore, we can observe that the GDR process follows preferably along the boundary of translational domains. Moreover, the porphyrin layer with the determined structure remains stable on the surface and after removing partially the terrace it is immediately re-adsorb into the same molecular structures.

A second series of images (see Fig. 4.30) was recorded at working potential -150mV vs Pt/PtI. Figure 4.30a shows a typical morphology of the H_2TMPyP layer adsorbed on the Au(100) electrode surface with four phases (from P_I to P_{IV}) and the step directions mainly along the molecular rows and along the diagonal of the unit cell of Phase I-IV. Herein we focus on the terrace marked by the thicker white dashed line, with two phases P_{II} and P_{III} and a disordered phase labeled by the letter D. A domain boundary between those phases is marked by the thinner white dashed line. Comparing this image to the rest of the series, we observe a dependence of the GDR process on the surface concentration of the H_2TMPyP molecules, i.e. the dissolution process proceed as follow: first dissolves the part of the terrace where is indicated the disordered phase of porphyrin molecules, second the less dense structure, which is the Phase III (surface concentration of ca. $3.016 \cdot 10^{13}$ molecules/cm^2) and at last Phase II (surface concentration of ca. $3.437 \cdot 10^{13}$ molecules/cm^2). This can lead to the conclusion that higher density of poprhyrin layer suppress the GDR process.

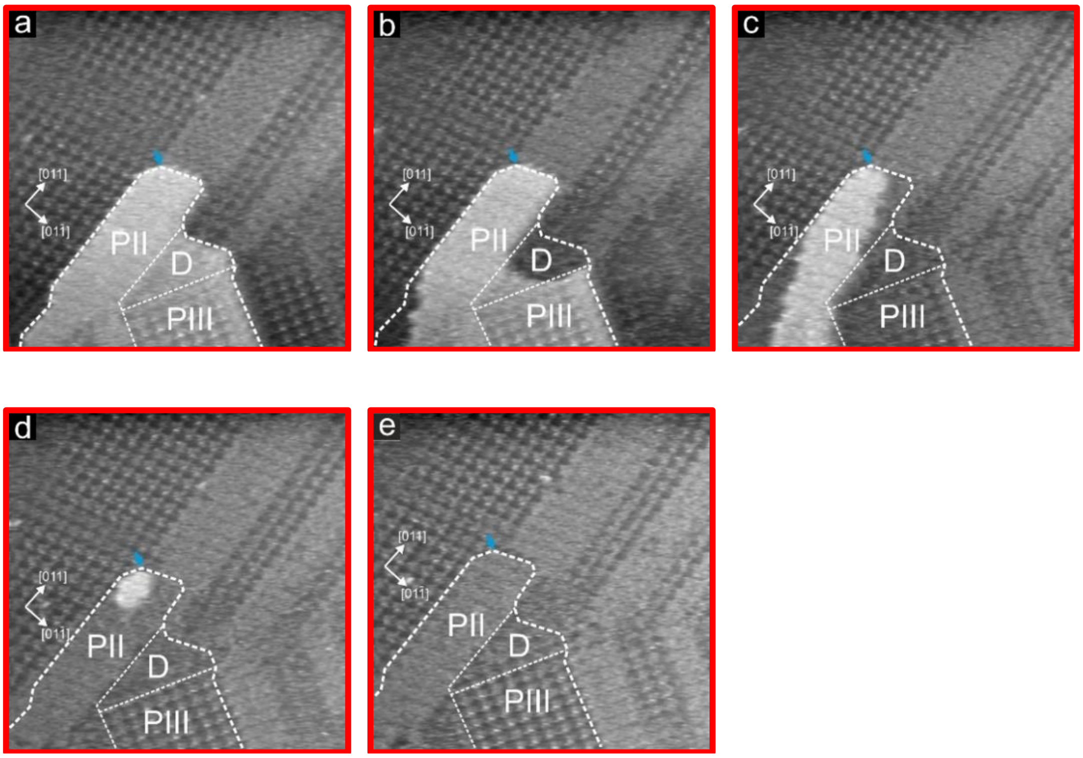

Figure 4.30: The oxidative gold dissolution reaction in the presence of H_2TMPyP on the I/Au(100), STM series: a-e) 42.35nm x 42.35nm, I_t = 1nA, U_b = -472mV, E = -150mV vs Pt/PtI.

4.3 H_2TTMAPP adsorption on iodine-modified Au(100) surface

4.3.1 Cyclic voltammetry

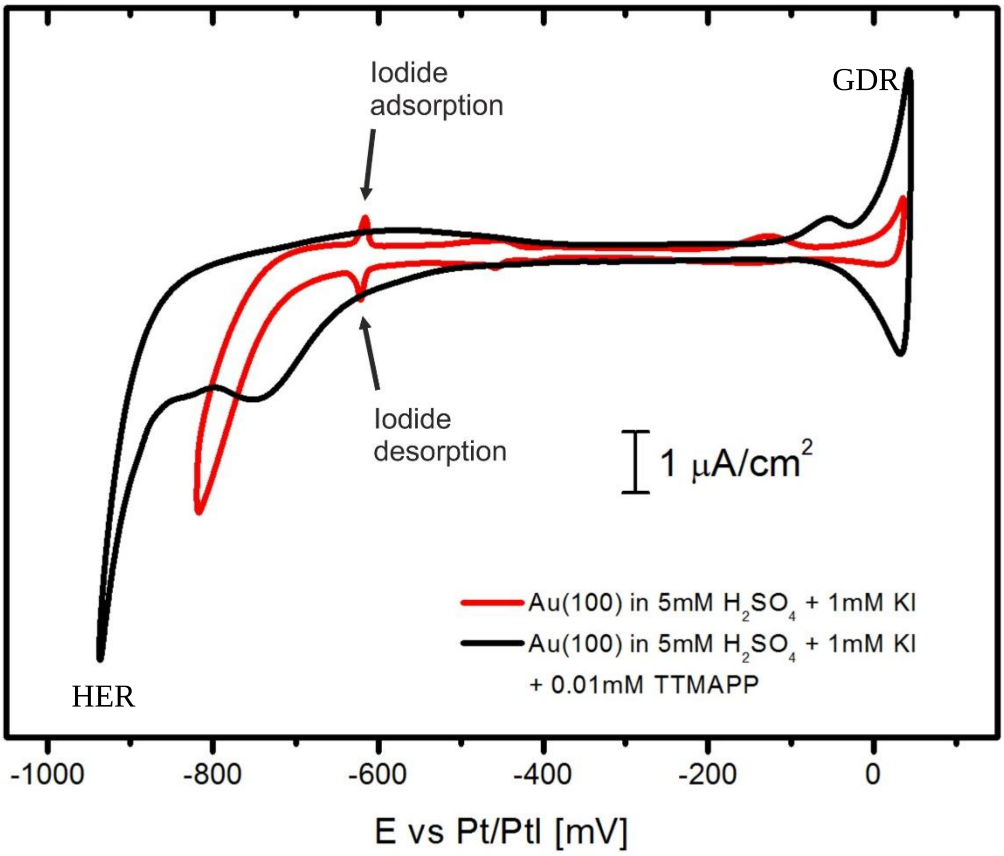

Figure 4.31: Cyclic voltammogram of a Au(100) surface in 5mM H_2SO_4 + 1mM KI electrolyte solution (red curve) and in the H_2TTMAPP containing electrolyte (black curve, 5mM H_2SO_4 + 1mM KI + 0.01mM H_2TTMAPP), dE/dt = 10mVs^{-1}.

Cyclic voltammograms of a Au(100) surface in pure supporting electrolyte (red curve) as well as in porphyrin containing solutions (black curve) are presented in Fig. 4.31. The potential window of the gold electrode in the 5mM H_2SO_4 + 1mM KI solution is limited by two chemical reactions, the oxidative gold dissolution reation (GDR) [58] at the anodic limit and the reductive hydrogen evolution reaction (HER) at the cathodic limit. After exchanging the 5mM H_2SO_4 + 1mM KI electrolyte for the one containing the H_2TTMAPP molecules we observe drastic changes in the CV curve. Comparing those two CVs we observe that the presence of the porphyrin species has an impact on the hydrogen evolution process, in that there is a considerable shift of the HER ($\Delta E \approx 120$mV) towards lower potentials, i.e. the HER is retarded by the presence of the molecules.

An additional modification from the CV of the porphyrin-free solution relates to the appearance of several anodic and cathodic current waves within the whole potential window. These further current features can be assigned to porphyrin redox processes as well as to structural changes or adsorption or desorption of molecules or iodine on the surface. First of all the shape of the CV curves with organic species depends strongly on the chosen cathodic potential limit. Therefore, by decreasing the limit of the cathodic potential systematically, a precise correlation of the cathodic to the respective anodic current wave in the reverse potential sweep can be achieved as shown in Fig. 4.32 and in the movie (move3.mp4) on the attached CD. When limiting the cathodic potential to E = -250mV and then -500mV vs Pt/PtI, no peak pairs appears in the curve 1 and 2 in Fig. 4.32. Extending the potential limit further to E = -710mV causes the appearance of peak pair $P_1/P_{1'}$ (curve 3 in Fig. 4.32). Continuing to decrease the cathodic potential limit to -760mV a second peak pair $P_2/P_{2'}$ emerges in curve 4 in Fig. 4.32. A third peak pair $P_3/P_{3'}$ becomes visible in curve 5 at a cathodic potential limit of -850mV, as shown in curve 5 in Fig. 4.32.

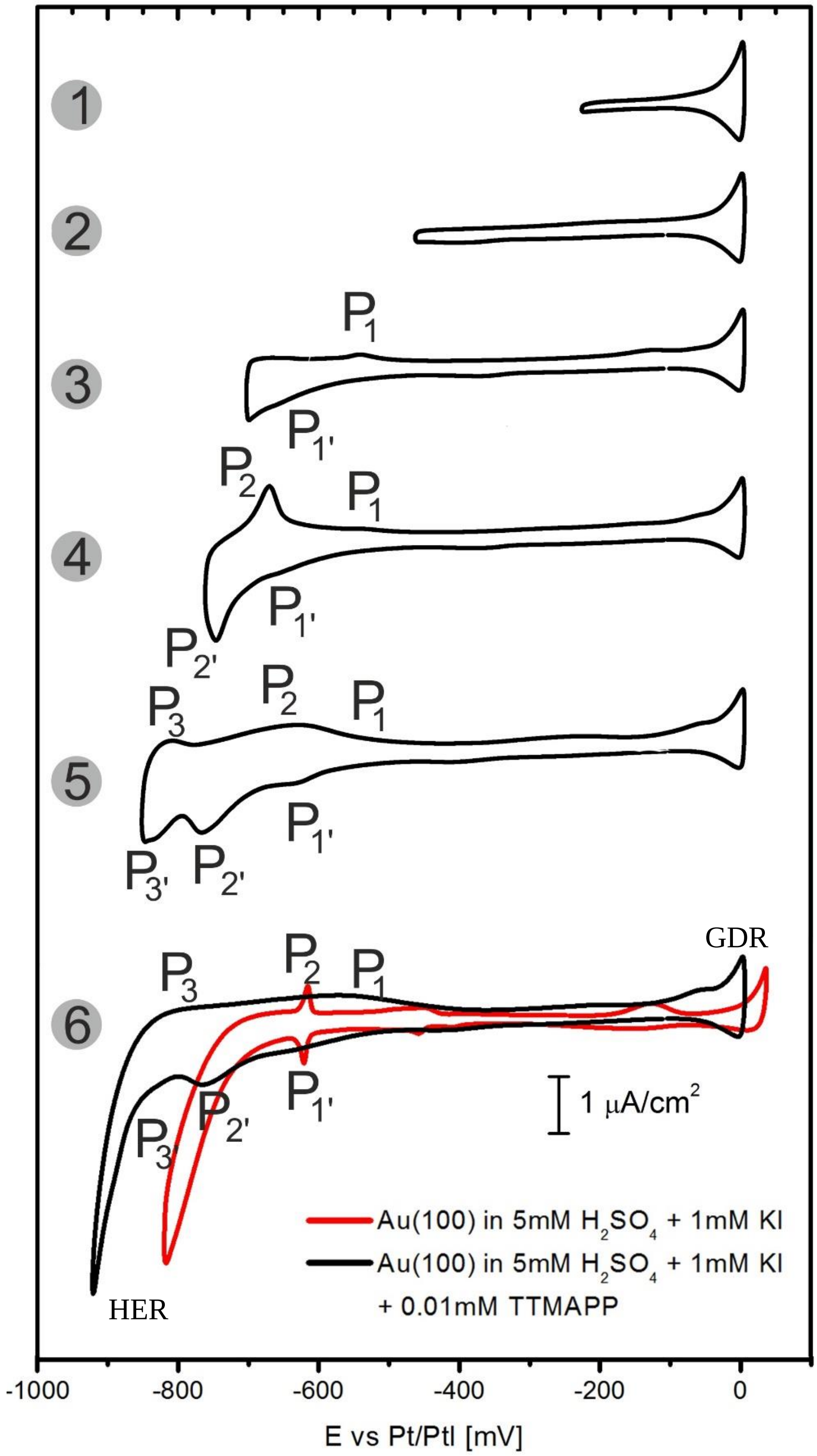

Figure 4.32: Appearance of anodic and cathodic current waves in the CV of Au(100) in the H_2TTMAPP containing electrolyte upon changing the cathodic potential limit, dE/dt= 10mVs^{-1}.

At this point, connecting the CV current waves of H_2TTMAPP molecules on an HOPG, copper electrodes (see Sec. 3.3.2.2) and the Au(100) electrode, it is possible to propose an assignment for the cathodic peak $P_{2'}$, which seems to correspond to the first reduction of the porphyrin molecules. In order to confirm the redox activity of the H_2TTMAPP molecules on the gold electrode concentration-dependent CV measurements were done (see Fig. 4.33). By the Randles-Sevcik equation (see sec. 2.5) the peak current densities of $P_{2'}$ should increase linearly with the porphyrin concentration in the solution. Instead the observed increase in the peak maximum ($P_{2'}$) by increasing ten times the molecular concentration of porphyrin molecules changes from $I_{P2'}$ = -0.62 µA (red line) to $I_{P2'}$ = -2.25µA (blue line) which give the ratio ca. 3.63, thus it is not linear. However, this nonlinear behaviour can be explained by the concomitant occurrence of not only first reduction of H_2TTMAPP molecules but also another surface process. This surface process is connected with the appearance of the anodic current peak P_2 in Fig. 4.32. Moreover, in the concentration-dependent measurements we do not observe an increase in the peak maximum of P_2, which excludes the re-oxidation of the porphyrin molecules, therefore, like in the case of chloride modified copper surfaces [56,78,79] we do not observe in the potential window of gold a re-oxidation peak of the H_2TTMAPP molecules. Furthermore, we observe a considerable shift in the position of peak P_2 (from -670mV to -570mV vs Pt/PtI) by restricting the cathodic potential (see movie3.mp4).

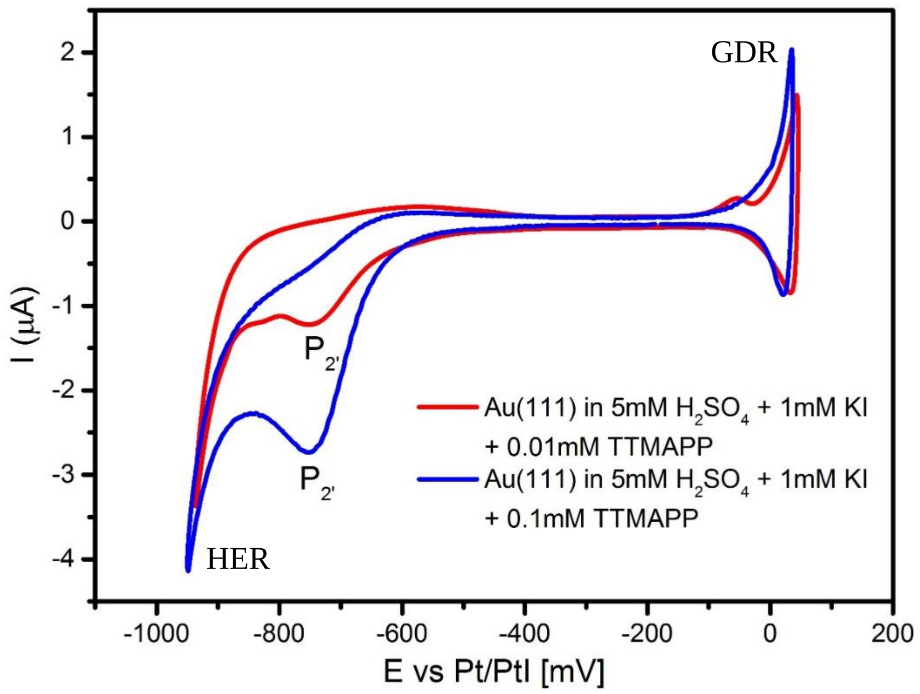

Figure 4.33: CV of Au(100) in 5mM H_2SO_4 + 1mM KI + 0.01mM H_2TTMAPP solution (red line) and Au(100) in 5mM H_2SO_4 + 1mM KI + 0.1mM H_2TTMAPP solution (blue line), dE/dt= 10mVs^{-1}.

Considering the CVs in the presence and the absence of porphyrin molecules in solution give a possibility to assign the peak pair $P_{1'}/P_1$ to a peak pair d'/d of desorption/adsorption of iodine on the surface (without organic layer). Interestingly, it can be observed that the desorption/adsorption peaks $P_{1'}/P_1$ of iodine in the presence of H_2TTMAPP molecules are shifted to more negative/positive (respectively) potential than peak pair d'/d. It seems that the organic layer hinders the iodine desorption as well as adsorption.

Further information about the origin of each current wave in the CV can be obtained from in-situ STM measurements which will be described subsequently.

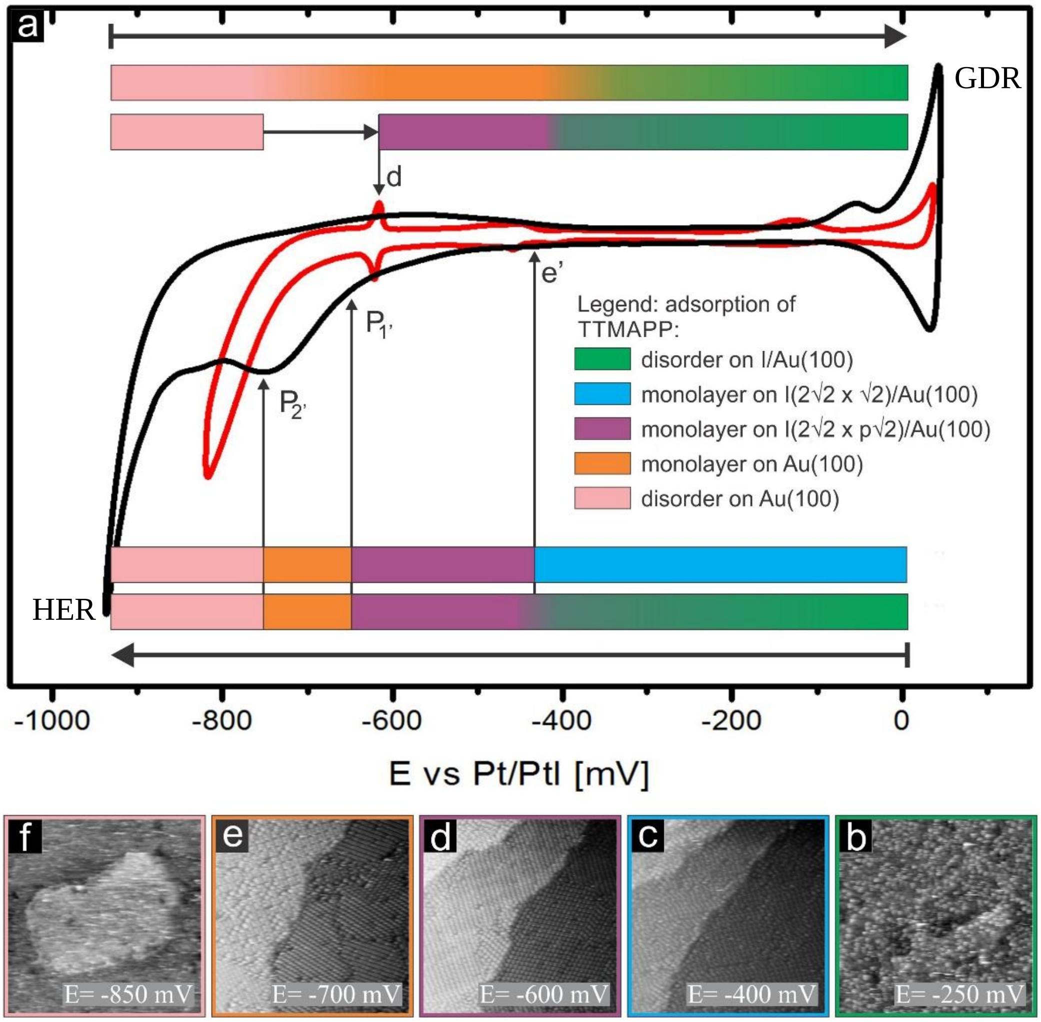

Figure 4.34: Potential window of an I modified Au(100) divided in five adsorption intervals of H_2TTMAPP molecules.

4.3.2 In-situ STM investigation

The initial electrochemical characterization of H_2TTMAPP adsorption on an I modified Au(100) surface gives information about possible drastic changes in the surface morphology due to the applied electrode potential (e.g. peak pair $P_{1'}/P_1$ which is related to adsorption/desorption of iodine). Although, not all changes on the surface can be attributed to characteristic peaks of current wave, especially if a process extends over a larger potential regime. An example of such behaviour was already presented in the case of the "*flexible superstructure*" in the subchapter of iodine adsorption on the Au(100) surface (see sec. 3.2.2.2). Furthermore, the observation of the shift in the position of the anodic peak P_2 (which from STM measurements was assigned to readsorption of porphyrin molecules) is correlated with the value of the limiting cathodic potentials: The more negative the latter the slower is the re-formation of an ordered structure in the anodic backscan. Nevertheless, by the STM measurements the Au potential window can be divided into five regimes as follow:

1. The first regime (blue colour in Fig. 4.34) is the self-assembly of a monolayer of H_2TTMAPP molecules on a $I(2\sqrt{2}x\sqrt{2})$/Au(100) surface, where we observe one ordered porphyrin phase (see Fig. 4.34c). Furthermore, this phase is observed only under specific conditions, i.e. when the supporting electrolyte was exchanged by a solution containing H_2TTMAPP molecules in the potential regime between -400mV and -300mV vs Pt/PtI. This regime initially is stable in the potential range of ca. -425mV vs Pt/PtI and GDR. This regime is described in detail in section 4.3.2.1.

2. The next regime (violet colour in Fig. 4.34) in cathodic direction is located between ca. -425mV vs Pt/PtI and peak $P_{1'}$ where four H_2TTMAPP structures appear on the $I(2\sqrt{2}xp\sqrt{2})$/Au(100) (see Fig. 4.34d). The peak $P_{1'}$ was identified as the superposition of desorption of iodine and a phase transition of the porphyrin molecules. In anodic direction observation of the reappearance of the four H_2TTMAPP structures is possible when the potential is *jumped* from the disordered regime (beige) to the electrode potential between ca. -620mV (which corresponds to a peak *d* of the adsorption of iodine in the absence of organic molecules) and -400mV vs Pt/PtI. This sudden change prevents the creation of ordered structures on the iodine-free Au(100) surface from the third regime which inhibits readsoption of the iodine anions. Therefore, in anodic direction we observe a semi-reversible process. This regime is described in detail in section 4.3.2.2.

3. The third regime (orange colour in Fig. 4.34) in cathodic direction is located between peak pair $P_{1'}$ (desorption of iodine and phase transition) and $P_{2'}$

(reduction and disordering of H_2TTMAPP molecules). In anodic direction readsoption of individual molecules starts at ca. -750mV vs Pt/PtI and an ordered layer is re-established at ca. -700mV vs Pt/PtI and this ordered overlayer is observed until ca. -400mV vs Pt/PtI. This regime is represented by five ordered monolayer phases on the I-free (1x1) Au(100) surface. Furthermore, an exemplary STM image of this regime is shown in Figure 4.34e. This regime is described in detail in section 4.3.2.3.

4. The fourth (beige colour in Fig. 4.34) regime extends in cathodic direction from peak $P_{2'}$ till HER and in anodic direction from HER till ca. -700mV when an ordered layer of the third regime is re-established. An exemplary STM image of this regime is presented in Figure 4.34f. This regime is described shortly in section 4.3.2.3.1.

5. The fifth regime where we observe disordered H_2TTMAPP molecules on the I/Au(100) surface (green colour in Fig. 4.34) is located between GDR and reaches till ca. -400mV vs Pt/PtI with extended an transition to the second regime. An exemplary STM image of this regime is shown in Figure 4.34b. This regime is described shortly in section 4.3.2.2.1.

4.3.2.1 Monolayer adsorption of H_2TTMAPP on the I(2√2 x √2)/Au(100) surface

The measurements start with the preparation of a highly ordered iodine layer on the Au(100) surface which was initially checked by STM (see Section. 3.2.2.2). In order to prepare a H_2TTMAPP layer on the I(2√2 x √2)/Au(100) surface the supporting electrolyte was routinely exchanged by a solution containing 5mM H_2SO_4, 1mM KI and 0.1mM H_2TTMAPP in the potential regime between -400mV and -300mV vs Pt/PtI. STM measurements were carried out just after the electrolyte exchange immediately showing the porphyrin adsorption on top of the I/Au(100) substrate.

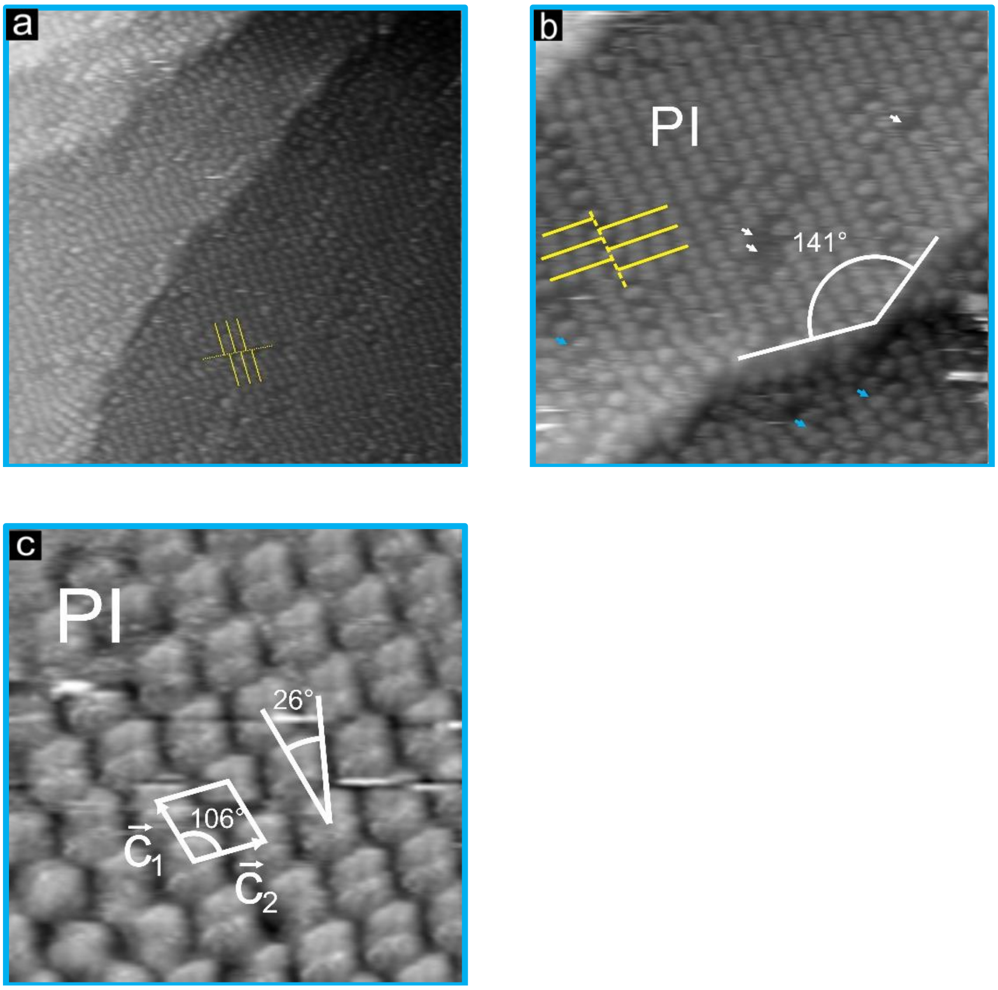

Figure 4.35: Self-assembly of H_2TTMAPP on an iodine-modified Au(100) electrode in the monolayer regime. a) 84.7nm x 84.7nm, I_t = 1nA, U_b = -555mV, E= -400mV vs Pt/PtI, b) 28.2nm x 28.2nm, I_t = 1nA, U_b = -555mV, E= -400mV vs Pt/PtI, c) 14.1nm x 14.1nm, I_t = 1nA, U_b = -606mV, E= -400mV vs Pt/PtI.

The H_2TTMAPP phase I is observed in the electrode potential range between -425mV vs Pt/PtI and GDR. A typical large scale STM image acquired at -400mV vs Pt/PtI and measured soon after the exposure of a iodine-modified Au(100) surface to the H_2TTMAPP containing electrolyte leads to the observation of a surface structure of the porphyrin adlayer on top of the $I(2\sqrt{2} \text{ x } \sqrt{2})$/Au(100) substrate, as displayed in Fig. 4.35. Each bright dot represents one H_2TTMAPP molecule. It is seen that the molecules are self-assembled into an ordered layer of molecular rows covering atomically flat terraces. Furthermore, by thorough examination of Fig. 4.35a-b one porphyrin phase is observed. Moreover, translation domains are observable which are denoted with yellow solid lines and the domain boundary between them marked by dashed yellow lines (see Fig. 4.35a-b). Additionally, we can observe a local disordering and missing molecules in the porphyrin structure marked by small blue and white arrows, respectively, in the Figure 4.35b.

The high resolution image in Fig. 4.35c illustrates the molecular arrangement and accentuates that the H_2TTMAPP molecules are arranged in rows. Each molecule is recognized by its square-like shape with characteristic four additional lobes placed at the corners of a square, indicating the flat-lying arrangement of the molecules on the surface. This flat-lying arrangement is due to the large molecular π system which has the tendency to maximize the π bonding to the surface [29-32,35,56]. The lattice unit-cell for the Phase I can be drawn as show in Figure 4.35c with the lattice parameters of $c_1 = 2.02 \pm 0.05$nm and $c_2 = 2.04 \pm 0.05$nm with an angle of ca. 106° between them. Individual molecules within one row are rotated by about +26° with respect to the row direction parallel to the $\overline{c_1}$ vector. Each unit cell includes one H_2TTMAPP molecule, which corresponds to a surface concentration of ca. $2.525 \cdot 10^{13}$ molecules/cm^2.

In order to check the potential stability of this Phase I a potentiodynamic STM experiment was done and is presented in the next subchapter (4.3.2.1.1). Hence, the porphyrin molecules in the monolayer regime do not undergo any further redox process, therefore, the changes which occur in the monolayer regime are not caused by a variation in the chemical state of the porphyrin but by a variation of the interaction between the porphyrin molecules and the substrate. Furthermore, a structural relation between the molecular structure and iodine underneath is shown in subchapter 4.3.2.1.2.

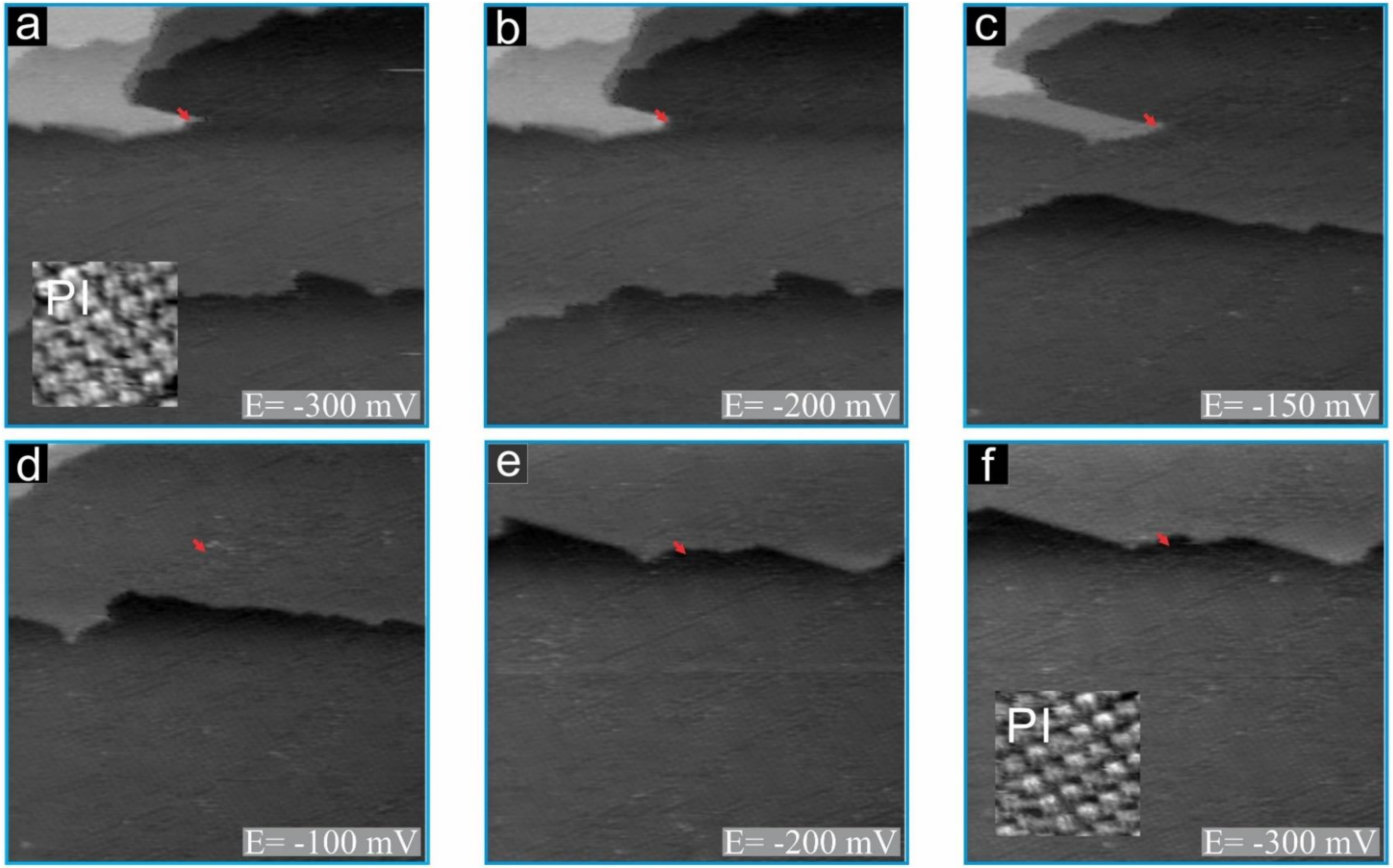

Figure 4.36: Potentiodynamic STM images of stability of Phase I on an iodine modified Au(100) electrode surface, STM series: 125.3nm x 125.3nm; a) I_t = 1nA, U_b = -510mV, inset: 11.4nm x 11.4nm; b) I_t = 1nA, U_b = -510mV; c) I_t = 1nA, U_b = -510mV; d) I_t = 1nA, U_b = -510mV; e) I_t = 1nA, U_b = -510mV; f) I_t = 1nA, U_b = -510mV, inset: 11.2nm x 11.2nm.

4.3.2.1.1 Potentiodynamic STM measurements.

The potentiodynamic STM measurements are presented in two sets of images (Fig. 4.36 and Fig. 4.37). Figure 4.36 shows a potential dependent series of STM images starting from the preparation of the Phase I at -300mV vs Pt/PtI (see inset on Fig. 4.36a). The red arrow in the Figure 4.36a-f indicates always the same position on the surface. From the starting point, the electrode potential was carefully scanned in the anodic direction. No changes where noticed until the electrode potential reached -150mV vs Pt/PtI, where a oxidative gold dissolution reaction is observed. Moreover, the Phase I is stable on the surface; even after partial dissolution of the terrace it is immediately re-adsorbed into the same molecular structure. After reaching the electrode potential of -100mV vs Pt/PtI where the oxidative gold dissolution reaction proceeds very strongly (see Fig. 4.36d) the potential was sweep back into cathodic direction. When the potential reached the starting point (-300mV vs Pt/PtI) the surface was investigated and no changes in the molecular lattice were observed (see Fig. 4.36f and inset in Fig. 4.36f). Further decreasing of the electrode potential is presented in Fig. 4.37a-d. The STM image in Figure 4.37a recorded at -400mV vs Pt/PtI shows again the Phase I. Changing the electrode potential to -450mV vs Pt/PtI leads to the observation of three new phases (see Fig. 4.37c-d). Comparing this phase transition observed by STM images to the CV of iodine suggests that this change in molecular layer is related to the change in the iodine lattice from the structure $(2\sqrt{2} \times \sqrt{2})$ to $(2\sqrt{2} \times p\sqrt{2})$ corresponding to the cathodic peak e’ in the cyclic voltammogram in Fig. 3.12.

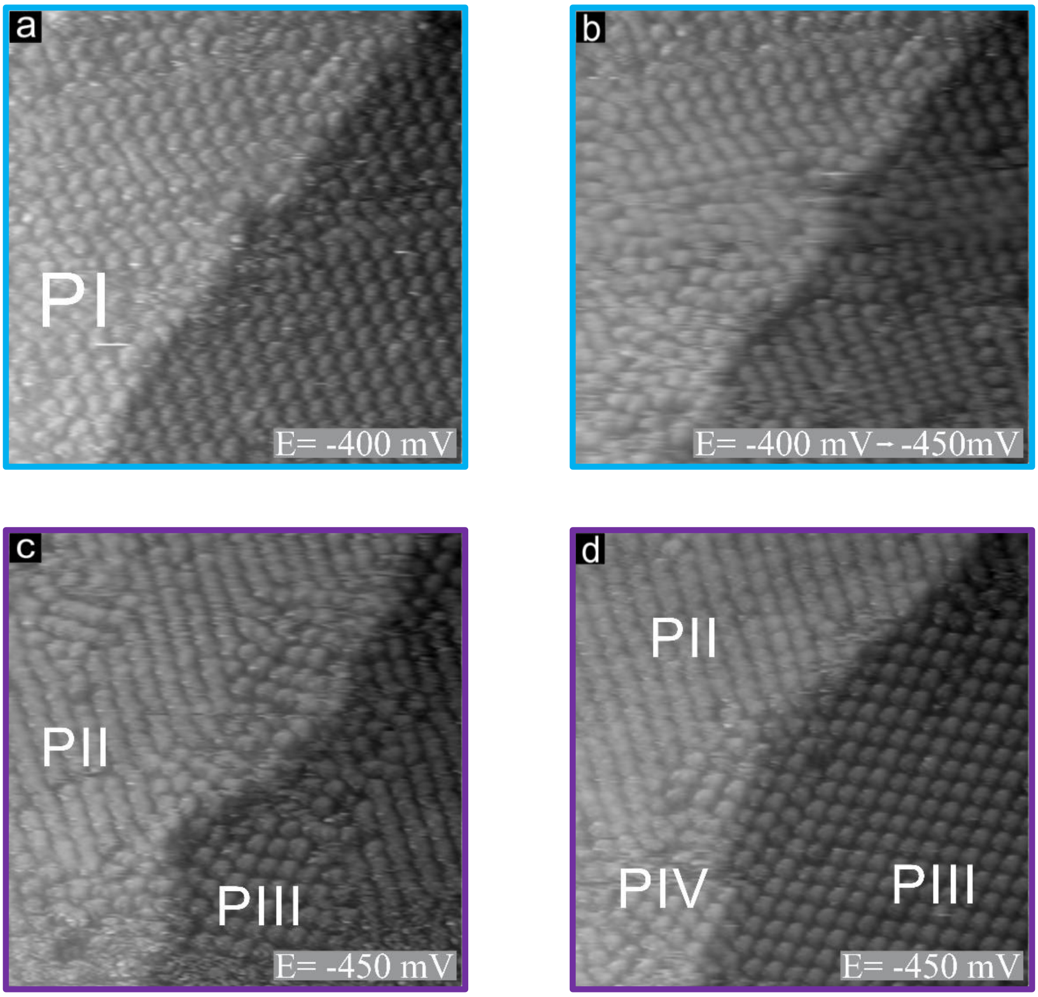

Figure 4.37: Potential induced phase transition of molecular adlayer on an iodine modified Au(100) electrode surface, STM series: 42.3nm x 42.3nm; a) I_t = 1nA, U_b = -314mV; b) I_t = 1nA, U_b = -314mV; c) I_t = 1nA, U_b = -314mV; d) I_t = 1nA, U_b = -314mV; e) I_t = 1nA, Ub = -314mV; f) I_t = 1nA, Ub = -314mV.

4.3.2.1.2 Structural correlation between the H_2TTMAPP adlayer and the substrate lattice.

In order to acquire information about the structural correlation between the porphyrin adlayer of Phase I and the substrate lattice underneath a set of STM images (Fig.4.38a-b) of 14.12nm x 14.12nm were recorded successively at the same surface area. The method to relate the porphyrin lattice to the structure underneath is the same as that applied for the H_2TMPyP molecules and is described in detail in subchapter 4.2.2.1.2.

Figure 4.38a in the upper part shows the molecular phase P_I together with the unit cell recorded at high tunneling *bias* (-606mV). The gradual change of the tunnelling *bias* from high (-606mV) to low (-17mV) enable us to tunnel through the molecular layer and to obtain a direct correlation between the structure of the organic adlayer and that of the underlying iodine lattice (lower part on Fig. 4.38a and Fig. 4.38b). After close analysis of the images presented in Figure 4.38 it is possible to present an accurate model of the phase I including the structural relationship between P_1 and the iodine and gold lattice underneath (see Fig. 4.39). The iodine lattice under phase I was found to be a (2√2 x √2) with directions [0 0 1] and [0 1 0], respectively, to the unit cell of iodine. All iodine anions are situated in 2-fold bridging sites on the Au(100) (1x1) gold lattice yielding the coverage of $\theta = 0.5$ or $62.58 \cdot 10^{13}$ iodine/cm^2. The NND for the (2√2x√2) structure along the √2 direction is 4.08Å and 4.56Å along the two diagonals of the unit cell.

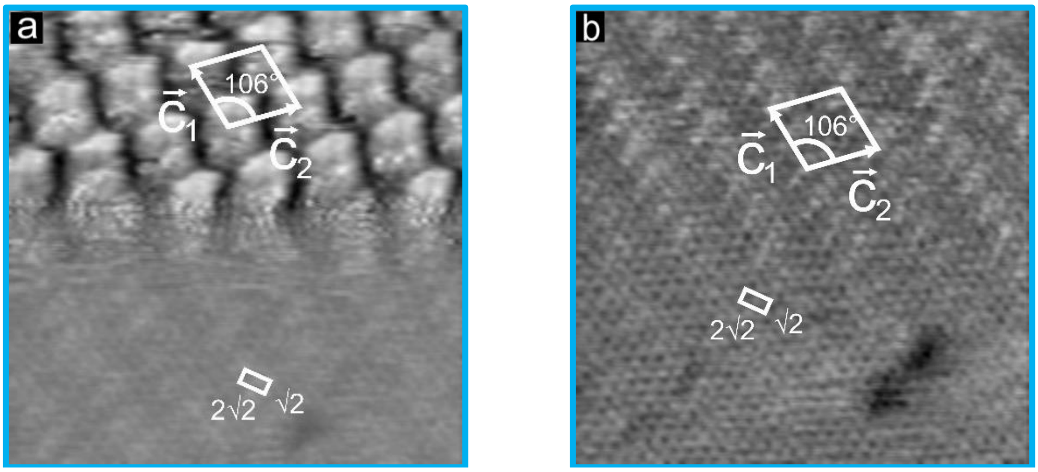

Figure 4.38: Structure correlation between the H_2TTMAPP layer of phases I and the underlying iodine and gold layer, a) upper part: Porphyrin layer at high tunneling bias: U_b = -606mV, lower part: Iodine layer underneath at low tunneling bias: U_b = -17mV, 14.12nm x 14.12nm, I_t = 1nA, E= -400mV vs Pt/PtI, b) Iodine layer underneath at low tunneling bias, 14.12nm x 14.12nm, I_t= 1nA, U_b = -17mV, E= -200mV vs Pt/PtI.

The $H_2TTMAPP$ layer of Phase I is described by vectors $\overline{c_1}$ and $\overline{c_2}$ with directions of $[0\quad \bar{4}\quad 3]$ and $[0\quad 4\quad 3]$, respectively. Therefore, the molecular rows of phase P_I do not follow any high symmetry direction of the substrate, neither of the iodine lattice nor of the Au(100) surface. The unit cell $(\overline{c_1}, \overline{c_2})$ as depicted in Fig.4.35c and Fig.4.38a with the lattice parameters of c_1 = 1.61nm and c_2 = 1.80nm, enclosing an angle of 106°, contains one molecule and can be related to the iodine lattice by the matrix:

$$\left(2\sqrt{2}\times\sqrt{2}\right)I - c\begin{pmatrix} -2 & -1 \\ 2 & 5 \end{pmatrix} - H_2TTMAPP$$

and likewise to the gold lattice by the matrix:

$$\left(1\times1\right)Au(100) - c\begin{pmatrix} -1 & -7 \\ 7 & 1 \end{pmatrix} - H_2TTMAPP$$

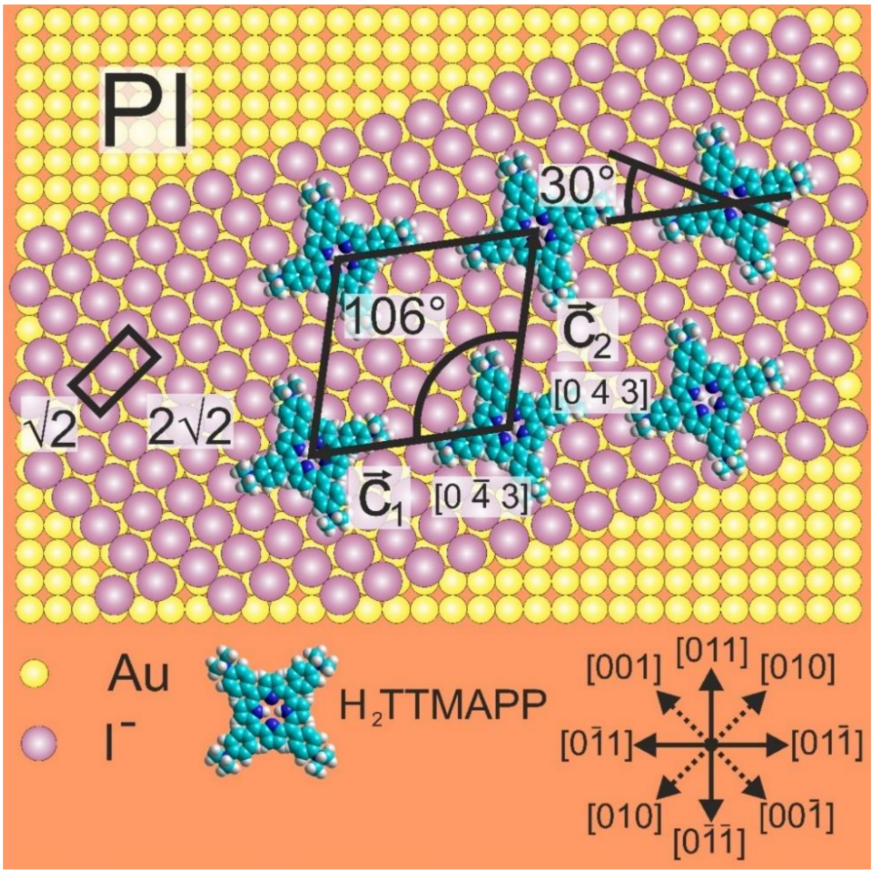

Figure 4.39: Structure model of phase P_I on the I(2√2 x √2)/Au(100) surface.

On the basis of this model the surface coverage of the porphyrin adlayer is calculated to be 0.0209 ML relative to the density of the gold layer, or $2.525 \cdot 10^{13}$ molecules/cm^2.

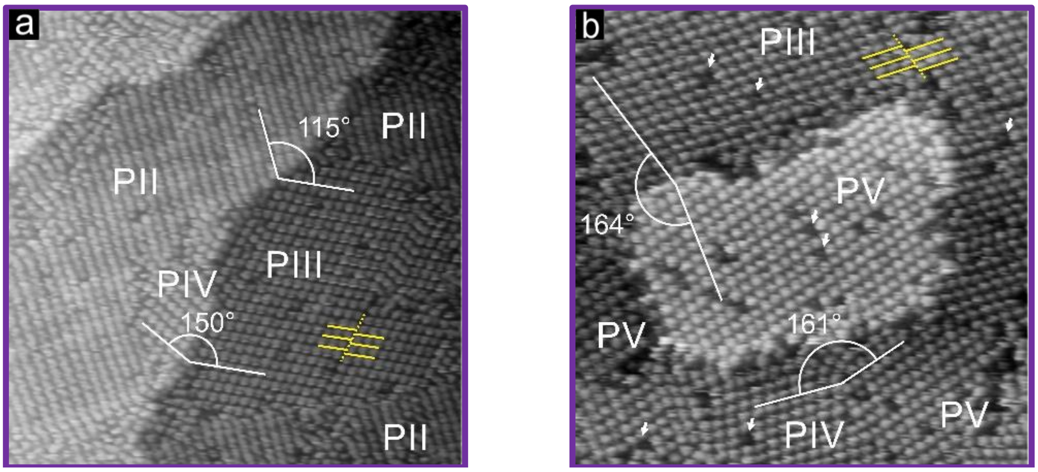

Figure 4.40: Ordered H$_2$TTMAPP adlayer on an iodine-modified Au(100) electrode in the I(2$\sqrt{2}$ x p$\sqrt{2}$)/Au(100) regime. a) 84.70nm x 84.70nm, I_t = 1nA, U_b = -314mV, E = -600mV vs Pt/PtI, b) 70.58nm x 70.58nm, I_t = 1nA, U_b = -402mV, E= -625mV vs Pt/PtI,

4.3.2.2 Monolayer adsorption of H$_2$TTMAPP on I(2$\sqrt{2}$ x p$\sqrt{2}$)/Au(100) surface

As presented in the potentiodynamic STM images in Figure 4.37 changing the electrode potential from the monolayer regime in cathodic direction leads to the observation of new porphyrin structures on the I(2$\sqrt{2}$ x p$\sqrt{2}$) /Au(100) surface. This regime in cathodic direction is situated between ca. -425mV vs Pt/PtI and peak P$_1$. In anodic direction the observation of the reappearance of the four H$_2$TTMAPP structures is possible when the potential is *jumped* from the disordered regime (beige) to the electrode potential between ca. -620mV (which corresponds to peak *d* of adsorption of iodine in the absence of organic molecules) and -400mV vs Pt/PtI. This sudden change prevents the creation of the ordered structures on the iodine-free Au(100) surface from the third regime (violet) which in turn would inhibit readsoption of the iodine anions.

Typical large scale STM images acquired within the described regime showing the surface structure of the H_2TTMAPP adlayer on top of the I(2√2 x p√2)/Au(100) surface are displayed in Fig. 4.40. It is clearly seen that the terraces are covered almost entirely by porphyrin molecules which are self-assembled into an ordered layer of molecular rows. Furthermore, by thorough examination four new coexisting porphyrin phases, namely PII - PV, are distinguishable in Figure 4.40a-b. Like in the case of the monolayer phase also translational domains are observable which are denoted with yellow solid lines and a domain boundary between them marked by a dashed yellow line (see Fig. 40a-b). Moreover, on all images in this regime missing molecules in the molecular layer can be detected, which are represented by dark spots on the STM images (marked by small white arrows in Fig. 4.40b).

The molecular arrangement within each phase of the porphyrin layer can be seen more clearly in the high resolution images in Fig. 4.41a-d. The molecules are ordered in rows. The shape of the individual molecules agrees with their square structure which again indicates that the molecules are lying flat on the surface. The unit-cell lattice for Phase II can be defined as shown in Figure 4.41a with the lattice parameters d_1 = 2.02 ± 0.05nm and d_2 = 2.04± 0.05nm and an angle of ca. 92° between them. Individual molecules within one row are rotated by about -13° with respect to the row direction parallel to the $\overline{d_2}$ vector. Each unit cell includes one H_2TTMAPP molecule, which corresponds to a surface concentration of ca. $2.221 \cdot 10^{13}$ molecules/cm^2. The unit cell of Phase III is presented in Figure 4.41b. The lattice constants are e_1 = 2.10 ± 0.05nm and e_2 = 3.87± 0.05nm enclosing an angle of about 72°. We can distinguish two different rows (denoted A and B in Fig. 4.41b). Molecules within one and the same row are all rotated in the same direction but the sense of rotation is different in alternating A and B rows. The rotation of the individual molecules within one row is about +13° or -13° with respect to the row direction parallel to the $\overline{e_1}$ vector. Each unit cell includes two H_2TTMAPP molecules, which corresponds to a surface concentration of ca. $2.588 \cdot 10^{13}$ molecules/cm^2. Furthermore, the angle between the vectors $\overline{d_2}$ and $\overline{e_2}$ is 115° (see Fig. 4.40a).

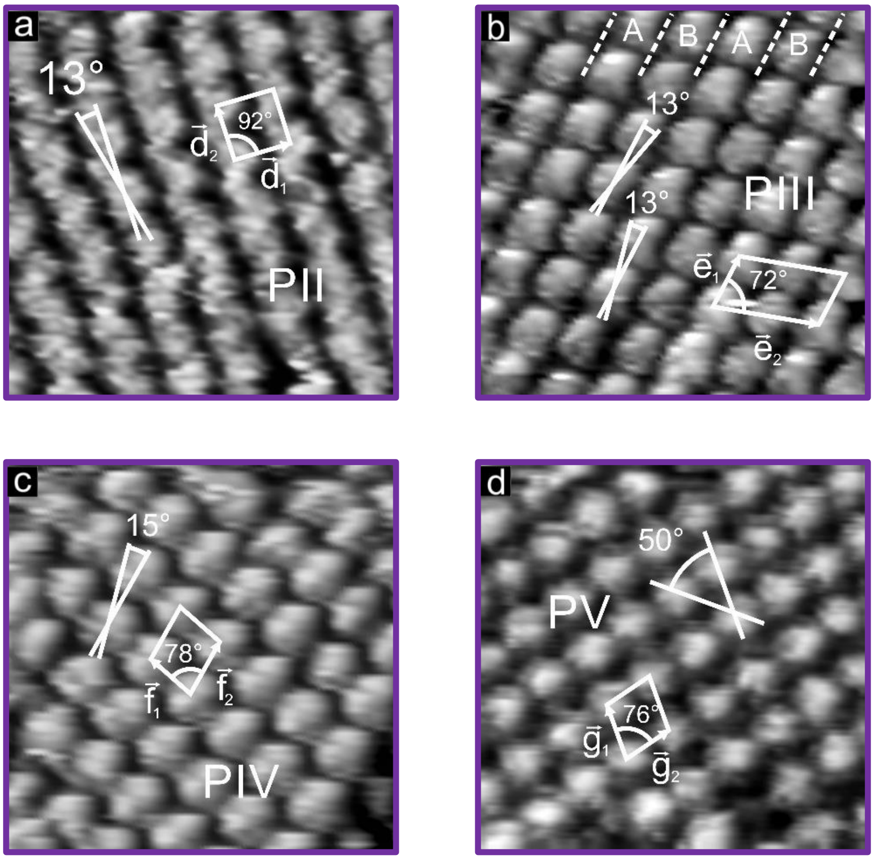

Figure 4.41: High-resolution images of an ordered H_2TTMAPP adlayer on an iodine-modified Au(100) electrode in the I(2√2 x p√2)/Au(100) regime. a) 14.60nm x 14.60nm, I_t = 1nA, U_b = -314mV, E= -600mV vs Pt/PtI. b) 14.10nm x 14.10nm, I_t = 1nA, U_b = -314mV, E= -600mV vs Pt/PtI; c) 13.90nm x 13.90nm, I_t = 1nA, U_b = -271mV, E= -600mV vs Pt/PtI; d) 14.10nm x 14.10nm, I_t = 1nA, U_b = -460mV, E= -600mV vs Pt/PtI.

The unit cell of Phase IV is presented in the Fig. 4.41c. The nearest neighbour distances between porphyrin molecules for P_{IV} are found to be f_1 = 1.95 ± 0.05nm and f_2 = 2.11± 0.05nm, respectively, and the angle between the two unit vectors is ca. 78°. The symmetry axis of the H_2TMPyP molecules in this case is rotated by an angle of about -15° with respect to the molecular row direction parallel to $\overline{f_1}$. One porphyrin molecule is contained in each unit-cell which corresponds to a surface concentration of ca. $2.485 \cdot 10^{13}$ molecules/cm^2. The angle between the vectors $\overline{e_2}$ of Phase III and $\overline{f_1}$ of Phase IV is ca. 150° which is shown in the Figure 4.40a. Figure 4.41d presents the unit cell of Phase V. The lattice constants are g_1 = 2.07 ± 0.05nm and g_2 = 1.88± 0.05nm enclosing an angle of 76°. All molecules within one row are rotated by about -50° with respect to the row direction which is parallel to the $\overline{g_1}$ vector. The unit-cell of P_V as indicated in Fig. 4.41d contains one porphyrin molecule which corresponds to a surface concentration of ca. $2.648{\cdot}10^{13}$ molecules/cm^2. As demonstrated in Fig. 4.40b the angle between the vectors $\overline{e_2}$ of Phase III and $\overline{g_1}$ of Phase V found to be 180° - 164° = 16°.

	P_I	P_{II}	P_{III}	P_{IV}	P_V
lattice constants [± 0.05nm]	c_1 = 2.02 c_2 = 2.04	d_1= 2.23 d_2 = 2.03	e_1 = 2.10 e_2 = 3.87	f_1 = 1.95 f_2 = 2.11	g_1= 2.07 g_2 = 1.88
angle [± 1°]	106°	92°	72°	78°	76°
molecule rotation [α ± 1°]	+30° vs $\bar{c}_1$	-13° vs $\bar{d}_2$	±32° vs $\bar{e}_1$	-15° vs $\bar{f}_1$	+50° vs $\bar{g}_1$
surface concentration [molecules/cm^2]	$2.525{\cdot}10^{13}$	$2.221{\cdot}10^{13}$	$2.588{\cdot}10^{13}$	$2.485{\cdot}10^{13}$	$2.648{\cdot}10^{13}$

Table 3. Parameters of individual phases.

Table 3 summarizes the relevant parameters of all ordered H_2TTMAPP structures on the I/Au(100) surface. From the resultant layer symmetry and orientation of the H_2TTMAPP molecule of each phase, representative models are proposed in Fig. 4.42. The surface concentration of the porphyrin phases within the monolayer of H_2TTMAPP on I(2√2 x p√2)/Au(100) decreases in the sequence: P_V>P_{III}>P_{IV}>P_{II}. This results in different surface concentrations suggesting a competition between these phases like in the case of H_2TMPyP molecules. As presented in subsection 4.3.1 within the monolayer potential range the porphyrin molecules do not undergo any redox process, i.e. no electron transfer process occurs. Therefore, the observed changes are caused only by a variation of the interaction between the porphyrin molecules and the substrate. In order to check in which potential regime the Phases II-V are stable and if there is any influence from the surface concentration potentiodynamic STM measurements were again carried out. Furthermore, a semi-reversibility of the third regime in anodic direction will be presented.

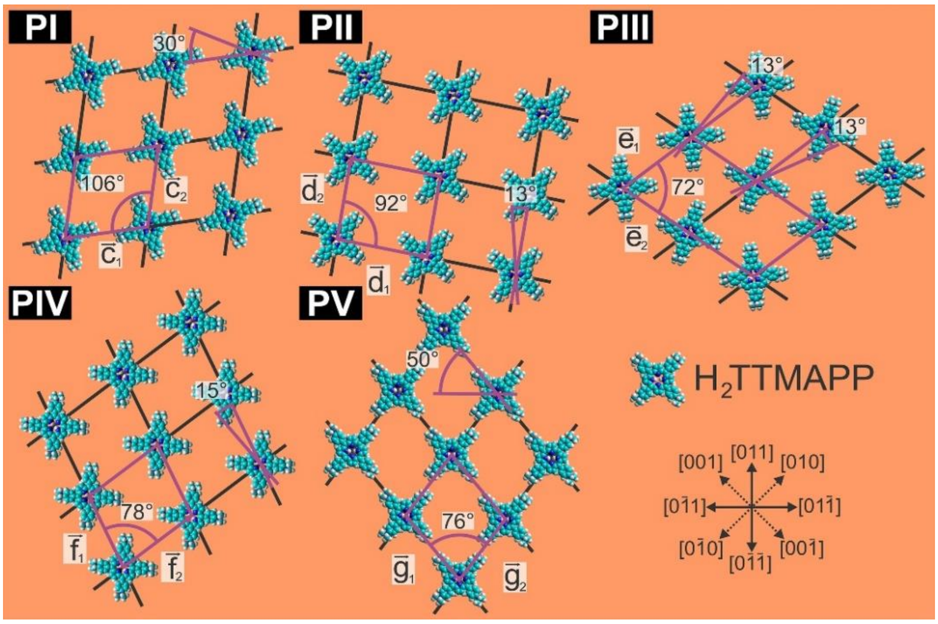

Figure 4.42: Schematic models of five ordered $H_2TTMAPP$ molecular phases on the I/Au(100) surface, with the corresponding vectors of the unit cells and the angles between them.

4.3.2.2.1 Potentiodynamic STM measurements.

The potentiodynamic STM measurements are presented in the five sets of images shown in Figs. 4.37; 4.44; 4.45; 4.46; 4.47. The series of images in Figures 4.44; 4.45; 4.46; 4.47 and 4.53; 4.54 from the section 4.3.2.3.1 are part of one potentiodynamic STM experiment which is presented as a movie (movie4_10fps.mp4) attached on CD to this thesis. It shows a direct correlation of the changes observed on the surface by the STM due to the applied electrode potential in anodic and cathodic direction to the cyclic voltammetry curve. Figure 4.43 shows a first frame of the movie4_10fps.mp4. On the left side of Fig. 4.43 is an

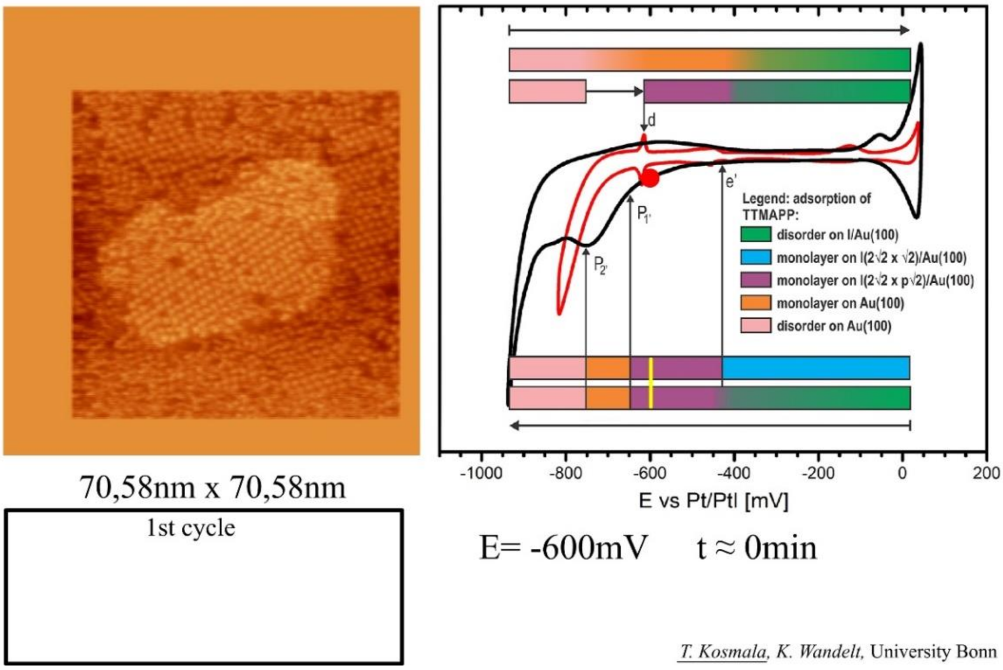

Figure 4.43: First frame of the movie4_10fps.mp4.

STM movie composed from 402 STM images taken one after another. The time needed to obtain one image and start the next one was around 30s, this means that the observed changes on the surface in the potentiodynamic STM measurement were continuously recorded in approximately 201min. The time meter is located on the right side under the CV plot (see Fig. 4.43) and it starts from t ≈ 0min and changes every 5min. The movie is exported with the speed of 10fps (frame per second), which with 402 frames gives a total time of 80.3s. The electrode potential at which each STM image is recorded is situated on the left of the time meter. Furthermore, on the CV plot (which is the same as in Fig. 4.34a) a red dot placed on the black curve moves along it showing the change of the electrode potential in anodic or cathodic direction. Moreover, on the coloured bars which representing the regimes of adsorption of the H_2TTMAPP molecules a yellow line is placed and shows exactly in which interval the STM images are taken. In the black rectangle essential informations are displayed describing the characteristic changes on the surface.

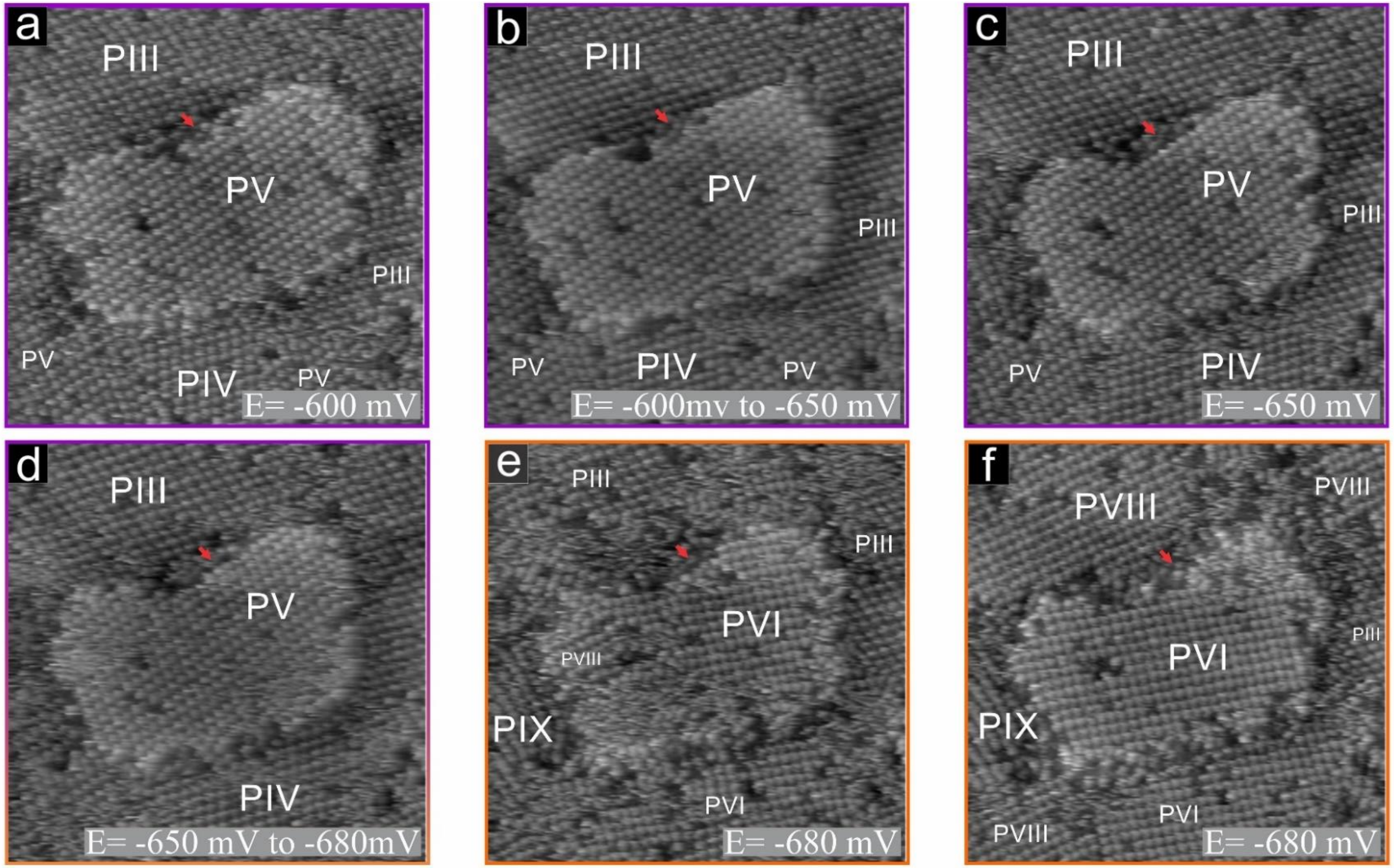

Figure 4.44: Potential induced phase transition of the molecular adlayer on iodine modified Au(100) electrode surface, STM series: 70.58nm x 70.58nm; a) I_t = 1nA, U_b = -460mV; b) I_t = 1nA, U_b = -402mV; c) I_t = 1nA, U_b = -402mV; d) I_t = 1nA, U_b = -365mV; e) I_t = 1nA, U_b = -365mV; f) I_t = 1nA, U_b = -365mV.

The potentiodynamic STM measurements presented in the movie4_10fps.mp4 started with the preparation of a highly ordered iodine layer that was first checked by STM (see Section. 3.2.2.2). Then this iodine-modified Au(100) surface was exposed to a 5mM H_2SO_4 + 1mM KI solution containing 0.01mM H_2TTMAPP in order to adsorb the porphyrin molecules. STM measurements were carried out just after the electrolyte exchange (in the I(2√2 x p√2) regime at the electrode potential -600mV vs Pt/PtI) immediately showing the porphyrin adsorption on top of the I/Au(100) substrate. From the starting point the electrode potential was gradually changed in cathodic direction. When the potential reached -850mV vs Pt/PtI the potential sweep was reversed into anodic direction and STM images were continuously recorded till -200mV vs Pt/PtI, were the electrode potential was changed in cathodic direction. Then the potential was systematically decreased down to -780mV vs Pt/PtI. Finally, from the electrode potential -780mV the potential was suddenly changed in anodic direction to -600mV vs Pt/PtI.

During this whole experiment one and a half cycle of the behaviour of H_2TTMAPP molecules on the I/Au(100) surface depending on applied electrode potential was recorded. Furthermore, the movie presents direct confirmation of the reversibility and semi-reversibility of the H_2TTMAPP structures on the I/Au(100) surface.

Figure 4.37 presented in section 4.3.2.1.1 shows a potential dependent series of STM images starting from the monolayer regime (blue colour in Fig. 4.34) at -400mV vs Pt/PtI. When the electrode potential is changed from -400mV to -450mV vs Pt/PtI a phase transition is observed along with the appearance of three molecular structures (P_{II}, P_{III} and P_{IV}) of the monolayer on (2√2 x p√2)/Au(100). This phase transition was related to the change in the iodine lattice from the structure (2√2 x √2) to (2√2 x p√2) and corresponds to the cathodic peak e' in the cyclic voltammonogram in Fig. 3.12. Further decrease of the working potential leads to disappearance of Phase II and appearance of Phase V (series of images not shown here) at around -600mV vs Pt/PtI. An even further decrease of the electrode potential is presented in Fig. 4.44a-f. These STM images are selected frames from movie4_10fps.mp4 covering the time from 2.5s to 7.7s (1st cycle) of the film. The first STM image in Fig. 4.44 recorded at -600mV vs Pt/PtI shows three phases P_{III}, P_{IV} and P_V. For these phases no significant changes are observed until the electrode potential reaches the cathodic peak $P_{1'}$ at -660mV vs Pt/PtI (see Fig. 4.43d-e). Peak $P_{1'}$ was assigned from the CV measurements (see Sec. 4.3.1) to desorption of iodine from the surface. Moreover, desorption of the iodine layer from the surface induces a phase transition and new ordered molecular structures are observed from the third regime (see Fig. 4.44d-e).

In order to present the semi-reversibility in the anodic direction of the second regime two series of images are presented. The first series shown on Figure 4.45 starts in the monolayer regime of H_2TTMAPP molecules on the iodine-free Au(100) surface at the potential -680mV vs Pt/PtI, where four porphyrin structures are observed. The STM images in Fig. 4.45 are selected frames from movie4_10fps.mp4 and cover the time from 23.7s to 42.1s (1st cycle) of the movie. Starting from the potential -680mV vs Pt/PtI the electrode potential was carefully scanned in the anodic direction. No drastic changes were observed till the electrode potential reached -400mV vs Pt/PtI (see Fig. 4.45e). At this potential we start to observe a phase transition from the orange regime to a disordered H_2TTMAPP regime on the I/Au(100) surface (green colour). Moreover, an oxidative gold dissolution reaction process starts to take place on the step edges at the potential ca. -350mV vs Pt/PtI. Changing the electrode potential even further in the anodic direction leads to an increasing disordering of the porphyrin molecules on the surface and increases the rate of the GDR process (see Fig. 4.45f). In this case we observe an inhibiting effect of the organic layer on the readsoption of iodine cations which is shifted toward positive potentials. The presented inhibiting effect of the organic layer on the readsoption of iodide cations in Fig. 4.45 can be assigned to the electrostatic interaction between the H_2TTMAPP molecules and the gold surface. Furthermore, re-adsorption of iodine ions leads to disordering of the porphyrin layer which favores the GDR process. Comparing the starting potential of an oxidative gold dissolution reaction for a monolayer regime (-150mV vs Pt/PtI) and the disordered regime (-350mV vs Pt/PtI) we can conclude that disordered H_2TTMAPP molecules promote the GDR process (see Fig. 4.36 and Fig. 4.45).

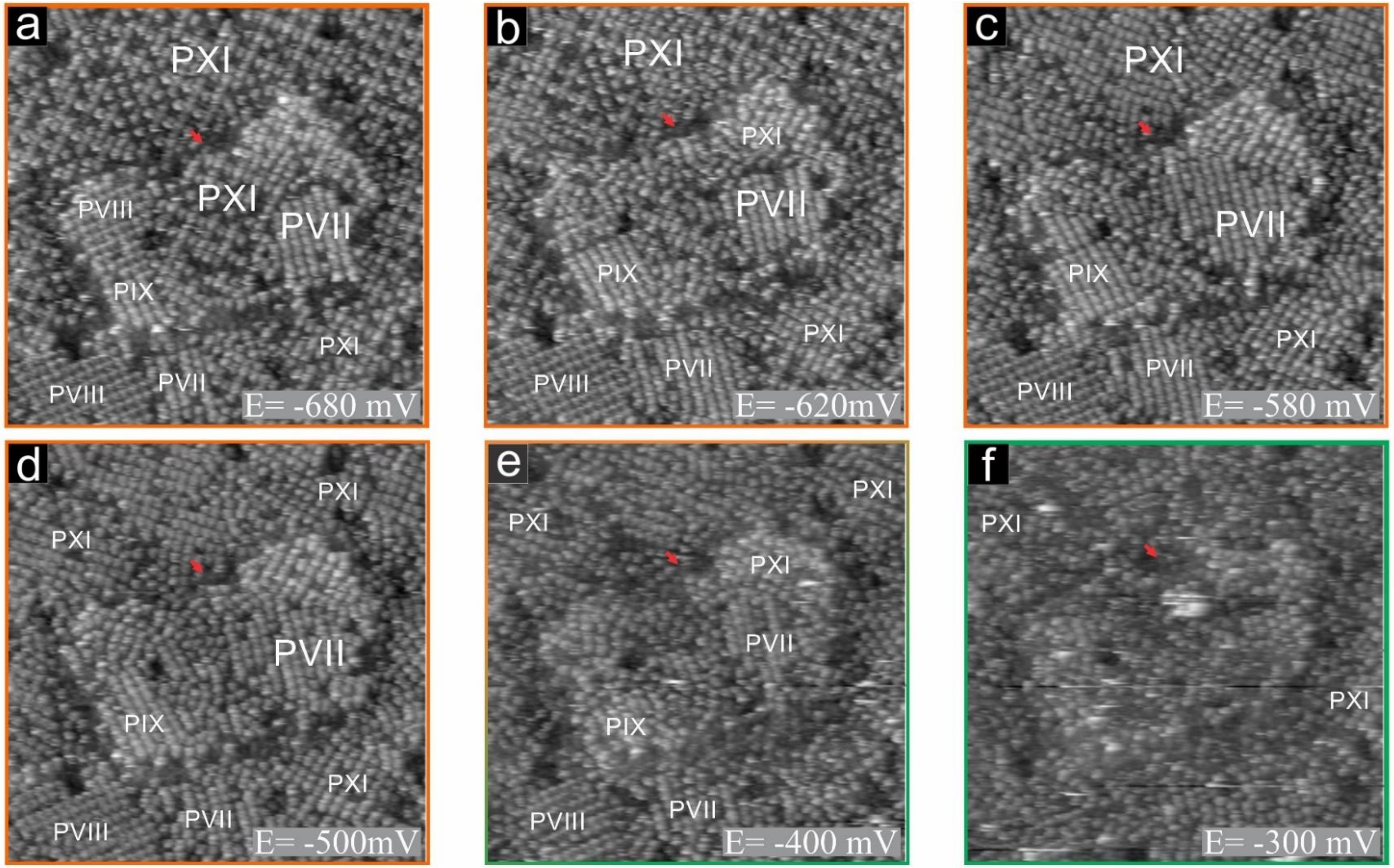

Figure 4.45: Potential induced phase transition of the molecular adlayer on iodine modified Au(100) electrode surface, STM series: 70.58nm x 70.58nm; a) I_t = 1nA, U_b = -338mV; b) I_t = 1nA, U_b = -370mV; c) I_t = 1nA, U_b = -447mV; d) I_t = 1nA, U_b = -502mV; e) I_t = 1nA, U_b = -571mV; f) I_t = 1nA, U_b = -649mV.

The second series shown on Figure 4.46 starts in the disorder regime on the Au(100) surface (beige colour) at the electrode potential -780mV vs Pt/PtI. The STM images in Fig. 4.46 are selected frames from movie4_10fps.mp4 and cover the time from 71.3s to 80.4s (2st cycle) of the film. In this situation from the working potential -780mV vs Pt/PtI, the electrode potential was suddenly changed to the electrode potential of -600mV vs Pt/PtI (see Fig. 4.46b), which is the regime where iodine ions re-adsorb on the surface in the *absence* of porphyrin species in the electrolyte. This fast change in electrode potential prevents the formation of an ordered porphyrin layer on the gold surface, which has an inhibiting effect on the readsoption of iodide ions, as was presented in the Fig. 4.45. In the next STM images (see Fig. 4.45c-f) in which the electrode potential was kept at -600mV vs Pt/PtI we observe a process of ordering of the three phases (namely: P_{II}, P_{III} and P_{IV}) from the second regime.

The last series of potentiodynamic STM images shown in Figure 4.47 starts in the disordered H_2TTMAPP regime on the I/Au(100) surface (green colour) at an electrode potential of -300mV vs Pt/PtI. These STM images in Fig. 4.47 are selected frames from movie4_10fps.mp4 and cover the time from 44.7s to 57.4s (1st cycle) of the film. The working potential -300mV vs Pt/PtI was changed in negative direction. When the potential reached -400mV vs Pt/PtI we start observing ordering of phases from the second regime (namely P_{II} and P_{III}) and the redeposition of gold atoms which takes place on the step edges of the island (see Fig. 4.47c). From the change of the shape of the island we can observe that the redeposition process is stopped at an electrode potential of -450mV vs Pt/PtI. During further decreasing of the working potential no significant changes of shape were observed anymore (see Fig. 4.47d-f). Although reducing the electrode potential and time improves ordering of the porphyrin phases from the second regime (violet colour).

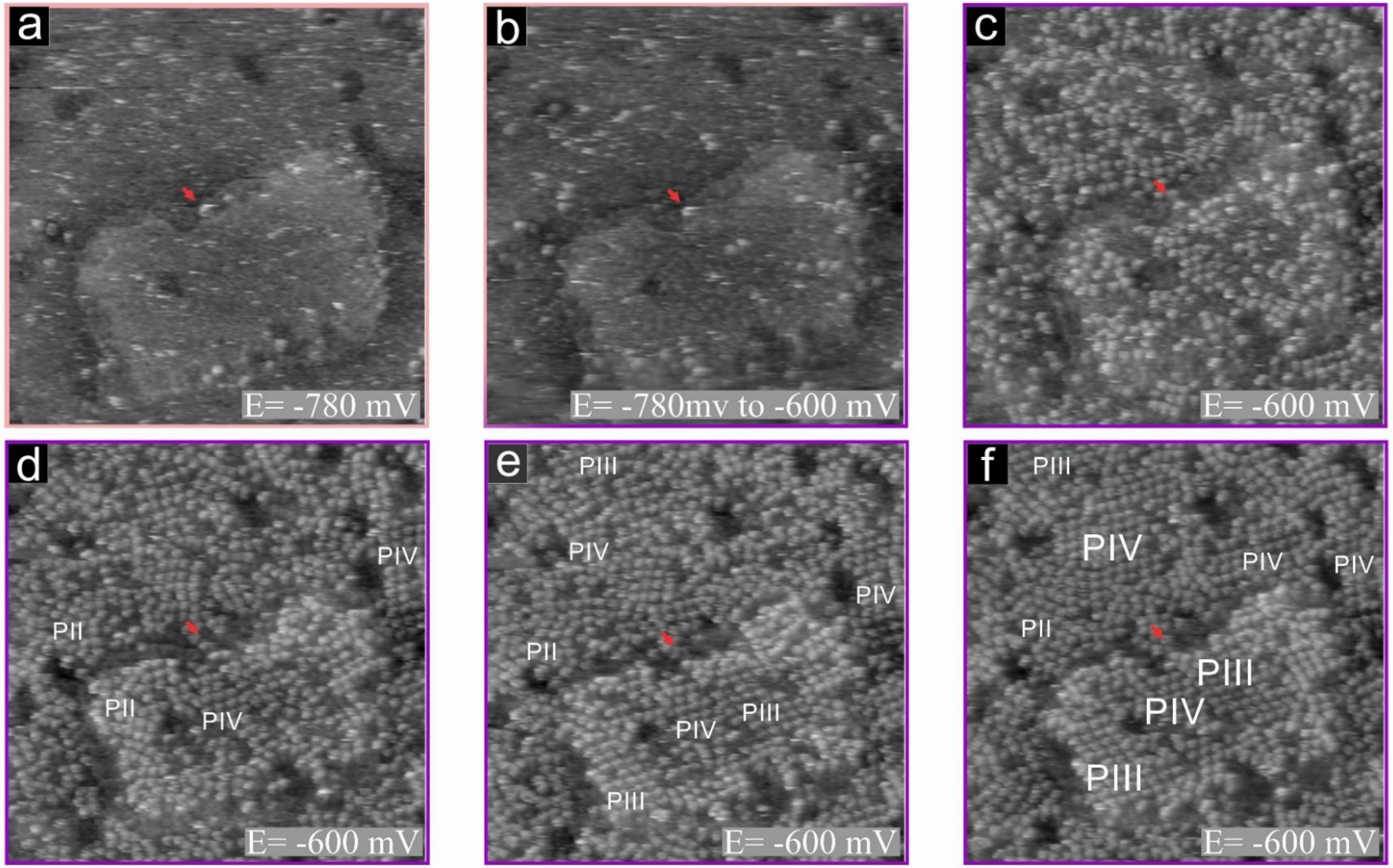

Figure 4.46: Potential induced phase transition of the molecular adlayer on iodine modified Au(100) electrode surface, STM series: 70.58nm x 70.58nm; a) I_t = 1nA, U_b = -320mV; b) I_t = 1nA, U_b = -430V; c) I_t = 1nA, U_b = -430mV; d) I_t = 1nA, U_b = -430mV; e) I_t = 1nA, U_b = -430mV; f) I_t = 1nA, U_b = -430mV.

It should be noted that the phase transitions between the first and the second regime, and between the second and third regime (Fig. 4.37 and 4.44, respectively) were observed essentially instantaneously upon changing the electrode potential. These phase transitions are driven by changes of the iodine structures, namely first to the change in the iodine lattice from the structure (2√2 x √2) to (2√2 x p√2) corresponding to the cathodic peak e' in the cyclic voltammogram in Fig. 3.12, and secondly the desorption of iodine from the surface which is related to the cathodic peak $P_{1'}$. Instead, in the series of images from Fig. 4.45, 4.46 and 4.47 the changes between the regimes are slow and not observed immediately upon changing the electrode potential. Furthermore, besides disappearance of Phase II and appearance of Phase V (which have the lowest and highest surface concentration in the second regime, namely $2.221 \cdot 10^{13}$ molecules/cm^2 and $2.648 \cdot 10^{13}$ molecules/cm^2) at the electrode potential ca. -600mV vs Pt/PtI there was no competition observed between H_2TTMAPP phases (P_{II}-P_V) despite to their different surface concentrations like in the case of H_2TMPyP molecules. From these observation we can conclude that the interaction between the H_2TTMAPP molecules and the iodine-modified gold is stronger than that for the H_2TMPyP molecules which manifests itself also in the reduced mobility of the H_2TTMAPP molecules and a longer ordering process of the H_2TTMAPP molecules.

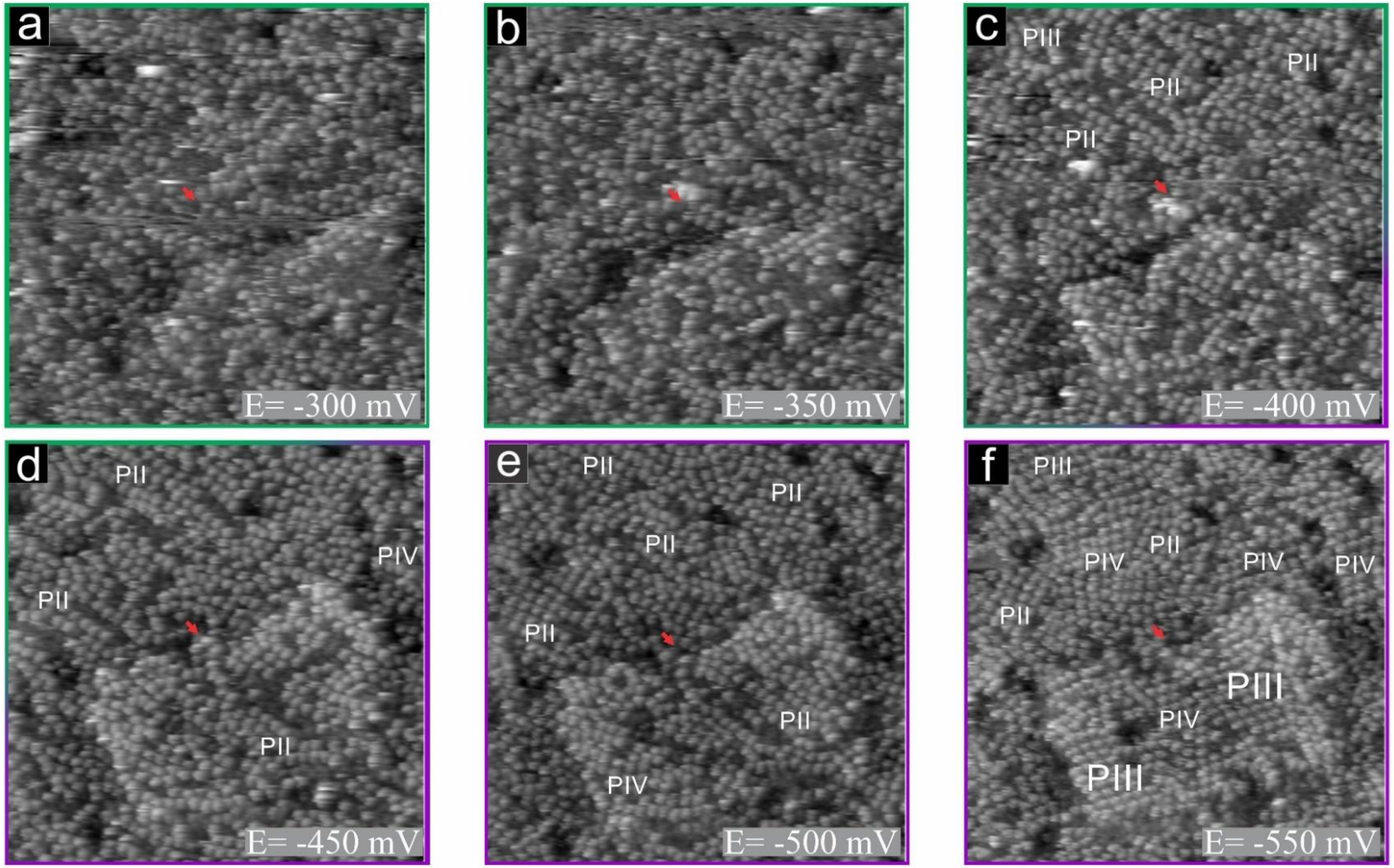

Figure 4.47: Potential induced phase transition of the molecular adlayer on iodine modified Au(100) electrode surface, STM series: 70.58nm x 70.58nm; a) I_t = 1nA, U_b = -700mV; b) I_t = 1nA, U_b = -685V; c) I_t = 1nA, U_b = -641mV; d) I_t = 1nA, U_b = -605mV; e) I_t = 1nA, U_b = -532mV; f) I_t = 1nA, U_b = -502mV.

4.3.2.3 Monolayer adsorption of H_2TTMAPP on Au(100) surface after I-desorption

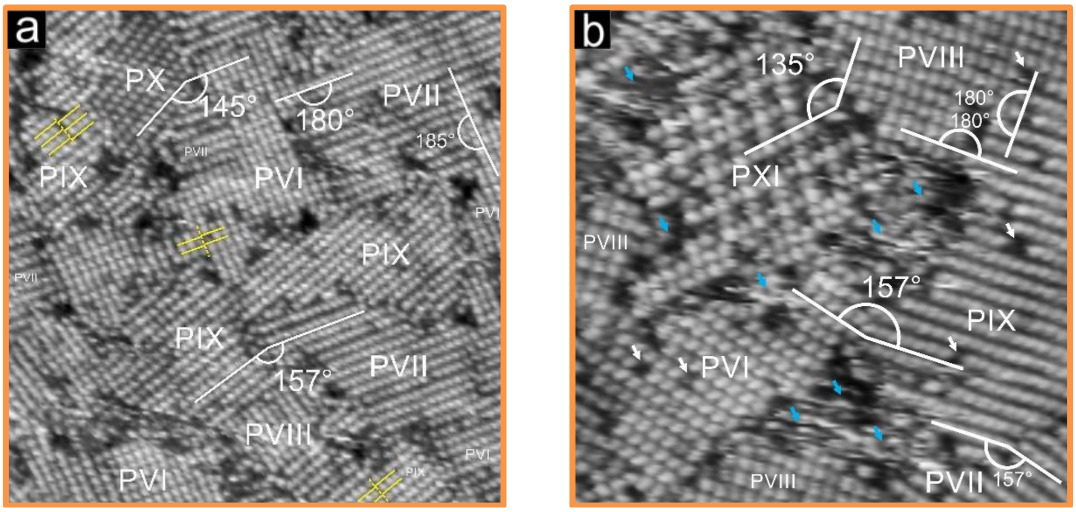

Figure 4.48: Ordered H_2TTMAPP adlayer on an iodine-free Au(100) electrode in the monolayer regime on I-free Au(100) surface. a) 121nm x 121nm, I_t = 1nA, U_b = -175mV, E = -700mV vs Pt/PtI, b) 69.14nm x 69.14nm, I_t = 1nA, U_b = -197mV, E= -700mV vs Pt/PtI.

The measurements started again with the preparation of a highly ordered iodine layer that was first checked by STM (see Section. 3.2.2.2). Then this iodine-modified Au(100) surface was exposed to a 5mM H_2SO_4 + 1mM KI solution containing 0.01mM H_2TTMAPP in order to adsorb the porphyrin molecules. STM measurements were carried out just after the electrolyte exchange (in the $I(2\sqrt{2}$ x $p\sqrt{2})$ regime) immediately showing the porphyrin adsorption on top of the I/Au(100) substrate. Next the electrode potential was changed to the working potential where an adsorption of monolayer porphyrin molecules on iodine-free (1x1) Au(100) surface occurs. This regime in cathodic direction is located between peak pair $P_{1'}$ (desorption of iodine and phase transition) and $P_{2'}$ (reduction and desorption of H_2TTMAPP molecules). In anodic direction readsoption of individual molecules starts at ca. -750mV vs Pt/PtI and an ordered layer is re-established at ca. -700mV vs Pt/PtI and this ordered overlayer inhibits I-readsorption until ca. -400mV vs Pt/PtI.

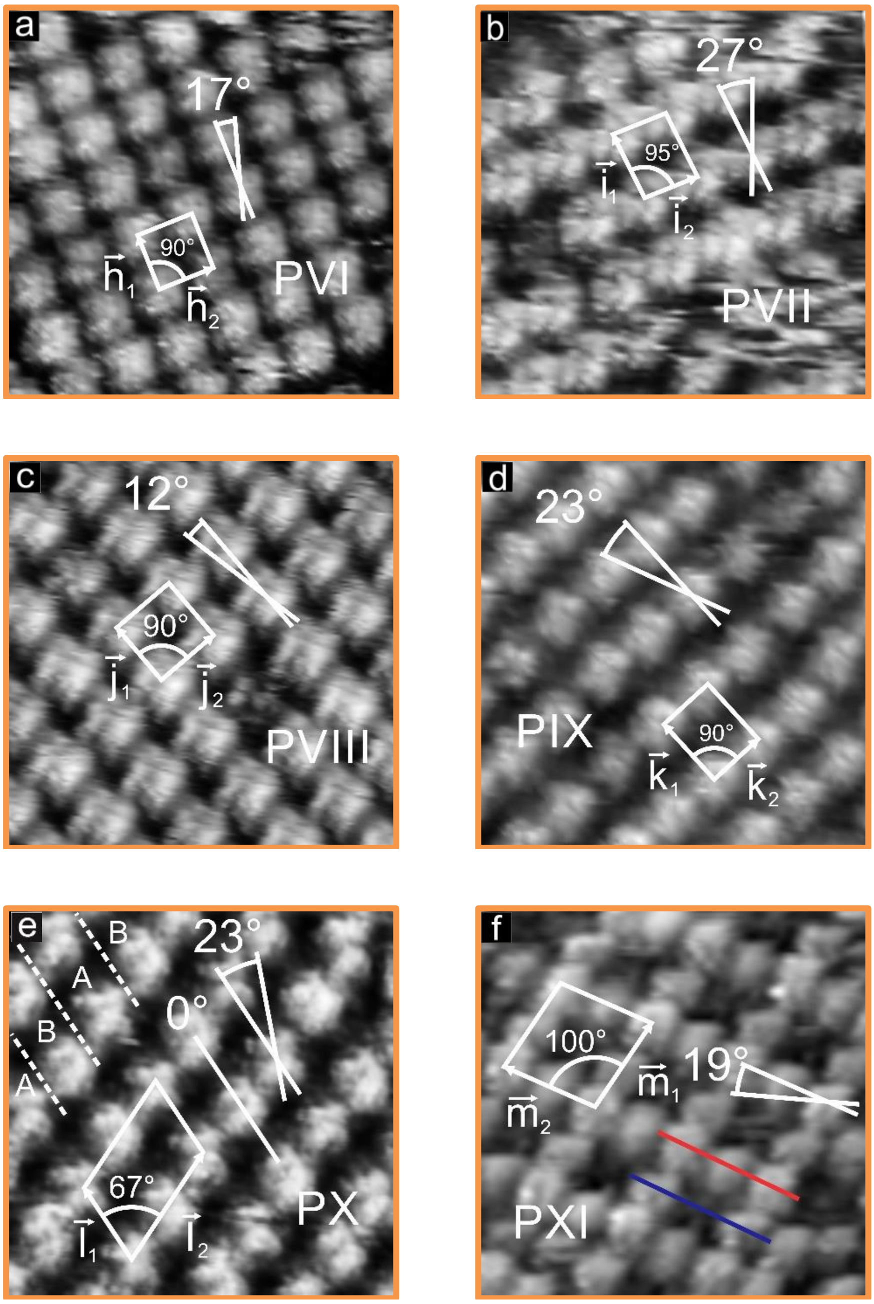

Figure 4.49: High-resolution images of an ordered H_2TTMAPP adlayer on an iodine-modified Au(100) electrode in the monolayer regime on iodine-free Au(100) surface. a) 10.50nm x 10.50nm, I_t = 1nA, U_b = -270mV, E= -700mV vs Pt/PtI. b) 10.40nm x 10.40nm, I_t = 1nA, U_b = -210mV, E= -700mV vs Pt/PtI; c) 9.50nm x 9.50nm, I_t = 1nA, U_b = -236mV, E= -700mV vs Pt/PtI; d) 10.50nm x 10.50nm, I_t = 1nA, U_b = -271mV, E= -700mV vs Pt/PtI; e) 9.50nm x 9.50nm, I_t = 1nA, U_b = -238mV, E= -700mV vs Pt/PtI; f) 12.80nm x 12.80nm, I_t = 1nA, U_b = -321mV, E= -700mV vs Pt/PtI.

Typical large scale STM images acquired at -700mV vs Pt/PtI showing the surface structure of the $H_2TTMAPP$ adlayer on top of the iodine-free (1x1) Au(100) surface are displayed in Fig. 4.48. It is seen that the molecules are self-assembled into an ordered layer of molecular rows covering the atomically flat terraces. Furthermore, careful examination of Fig. 4.48a-b yields the coexistence of six porphyrin phases, namely PVI - PXI. Within each phase translation domains were observable. Exemplary translational domains are shown in Figure 4.48a which are denoted with yellow solid lines and the domain boundary between them marked by dashed yellow lines. Moreover, on all images in this regime missing molecules within the molecular layer can be detected, which are represented by dark spots on the STM images (marked by small white arrows in Fig.4.48b). Furthermore, between the domain boundaries of the $H_2TTMAPP$ phases regions of disorder can been seen (marked by small blue arrows in Fig. 4.48b).

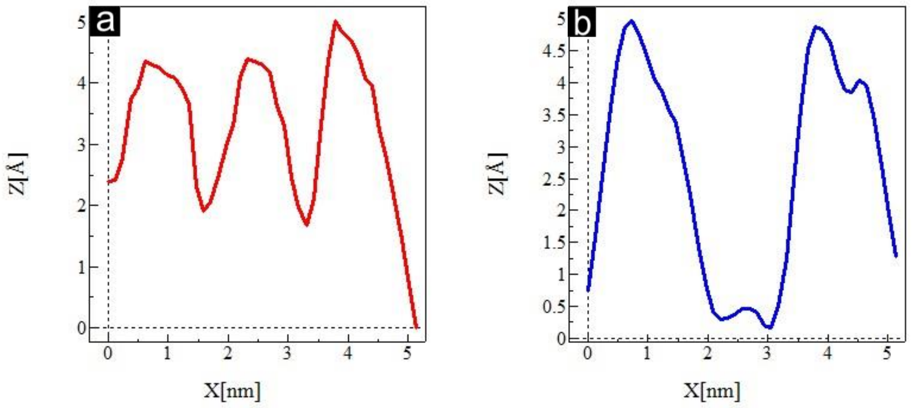

Figure 4.50: Cross section along the a) red line and b) blue line in Fig. 4.47f.

High resolution STM images as seen in Fig. 4.49a-f reveal more details about the molecular arrangement within each phase of the porphyrin layer. The shape of the individual molecules agrees with their quadratic structure which, in turn, indicates that the molecules are lying flat on the surface. The porphyrin molecules within each phase are arranged in rows. The lattice unit-cell for the Phase VI can be drawn as show in Figure 4.49a with the lattice parameters of $h_1 = 1.55 \pm 0.05$nm and $h_2 = 1.55 \pm 0.05$nm with an angle of ca. 90° between them. Individual molecules within one row are rotated by about +17° with respect to the row direction parallel to the $\overline{h_1}$

vector. Each unit cell includes one H_2TMPyP molecule, which corresponds to a surface concentration of ca. $4.162 \cdot 10^{13}$ molecules/cm^2. Phase VII with its corresponding unit-cell is presented in Figure 4.48b. The lattice constants are i_1 = 1.55 ± 0.05nm and i_2 = 1.93 ± 0.05nm enclosing an angle of 95°. All molecules within one row are rotated with respect to the row direction along the $\overline{\iota_1}$ vector by about +27°. As in the case of Phase VI each unit cell includes one porphyrin molecule, consequently resulting in a surface concentration of ca. $3.356 \cdot 10^{13}$ molecules/cm^2. Furthermore, vectors $\overline{h_2}$ of Phase VI and $\overline{\iota_2}$ have the same value and direction. In the case of vectors $\overline{h_1}$ and $\overline{\iota_1}$ the angle between them is found to be 5° (see Fig. 48a). Phase VIII with denoted unit-cell is presented in Figure 4.49c. The lattice constants are j_1 = 1.63 ± 0.05nm and j_2 = 1.63 ± 0.05nm enclosing an angle of ca. 90°. Individual molecules within one row are rotated by about -12° with respect to the row direction parallel to the $\overline{\jmath_1}$ vector. The unit-cell of Phase VIII as indicated in Fig. 4.49c contains one porphyrin molecule which corresponds to a surface concentration of ca. $3.764 \cdot 10^{13}$ molecules/cm^2. Phase IX with its corresponding unit-cell is shown in Figures 4.49d. The nearest neighbour distance between porphyrin molecules of Phase IX were found to be k_1 = 1.63 ± 0.05nm and k_2 = 2.04 ± 0.05nm with an angle of about 90°. In this case the symmetry axes of the porphyrin molecules are rotated with respect to the molecular row direction parallel to $\overline{k_1}$ by an angle of about -23°. Furthermore, the $\overline{\jmath_1}$ and $\overline{\jmath_2}$ vectors are parallel to the $\overline{k_1}$ and $\overline{k_2}$ vectors, respectively, and $\overline{\jmath_1}$ and $\overline{k_1}$ have the same value (see Fig. 4.48b). Moreover, Fig. 4.48a shows Phase VII and IX with the angle of ca. 180° - 157°= 23° between the vectors $\overline{\iota_2}$ and$\overline{k_2}$. Each unit-cell of Phase IX contains one molecule which corresponds to a surface concentration of ca. $3.007 \cdot 10^{13}$ molecules/cm^2. The unit cell of Phase X is presented in the Figure 4.49e. The lattice constants are l_1 = 2.08 ± 0.05nm and l_2 = 3.12± 0.05nm enclosing an angle of about 67°. We can distinguish two different types of rows (denoted A and B in Fig. 4.49e). Molecules within one and the same row are all rotated in the same direction but the sense of rotation is different in A and B rows. The rotation of the individual molecules within one row is about +23° or 0° with respect to the row direction parallel to the $\overline{l_1}$ vector. Each unit cell includes two H_2TTMAPP molecules, which corresponds to a surface concentration of ca. $3.348 \cdot 10^{13}$ molecules/cm^2. As demonstrated in Fig. 4.48a the angle between the vectors $\overline{h_2}$ of Phase VI and $\overline{l_2}$ is found to be 180° - 145° = 35°.

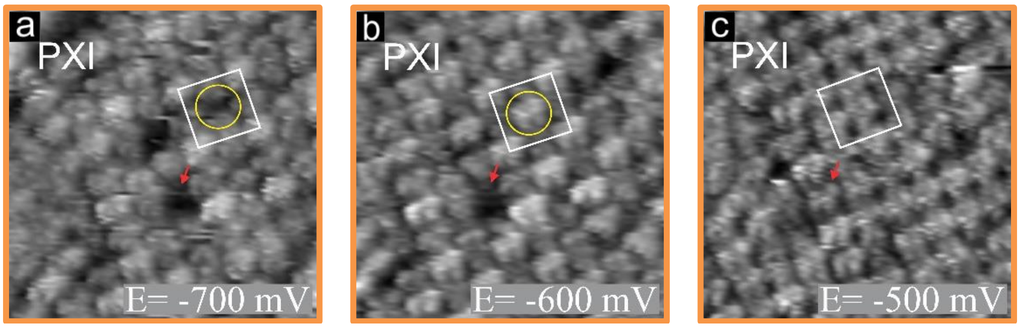

Figure 4.51: Potential induced adsorption of missing molecules in the Phase XI; a) 17.70nm x 17.70nm, I_t = 1nA, U_b = -283mV, E= -700mV vs Pt/PtI. b) 17.70nm x 17.70nm, I_t = 1nA, U_b = -245mV, E= -600mV vs Pt/PtI; c) 17.70nm x 17.70nm, I_t = 1nA, U_b = -236mV, E= -500mV vs Pt/PtI.

Finally the unit-cell of Phase XI acquired at the electrode potential -700mV vs Pt/PtI can be drawn as shown in Figure 4.49f. The lattice constants are m_1 = 3.22 ± 0.05nm and m_2 = 3.17 ± 0.05nm enclosing an angle ca. 100°. All molecules within one row are rotated with respect to the row direction parallel to the $\overline{m_2}$ vector by about -19°. An interesting observation is that at this electrode potential we observe a missing molecule in the centre of the unit-cell (see Fig. 4.48b). This observation is supported with the profile lines denoted by the red and blue line on the Fig. 4.49f and presented in Figure 4.50a-b, respectively. Furthermore, the series of images presented in the Figure 4.51 shows that changing of working potential in anodic direction from -700mV to -500mV vs Pt/PtI leads to adsorption of H_2TTMAPP molecules in the empty spaces. Moreover, as can be seen on the Figures 4.49f and 4.51a-b the molecules at the corners of the unit-cell are brighter than the molecules between them. Therefore, the surface concentration changes depending on the electrode potential from ca. $2.984 \cdot 10^{13}$ molecules/cm^2 (where each unit-cell include three molecules) to ca. $3.979 \cdot 10^{13}$ molecules/cm^2 (where each unit-cell contain four molecules).

	P_{VI}	P_{VII}	P_{VIII}	P_{IX}	P_{X}	P_{XI}
lattice constants [± 0.05nm]	h_1 = 1.55 h_2 = 1.55	i_1= 1.93 i_2 = 1.55	j_1 = 1.63 j_2 = 1.63	k_1 = 1.63 k_2 = 2.04	l_1= 2.08 l_2 = 3.12	m_1= 3.22 m_2 = 3.17
angle [± 1°]	90°	95°	90°	90°	67°	100°
molecule rotation [α ± 1°]	+17° vs $\overline{h}_1$	+27° vs $\overline{d}_2$	-12° vs $\overline{j}_1$	-23° vs $\overline{k}_1$	+23° vs $\overline{l}_1$ or 0° vs $\overline{l}_1$	-19° vs $\overline{m}_2$
surface concentration [molecules/cm^2]	$4.162\cdot10^{13}$	$3.356\cdot10^{13}$	$3.764\cdot10^{13}$	$3.007\cdot10^{13}$	$3.348\cdot10^{13}$	$2.984\cdot10^{13}$ and $3.979\cdot10^{13}$

Table 4. Parameters of individual phases.

Table 4 summarizes the relevant parameters of all phases (P_{VI}-P_{XI}) observed in the regime of H_2TTMAPP adsorption on the iodine-free Au(100) surface. Based on the experimental results of the symmetry and orientation of the H_2TTMAPP molecules, a schematic model of the ordered H_2TTMAPP molecules is proposed for each phase in Fig. 4.52. The surface concentration of porphyrin molecules within the monolayer adsorption of H_2TTMAPP on Au(100) surface decreases in the sequence: P_{VI}>P_{XIb}>P_{VIII}>P_{VII}>P_{X}>P_{IX}>P_{XIa}, where P_{XIb} and P_{XIa} represent structures with four and three molecules in the unit-cell, respectively. Hence, the porphyrin molecules in the monolayer on Au(100) regime do not undergo any redox process, therefore, the changes which occur in the third regime are not caused by a variation in the chemical state of the porphyrin but by a variation of the interaction between the porphyrin molecules and the substrate. In order to check in which potential regime the Phases II-V are stable and if there is any influence from the surface concentration potentiodynamic STM measurements were carried out. Moreover, a structural correlation between the porphyrin adlayer and the substrate lattice underneath was done.

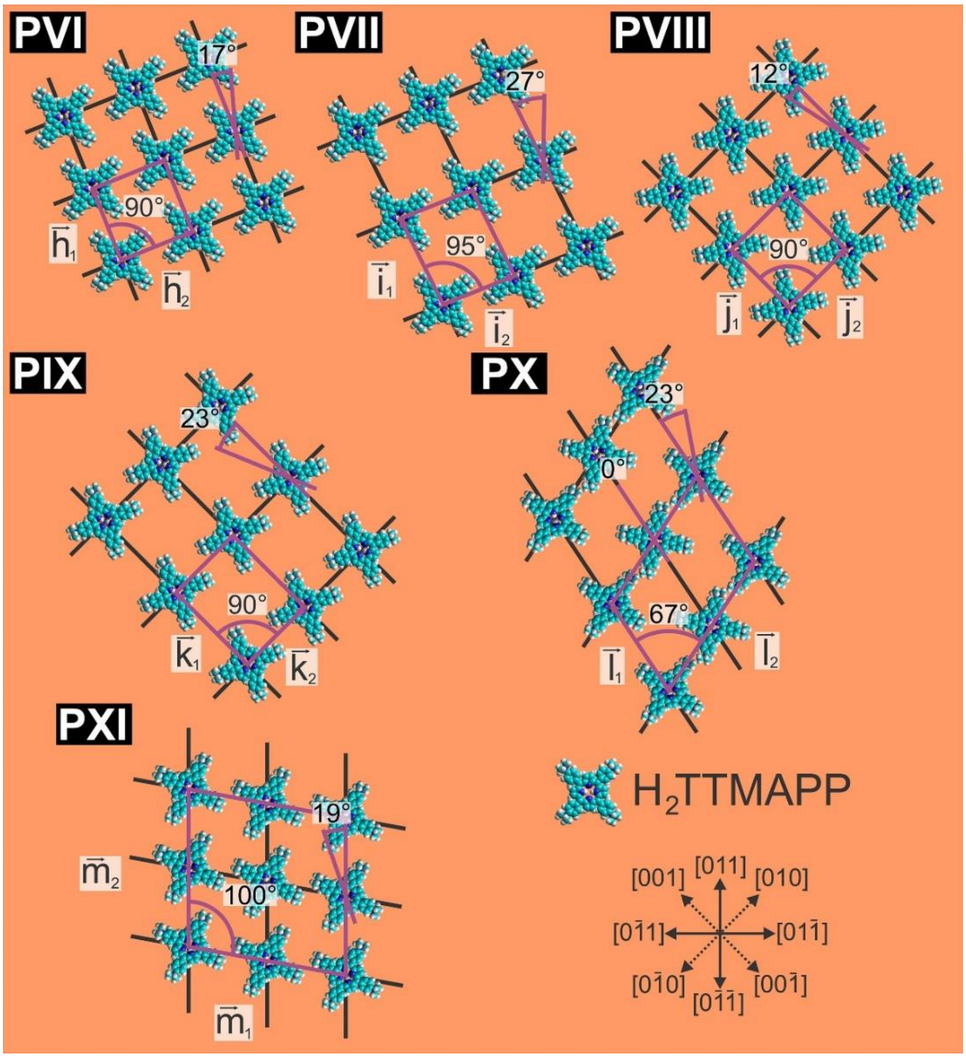

Figure 4.52: Schematic model of five ordered H_2TTMAPP molecular phases on iodine-free (1x1) Au(100) surface, with the corresponding vectors of the unit cells and the angles between them.

4.3.2.3.1 Potentiodynamic STM measurements.

The potentiodynamic STM measurements are presented in the four sets of images in Figs. 4.44; 4.45; 4.53 and 4.54. Figure 4.44 presented in section 4.3.2.2.1 belongs to the first cycle in the movie4_10fps.mp4 covering the time from 2.5s to 7.7s, shows a potential dependent series of STM images starting from the monolayer on $(2\sqrt{2}$ x $p\sqrt{2})$/Au(100) at -600mV vs Pt/PtI. When the electrode potential is changed from -650mV to -680mV vs Pt/PtI a phase transition is observed along with appearance of three molecular structures (P_{VI}, P_{VIII} and P_{IX}) of the monolayer on the I-free Au(100). This phase transition is related to the peak $P_{1'}$ and was assigned to desorption of iodine from the surface. An even further decrease of the electrode potential is presented in Fig. 4.53a-f. This series of images belongs to the second cycle in the movie4_10fps.mp4 covering the time from 65.9s to 71.2s. Figure 4.53a recorded at -680mV vs Pt/PtI shows six H_2TTMAPP phases observed in the monolayer regime on Au(100), namely: P_{VI}, P_{VII}, P_{VIII}, P_{IX}, P_X and P_{XI}. Comparing the images from Fig. 4.44f (from the 1st cycle of movie4_10fps.mp4) and 4.53a (from the 2nd cycle of movie4_10fps.mp4) suggests a random distribution of the H_2TTMAPP structures in the monolayer regime after phase transition from the monolayer on the $(2\sqrt{2} \times p\sqrt{2})$/Au(100). From the electrode potential -680mV vs Pt/PtI the potential was systematically decreased without significant changes on the surface (see Fig. 4.53b) until the potential reached -720mV vs Pt/PtI, where we start to observe at the domain boundaries a disordering of the porphyrin molecules on the Au(100) surface (see Fig. 4.53c). When the potential reaches the maximum of peak $P_{2'}$ at -750mV vs Pt/PtI a phase transition is observed to a disordered phase of porphyrin molecules (see Fig. 4.53d-e). As can be seen in the Figure 4.53f recorded at an electrode potential of -780mV vs Pt/PtI we can still observe on the surface mobile single molecules (denoted by white circles in Fig. 4.53f). Peak $P_{2'}$ was assigned from the CV measurements (see Sec. 4.3.1) to the first reduction of the H_2TTMAPP molecules and also to another surface process which from the potentiodynamic STM measurements can be assigned to the disordering of porphyrin molecules on the iodine-free gold surface. It seems that the first reduction of the H_2TTMAPP molecules and negative electrode potentials weaken the adsorbate-substrate interaction which causes an increase of the mobility of the porphyrin molecules on the iodine-free gold surface.

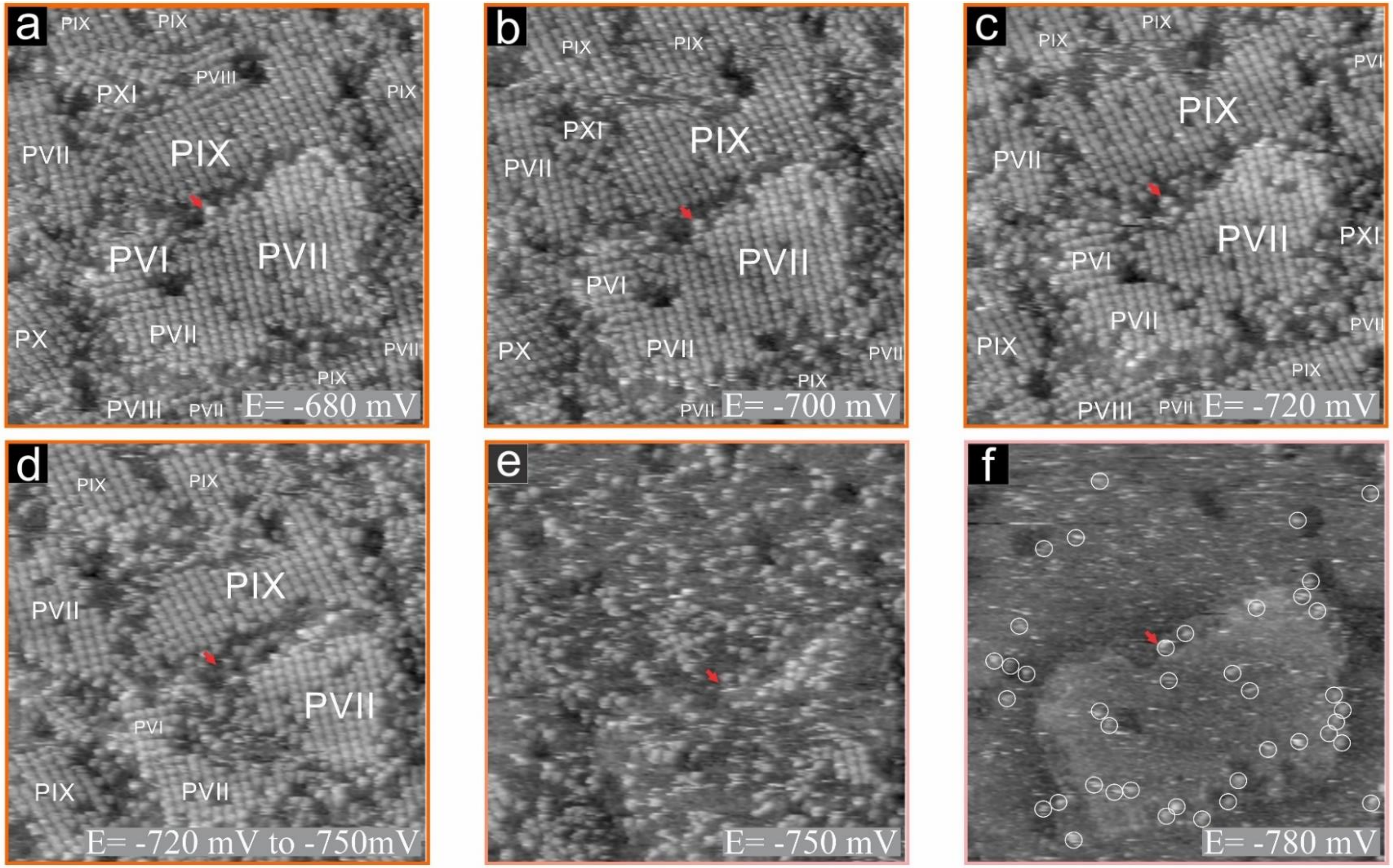

Figure 4.53: Potential induced phase transition of the molecular adlayer on iodine-free Au(100) electrode surface, STM series: 70.58nm x 70.58nm; a) I_t = 1nA, U_b = -313mV; b) I_t = 1nA, U_b = -313mV; c) I_t = 1nA, U_b = -322mV; d) I_t = 1nA, U_b = -320mV; e) I_t = 1nA, U_b = -320mV; f) I_t = 1nA, U_b = -320mV.

The next potential dependent series of STM images presented in Figure 4.54 belongs to the first cycle in the movie4_10fps.mp4 covering the time from 11.4s to 21.5s starting from the disordered regime on Au(100) at -850mV vs Pt/PtI (see Fig. 4.54a). Changing the electrode potential in anodic direction leads to an increase of the adsorbate-substrate interactions which in the first place reduce the mobility of the porphyrin molecules (see Fig. 4.54b-d) and in the end create a 2D condensed ordered H_2TTMAPP adlayer of the orange regime (see Fig. 4.54e-f). In Figures 4.54e-f we can distinguish four porphyrin phases, namely: P_{VII}, P_{VIII}, P_{IX} and P_{XI}. It should be noted that like in the case of phase transitions from the second to the third regime in cathodic direction the distribution of the H_2TTMAPP structures was random. Further increasing the electrode potential is presented in Fig. 4.45 (in the section 4.3.2.2.1) which belongs to the first cycle in the movie4_10fps.mp4 covering the time from 23.7s to 42.1s, shows a continuation of the series presented in Fig. 4.54 starting at the electrode potential -680mV vs Pt/PtI (see Fig. 4.44a) with four phases (P_{VII}, P_{VIII}, P_{IX} and P_{XI}). During increasing the working potential we observe a small change of the size of individual domains of distinguished structures (see Fig. 4.45a-d). Furthermore, as already described in the previous section by changing the electrode potential we observe an adsorption of H_2TTMAPP molecules in the empty spaces of the phase XI. When the electrode potential reaches -400mV vs Pt/PtI we observe a phase transition from the orange regime to a disordered H_2TTMAPP regime on the I/Au(100) surface (green colour) (see Fig. 4.45e). This change as explained in section 4.3.2.2.1, is caused by readsorption of the iodine ions.

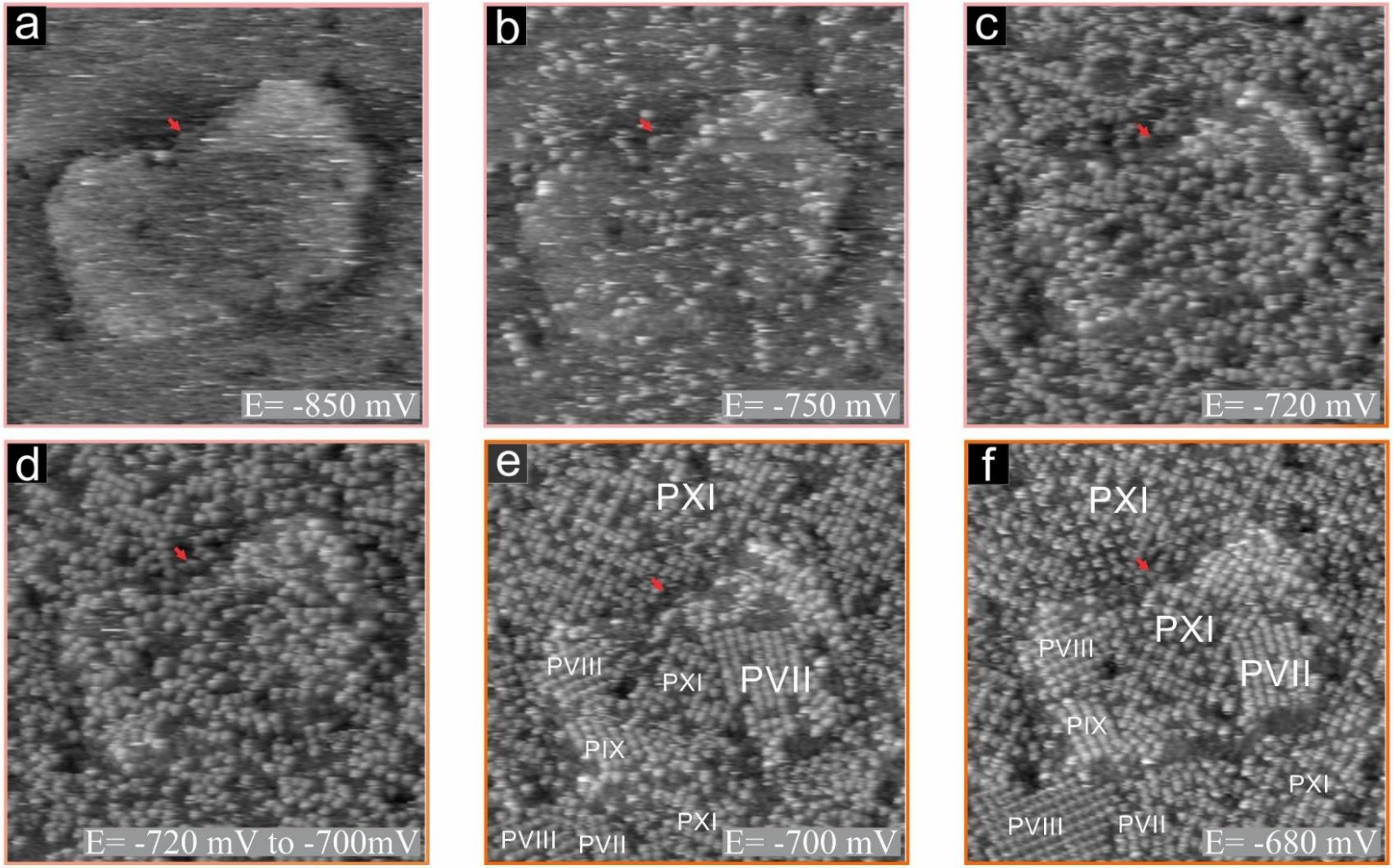

Figure 4.54: Potential induced phase transition of the molecular adlayer on iodine-free Au(100) electrode surface, STM series: 70.58nm x 70.58nm; a) I_t = 1nA, U_b = -244mV; b) I_t = 1nA, U_b = -314mV; c) I_t = 1nA, U_b = -314mV; d) I_t = 1nA, U_b = -338mV; e) I_t = 1nA, U_b = -338mV; f) I_t = 1nA, U_b = -338mV.

4.3.2.3.2 Structural correlation between porphyrin adlayer and the substrate lattice.

The structural relationship of the porphyrin adlayer and the gold lattice underneath is achieved by the same method that was applied for the H_2TMPyP molecules and is described in detail in subchapter 4.2.2.1.2. Figures 4.55, 4.57 and 4.59 show the porphyrin adlayer with phases in the monolayer adsorption of H_2TTMAPP on the Au(100) surface and their relationship to the gold lattice underneath. After close analysis of the images presented in Figure 4.55 for phases P_{VI} and P_{VII}, Figure 4.57 for phases P_{VIII} and P_{IX}, and in Figure 4.59 for phases P_X and P_{XI} it is possible to present accurate structure models of all porphyrin phases including structural relationship between them and the gold lattice underneath (see Fig. 4.56 for P_{VI} and P_{VII}, Fig. 4.58 for P_{VIII} and P_{IX} and Fig. 4.60 for P_X and P_{XI}).

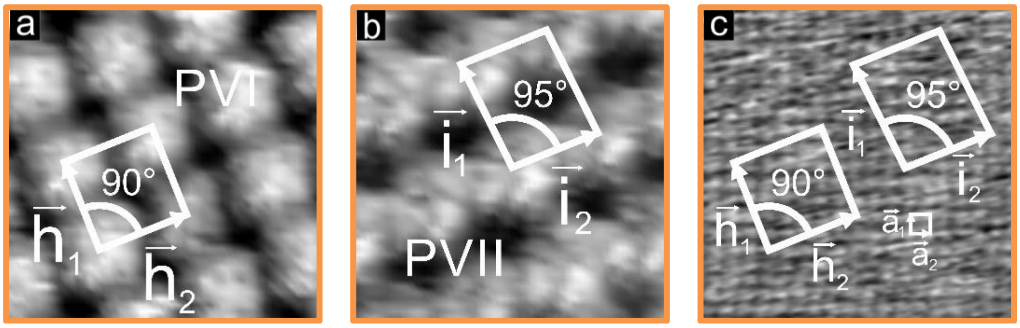

Figure 4.55: Structure correlation between the H_2TTMAPP layer of phases P_{VI} and P_{VII} with the underlying gold layer, porphyrin layer of phase VI (a) and phase VII (b) at high tunnelling bias, a) 5.30nm x 5.30nm, I_t = 1nA, U_b = -270mV, E= -700mV vs Pt/PtI; b) 5.30nm x 5.30nm, I_t = 1nA, U_b = -270mV, E= -700mV vs Pt/PtI; c) exemplary STM image of gold layer found underneath H_2TTMAPP layer at low tunnelling bias, 5.30nm x 5.30nm, I_t= 1nA, U_b = -17mV, E= -700mV vs Pt/PtI.

Phase VI and VII

Figure 4.55a-b shows the porphyrin adlayer with phases P_{VI} and P_{VII}, respectively, and in Fig. 4.55c an exemplary image of the gold lattice recorded underneath both structures. After close analysis of the images presented in Figure 4.55 it is possible to present again accurate structure models of the Phases VI and VII including the structural relationship between P_{VI} and P_{VII} and the gold lattice underneath (see Fig. 4.56). The H_2TTMAPP layer of Phase VI is described by vectors $\overline{h_1}$ and $\overline{h_2}$ with directions of $[0 \quad 7 \quad 3]$ and $[0 \quad 7 \quad \bar{3}]$, respectively, and Phase VII is described by vectors $\overline{\imath_1}$ and $\overline{\imath_2}$ with directions of $[0 \quad 1 \quad 3]$ and $[0 \quad 7 \quad \bar{3}]$, respectively. Furthermore, vectors $\overline{h_2}$ of Phase VI and $\overline{\imath_2}$ have the same value and direction. Moreover, the molecular rows of phase P_{VI} and P_{VII} do not follow any high symmetry direction of the underlying gold lattice. Furthermore, the molecular symmetry axis of individual molecules of phase P_{VI} and P_{VII} which are centered atop of gold atom do not follow any high symmetry direction of the underlying gold lattice. The unit cell for Phase VI $(\overline{h_1}, \overline{h_2})$ as depicted in Fig. 4.49a and Fig. 4.55a with the lattice parameters of h_1 = 1.55nm and h_2 = 1.55nm, enclosing an angle of 90°, contains one molecule and can be related to the gold lattice by the matrix:

$$\begin{pmatrix} \bar{h}_1 \\ \bar{h}_2 \end{pmatrix} = \begin{pmatrix} 5 & -2 \\ 2 & 5 \end{pmatrix} \begin{pmatrix} \bar{a}_1 \\ \bar{a}_2 \end{pmatrix}$$

On the basis of this model the surface coverage of the porphyrin adlayer is calculated and found to be 0.035 ML relative to the density of the gold layer, or $4.162 \cdot 10^{13}$ molecules/cm^2.

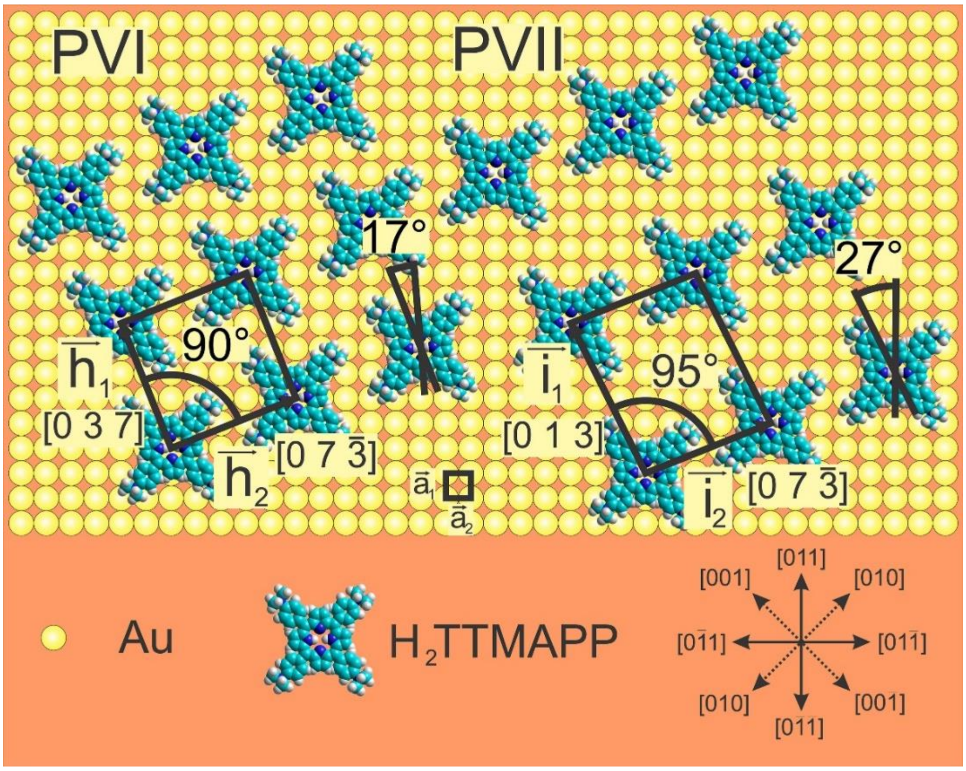

Figure 4.56: Structure model of the P_{VI} and P_{VII} on iodine modified Au(100) surface.

The unit cell for phase VII ($\bar{\imath}_1, \bar{\imath}_2$) as outlined in Fig. 4.49b and Fig. 4.55b with the lattice parameters of i_1 = 1.93nm and i_2 = 1.55nm, enclosing an angle of 95°, contains one molecule and can be related to the gold lattice by the matrix:

$$\begin{pmatrix} \bar{i}_1 \\ \bar{i}_2 \end{pmatrix} = \begin{pmatrix} 6 & -3 \\ 2 & 5 \end{pmatrix} \begin{pmatrix} \bar{a}_1 \\ \bar{a}_2 \end{pmatrix}$$

The molecular surface coverage is also calculated and found to be about 0.028 ML related to the gold lattice underneath or $3.356 \cdot 10^{13}$ molecules/cm^2.

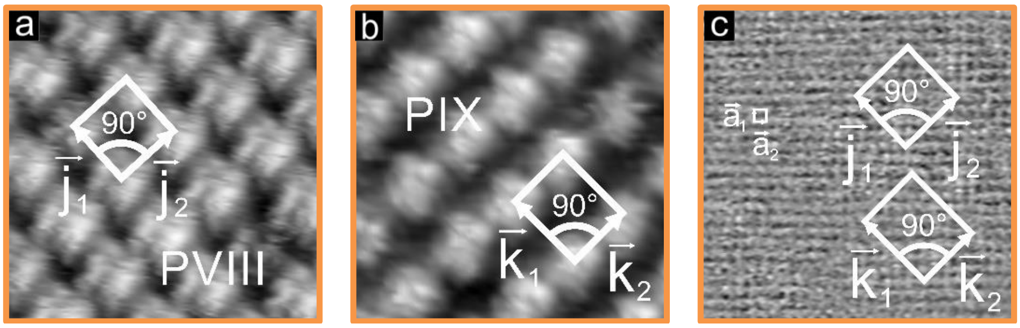

Figure 4.57: Structure correlation between the H_2TTMAPP layer of phases P_{VIII} and P_{IX} with the underlying gold layer, porphyrin layer of phase VI (a) and phase VII (b) at high tunnelling bias, a) 7.60nm x 7.60nm, I_t = 1nA, U_b = -236mV, E= -700mV vs Pt/PtI; b) 7.60nm x 7.60nm, I_t = 1nA, U_b = -271mV, E= -700mV vs Pt/PtI; c) exemplary STM image of gold layer found underneath H_2TTMAPP layer at low tunnelling bias, 7.60nm x 7.60nm, I_t= 1nA, U_b = -12mV, E= -700mV vs Pt/PtI.

Phase VIII and IX

The porphyrin adlayer of phases P_{VIII} and P_{IX} is shown in Figure 4.57a-b, respectively, and an exemplary STM image of the gold lattice recorded underneath of both phases in Fig. 4.57c. After close analysis of the images presented in Figure 4.57 it is possible to present an accurate structure model of the Phase VIII and IX including the structural relationship between P_{VIII} and P_{IX} and the gold lattice underneath (see Fig. 4.58). The H_2TTMAPP layer of Phase VIII is described by vectors $\overline{j_1}$ and $\overline{j_2}$ with directions of $[0 \quad 0 \quad 1]$ and $[0 \quad 1 \quad 0]$, respectively, and Phase IX is described by vectors $\overline{k_1}$ and $\overline{k_2}$ with directions of $[0 \quad 0 \quad 1]$ and $[0 \quad 1 \quad 0]$, respectively. Furthermore, vectors $\overline{j_1}$ and $\overline{j_2}$ of P_{VIII} and vectors $\overline{k_1}$ and $\overline{k_2}$ of P_{IX} have the same direction, respectively. Moreover, vectors $\overline{j_2}$and $\overline{k_2}$ have the same value. Consequently the molecular rows along the vectors of Phases VIII and IX run diagonally to the high symmetry directions of the gold lattice. Furthermore, the molecular symmetry axis of individual molecules of phase P_{VIII} and P_{IX} which are centered atop of gold atoms do not follow any high symmetry direction of the underlying gold lattice. The unit cell for Phase VIII $(\overline{j_1},\ \overline{j_2})$ as depicted in Fig. 4.49c and Fig. 4.57a with the lattice parameters of j_1 = 1.63nm and j_2 = 1.63nm, enclosing an angle of 90°, contains one molecule and can be related to the gold lattice by the matrix:

$$\begin{pmatrix} \bar{j}_1 \\ \bar{j}_2 \end{pmatrix} = \begin{pmatrix} 4 & -4 \\ 4 & 4 \end{pmatrix} \begin{pmatrix} \bar{a}_1 \\ \bar{a}_2 \end{pmatrix}$$

On the basis of this model the surface coverage of the porphyrin adlayer is calculated and found to be 0.031 ML relative to the density of the gold layer, or $3.764 \cdot 10^{13}$ molecules/cm^2.

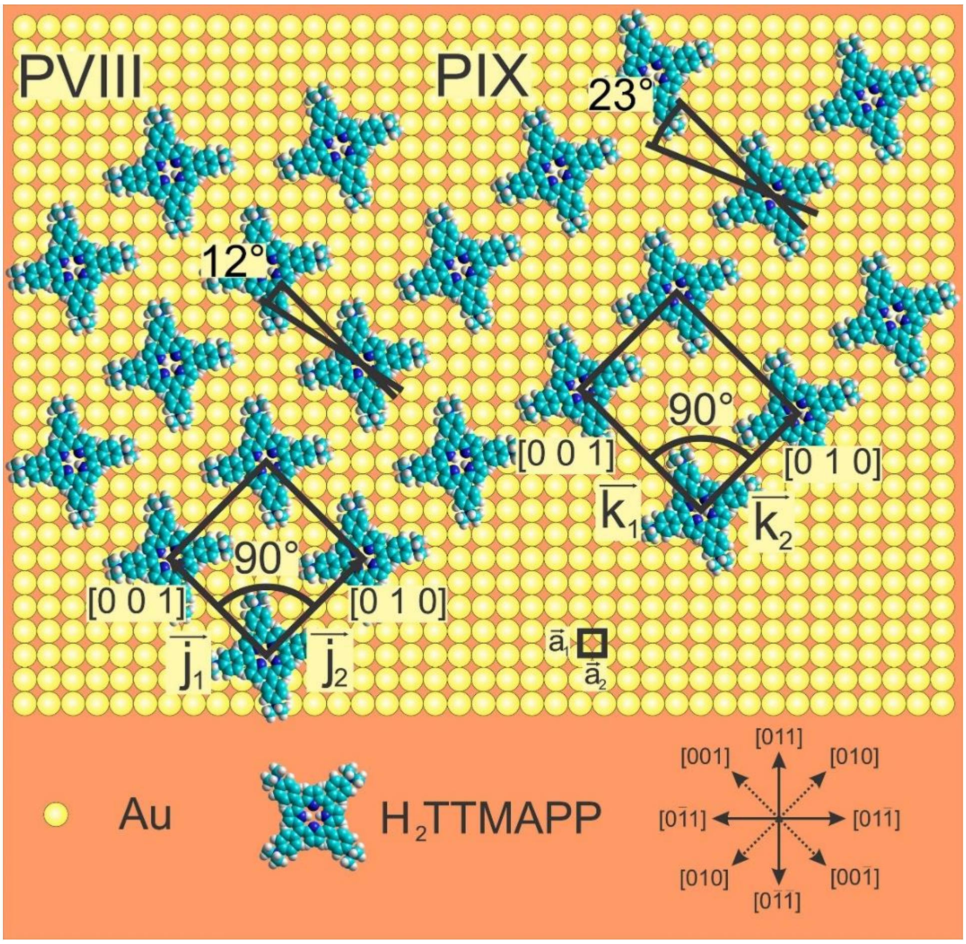

Figure 4.58: Structure model of the P_{VIII} and P_{IX} on iodine modified Au(100) surface.

The unit cell for Phase IX $(\overline{k_1}, \overline{k_2})$ as depicted in Fig. 4.49d and Fig. 4.57b with the lattice parameters of k_1 = 1.63nm and k_2 = 2.04nm, enclosing an angle of 90°, contains one molecules and can be related to the gold lattice by the matrix:

$$\begin{pmatrix} \bar{k}_1 \\ \bar{k}_2 \end{pmatrix} = \begin{pmatrix} 5 & -5 \\ 4 & 4 \end{pmatrix} \begin{pmatrix} \bar{a}_1 \\ \bar{a}_2 \end{pmatrix}$$

On the basis of this model the surface coverage of the porphyrin adlayer is calculated and found to be 0.025 ML relative to the density of the gold layer, or $3.007 \cdot 10^{13}$ molecules/cm^2.

Phase X and XI

Figure 4.59a-c shows the porphyrin adlayer of phases P_X and P_{XI}, respectively, and in Fig. 4.59b-d a subsequently recorded gold lattice underneath, both structures at the same surface area. After close analysis of the images presented in Figure 4.59 it is possible to present accurate structure models of the Phases X and XI including the structural relationship between P_X and P_{XI} and the gold lattice underneath (see Fig. 4.60).

The H_2TTMAPP layer of Phase X is described by vectors $\overline{l_1}$ and $\overline{l_2}$ with directions of $[0 \quad 1 \quad 5]$ and $[0 \quad 5 \quad 1]$, respectively. Therefore, the molecular rows of phase P_X do not follow any high symmetry direction of the substrate. Considering the adsorption site of the single molecules it seems that the center of individual porphyrin molecules on the corners of the unit-cell (row A in Fig. 4.49e) are situated atop of gold atoms, whereas the H_2TTMAPP molecules of the row B are occupying 2-fold bridging sites of the gold lattice. This result seems to be connected with the observed different rotation of the molecular symmetry axis of individual molecules for the rows A and B in Fig. 4.49e which is about +23° or 0°, respectively, with respect to the row direction parallel to the $\overline{l_1}$ vector. The unit cell of Phase X $(\overline{l_1}, \overline{l_2})$ as depicted in Fig. 4.49e and Fig. 4.59a with the lattice parameters of l_1 = 2.08nm and l_2 = 3.12nm, enclosing an angle of 67°, contains 2 molecules and can be related to the gold lattice by the matrix:

$$\begin{pmatrix} \bar{l}_1 \\ \bar{l}_2 \end{pmatrix} = \begin{pmatrix} 6 & -4 \\ 9 & 6 \end{pmatrix} \begin{pmatrix} \bar{a}_1 \\ \bar{a}_2 \end{pmatrix}$$

On the basis of this model the surface coverage of the porphyrin adlayer is calculated to be 0.0280 ML relative to the density of the gold layer, or $3.348 \cdot 10^{13}$ molecules/cm^2.

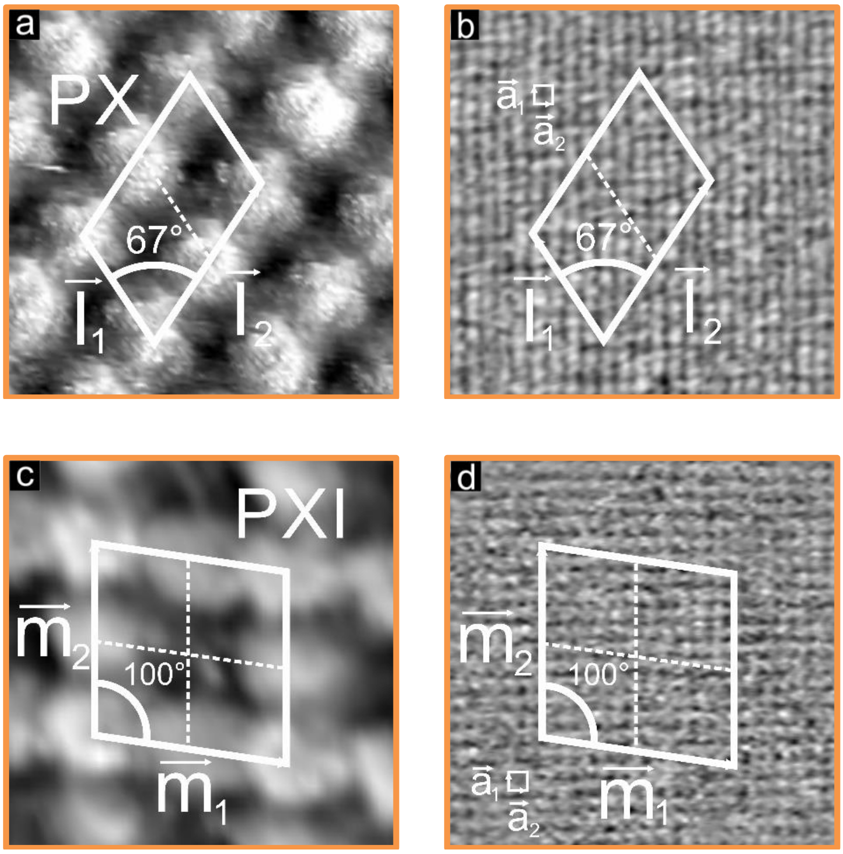

Figure 4.59: Structure correlation between the H_2TTMAPP layer of phases P_X and P_{XI} with the underlying gold layer, porphyrin layer of phase X (a) and phase XI (c) at high tunnelling bias, gold underneath the porphyrin layer of P_X (b) and P_{XI} (d) at low tunnelling bias; a) 6.60nm x 6.60nm, I_t = 1nA, U_b = -236mV, E= -700mV vs Pt/PtI; b) 6.60nm x 6.60nm, I_t= 1nA, U_b = -12mV, E= -700mV vs Pt/PtI; c) 6.60nm x 6.60nm, I_t = 1nA, U_b = -271mV, E= -700mV vs Pt/PtI; d) 6.60nm x 6.60nm, I_t= 1nA, U_b = -8mV, E= -700mV vs Pt/PtI.

The H_2TTMAPP layer of Phase XI is described by vectors $\overline{m_1}$ and $\overline{m_2}$ with directions of $[0 \quad 9 \quad \overline{13}]$ and $[0 \quad 1 \quad 1]$, respectively. Therefore, the molecular rows in the direction of the vector $\overline{m_2}$ run parallel to the close-packed atom rows of the Au(100) surface. Instead the molecular row along the vector $\overline{m_1}$ do not follow any high symmetry direction of the substrate. Furthermore, the molecular symmetry axis of individual molecules of phase P_{XI} do not follow any high symmetry direction of the underlying gold lattice either. Considering the adsorption site of the individual molecules it seems that the center of individual porphyrin molecules on the corners of the unit-cell (see Fig. 4.49f and Fig. 4.59c) are located atop of gold atoms, whereas the H_2TTMAPP molecules between them are occupying 2-fold bridging sites of the gold lattice. Moreover, it was found that the center of individual molecules which adsorb by changing the electrode potential in anodic direction (center of the unit-cell) are placed at the 4-hollow site of the gold lattice. The unit cell of Phase X $(\overline{m_1}, \overline{m_2})$ as depicted in Fig. 4.49f and Fig. 4.59c with the lattice parameters of m_1 = 3.22nm and m_2 = 3.17nm, enclosing an angle of 100°, contains 3 or 4 molecules (depending on electrode potential) and can be related to the gold lattice by the matrix:

$$\begin{pmatrix} \overline{m}_1 \\ \overline{m}_2 \end{pmatrix} = \begin{pmatrix} -2 & 11 \\ 11 & 0 \end{pmatrix} \begin{pmatrix} \overline{a}_1 \\ \overline{a}_2 \end{pmatrix}$$

On the basis of this model the surface coverage of the porphyrin adlayer is calculated and found to be 0.0249 ML (3 molecules) or 0.0332 ML (4 molecules) relative to the density of the gold layer, or $2.984 \cdot 10^{13}$ molecules/cm^2 and ca. $3.979 \cdot 10^{13}$ molecules/cm^2, respectively.

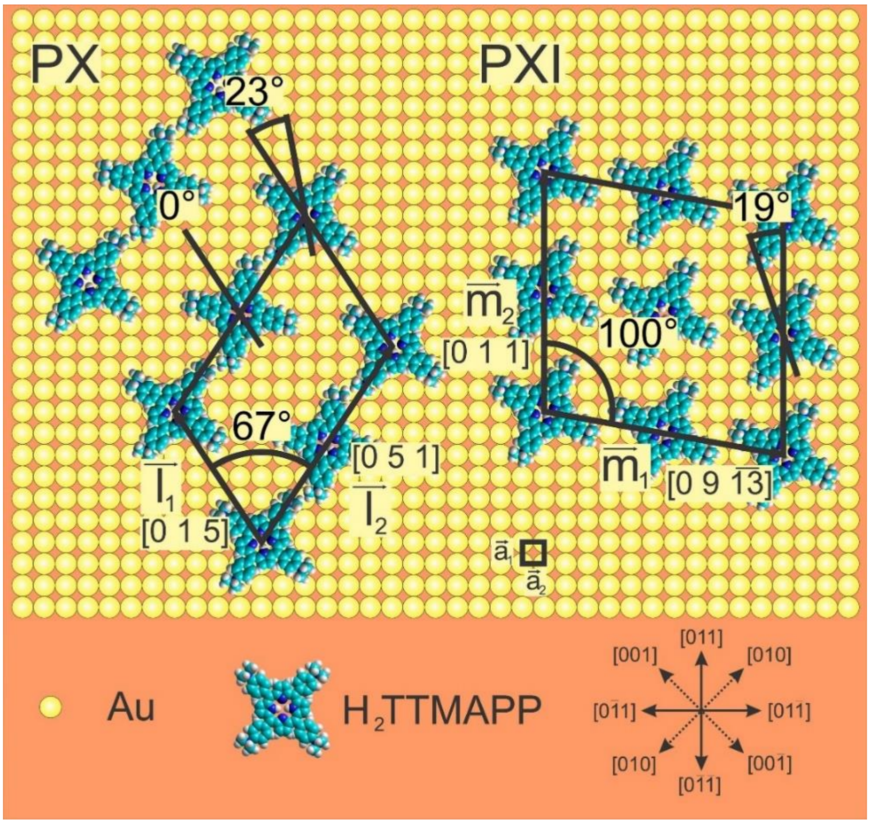

Figure 4.60: Structure model of the P_{VIII} and P_{IX} on iodine modified Au(100) surface.

Chapter V

Discussion and conclusion

Molecular self-assembled layers on solid surface play an increasingly important role in modern material sciences. The capability of many organic molecules to spontaneously self-assemble into monomolecular layers on suitable solid substrate may lead to functional surface with broad applications as electronic devices with nanometer dimension, as catalysts in the field of “green energy”, as well as novel light-stimulated sensors etc. to mention a few. For this reasons, the investigation of self-assembly layers has motivated surface scientists to use their wide arsenal of high resolution techniques in order to investigate the assembly mechanisms and composite properties of molecular films in order to form the basis for a rational design of their functionality.

Since larger organic molecules tend to be thermally labile, these molecules are better deposited from solution; besides, deposition from solution appears more economic than from the vapour phase in vacuum. Furthermore, by applying electrochemical techniques, the electrochemical potential is an additional parameter to control the deposition and growth of organic layer.

For this purpose the present thesis aims to contribute to the "Characterization of organic molecules at metal/electrolyte interfaces ". Specifically, for the first time, the self-assembly of H_2TMPyP and H_2TTMAPP molecules on an iodine-modified Au(100) surface has been investigated by a combination of Cyclic Voltammetry and in-situ STM. The self-assembly of the porphyrin molecules has been investigated in the whole potential window of the Au(100) surface, i.e. under non-reactive as well as reactive conditions. Study of the molecular adsorption, potential dependent structures and structural transitions as well as the gold oxidation mechanism in the presence of the molecules are presented.

In the whole potential window, i.e. under non-reactive as well as reactive conditions the internal structure of individual H_2TMPyP and as well H_2TTMAPP molecules was observed to be square shaped with four additional lobes placed at the corners of the square. The four lobes correspond to the four positively charged N-methyl 4-pyridyl groups in the case of H_2TMPyP or trimethylammonio phenyl groups for the H_2TTMAPP. This observation reveals a flat lying configuration of the molecules on the substrate which is expected due to a combination of the large

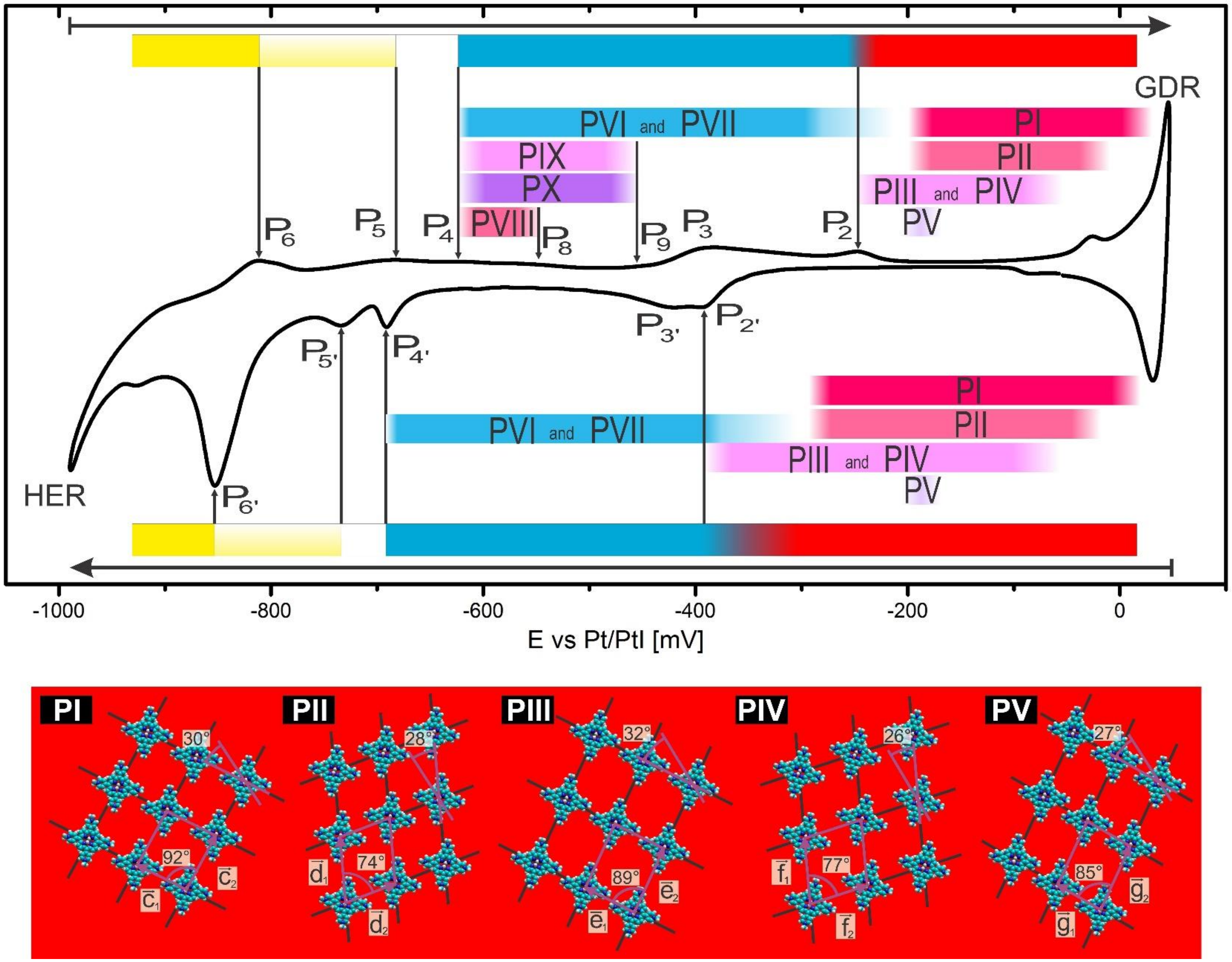
GDR
HER
PVI and PVII
PI
PII
PIX
PX
PIII and PIV
PVIII
PV
P_6
P_5
P_4
P_8
P_9
P_3
P_2
$P_{3'}$
$P_{2'}$
$P_{5'}$
$P_{4'}$
$P_{6'}$
-1000
-800
-600
-400
-200
0
E vs Pt/PtI [mV]
PI
30°
92°
$\vec{c}_1$
$\vec{c}_2$
PII
28°
74°
$\vec{d}_1$
$\vec{d}_2$
PIII
32°
89°
$\vec{e}_1$
$\vec{e}_2$
PIV
26°
77°
$\vec{f}_1$
$\vec{f}_2$
PV
27°
85°
$\vec{g}_1$
$\vec{g}_2$

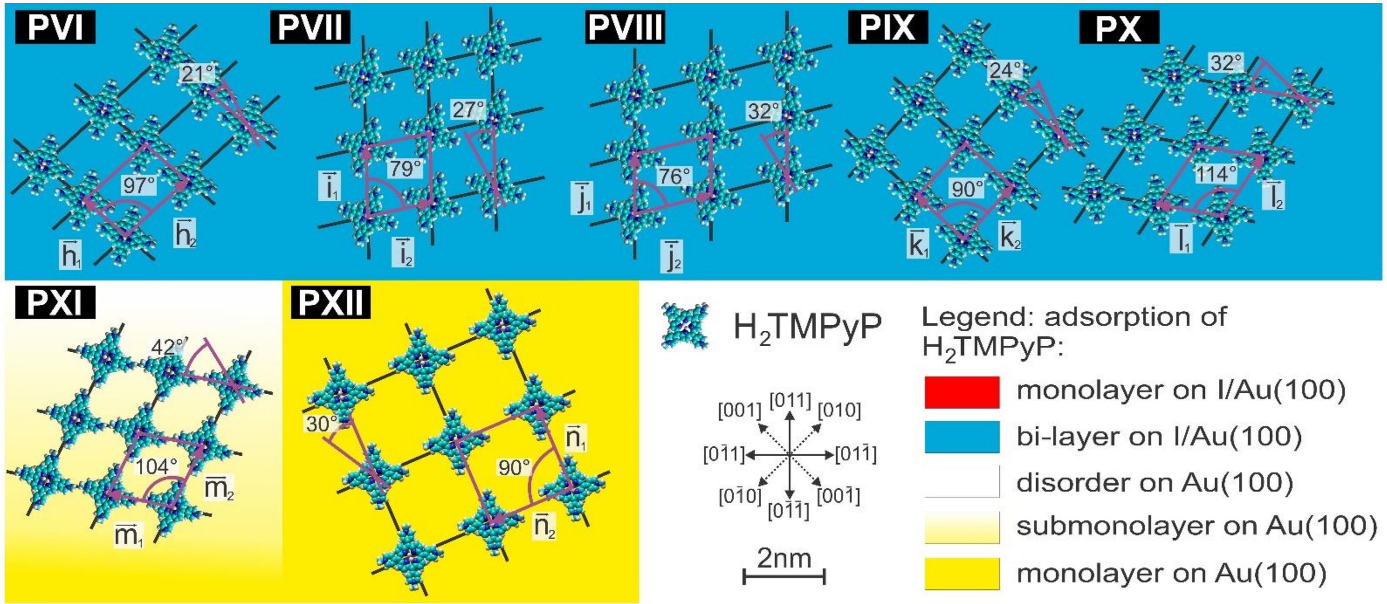

	P_{I}	P_{II}	P_{III}	P_{IV}	P_{V}	P_{VI}	P_{VII}	P_{VIII}	P_{IX}	P_{X}	P_{XI}	P_{XII}
lattice constants [± 0.05nm]	$c_1 = 1.61$ $c_2 = 1.80$	$d_1 = 1.94$ $d_2 = 1.56$	$e_1 = 1.61$ $e_2 = 2.06$	$f_1 = 1.94$ $f_2 = 1.76$	$g_1 = 1.46$ $g_2 = 2.06$	$h_1 = 1.36$ $h_2 = 2.05$	$i_1 = 1.74$ $i_2 = 1.63$	$j_1 = 1.49$ $j_2 = 1.96$	$k_1 = 1.58$ $k_2 = 1.77$	$l_1 = 1.62$ $l_2 = 1.78$	$m_1 = 1.62$ $m_2 = 1.78$	$n_1 = 2.19$ $n_2 = 2.19$
angle [± 1°]	92°	74°	89°	77°	85°	97°	79°	76°	90°	76°	104°	90°
molecule rotation [α ± 1°]	+30° vs $\bar{c}_1$	-28° vs $\bar{d}_1$	+32° vs $\bar{e}_1$	+26° vs $\bar{f}_1$	+27° vs $\bar{g}_1$	+21° vs $\bar{h}_1$	-27° vs $\bar{i}_1$	-32° vs $\bar{j}_1$	+24° vs $\bar{k}_1$	+32° vs $\bar{l}_1$	+42° vs $\bar{m}_1$	-30° vs $\bar{n}_1$
surface concentration [molecules/cm²]	$3.453 \cdot 10^{13}$	$3.437 \cdot 10^{13}$	$3.016 \cdot 10^{13}$	$3.014 \cdot 10^{13}$	$3.333 \cdot 10^{13}$	$3.614 \cdot 10^{13}$	$3.592 \cdot 10^{13}$	$3.529 \cdot 10^{13}$	$3.556 \cdot 10^{13}$	$3.574 \cdot 10^{13}$	$3.751 \cdot 10^{13}$	$2.085 \cdot 10^{13}$

Figure 5.1: Summary of the results of self-assembly of H_2TMPyP on iodine modified Au(100) electrode surface.

π-system of the porphyrin ring and the four positively charged groups at the corners. Therefore, it is energetically favorable for the porphyrins molecules to lie parallel to the substrate in order to maximize the van der Waals as well as the electrostatic interactions with the anion precovered surface. In fact, the flat lying mode of porphyrins was already repeatedly reported in the literature [29-32,35,56,78-79]. Moreover, the formation of the lateral ordering of the porphyrin molecules in the form of rows as seen in the STM images with different angles of rotation of the symmetry direction of the individual molecules with respect to the direction of the molecular row may be regarded as a consequence of adsorbate-adsorbate interactions, namely the electrostatic repulsive forces between positively charged N-methyl 4-pyridyl and trimethylammonio phenyl groups.

H_2TMPyP

The self-assembly of H_2TMPyP molecules on the iodine modified Au(100) surface turned on to be strongly potential dependent. In the whole accessible potential window the formation of twelve molecular structures (P_I-P_{XII}) is observed which were divided into four regimes. Each one of the structures differs drastically from all others and can be strictly correlated with an observed current feature in the CV curve (see Fig. 5.1). The first regime (red colour in Fig. 5.1) starts from the oxidative gold dissolution reaction and extends to the peak pair $P_{2'}/P_2$ where we observe a self-assembly of a monolayer of H_2TMPyP molecules on the I/Au(100) surface with five different ordered porphyrin phases (P_I-P_V). The next regime (blue colour in Fig. 5.1) is located between the peak pairs $P_{2'}/P_2$ and $P_{4'}/P_4$ where we observe the self-assembly of bi-layer structures on the I/Au(100) surface with five different ordered porphyrin bi-layer phases (P_{VI}-P_X). The peak pair $P_{2'}/P_2$ was related to a structural phase transition between a monolayer/bi-layer and bi-layer/monolayer regime, and a concomitant reduction/oxidation (which takes place directly on the surface) of the porphyrin molecules, accompanied by adsorption/desorption and reduction/oxidation of molecules of the second layer, respectively. Whereas the peak pair $P_{3'}/P_3$ corresponds to the reduction/oxidation, respectively, of molecules from the bulk solution. The peak pair $P_{4'}/P_4$ was characterized as arising from desorption/adsorption of iodide which leads to the disordering/ordering of the porphyrin layer within the bi-layer regime.

Considering the monolayer and bi-layer regimes (red and blue colour in Fig. 5.1, respectively) in which the H_2TMPyP molecules adsorb on the iodine modified Au(100) surface we can conclude that the phase transition between the first and the second regime is associated with the first redox process which alters the chemical state of the porphyrin molecules. But on the other hand, it is found that within the monolayer regime a competition was observed between the five phases (P_I-P_V) with a strict relationship of their respective surface concentration and existence regimes to the applied electrode potential. Hence, the transitions between the monolayer phases is not caused by a change in the chemical state of the porphyrin molecules but by a variation of the interaction between the porphyrin molecules and the substrate only. Moreover, from the structural correlation between the porphyrin adlayer and the substrate lattice it is shown that these observed phase transitions are caused by a change of the underlying iodine lattice as a function of the electrode potential. For instance, the analysis of the two ordered phases I and III of H_2TMPyP on I/Au(100) gave the following result: The transition of Phase I to Phase III when going from more positive to more negative potentials, is accompanied with a concomitant decrease of the surface coverage by about 4.4% from Phase I ($3.453 \cdot 10^{13}$ molecules/cm^2) to Phase III ($3.016 \cdot 10^{13}$ molecules/cm^2) due to a rearrangement of the iodide lattice underneath with a change of the anion coverage by about 17.7% from the iodide lattice under Phase I ($62.58 \cdot 10^{13}$ iodine/cm^2) to the iodide lattice under Phase III ($59.81 \cdot 10^{13}$ iodine/cm^2). A similar behaviour of increasing molecular surface coverage by increasing the electrode potential is observed for the bi-layer regime in the anodic sweep, where a phase competition between the phases P_{VI}-P_X is observed due to the surface concentration and applied electrode potential. This indicates that self-assembly of the H_2TMPyP molecules on I/Au(100) is governed by the density of the iodine anion layer which determines the number of organic cations which are electrostatically attracted to the surface. However, in the literature, iodide layers on noble metal surfaces such as Au and Pt were found to be hydrophobic and almost uncharged [33]. Another study on the Cu(100) surface reported the same [80]. Therefore, the interaction of porphyrin with iodide on Au, Pt, Ag and Cu was suggested to be mainly of van der Waals type. However, the present results show a clear dependence of the ordering of the self-assembled porphyrin layers on the potential due to the variation of electrostatic interaction between porphyrin cations and the iodine ions. Moreover, a bi-layer formation of reduced H_2TMPyP species was also observed on Cl/Cu(111) surface [35] but not on Cl/Cu(100). It was suggested that the higher density of Cl^- anions on the Cu(111) surface as compared to Cu(100) and the concomitant stronger electrostatic interaction between the negatively charged Cl/Cu(111) surface and the positively charged porphyrin cations plays a decisive role in the formation of the porphyrin bi-layer. This means that not only van der Waals interactions between the porphyrin molecules and the polarized substrate play an important role, but also the electrostatic interactions between these molecules and the iodide layer.

The third regime (white and white-yellow colour in Fig. 5.1) extends from peak pair $P_{4'}/P_4$ over $P_{5'}/P_5$ to $P_{6'}/P_6$, and the fourth regime (yellow colour in Fig. 5.1) is located between $P_{6'}/P_6$ and the HER. The peak pair $P_{4'}/P_4$ was characterize as desorption/adsorption of iodide which leads to the disordering/ordering of the porphyrin layer of the bi-layer regime. Accordingly, between the peak pairs $P_{4'}/P_4$ and $P_{5'}/P_5$ a disordered layer of the reduced H_2TMPyP molecules on the I-free Au(100) surface was observed. Lowering the electrode potential further below the peak pair $P_{5'}/P_5$ and till peak pair $P_{6'}/P_6$ results in sporadic observation of sub-monolayer coverages (P_{XI}) of porphyrin molecules on the I-free gold surface. The peak pair $P_{6'}/P_6$ was characterize as ordering and disordering of a monolayer (P_{XII}) of H_2TMPyP molecules on the iodine-fee Au(100) surface. Moreover, peak $P_{6'}$ was associated with the second reduction step of the porphyrin molecules. In these sub-monolayer and monolayer regimes on the I-free (1x1) Au(100) surface (white-yellow and yellow colour in the Fig. 5.1) direct electrostatic interactions between the organic cations and the metal electrode play a crucial role in the self-assembly of the porphyrin molecules. It can be found in literature that H_2TMPyP under non-reactive conditions (before the first reduction) is strongly adsorbed directly on Au(111) and, thus does not form ordered layers due to this strong substrate-adsorbate interaction [30]. In the present case the porphyrin molecules adsorbed on the I-free gold surface are in reduced form. In this case that the positive charge on the reduced species, i.e. $[H_4TMPyP(-II)]^{+4}$, is lower than on the free base $[H_2TMPyP(0)]^{+4}$ molecules. Therefore, the electrostatic interaction is considerably weaker, which results in an increased mobility of the reduced species on the I-free (1x1) Au(100) surface. This is manifested by the first observation of disordered molecules on the surface between the peak pairs $P_{4'}/P_4$ and $P_{5'}/P_5$. However, by changing the electrode potential in cathodic direction, i.e. increased electrostatic interaction between the negatively charged surface and the reduced but still positively charged H_2TMPyP species results in the observation of a sub-monolayer between the peak pairs $P_{5'}/P_5$ and $P_{6'}/P_6$. Moreover, further lowering the electrode potential (which increases the electrostatic interaction further) leads to the second reduction step of the H_2TMPyP molecules and the observation of the full monolayer of organic cations on the I-free (1x1) Au(100) surface, demonstrating the delicate influence of the substrate-adsorbate interactions.

$H_2TTMAPP$ and comparison with H_2TMPyP

The self-assembly of $H_2TTMAPP$ molecules on the iodine modified Au(100) surface results in the observation of eleven molecular structures (P_I-P_{XI}) in the whole potential window which are divided into five regimes. Each one of the structures differs again drastically from all others and can be correlated with an observed current feature in the CV curve (see Fig. 5.2). The first, second and fifth regime present the self-assembly of the porphyrin molecules on the iodine modified Au(100) surface and will be considered first. In the first regime (blue colour in Fig. 5.2) we observe only one ordered porphyrin phase (P_I). This phase was observed only under specific conditions, i.e. when the adsorption process of the porphyrin molecules started at an electrode potential between ca. -400mV and -300mV vs Pt/PtI. In this potential range the iodine lattice in the absence of molecular species was found to be $(2\sqrt{2} \times \sqrt{2})$. The same iodine structure was found underneath Phase I (see Fig. 4.38). Moreover, this phase initially is stable in anodic direction, i.e. no changes in molecular structure occur in the potential range between ca. -425mV vs Pt/PtI and the GDR which starts at -150mV vs Pt/PtI. The first phase transition to the second regime (violet colour on the Fig. 5.2) is observed when going below -425mV vs Pt/PtI. This phase transformation is suggested to be related to the change in the iodine lattice from the $(2\sqrt{2} \times \sqrt{2})$

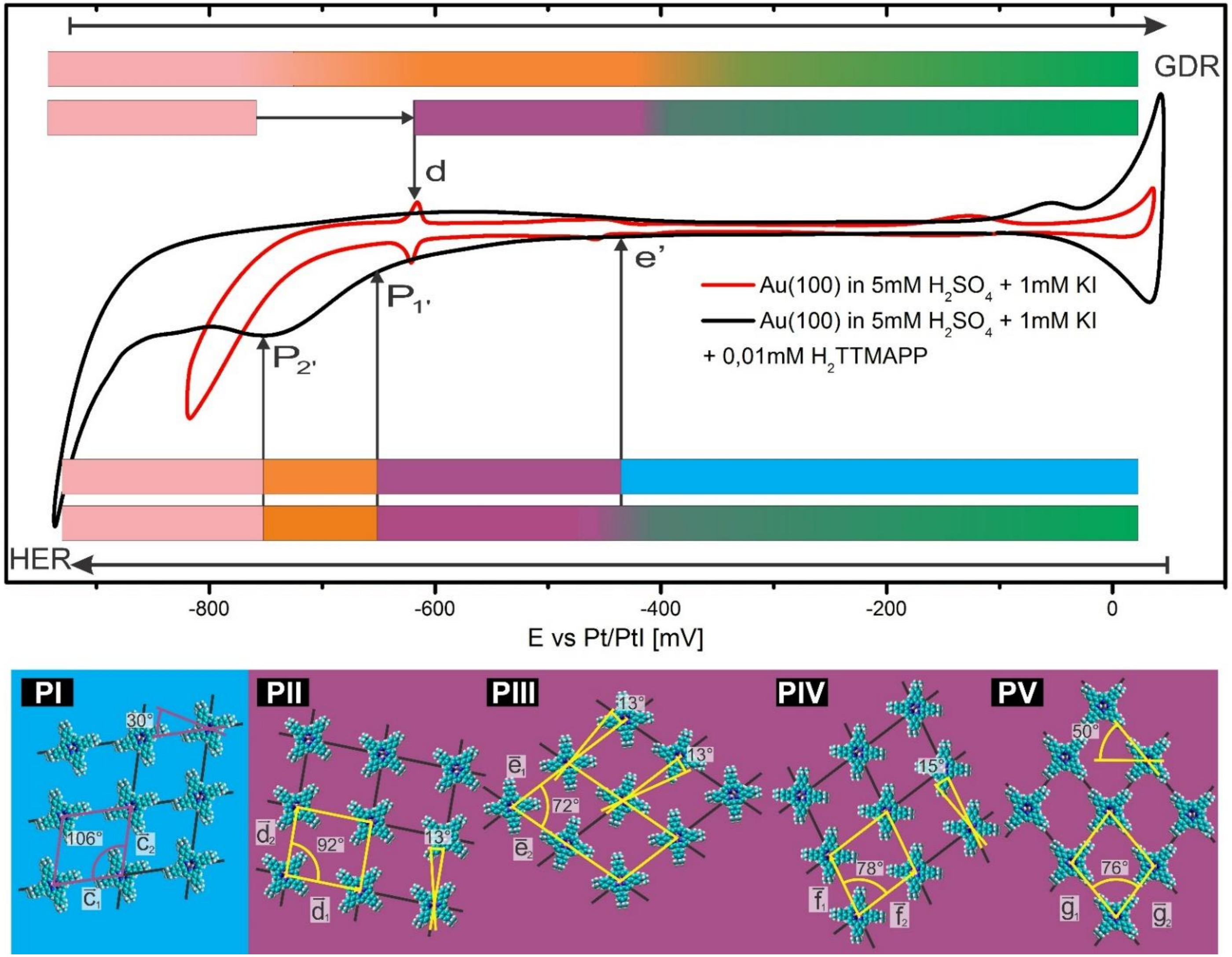
GDR
d
e'
P1'
P2'
Au(100) in 5mM H2SO4 + 1mM KI
Au(100) in 5mM H2SO4 + 1mM KI
+ 0,01mM H2TTMAPP
HER
-800
-600
-400
-200
0
E vs Pt/PtI [mV]
PI
30°
106°
c1
c2
PII
92°
13°
d1
d2
PIII
13°
13°
72°
e1
e2
PIV
15°
78°
f1
f2
PV
50°
76°
g1
g2

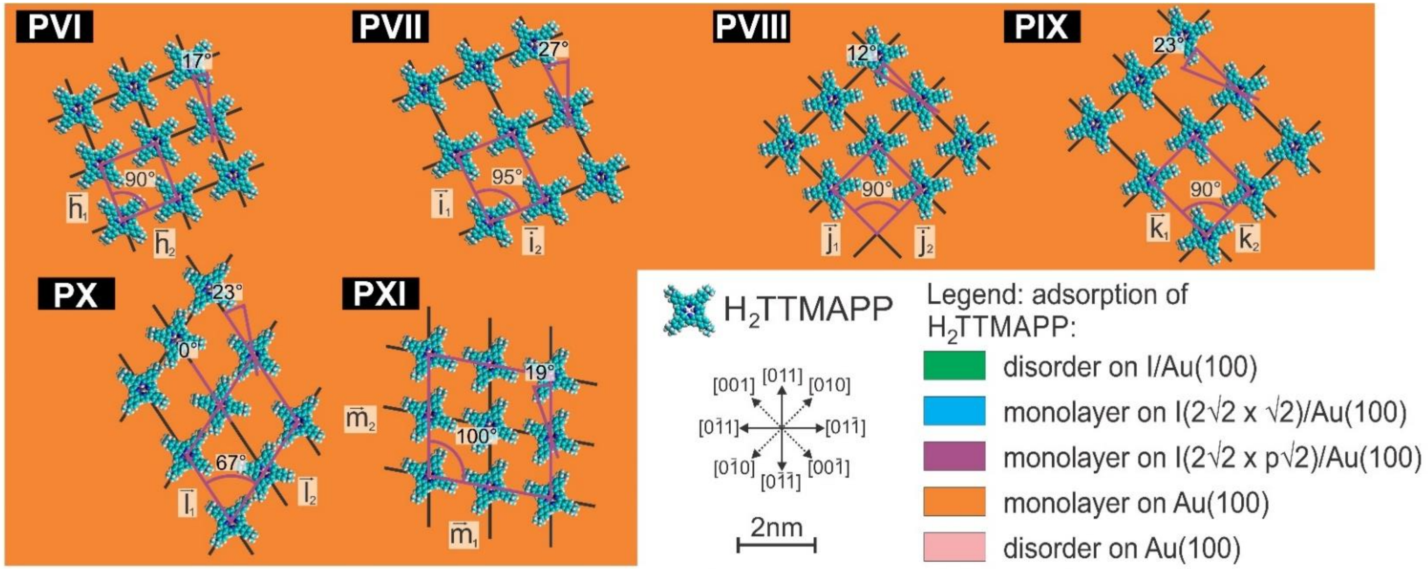

	P_I	P_{II}	P_{III}	P_{IV}	P_V	P_{VI}	P_{VII}	P_{VIII}	P_{IX}	P_X	P_{XI}
lattice constants [± 0.05nm]	$c_1 = 2.02$ $c_2 = 2.04$	$d_1 = 2.23$ $d_2 = 2.03$	$e_1 = 2.10$ $e_2 = 3.87$	$f_1 = 1.95$ $f_2 = 2.11$	$g_1 = 2.07$ $g_2 = 1.88$	$h_1 = 1.55$ $h_2 = 1.55$	$i_1 = 1.93$ $i_2 = 1.55$	$j_1 = 1.63$ $j_2 = 1.63$	$k_1 = 1.63$ $k_2 = 2.04$	$l_1 = 2.08$ $l_2 = 3.12$	$m_1 = 3.22$ $m_2 = 3.17$
angle [± 1°]	106°	92°	72°	78°	76°	90°	95°	90°	90°	67°	100°
molecule rotation [α ± 1°]	+30° vs $\overline{c}_1$	-13° vs $\overline{d}_2$	±32° vs $\overline{e}_1$	-15° vs $\overline{f}_1$	+50° vs $\overline{g}_1$	+17° vs $\overline{h}_1$	+27° vs $\overline{d}_2$	-12° vs $\overline{j}_1$	-23° vs $\overline{k}_1$	+23° vs $\overline{l}_1$ or 0° vs $\overline{l}_1$	-19° vs $\overline{m}_2$
surface concentration [molecules/cm²]	$2.525 \cdot 10^{13}$	$2.221 \cdot 10^{13}$	$2.588 \cdot 10^{13}$	$2.485 \cdot 10^{13}$	$2.648 \cdot 10^{13}$	$4.162 \cdot 10^{13}$	$3.356 \cdot 10^{13}$	$3.764 \cdot 10^{13}$	$3.007 \cdot 10^{13}$	$3.348 \cdot 10^{13}$	$2.984 \cdot 10^{13}$ and $3.979 \cdot 10^{13}$

Figure 5.2: Summary of the results of self-assembly of $H_2TTMAPP$ on iodine modified Au(100) electrode surface.

to (2√2 x p√2) structure and corresponds to the cathodic peak e' on the cyclic voltammogram in Fig. 5.2. The observed stability regime in anodic direction, where the iodine layer without porphyrin molecules in solution goes from the (2√2 x √2) over the *"flexible superstructures"* to a *pseudo-hex-rot* structure, suggests a strong porphyrin-substrate interaction where the adlayer of molecules prevents a change in the iodide structure. Furthermore, after the phase transition in cathodic direction to the second molecular regime the first regime was not observed any more in this potential range, instead a disordered distribution of H_2TTMAPP molecules was observed (fifth regime denoted with green colour in Fig. 5.2). Apparently a strong adsorbate-substrate interaction reduces the mobility of the H_2TTMAPP molecules preventing the rearrangement of molecules to form an ordered layer. Moreover, the phase transition in cathodic direction from the disordered regime (green colour in Fig. 5.2) to the second regime (violet colour on the Fig. 5.2), where we observe four ordered structures (P_{II}-P_V), the ordering process is slow. Hence, the phase transition from the disordered regime to the second regime is not caused by a variation in the chemical state of the porphyrin but by a variation of the interaction between the porphyrin molecules and the substrate. Therefore, it seems that the density of the iodine anions is lowered by the reduction of the electrode potential and this results in a weakening of the porphyrin-substrate interaction which allows ordering of the porphyrin structures. But on the other hand besides disappearance of Phase II and appearance of Phase V (which have the lowest and highest surface concentration in the second regime, namely $2.221 \cdot 10^{13}$ molecules/cm^2 and $2.648 \cdot 10^{13}$ molecules/cm^2) at the electrode potential of ca. -600mV vs Pt/PtI there was no observed competition observed between the H_2TTMAPP phases (P_{II}-P_V) due to their different surface concentrations at given electrode potential. It appears that the porphyrin-substrate interaction is still strong enough so that after reaching equilibrium, i.e. after the ordering process, it prevents a change in the iodide structure and, hence, the competition between them. The second regime (violet colour in Fig. 5.2) in cathodic direction extends between ca. -425mV vs Pt/PtI and peak $P_{1'}$ at -660mV vs Pt/PtI. The peak $P_{1'}$ was identified with the desorption of iodine and the resultant phase transition to the porphyrin layers which adsorbs on the I-free (1x1) Au(100) surface. In anodic direction the observation of the reappearance of the four H_2TTMAPP structures was possible when the electrode potential is quickly/suddenly changed from the disordered regime (beige colour in Fig. 5.2) to an electrode potential between ca. -620mV (which correspond to the peak *d* of adsorption of iodide in the absence of organic molecules) and -400mV vs Pt/PtI. This sudden change prevents the creation of an ordered structures on the I-free Au(100) surface from the third regime (orange colour in Fig. 5.2) which in turn inhibits re-adsorption of the iodine anions.

At this point from the observation for both porphyrin molecules we can conclude that the interaction between the $H_2TTMAPP$ molecules and the iodine-modified gold is stronger than that of the H_2TMPyP molecules which manifests itself in a reduced mobility of the $H_2TTMAPP$ molecules and a stabilization of the iodine phases over a wider potential regime. This observation can be rationalized with the four highly polarized trimethylamine groups of the $H_2TTMAPP$ molecules which interact stronger with the iodine layer than the N-methyl 4-pyridyl group of the H_2TMPyP molecules. This again supports the notion that not only van der Waals interactions between the porphyrin and the substrate play an important role, but also electrostatic interactions between these molecular cations and the iodine layer.

The third and fourth regime present the self-assembly of the $H_2TTMAPP$ molecules on the I-free (1x1) Au(100) surface where an electrostatic interaction should play a crucial role. The third regime (orange colour in Fig. 5.2) includes a self-assembly of a monolayer of the $H_2TTMAPP$ molecules on the I-free (1x1) Au(100) surface with five different ordered porphyrin phases (P_{VI}-P_{XI}). In cathodic direction this regime is located between peak pair $P_{1'}$ and $P_{2'}$. Peak $P_{1'}$ which was characterized as desorption of iodine which causes the phase transition of porphyrin molecules from the second to the third regime. The observation of the $H_2TTMAPP$ phase just after desorption of iodine, in comparison to the H_2TMPyP molecules where after desorption of the iodine the disordered layer was observed can be attributed to a different redox state of both porphyrin molecules. At this electrode potential H_2TMPyP is in reduced form i.e. $[H_4TMPyP(-II)]^{+4}$, for which the mean positive charge is lower than on the free base $[H_2TTMAPP(0)]^{+4}$ molecular cations. This results in stronger adsorbate-substrate interaction and reduced mobility. Moreover, this reduced mobility of the porphyrin molecules is manifested by the absence of competition between the phases due to their different surface concentration. Furthermore, in anodic direction we observe an inhibiting effect of the organic layer on the readsoption of iodine ions which is shifted toward a more positive potential (ca. -400mV vs Pt/PtI). This inhibiting effect of the organic layer on the readsoption of iodine ions supports stronger electrostatic interactions between the free base $[H_2TTMAPP(0)]^{+4}$ molecules and the gold surface than the reduced species of $[H_4TMPyP(-II)]^{+4}$ and the substrate. Moreover, the first reduction of the $H_2TTMAPP$, which was assigned to the peak $P_{2'}$, lowers the overall positive charge of the $H_2TTMAPP$ molecules and which results in an increased mobility and disordering of the reduced species on the iodine-free gold surface.

At this state several other observations can be addressed which distinguished the behaviour of the $H_2TTMAPP$ molecules from that of the H_2TMPyP molecules on this.

- GDR: an oxidative gold dissolution reaction in the absence of porphyrin molecules in the solution starts at an electrode potential of ca. -80mV vs Pt/PtI. In the presence of H_2TMPyP molecules the starting potential for GDR was found to be ca. -150mV vs Pt/PtI. In turn, in the case of $H_2TTMAPP$ we can distinguish two situation: In the monolayer regime (blue colour in Fig. 5.2) where we observe an ordered layer of porphyrin molecules the GDR starts at ca. -150mV vs Pt/PtI, while in the case of a disordered layer it starts at ca. -350mV vs Pt/PtI i.e. much earlier. In both cases the porphyrin molecules promote the GDR process. This observation suggest the incorporation of the gold atom in the central porphyrin ring in order to form the corresponding AuTMPyP or AuTTMAPP species in a so called “metallization” reaction, which was observed in the case of adsorbed H_2TMPyP molecules on the Cl/Cu(100) surface [35].

- Desorption of iodine: in both cases the organic layer hinders the desorption of the iodine layer from the surface, but there is a considerable shift between H_2TMPyP and $H_2TTMAPP$ molecules. The desorption of iodine in the absence of organic molecules is observed at an electrode potential of -623mV vs Pt/PtI, in the presence of H_2TMPyP and $H_2TTMAPP$ it is at -700mV vs

Pt/PtI and -660mV vs Pt/PtI, respectively. The lower electrode potential of iodine desorption in the presence of H_2TMPyP molecules can be explained by the higher average surface concentration of these molecules (1.4 larger than for $H_2TTMAPP$); the higher density of H_2TMPyP molecules stabilizes the iodine layer.

- Re-adsorption of iodine: in the case of H_2TMPyP molecules no influence on the readsorption of iodine is observed. The readsorption of iodine in absence of organic molecules is observed at -618mV vs Pt/PtI, where in case of H_2TMPyP at -615mV vs Pt/PtI. Considering the $H_2TTMAPP$ molecules a two situations are in consideration: in the first when starting from the orange regime (see Fig.5.2) with ordered $H_2TTMAPP$ structure the readsoption of iodine starts at ca. -400mV vs Pt/PtI. In this case we observe an inhibiting effect of the organic layer on the readsoption of iodine cations due to the electrostatic interaction between the $H_2TTMAPP$ molecules and the gold surface. In the second situation when the potential is *jumped* from the disordered regime (beige colour in Fig. 5.2) to the electrode potential more positive than -618mV vs Pt/PtI (which corresponds to a peak *d* of the adsorption of iodine in the absence of organic molecules) prevents the creation of ordered structures on the iodine-free Au(100) surface from the third regime (orange colour in Fig.5.2), which first leads to readsorption of the iodine due to its higher mobility and then the $H_2TTMAPP$ molecules.

- The average surface concentration of porphyrin molecules on I/Au(100) and I-free Au(100): it is obvious that the size of the organic molecules is one of the factors which dictates the molecular density of the porphyrins adlayer. But it should be also considered a repulsive interactions of the functional groups of the porphyrin molecules. Thus, the average surface concentration for H_2TMPyP and $H_2TTMAPP$ on a I/Au(100) surface are $3.412 \cdot 10^{13}$ molecules/cm^2 and $2.493 \cdot 10^{13}$ molecules/cm^2, respectively, i.e. more H_2TMPyP molecules fit on the surface due to their smaller size, and moreover, stronger repulsive interaction between the trimethylammonio phenyl groups than N-methyl 4-pyridyl groups reduce the density of these molecules futher.

In the other hand the average surface concentration of H_2TTMAPP on a I-free Au(100) surface is $3.514 \cdot 10^{13}$ molecules/cm^2 and is higher than the average surface concentration for H_2TTMAPP and even for H_2TMPyP on a I/Au(100). Due to the fact that H_2TTMAPP on I/Au(100) and I-free Au(100) is in the same chemical state the higher molecular density of H_2TTMAPP can be simply explained by stronger electrostatic interaction between the I-free gold surface than the iodine-modified gold surface. Therefore, the average surface concentration is a balance between the adsorbate-substrate and adsobate-adsorbate interaction: On one side the size of the organic molecules and repulsive electrostatic interaction between the molecules (adsobate-adsorbate) and on the other side attractive interaction between the molecules and the substrate (adsorbate-substrate) play a role.

As a summary on the role of the interactions in the characterized ordered porphyrin layers on iodine modified Au(100) surface, it can be said that the intermolecular interaction is primarily based on the repulsive electrostatic interaction between the positively charge N-methyl 4-pyridyl groups in the case of H_2TMPyP or trimethylammonio phenyl groups for the H_2TTMAPP. This electrostatic interaction plays a decisive role for the structure formation in an ordered layer. In the case of interlayer interaction not only the van der Waals interactions between the porphyrins molecules and the substrate play an important role, but also the electrostatic interactions between these molecules and the iodine layer. Moreover, from the comparison of the self-assembly of H_2TMPyP and H_2TTMAPP molecules surface mobility of adsorbed molecules appears as a key factor for the ordering process. The comparative study presented here for the two molecules H_2TMPyP and H_2TTMAPP and the obtained results clearly shows that the self-assembly process is the results of a delicate balance between all interactions between the molecules themselves and to the substrate.

Bibliography

[1] J. V. Barth, G. Costantini, and K. Kern, *Nature*, vol. 437, no. 7059, pp. 671–679, (2005).

[2] D. G. Castner, B.D. Ratner, *Surf. Sci.*, vol. 500, pp. 28 – 60, (2002).

[3] F. Vögtle, *Supramolecular Chemistry*, Wiley, Chichester, Great Britain, (1991).

[4] J.-M. Lehn, *Supramolecular Chemistry*, VCH, Weinheim, Germany, (1995).

[5] V. Balzani, M. Venturi, A. Credi, *Molecular Devices and Machines*, Wiley/VCH, (2002).

[6] V. Balzani, A. Credi, F.M. Raymo, J.F. Stoddart, *Angew. Chem. Int. Ed.,* vol. 39, pp. 3348-3391, (2000)

[7] C. Safarowsky, A. Rang, C.A. Schalley, K. Wandelt, P. Broekmann, *Electrochimica Acta,* vol. 50, pp. 4257 – 4268, (2005).

[8] N. L. Oleinick, H. H. Evans, *Radiat. Res.*, vol. 150, pp. 146 – 156, (1998).

[9] J. P. Lei, H. X. Ju, and O. Ikeda, *Electrochim. Acta,* vol. 49, no. 15, pp. 2453 – 2460, (2004).

[10] A. Goldoni, *Elettra highlights*, Trieste, pp. 64 - 65 (2001–2002).

[11] R. M. Ion and S. Dreve, *First International Conference on Complexity and Intelligence of the Artificial and Natural Complex Systems. Medical Applications of the Complex Systems. Biomedical Computing*, pp. 191 - 196, (2008).

[12] K. Lang, J. Mosinger, D. M. Wagnerova, *Coord. Chem. Rev.,* vol. 248, pp. 321-350, (2004).

[13] M. G. Vicente, *Curr. Med. Chem. Anti-Canc. Agents.*, no. 1, pp. 175 - 194, (2001).

[14] N. L. Oleinick, H. H. Evans, *Radiat. Res.*, vol. 150, pp. 146 – 156, (1998).

[15] J. P. Lei, H. X. Ju, and O. Ikeda, *Electrochim. Acta,* vol. 49, no. 15, pp. 2453 – 2460, (2004).

[16] R. Purrello, S. Gurrieri, and R. Lauceri, *Coord. Chem. Rev.,* vol. 192, pp. 683 – 706, (1999).

[17] T. Hirano, T. Torimoto, K. Takagi, *Nanosci. Nanotechnol.*, no. 1, pp. 495 – 500, (2009).

[18] K. Lang, J. Mosinger, D. M. Wagnerova, *Coord. Chem. Rev.,* vol. 248, pp. 321-350, (2004).

[19] M. G. Vicente, *Curr. Med. Chem. Anti-Canc. Agents.*, no. 1, pp. 175 - 194, (2001).

[20] N. L. Oleinick, H. H. Evans, *Radiat. Res.*, vol. 150, pp. 146 – 156, (1998).

[21] Y. Kobayashi, M. Maniki, K. Nakamura, *Cancer biotherapy & radiopharmaceuticals*, vol. 11, no. 3, pp. 198-202, (1996).

[22] R. J. J. Fiel, *Biomol. Struct. Dyn.*, vol. 6, pp. 1259 – 1274, (1989).

[23] L. G. Marzilli, *New. J. Chem.,* vol. 14, pp. 409 - 420. (1990).

[24] R. F. Pasternack, E. J. Gibbs, *Met. Ions. Biol. Syst.,* vol. 33, pp. 367 – 397, (1996).

[25] T. Hirano, T. Torimoto, K. Takagi, *Nanosci. Nanotechnol.*, no. 1, pp. 495 – 500, (2009).

[26] I. Leray, M. C. Vernieres, and C. Bied-Charreton, *Sens. Actuators, B,* vol. 54, no. 3, pp. 243–251, (1999).

[27] H. Zhang, Y. Sun, P. Zhang, K. Ye, J. Zhang, Y. Wang, *Chinese Science Buelletin,* vol. 50, no.16, pp.1699-1702, (2005).

[28] D. Delmarre, R. Meallet, C. Bied-Charreton, and R. B. Pansu, J. *Photochem. Photobiol.,* A, vol. 124, no. 1-2, pp. 23–28, (1999).

[29] M. Kunitake, N. Batina, and K. Itaya, *Langmuir,* vol. 11, no. 7, pp. 2337 – 2340, (1995).

[30] M. Kunitake, U. Akiba, N. Batina, and K. Itaya*, Langmuir*, vol. 13, no. 6, pp. 1607 – 1615, (1997).

[31] M. Schneider, *In situ Charakterisierung von Porphyrin-Schichten auf einer Iodid-modifizierten Gold(111)-Elektrode*, Diploma thesis, University of Bonn, (2009).

[32] T. Kosmala, *Selforganization phenomena of organic molecules at metal/electrolyte interfaces,* Master Thesis, University of Wroclaw, (2011).

[33] K. Ogaki, N. Batina, M. Kunitake, and K. Itaya, *J. Phys. Chem.,* vol. 100, no. 17, pp. 7185 – 7190, (1996).

[34] K. Sashikata, T. Sugata, M. Sugimasa, and K. Itaya, *Langmuir*, vol. 14, no. 10, pp. 2896 – 2902, (1998).

[35] Nguyen Thi Minh Hai, *Preparation and characterization of copperiodide thin films and organic supramolecular layers at copper/electrolyte interfaces,* PhD thesis, University of Bonn, (2007).

[36] Southampton Electrochemistry Group, University of Southampton, *Instrumental methods in electrochemistry,* Horwood Publishing, (Copyright © 2001). ISBN: 1-898563-80-2.

[37] F. Scholz (Ed.), *Electroanalytical Methods: Guide to Experiments and Applications,* Springer-Verlag Berlin Heidelberg, (Copyright © 2002). ISBN: 3-540-42229-2.

[38] J. Wang, *Analytical Electrochemistry*, Wiley-VCH Publishing, (Copyright © 2001). ISBN: 0-471-22823-0.

[39] http://www.cartage.org.lb/en/themes/sciences/Chemistry/Electrochemis/Electrochemical/ ElectricalDouble/ElectricalDouble.htm (accessed April 2010).

[40] G. Binnig and H. Rohrer, *Surface Science*, vol. 126, pp. 236-244, (1983).

[41] R.L. Liboff, *Introductory quantum mechanics,* Addison-Wesley Publishing, (Copyright © 1980). ISBN: 0-201-12221-9.

[42] D. Grodzińska, *Badanie charakteru wzrostu Pb (<1 ML) na powierzchni (110) kryształu molibdenu z zastosowaniem skaningowej mikroskopii tunelowe,* Master thesis, University of Wrocław, (2007).

[43] C. J. Chen, *Introduction to Scanning Tunneling Microscopy*, Oxford University Press Publishing, (Copyright © 1993). ISBN:0-19-507150-6.

[44] M. Wilms, M. Kruft, G. Bermes, and K. Wandelt, *Rev. Sci. Instrum.*, vol. 70, no. 9, pp. 3641–3650, (1999).

[45] C. G. Schlaup, *Rastertunnelmikroskopische Untersuchungen zur Elektrochemie kupfermodifizierter Au(111)-Elektroden in alkalischen sulfidhaltigen Elektrolyten,* Diploma thesis, University of Bonn, (2005).

[46] "Gold." http://en.wikipedia.org/wiki/Gold (accessed May 2010).

[47] http://www.webelements.com/gold/ (accessed May 2010).

[48] Xiao-Qian Wang, *Phys. Rev. Let.*, vol. 67, no. 25, pp. 3547-3550, (1991).

[49] D. M. Kolb, J. Schneider, *Sur. Sci.,* vol. 162, pp. 764-775, (1985).

[50] X. Gao, G. J. Edens, A. Hamelin, M. J. Weaver, *Sur. Sci.*, vol.296, is. 3, pp. 333-351, (1993).

[51] X. Gao, G. J. Edens, Fan-Chen Liu, A. Hamelin and M. J. Weaver, *J. Phys. Chem.*, vol. 98, pp. 8086-8095, (1994).

[52] J. Valenzuela-Benavides, M. Herrera-Zaldivar, *Sur. Sci.*, vol. 592, pp. 150-158, (2005).

[53] K. Yamazaki, K. Takayanagi, Y. Tanishiro and K. Yagi, *Sur. Sci.*, vol. 199, pp. 595-608, (1988).

[54] H. Zhang, Y. Sun, P. Zhang, K. Ye, J. Zhang and Y. Wang, *Chinese Science Bulletin,* vol. 50, pp. 1699-1702, (2005).

[55] H. Ibach, C. E. Bach, M. Giesen, A. Grossmann, Surf. Sci. 375, pp. 107-119, (1997).

[56] Thanh Hai Phan, *In-situ characterization of self-assembled organic layers at anion modified metal/electrolyte interfaces,* PhD thesis, University of Bonn, (2012)

[57] O. M. Magnussen, *Chem. Rev.*, vol. 102, no. 3, pp. 679-726, (2002).

[58] P. H. Qi, J. B. Hiskey, *Hydrometallurgy,* vol. 32, pp. 161-179, (1993).

[59] G. S. Kottas, L. I. Clarke, D. Horinek, and J. Michl, *Chem. Rev.*, vol. 105, no. 4, pp. 1281–1376, (2005).

[60] D. M. Vriezema, M. C. Aragones, J. A. A. W. Elemans, J. J. L. M. Cornelissen, A. E. Rowan, and R. J. M. Nolte*, Chem. Rev.*, vol. 105, no. 4, pp. 1445–1489, (2005).

[61] X. L. Guo, Z. C. Dong, A. S. Trifonov, K. Miki, K. Kimura, and S. Mashiko, *Appl. Surf. Sci.*, vol. 241, no. 1-2, pp. 28–32, (2005).

[62] X. L. Guo, Z. C. Dong, A. S. Trifonov, K. Miki, K. Kimura, and S. Mashiko, *Appl. Phys. A*, vol. 81, no. 2, pp. 367–370, (2005).

[63] F. Buchner, V. Schwald, K. Comanici, H. P. Steinruck, and H. Marbach, *ChemPhysChem,* vol. 8, no. 2, pp. 241–243, (2007).

[64] K. Flechtner, A. Kretschmann, L. R. Bradshaw, M. M. Walz, H. P. Steinruck, and J. M. Gottfried, *J. Phys. Chem. C*, vol. 111, no. 16, pp. 5821–5824, (2007).

[65] A. Kretschmann, M. M. Walz, K. Flechtner, H. P. Steinruck, and J. M. Gottfried, *Chem. Commun.*, vol. -, no. 6, pp. 568–570, (2007).

[66] J. M. Gottfried, K. Flechtner, A. Kretschmann, T. Lukasczyk, and H. P. Steinruck, *J. Am. Chem. Soc.,* vol. 128, no. 17, pp. 5644–5645, (2006).

[67] Y. He, T. Ye, and E. Borguet, *J. Am. Chem. Soc.*, vol. 124, pp. 11964–11970, (2002).

[68] W. Mizutani, M. Shigeno, M. Ono, and K. Kajimura, *Appl. Phys. Lett.,* vol. 50, no. 20, pp. 1974-1976, (1990).

[69] C. L. Claypool, F. Faglioni, W. A. Goddard III, H. B. Gray, N. S. Lewis and R. A. Marcus, *J. Phys. Chem. B*, vol. 101, pp. 5978-5995, (1997).

[70] http://www.surfacesciencenetwork.com/theses/YunBaiDissertation.pdf

[71] K. Gentz, and K. Wandelt, *Chimia*, vol. 66, no. 1/2, pp. 1-7, (2012).

[72] W. Schmickler, *Chem. Rev.*, vol. 96, pp. 3177-3200, (1996).

[73] J. Pan, T. W. Jing, S. M. Lindsay, *J. Phys. Chem.*, vol. 98, no. 16, pp. 4205–4208, (1994).

[74] A. Vaught, T. W. Jing, S. M. Lindsay, *Chem. Phys. Lett.*, vol. 236, pp. 306-310 (1995).

[75] K. L. Sebastian, G. Doyen, *Surf. Sci. Lett.*, vol. 290, pp. L703-L710, (1993).

[76] G. Nagy and T. Wandlowski, *Langmuir*, vol. 19, pp. 10271-10280, (2003).

[77] W. Schindler, M. Hugelmann, *Surf. Sci.*, vol. 541, pp. L643-L648, (2003).

[78] Thanh Hai Phan and K. Wandelt, *Int. J. Mol. Sci.,* vol. 14, pp. 4498-4524, (2013).

[79] Thanh Hai Phan and K. Wandelt, *Surf. Sci.*, vol. 607, pp. L82-L91, (2013).

[80] S. Huemann, N. T. M. Hai, P. Broekmann, K. Wandelt, H. Zajonz, H. Dosch, and F. Renner, *J. Phys. Chem. B*, vol. 110, no. 49, pp. 24955–24963, (2006).

[81] R. Sonnenfeld and P. K. Hansma, *Science*, vol. 232, no. 4747, pp. 211-213, (1986).

Acknowledgement

First and foremost, my greatest appreciation and thanks go to Prof. Dr. Dr. h.c. Klaus Wandelt, who has been a tremendous mentor for me. I would like to thank him for his guidance over all the period of my Ph.D. studies and for allowing me to grow as a research scientist. His advice on both research as well as on my career have been invaluable. I am deeply indebted for his fundamental role in my doctoral work, for patiently supervising me, and always guiding me in the right direction. I have learned a lot from him, without his help I could not have finished my dissertation successfully.

I would also like to thank my committee members, Prof. Dr. T. Bredow, Prof. Dr. A. Lützen and Prof. Dr. W. Barthlott for dedicating a part of their limited time to the evaluation of my thesis and the related exam.

I would like to express my thanks to Dr. Michael Liesenfeld, M.Sc. Emilia Sak-Saracino, Dr. Martino Saracino and Dr. Thanh Hai Phan for introduction me into EC-STM and all colleagues and friends (too many to list here but they know who is meant!) providing support and friendship that I needed during my Ph.D. studies.

My particular gratitude goes to Hamed Alaei, for his companionship and extraordinary discussions during my time in Bonn.

Finally, I want to thank my parents and Siria, for their love and faith in me and allowing me to be as ambitious as I wanted.